Important Notice

UNIVERSITY OF CALGARY

Prestack depth migration methods for isotropic and polar anisotropic media

by

Xiang Du

A THESIS

SUBMITTED TO THE FACULTY OF GRADUATE STUDIES

IN PARTIAL FULFILMENT OF THE REQUIREMENTS FOR THE

DEGREE OF DOCTOR OF PHILOSOPHY

DEPARTMENT OF GEOLOGY AND GEOPHYSICS

CALGARY, ALBERTA

APRIL, 2007

UNIVERSITY OF CALGARY

FACULTY OF GRADUATE STUDIES

The undersigned certify that they have read, and recommend to the Faculty of Graduate Studies for acceptance, a thesis entitled "Prestack depth migration methods for isotropic and polar anisotropic media" submitted by Xiang Du in partial fulfilment of the requirements of the degree of Doctor of Philosophy.

Supervisor, Dr. John C. Bancroft, Department of Geology and Geophysics

Co-Supervisor, Dr. Don C. Lawton, Department of Geology and Geophysics

Dr. Larry R. Lines, Department of Geology and Geophysics

Dr. Edward, S. Krebes, Department of Geology and Geophysics

Dr. J. A. Rod Blais, Department of Geomatics Engineering

External Examiner, Dr. Ron Hinds, Talisman Energy Incorporated

Date

Abstract

Several prestack depth wave-equation-based migration algorithms are investigated in this thesis. The algorithms fall into two categories — those based on two-way (reverse-time) wave equations and those based on one-way wave equations (downward-continuation migration methods, such as phase-shift-plus-interpolation (PSPI), split-step Fourier method (SSF), and implicit finite-difference (IFD)). Some improvements on these methods are presented and their corresponding anisotropic depth migration algorithms are designed, analyzed and evaluated.

An operator based on finite-element and finite-difference methods is presented and analyzed for seismic modelling and reverse-time migration, which has looser stability constraints and allows irregular grids to improve the efficiency and resolution of wavefield extrapolation.

A technique is formulated for downward-continuation Fourier methods (PSPI, SSF and IFD) to implement migration from near-surface topography. These three depth migration methods are analyzed in their performance with regard to speed and resolution through numerical and field examples.

The migration methods (reverse-time, PSPI, IFD and SSF) are extended to handle transversely isotropic media (TI). Anisotropic reverse-time migration and PSPI successfully deal with tilted TI media, whereas anisotropic IFD can only process VTI media and anisotropic SSF is only suitable in simple anisotropic cases. Many numerical and physical examples are applied to validate the anisotropic migration algorithms and illustrate the characteristics of each method in terms of efficiency and resolution.

Acknowledgements

Dedication

For my family across the miles

Table of Contents

List of Tables

List of Figures

xi

List of Symbols and Abbreviations

Symbol	Definition
c_{ijkl}	Stiffness tensor
e_{ij}	Strain tensor
σ_{ij}	Stress tensor
ε, δ	P-wave anisotropy parameter defined by Thomsen
ρ	Density
θ	Phase angle
ϕ	Group angle
$v(\theta)$	Phase velocity
p	Ray parameter
$P(x,z,t)$	Pressure wavefield
v_p	P-wave phase velocity
v_{sv}	SV-wave phase velocity
g	Group velocity
M	Cartesian rotation operator
x, z	Cartesian spatial coordinates
r, θ	Polar spatial coordinates
s_x, s_z	Horizontal and vertical slowness
k_x, k_z	Horizontal and vertical wavenumber
ω	Angular frequency
Ω	Spatial domain
$\partial\Omega$	Boundary of spatial domain
A-IFD	Anisotropic implicit finite-difference method
A-Kirchhoff	Anisotropic Kirchhoff depth migration method
A-PSPI	Anisotropic phase-shift-plus-interpolation migration method
A-RT	Anisotropic reverse-time migration method
A-SSF	Anisotropic split-step Fourier method
FD	Finite-difference
FDM	Finite-difference method
FEM	Finite-element method
FE-FD	Finite-element and finite difference
FE-FDM	A combined finite-element and finite-difference method
IFD	Implicit finite-difference migration method
ODE	Ordinary differential equation
PDE	Partial differential equation
PSPI	Phase-shift-plus-interpolation migration method
RT	Reverse-time migration method
SSF	Split-step Fourier migration method
TI	Transverse isotropy (anisotropy with radial axes of symmetry)
TTI	Transverse isotropy with a tilted axis of symmetry
VTI	Transverse isotropy with a vertical axis of symmetry

Chapter One: Introduction

1.1 Overview

Areas of complex geology, such as the Canadian Foothills and mountain belts around the world, are dominated by a series of thrust faults, imbricate structures and steeply dipping formations. Conventional seismic processing, that includes such steps as scaling, deconvolution, statics and velocity analysis, the application of dip-moveout (DMO) correction, and common-midpoint (CMP) stacking, does not produce adequately valid structural images for interpretation. Seismic migration is required to provide an essential tool for sufficiently understanding complex geology by creating a true image of structures within the Earth. Migration is a process that removes the distortions from reflection records by moving reflection events to their correct spatial locations and by collapsing the diffraction energy from unmigrated records to their scattering points (Gray et al., 2001). It can be performed as post-stack or prestack, in time or depth, or in two- (2D) or three-dimensions (3D).

The CMP stack closely represents the common depth point (CDP) in simple geological areas, so the post-stack time or depth migration will provide a good image of the subsurface. In areas of complex geology, however, the CMP stack ceases to be equivalent to a zero-offset seismic section and time or depth migration prior to stacking becomes necessary (Yilmaz, 1987). For these areas, prestack depth migration can be used to provide a more interpretable subsurface image.

With the increase in the performance of computer hardware and the increasing requirements for exploration accuracy, many prestack depth migration methods have been developed. In the context of this thesis, I have organized these methods into two

categories: ray-based methods and wavefield extrapolation methods. All of these prestack depth migration methods result from either the acoustic or elastic wave equation and depend more or less on high-frequency approximation. With the concept of up-going and down-going waves split from the acoustic wave equation, the wavefield extrapolation methods can be further subdivided into one-way wave equation migrations and two-way wave equation migrations. Each migration algorithm demonstrates its own characteristic blend of speed and accuracy, which also means that the choice of migration algorithm affects the quality of the resultant seismic image.

Apart from the migration algorithm itself, there are many other factors that affect the seismic images from which interpretations are made. These include, for example, static corrections or topographic variations, the consideration of intrinsically anisotropic behaviour, and the velocity model used for the migration. The topography problem and anisotropic phenomena are more obvious in the Canadian Foothills. These factors that may affect the seismic image will be discussed in the following sections.

1.2 Depth migration algorithms

1.2.1 Ray-based and/or gridded traveltime methods

Ray-based migration methods, such as the Kirchhoff (Schneider, 1978) and Gaussian beams migrations (Hill, 1990), are the most popular methods used for 3D prestack depth migration in the oil industry. The popularity is due to their flexibility in dealing with irregularly sampled 3D datasets, relatively higher computational efficiency, and generally good imaging capabilities. The basic characteristic of ray-based methods is their dependence on ray-tracing to obtain the traveltimes that are used for the migration mapping. The ray-based migration is utilized on data in the (x, t) domain by searching the

input data along the calculated diffraction curve for the respective point scatters that are summed and placed at the corresponding image point in the (*x, z*) domain. Dependent on the traveltime calculation, Kirchhoff migration shows great versatility in handling the irregular recording geometry and capability for easy extension from isotropic algorithms to anisotropic media.

In complex geological structures, where multipathing occurs, and beneath rugose horizons such as faulted salt domes, ray-tracing may fail to obtain the proper traveltimes, thus leading to poor subsurface imaging. Recently, several methods have been developed to overcome such problems; for example, maximum-energy traveltime method (Nichols, 1996), the semi-recursive Kirchhoff migration method (Bevc, 1997), and the common-angle imaging gather migration method (Xu et al., 1998). Although these methods partially solve the multi-pathing problem, the improvements unfortunately increase algorithmic complexity and computational cost, hence losing some of the advantage of the ray-based methods. Traveltimes may also be computed directly on a grid (Popovici and Sethian, 1998) which computes the first arrival traveltimes. The use of the traveltimes could result in relatively poor imaging quality in complex structures.

1.2.2 Two-way wave equation migration method

Methods based on the full wave equation are capable of providing solutions for arbitrary complex media since all reflections, including all multiples, are involved in computations (Baysal et al., 1983; Whitmore et al., 1983; McMechan, 1983; Mulder and Plessix, 2004). Compared with Kirchhoff depth migration and the one-way wave equation methods, two-way migration methods require significantly greater computational resources. However, their advantages are that they deal with multiarrivals, have virtually no dip limitation and

enable imaging of overturned reflections. Reverse-time migration is typically representative of two-way equation migration methods, solving the two-way acoustic or elastic wave equation by backward extrapolation in time, allowing for waves propagating in all directions, and correctly handling both multiarrivals and phase changes due to caustics. Reverse-time migration has been studied in detail for many years. Chang and McMechan (1987a, 1987b) applied reverse-time migration on offset vertical seismic profiling (VSP) data and implemented reverse-time migration using the elastic wave equation. Teng and Dai (1989) used a finite-element method to complete prestack reverse-time migration for elastic waves. Chang and McMechan (1994) extended reverse-time migration from 2D to 3D elastic prestack migration. Wu et al. (1996) provided a detailed analysis of the use of high-order finite-difference schemes in 3D reverse-time migration. A lot of real data have been successfully migrated with reverse-time migration, such as prestack reverse-time depth migration of an Alberta foothills data set (the Husky experience) (Wu et al., 1998); 3D reverse-time migration for exploration-scale 3D seismic data (Mufti et al., 1998); 3D reverse-time migration of SEG/EAGE salt data set using the acoustic wave equation (Yoon, et al., 2004), and so on.

Although reverse-time migration is potentially the most accurate method in the sense of faithfully honouring the wave equation, it also faces two challenging problems: artifacts from imaging condition in the prestack migration and computational issues. Undesired reflections from interfaces in the velocity models are easily suppressed in post-stack reverse-time migration by forcing the acoustic impedance to be constant; however, the zero-lag cross-correlation imaging in prestack reverse-time migration suffers from the creation of imaging artifacts when there is complex wave propagation (Valenciano and

Biondi, 2002). Unwanted correlation to headwaves, diving waves, and backscattered waves appear as image artifacts. Direct arrivals can be muted from shot gathers prior to migration. However, backscattered waves are difficult to deal with. Yoon et al. (2004) suggested using the Poynting vector (the direction of the wavefield), to modify the zero-lag cross-correlation imaging condition. Fletcher et al. (2005) applied a directional damping term to the non-reflecting wave equation in areas of the velocity model where unwanted reflections occur. Although these solutions solve part of the problem, they require additional costs in storage and calculation on top of the already very significant costs of the method itself. Since reverse-time migration is just the finite-difference (FD) wave equation modelling run in reverse (Gray et al., 2001), it has the same problem with stability and numerical dispersion in FD modelling. To properly sample the wavefield, the size of grid cells must decrease to avoid the phenomena of numerical dispersion when the maximum frequency of the data increases. For stability reasons, the size of the time steps must decrease as the size of the grid cells decreases. Therefore, reverse-time migration method becomes the most expensive method when compared with other migration methods. Mufti et al., (1998) suggested using variable-grid finite-difference operators for 3D depth migration. Dong (2000) forwarded a finite-difference and finite-element operator (FE-FD), in which the depth direction can be partitioned with irregular grid. Du and Bancroft (2004) gave a detailed analysis of the accuracy and stability characteristics of this operator. Irregular partitioned grids are applied in the reverse-time migration to reduce the computation cost while maintaining a certain level of accuracy (Du and Bancroft, 2005).

1.2.3 One-way wave equation downward-continuation depth migration methods

In recent years, wavefield downward-continuation seismic imaging methods have been widely applied as computational power has steadily increased. Exploration for oil and gas has extended to areas with more complex structures, exhibiting strong lateral variations in seismic velocity. Wavefield downward-continuation enables geophysicists to predict wavefields in the subsurface by propagating the recorded seismic wavefield through an appropriate surface velocity model. The essence of wavefield downward-continuation depth migration methods is a recursive wavefield extrapolation based on one-way wave equations (Berkhout, 1981). The term "recursive" implies that the output wavefield from the last extrapolation is used as the input wavefield for the next extrapolation. Wavefield downward-continuation imaging methods typically show a superior capability for imaging complex structures compared with non-recursive ray-based methods such as diffraction-stack or Kirchhoff migration. It is widely accepted (Bevc and Biondi, 2002; Soubaras, 2002) that recursive extrapolators provide a more accurate solution to the wave equation over a wider range of velocities and seismic frequencies. Therefore, they can more easily deal with complex wave phenomena such as complex scattering.

Many algorithms have been developed that fall into the category of recursive wavefield extrapolation, such as the implicit finite-difference method (Claerbout, 1985); the explicit space-frequency extrapolation (often called *f-x*) method (Berkhout, 1981); phase-shift-plus-interpolation method (PSPI) (Gazdag and Sguazerro, 1984); the split-step Fourier method (Stoffa et al., 1990) and non-stationary phase shift method (NSPI) (Margrave and Ferguson, 1999). With various levels of approximation to one-way wave equations in the $x - \omega$ domain, the implicit finite-difference method results in corresponding levels of dip

accuracy by solving a linear system of coupled equations, such as 15°, 45°, 65°, 80°, and 90° accuracy finite-difference migration methods. A typical example of implicit extrapolation is the well-known 45° finite-difference method for depth migration (Claerbout, 1985). In contrast to the implicit methods of extrapolation, the *f-x* method approximates the extrapolation operator as finite impulse response filters (Berkhout, 1981) in the $x - \omega$ domain. At each frequency ω, the output wavefield is obtained by convolving the input wavefield with an extrapolator that can accommodate local velocity variations. In contrast to the extrapolation methods mentioned above in the $x - \omega$ domain, the implementation of the PSPI, NSPI and split-step Fourier methods is carried out in the $k_x - \omega$ (wavenumber-frequency) domain. The PSPI method uses a set of chosen constant reference velocities to compute reference wavefields with phase-shift in the $k_x - \omega$ domain, and interpolates the extrapolated wavefield through the reference wavefields. The accuracy of extrapolation is strongly related to the number of reference constant velocities. A split-step extrapolator decomposes the slowness field into a constant reference field and a scattering field, which is developed based on perturbation theory. This infers that the method is not very capable of handling strong lateral velocity variations. The NSPI method is a transpose of PSPI that performs a simultaneous forward-Fourier transform with wavefield extrapolation. Compared with PSPI, NSPI shows wavefront "healing" in areas with lateral velocity discontinuities while PSPI maintains discontinuities in the wavefield (Margrave and Ferguson, 1999).

1.3 Depth migration from surface topography

In mountainous areas such as the Canadian Foothills, topographic variation often exceeds several hundred meters. Static correction, assuming near-surface vertical ray-paths, is often insufficiently accurate to produce acceptable wavefields at the datum when the near-surface geology is complicated. Wave-equation redatuming is often required in these cases (Berryhill, 1984; Shtivelman and Canning, 1988). However, redatuming results in the loss of a near-surface image, which is often important for correlation analysis between a seismic image and actual geological outcrops. Direct imaging from topography improves this situation. Prestack migration from topography does not suffer from either the shortcoming of datum statics corrections or the assumption that common-mid-points (CMPs) are the same as common-reflection points (CRPs). The problem in this specific region has been addressed by several authors. Gray and Marfurt (1995) showed improved near-surface images that were migrated from topography on a Foothills model by Kirchhoff depth migration. McMechan and Chen (1990) proposed a method for performing prestack reverse-time migration directly from the recording surface. Lines et al. (1996) also applied prestack reverse-time migration with eikonal solvers and finite-difference wave equation solutions to real data. Better imaging quality of the shallow steeply-dipping reflections was obtained using prestack depth migration from topography over conventional processing from a flat datum. A technique (Reshef, 1991) downward continues the wavefield from a flat datum surface to the actual recording surface without changing the wavefield until it passes through the recording surface. Mi and Margrave (2001b) used a similar approach to carry out the NPSP migration from surface topography. A zero-velocity layer between surface and datum is set to produce a

9

downward-continuation time migration (Beasley and Lynn, 1992). The schemes of wave-equation datuming, elevation static correction and migration from surface topography are shown in Figure 1.1.

(a)

(b)

(c)
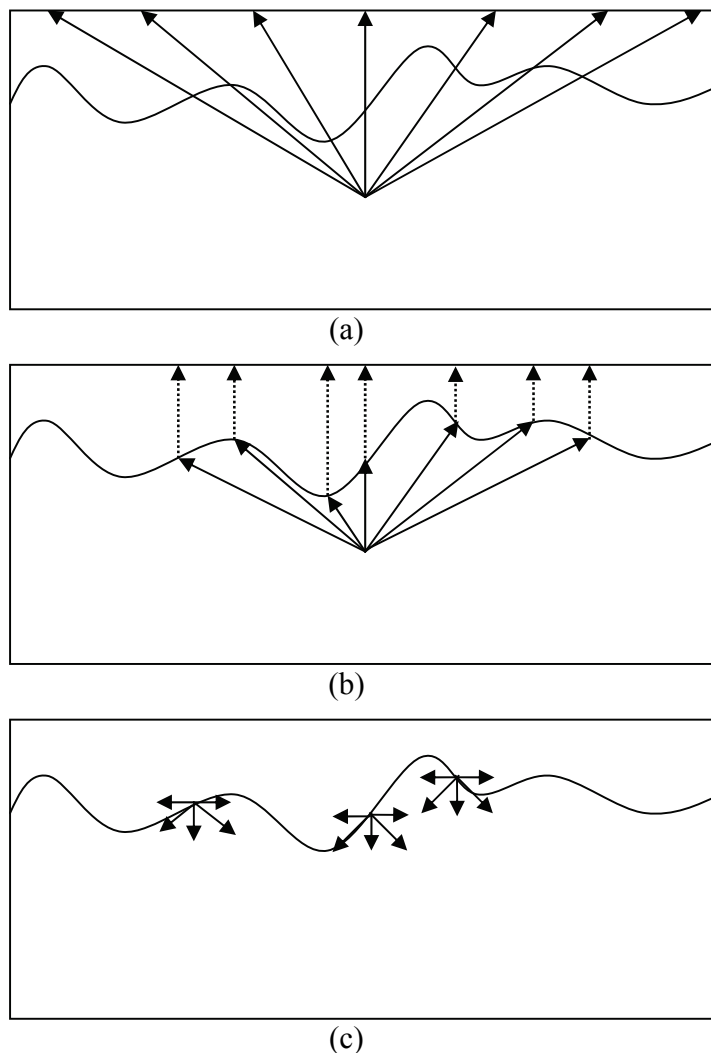
Figure 1.1 Schemes showing raypaths associated with (a) wave-equation datuming, (b) elevation static correction of a wavefield from a recording surface to a higher datum elevation, and (c) the migration from surface topography.

1.4 Anisotropic depth migration for anisotropic media

In recent years, with the increasing need for exploration accuracy, there has been increasing interest in imaging issues related to P-wave anisotropy. To this point, we can

no longer ignore seismic velocity anisotropy in seismic data processing. Laboratory and field studies (e.g. Jones and Wang, 1981; Banik, 1984; Crampin et. al, 1985; Johnston and Christensen, 1995; Vernik and Liu, 1997; Leslie and Lawton, 1999) have provided compelling evidence that shales and thin beds with alternating high and low isotropic velocities exhibit intrinsic polar anisotropy. Note that the term polar anisotropy refers to the same properties as transverse isotropy (TI). With the context of this thesis, I will use the TI term due to its common use in the literature. In these TI cases, such an assumption that anisotropy is negligible, may result in imaging problems and mispositioning errors, as has been studied by several authors (Larner and Cohen, 1993; Alkhalifah and Larner, 1994; Isaac and Lawton, 1999). Incorporating anisotropic effects in prestack depth migration can address the issue of mispositioning and misfocussing reflectors beneath dipping anisotropic layers. With more attention being paid to anisotropic effects on seismic imaging, a lot of migration algorithms have been adapted from the handling of isotropic cases to deal with anisotropic ones. Alkhalifah (1995) proposed Gaussian-beam depth migration for transversely isotropic media with vertical symmetrical axes (VTI). Kirchhoff true amplitude migration techniques (Tong et al., 1998) are applied to anisotropic media. Vestrum et al. (1999) adopted a ray-tracing algorithm to image structures below dipping TI media. Several methods have been proposed that are based on wavefield extrapolation in laterally varying VTI media. Rousseau (1997) and Ferguson and Margrave (1998) extended the phase-shift-plus-interpolation and non-stationary phase-shift methods to transversely isotropic media. Ristow and Ruhl (1997) presented an implicit 2D depth migration scheme for VTI media based on coefficients of the finite-difference equation. Han (2000) forwarded two prestack converted-wave

migration algorithms for VTI media, including anisotropic PSPI, by analytically solving k_z with the Christoffel equation and an anisotropic FD algorithm. Zhang et al. (2001) proposed a short spatial convolution operator to extrapolate the wavefields recursively in the space-frequency domain for P- and -SV waves in dipping TI media. Zhang et al. (2002) presented a finite-difference scheme for the computation of first arrival traveltime on regular grids for TI media. Baumstein and Anderson (2003) combined the phase-shift and explicit correction operators to reduce costs by using a shorter explicit correction operator. Kumar et al. (2004) carried out a 2D Kirchhoff migration based on their traveltime algorithm. Du et al. (2005) derived the P- and SV-wave equations for dipping TI media and presented the anisotropic reverse-time migration for dipping TI media. Three prestack anisotropic migration algorithms (Kirchhoff method, PSPI method and reverse-time) (Du et al., 2006) for dipping TI are evaluated with regard to speed and accuracy. Zhu et al. (2006) extended Gaussian-beam depth migration methods to handle anisotropic media.

1.5 Contributions of this thesis

As a whole, this thesis focuses on prestack depth migration algorithms. The finite-element and finite-difference (FE-FD) operator is developed and applied to the reverse-time migration to improve computational stability and efficiency. The topography problem with downward-continuation wavefield extrapolation methods is investigated, and a new technique is provided to implement prestack depth migration from surface topography, including a prestack phase-shift-plus-interpolation method, a prestack split-step Fourier method and a prestack implicit finite-difference method. For polar anisotropic media, four prestack depth migration methods (anisotropic reverse-time,

anisotropic phase-shift-plus interpolation, anisotropic implicit finite-difference and anisotropic split-step) are presented to accommodate anisotropy. The research objectives that have been achieved are shown in Table 1.1. "Yes" indicates success while "No" denotes requiring future work. A slash means not being considered in this dissertation.

Table 1.1 The migration algorithm research objectives

	Two-way wave equation	One-way wave equation downward-continuation methods		
	Reverse-time migration	PSPI	SSF	IFD
FE-FD operator (isotropy)	Yes			
Topography (isotropy)		Yes	Yes	Yes
VTI	Yes	Yes	No lateral variations	Yes
TTI	Yes	Yes	No lateral variations	No

The contributions of the thesis in detail are as follows:

1. Introduction and analysis of stability and accuracy for a FE-FD operator.

2. Introduction and analysis of a FE-FD operator with irregular grids for seismic modelling and reverse-time migration.

3. Implementation of post-stack and prestack reverse-time migrations using the FE-FD operator and traveltimes generated using the upwind finite-difference scheme based on the Eikonal equation.

4. Presentation of a new technique for downward-continuation wavefield extrapolation to implement migration from surface topography.

5. Application of this technique in (4) to prestack depth migration algorithms, such as phase-shift-plus-interpolation, split-step Fourier, and the implicit finite-difference method

from irregular surfaces, with analysis of the imaging quality and efficiency differences between them.

6. Derivation and analysis of the individual P- and SV-wave equations for tilted transversely isotropic media.

7. Implementation of an anisotropic post-stack reverse-time migration with the pseudo-spectral method (Fornberg, 1987). Stability and accuracy using the Fourier method for the anisotropic wave equation are analyzed.

8. Completion of the prestack anisotropic reverse-time migration with the zero-lag cross-correlation imaging condition, with traveltimes calculated using the anisotropic ray-tracing method for tilted TI media.

9. Analytic solution of the vertical wavenumber for the complicated quartic equation, which is derived from the dispersion equation for tilted TI media.

10. With the analytical solution for the vertical wavenumber, the post-stack and prestack anisotropic PSPI migration algorithms for tilted TI media are completed.

11. A comparison of performance, in terms of efficiency and resolution, of three anisotropic migration methods (prestack Kirchhoff depth, prestack phase-shift-plus-interpolation, and prestack reverse-time in tilted TI media) based on totally different principles.

12. Extension of the implicit finite-difference method to handle VTI media with anisotropic implicit operators obtained through Taylor series expansion and optimization methods. With the vertical wavenumber calculation in TI media, the split-step method is also extended to deal with the TI media, but using simple anisotropy parameters.

1.6 Thesis structure

In Chapter 2, a detailed theoretical review of two-way wave equation migration methods, one-way downward-continuation wave extrapolation methods, and the nature of anisotropy is given.

In Chapter 3, the theory behind the FE-FD operator is introduced and then analyzed for stability and accuracy. With this operator for irregular grids, we achieve wavefield extrapolation with greater efficiency in comparison to the conventional FD operator. Traveltime calculations using the upwind finite-difference method is introduced, which combines with the FE-FD operator to implement the prestack reverse-time migration. Post-stack and prestack depth migrations of the Marmousi dataset are generated using this operator, and the results compared alongside those using the Kirchhoff migration method and several one-way downward-continuation methods.

In Chapter 4, a new technique for one-way downward-continuation wavefield extrapolation is presented and applied to the prestack PSPI, split-step Fourier, and implicit finite-difference migration methods. A Foothills numerical model incorporating topography is used to verify the technique. Real data is also migrated from topography using the prestack Kirchhoff migration and split-step methods, to highlight some of the differences between ray-based and wave-equation-based methods. Migration from surface topography is also compared with the same after static correction.

In Chapter 5, P- and SV-wave equations are derived for tilted TI media, and analyzed for the accuracy. The pseudo-spectral method is used to solve the coupled equations and its accuracy and stability are studied. With traveltimes generated by anisotropic ray-tracing, I implement the prestack anisotropic reverse-time migration. The validity of the

anisotropic migration algorithms for both post-stack and prestack migrations, are tested using numerical and physical data.

In Chapter 6, a frequency domain equation for tilted TI media is derived, and a scheme is put forward to analytically solve this equation to obtain the vertical wavenumber, which is then applied to the phase-shift calculation in the PSPI migration algorithms. An assumption for the relationship between reference anisotropy parameters and reference lateral velocities is made to limit the number of reference wavefields. Numerical and physical data are processed to validate the post-stack and prestack anisotropic PSPI migration algorithms.

In Chapter 7, performance comparisons are made between the anisotropic Kirchhoff depth migration method and the above two newly developed anisotropic migration methods (which are based on ray theory, one-way wave equations, and two-way wave equations), focusing on speed and accuracy. Each anisotropic algorithm is also compared with its isotropic counterpart regarding computational cost.

In Chapter 8, implicit finite-difference and split-step Fourier migration methods are studied in their handling of TI media. Anisotropic implicit finite-difference method can well accommodate VTI media, whereas the anisotropic split-step method can only deal with simple anisotropic parameters in TI media. Both algorithms face challenging problems in processing tilted TI media.

In Chapter 9, I draw some final conclusions and provide future work.

Chapter Two: Reviews of prestack depth migration methods and anisotropy

2.1 Review of two-way wave equation migration method

The two-way wave equation migration method was initially described by several authors (Baysal et al., 1983; Whitmore et al., 1983; McMechan, 1983) through the use of reverse-time backward extrapolation. Mulder and Plessix (2002, 2005) used a two-way wave equation to implement the iterative migration by least-squares approximation of the seismic data. Both migration methods are based on the acoustic wave equation

$$\frac{\partial^2 P(x,z,t)}{\partial x^2} + \frac{\partial^2 P(x,z,t)}{\partial z^2} = \frac{1}{v^2}\frac{\partial^2 P(x,z,t)}{\partial t^2}, \qquad (2.1)$$

where $P(x, z, t)$ is the pressure wavefield, v is the velocity, z is the depth, x is the lateral direction, and t is the time variation. The equation is a second-order partial differential equation containing the second partial difference only. The conventional implementation of the reverse-time migration is relatively simple, only requiring the solution of a discretized version of the acoustic equation by the finite-difference method (FDM).

FDM is a very popular numerical method in geophysics as it is capable of handling complex velocity models and is efficient. The most prominent early researcher applying FDM to seismologic problems was Alterman (1968). She and her co-workers developed numerous discrete solutions to the second-order elastic wave equations in homogeneous regions through the use of explicit time integration methods. Virieux (1986) developed the first of the currently very popular staggered-grid finite-difference algorithms based on first-order equations to simulate the P-SV wave propagation. Dablain (1986) applied a high-order difference method to solve the scalar wave equation and analyzed the characteristics of temporal and spatial dispersion. A set of indices i, j and n is chosen to

establish a discretization model with different grid spacing Δx, Δy and Δt in x, y and t, respectively. We can use central uniform finite-difference schemes to approximately compute the second partial derivations (Lines et al., 1999). The conventional way to deal with temporal second-derivatives, the second-order approximation is applied, such as

$$\frac{\partial^2 P}{\partial t^2} \approx \frac{1}{\Delta t^2}(P[i]_j^{n-1} - 2P[i]_j^n + P[i]_j^{n+1}). \tag{2.2}$$

In the spatial domain, the second-order or fourth-order approximation is normally chosen, with second order being

$$\frac{\partial^2 P}{\partial x^2} \approx \frac{1}{\Delta x^2}(P[i-1]_j^n - 2P[i]_j^n + P[i+1]_j^n), \tag{2.3}$$

and fourth-order being

$$\frac{\partial^2 P}{\partial x^2} \approx \frac{1}{12\Delta x^2}(-P[i-2]_j^n + 16P[i-1]_j^n - 30P[i]_j^n + 16P[i+1]_j^n - P[i+2]_j^n). \tag{2.4}$$

For the second-order approximation, to avoid frequency dispersion, the computational grid required is considerably finer, which should be sampled at about ten points per wavelength. Higher order differences involve more operations but we need sample the wavefield at fewer points per wavelength. For 4th order in spatial domain, it is about four points per wavelength. The higher order differences in spatial domain encounter stability problems. The stability formula for finite-difference computations is

$$\frac{v\Delta t}{h} \leq \alpha, \tag{2.5}$$

where h is a grid size and α is stability limit value. As a recipe for stability in finite-difference wave equation computation (Lines et al., 1999), we can find the higher the order difference, the smaller the constraint value for stability conditions as Table 2.1.

Table 2.1 Stability limits for 1D, 2D and 3D models using second- and fourth-order finite differences (Lines et al., 1999)

Dimension	Second Order	Fourth Order
1-D	1	$\dfrac{\sqrt{3}}{2}$
2-D	$\dfrac{1}{\sqrt{2}}$	$\sqrt{\dfrac{3}{8}}$
3-D	$\dfrac{1}{\sqrt{3}}$	$\dfrac{1}{2}$

The discretized version of the acoustic equation can also be solved by the finite-element method (FEM). FEM fully discretizes the equation into a system of algebraic equations with discrete nodal values as the basic unknowns. Because of the large demands it places on computer time and memory, there has been little published work on solutions to seismic exploration problems, in comparison to the FDM. Some of the earliest applications of FEM modelling to seismic wave propagation came from the Lysmer team (Lysmer and Drake, 1972) who solved the elastic wave equations in the frequency domain. Hughes (1987) fully discretized the wave equation in the spatial domain into ordinary differential equations (ODEs) and solved them with the FDM. Kay and Krebes (1996) successfully implemented seismic modelling in non-ideal media with the FEM. The FEM was first applied to reverse-time migration by Teng and Dai (1989), who pointed out that FEM migration is a very accurate method solving the problems of arbitrary shape domain, lateral velocity variations, and complex and dipping interfaces. Dong (2002) forwarded a combined finite-element and finite-difference method (FE–FDM), which is a numerical method that partially uses FDM and FEM in the spatial domain to solve partial differential equations (PDEs). In contrast to FEM, FE-FDM semi-

discretizes the PDEs using the FEM in a partial spatial domain into a coupled system of PDEs. Therefore, these PDEs still depend continuously upon both time and space (although not all the space dimensions), and are solved with FDM. Thus, the strengths of FEM, such as adaptation to arbitrary domains and boundaries, are partially retained. The shortcomings of FEM, such as its large demand on computer memory and high computation cost, are reduced because of the semi-discretization. Compared with FDM, the computation cost is a little more due to the FEM semi-discretization. Du and Bancroft (2004) gave a detailed analysis of this method. The authors prefer to describe it as a finite-difference operator based on Galerkin's method from the viewpoint of final discretization computation, but it is still called FE-FDM to avoid confusion. With this idea, in comparison to the FD operator of the same order accuracy, the FE-FD operator exhibits looser stability limit. The difference between the FD and FE-FD operators is simply shown in Figure 2.1 where 2nd order FD operators are involved in five points' calculations whereas 2nd order FE-FD operators require nine points at the centre time slice. Making full use of the irregular discretization along the depth direction, Du and Bancroft (2005) showed improved efficiency with these irregular grids for reverse-time migration. More details of this method will be presented in Chapter 3.
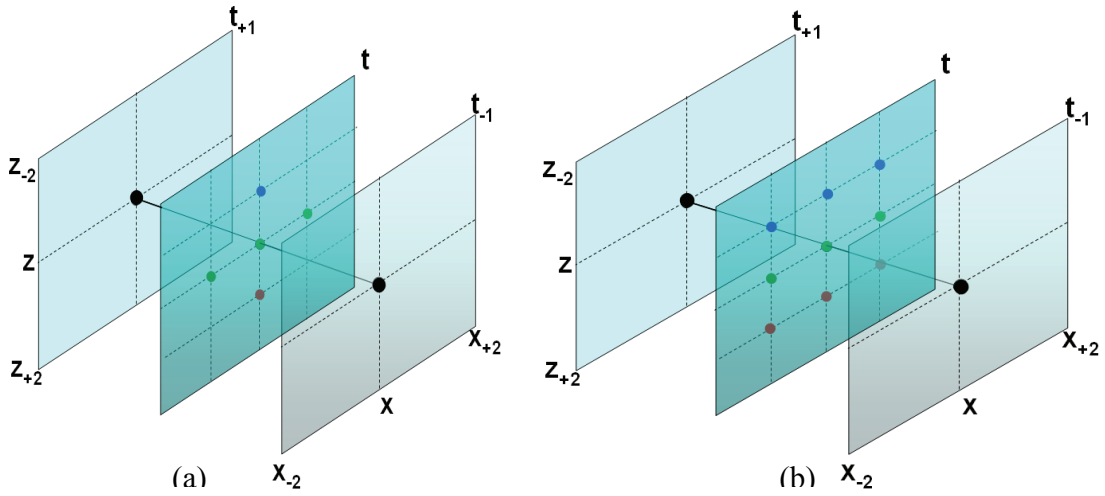
Figure 2.1 FD and FE-FD operators: (a) conventional 2nd order FD operators; (b) 2nd order FE-FD operators.

2.2 Review of one-way wave equation extrapolation methods

Again starting from the 2D acoustic wave equation (Equation (2.1)), with a spatial Fourier transform in the z direction and a temporal Fourier transform, we have the equation in the frequency-wavenumber domain

$$\frac{\partial^2 P}{\partial z^2} = (k_x^2 - \frac{\omega^2}{v^2})P,$$ (2.6)

where k_x is the wavenumber in the lateral (i.e. x-) direction, and ω is the frequency. Taking the Fourier transform in the z-direction, we can obtain the frequency-dispersion relationship (Yilmaz, 1987)

$$k_x^2 + k_z^2 = \frac{\omega^2}{v^2},$$ (2.7)

or

$$k_z = \pm\sqrt{\frac{\omega^2}{v^2} - k_x^2};$$ (2.8)

and its corresponding one-way wave equation,

$$\frac{\partial P}{\partial z} = \pm i k_z P , \qquad (2.9)$$

where the $\pm$ signs denote the downward and upward wavefields, respectively. Analytical solutions for this one-way wave equation are

$$P(z + dz, k_x, \omega) = P(z, k_x, \omega) e^{\pm i k_z dz} . \qquad (2.10)$$

Wavefield extrapolation involves a simple phase-shift in the frequency-wavenumber domain.

2.2.1 The PSPI method

PSPI is a rational attempt to build an approximate extrapolation through $v(x)$ from a set of reference velocities, $\{v_j\}$. To implement wavefield extrapolation from $z = 0$ to $z = \Delta z$, we go through the following steps: After an initial Fourier transform over time, we have the wavefield $P(x, 0, \omega)$ at $z = 0$, where ω is the temporal frequency. Phase-shift extrapolation with each v_j produces a reference wavefield $P_{vj}(x, \Delta z, \omega)$, which is given by

$$P_{vj}(x, \Delta z, \omega) = \int_{-\infty}^{+\infty} \varphi(k_x, 0, \omega) \alpha_{vj}(k_x, \omega) e^{i k_x x} dx , \qquad (2.11)$$

where

$$\varphi(k_x, 0, \omega) = \int_{-\infty}^{+\infty} P(x, 0, \omega) e^{-i k_x x} dk_x , \qquad (2.12)$$

is the forward Fourier transform of the input data in the frequency domain, and the phase-shift operator, α_{vj}, is

$$\alpha_{vj}(k_x,\omega) = \begin{cases} e^{i\Delta z k_{zj}}, |k_x| \leq \dfrac{\omega}{v_j} \\ e^{-|i\Delta z k_{zj}|}, |k_x| > \dfrac{\omega}{v_j} \end{cases}, \qquad k_{zj} = \sqrt{\dfrac{\omega^2}{v_j^2} - k_x^2} \,. \qquad (2.13)$$

The definition of phase-shift operator, α_{vj}, ensures that evanescent energy suffers from exponential decay. A fundamental assumption for PSPI is that the desired extrapolation is equivalent to a reference velocity. That is

$$P_{v(x)}(x,\Delta z,\omega) = P_{vj}(x,\Delta z,\omega), \qquad (2.14)$$

if $v(x) = v_j$.

An approximation to $P_{v(x)}(x,\Delta z,\omega)$ is formed by some sort of linear (in terms of velocity) interpolation (LI),

$$P_{v(x)}(x,\Delta z,\omega) = \mathrm{LI}(P_{vj}(x,\Delta z,\omega), P_{vj+1}(x,\Delta z,\omega)), \text{ where } v_j \leq v(x) \leq v_{j+1}. \quad (2.15)$$

To maintain high accuracy for small dip, Gazdag and Sguazzero (1984) introduced a laterally varying time-shift in the $x - \omega$ domain as a pre-processor for the input data. The modified field $P^*(x,\Delta z,\omega)$ is

$$P^*(x,\Delta z,\omega) = P(x,\Delta z,\omega)e^{i\frac{\omega}{v(x)}dz} \,. \qquad (2.16)$$

So PSPI turns into a dual-domain method. In the wavenumber domain, the time-shift will be compensated by the $\dfrac{\omega}{v_j}dz$ term and the phase-shift item will be rewritten as

$$\alpha_{vj}(k_x,\omega) = \begin{cases} e^{i\Delta z(k_{zj}\mp\frac{\omega}{v_j})}, |k_x| \leq \dfrac{\omega}{v_j} \\ e^{-|i\Delta z k_{zj}|\mp i\Delta z\frac{\omega}{v_j}}, |k_x| > \dfrac{\omega}{v_j} \end{cases}, \qquad k_{zj} = \sqrt{\dfrac{\omega^2}{v_j^2} - k_x^2} \,. \qquad (2.17)$$

The time-shift term is important in the implementation of PSPI algorithm, and is actually nothing but the thin-lens term, which also appears in other recursive methods, such as the split-step Fourier and implicit finite-difference methods to be discussed later. The accuracy of PSPI is directly related to the number of reference velocities used at each depth step, while the number is dependent on the level of lateral velocity variation at that depth. Bagaini et al. (1995) proposed an adaptive choice for the reference velocities at each depth step determined by the statistical distribution of velocity within that depth step.

2.2.2 The split-step Fourier method

The split-step Fourier method (SSF) (Stoffa et al., 1991) involves a wavefield extrapolation in the frequency-wavenumber domain and a local velocity correction with thin-lens term in the frequency-space domain, which means that it is also a dual-domain method. SSF is based on perturbation theory, according to which we can split the laterally varying slowness field into a constant term and a small perturbation,

$$s(x,z) = s_0(z) + \Delta s(x,z),$$ (2.18)

where s_0 is the reference slowness that can be specified as the mean or average, and Δs is the variation. For an acoustic wave in the frequency domain, it is

$$\nabla^2 P(x,z,\omega) + \omega^2 s^2 P(x,z,\omega) = 0,$$ (2.19)

where $P(x,z,\omega)$ is the wavefield in the frequency and space domains. Substituting Equation (2.18) into Equation (2.19), we have

$$\nabla^2 P(x,z,\omega) + \omega^2 s_0^2 P(x,z,\omega) = -\omega^2 (2s_0\Delta s + \Delta s^2) P(x,z,\omega)).$$ (2.20)

Omitting the higher-order item Δs^2, the equation becomes

$$\nabla^2 P(x,z,\omega) + \omega^2 s_0^2 P(x,z,\omega) = -S(x,z,\omega),$$ (2.21)

where $S(x,z,\omega) = \omega^2 2s_0 \Delta s P(x,z,\omega)$. The homogenous acoustic wave equation has been transformed into the inhomogeneous wave equation by the inclusion of the source item $S(x,z,\omega)$ due to the slowness variation. The solution to the inhomogeneous equation is summarized in the following steps:

- Transform wavefield from the spatial domain to the wavenumber domain and apply a phase-shift based on the vertical wavenumber computed by the reference slowness,

$$P^*(z + \Delta z, k_x, \omega) = P(z, k_x, \omega) \exp[\pm i\sqrt{\omega^2 s_0^2 - k_x^2} \, dz]. \qquad (2.22)$$

- Inverse Fourier transform $P^*(z + \Delta z, k_x, \omega)$ back to $P^*(z + \Delta z, x, \omega)$,

$$P^*(z + \Delta z, x, \omega) = \int_{-\infty}^{+\infty} P(z + \Delta z, k_x, \omega) e^{-ik_x x} dk_x. \qquad (2.23)$$

- In the space and frequency domains, apply a second phase-shift due to the perturbation in the slowness,

$$P(z + \Delta z, x, \omega) = P^*(z + \Delta z, x, \omega) \exp[\pm i(\frac{\omega}{v(x,z)} - \frac{\omega}{v_0(z)}) dz]. \qquad (2.24)$$

The second phase-shift is also called thin-lens correction, but its sequence of operation is exactly opposite to that of PSPI. For PSPI, the thin-lens correction is done first, prior to the wavefield extrapolation in the wavenumber domain. Instead of using multiple-reference velocities to propagate the wavefield, SSF uses only one reference slowness (such as the average velocity or mean velocity), which benefits the efficiency of its algorithm compared with PSPI.

When there are strong variations in the velocity field, the perturbation theory will fail, which means more than one reference velocity has to be used for SSF. Thus with more multiple-reference velocities, the cost of SSF increases to that of PSPI.

2.2.3 The implicit finite-difference method

Since Claerbout put forward the implicit finite-difference method for migration in the early 1970s, it has been extensively used in seismic imaging. Unlike the dual-domain implementations of PSPI and SSF, implicit finite-difference also works in the frequency-space domain, which shows that it is well adapted to arbitrary lateral velocity variation. Still, starting from the one-way wave equation in the frequency-wavenumber domain, we approximate the square-root appearing in k_z with continued fractions. For the square-root function,

$$R = \sqrt{1 - S^2} \, , \tag{2.25}$$

where S denotes some variable, we have the following recurrence relationship

$$R_{n+1} = 1 - \frac{S^2}{1 + R_n} . \tag{2.26}$$

When $n \to \infty$, R_n converges to R. For the second recurrence, we have

$$R_2 = 1 - \frac{S^2}{1 + R_1} . \tag{2.27}$$

Using the Taylor series expansion, we can approximate

$$R_1 = 1 - \frac{S^2}{2} . \tag{2.28}$$

Thus we can obtain the second-order approximation,

$$R_2 = 1 - \frac{0.5S^2}{1 - 0.25S^2} . \tag{2.29}$$

Using this equation to approximate the one-way frequency-wavenumber domain equation, we get

$$k_z = \frac{\omega}{v}(1 - \frac{0.5S^2}{1 - 0.25S^2}), \tag{2.30}$$

where $S = \frac{v}{\omega}k_x$, which is the conventional 45° one-way wave equation. Further expansion can improve accuracy, but it becomes harder to implement the high-order approximation efficiently. Lee and Suh (1985) used a least-squares optimization technique to resolve the dipping limitation of the implicit finite-difference algorithm. The basic idea is to use a cascaded series to match the one-way frequency-wavenumber domain equation as

$$k_{zopt} = \frac{\omega}{v}(1 - \sum_i \frac{\alpha_i S^2}{1 - \beta_i S^2}); \tag{2.31}$$

where k_{zopt} is the optimized approximation of k_z, and $S \equiv \frac{v}{\omega}k_x$, and α_i and β_i are the coefficients. The difference between k_{zopt} and k_z is minimized by adjusting variable parameters α_i and β_i over the range of 0° to 90°. The optimization coefficients are solutions of the normal equations derived from the standard least-squares method. With the help of different pairs of optimized coefficients, the dipping accuracy can reach certain levels, such 65°, 80°, 87°, and even 90°. With the relationship $k_z \leftrightarrow -i\partial_z$ and $k_x \leftrightarrow -i\partial_x$, the frequency dispersion equation in the space-frequency domain will become

$$\frac{\partial P(x,z,\omega)}{\partial z} = -\hat{i}\frac{\omega}{v}(1+\sum_i \frac{\alpha_i S_i^2}{1+\beta_i S_i^2})P(x,z,\omega),\qquad(2.32)$$

where $\hat{i}$ denotes the image number. The factor $i\frac{\omega}{v}$ is the thin-lens that we called in PSPI and SSF algorithms, which is responsible for the time-shifting in wavefields. The second term, called the diffraction term, serves to collapse the diffraction hyperbolas of seismic data. The thin-lens term is solved analytically, and the diffraction term is solved by using an implicit finite-difference method, which is the reason for its name. Since the wavefield $P(x,z,\omega)$ of the equation is related to the time-shift wavefield $P^*(x,z,\omega)$, it can be written as

$$P(x,z,\omega) = P^*(x,z,\omega)e^{-i\omega\frac{z}{v}}.\qquad(2.33)$$

Substituting it into Equation (2.32), we have

$$\frac{\partial P^*(x,z,\omega)}{\partial z} = -\hat{i}\frac{\omega}{v}\sum_i \frac{\alpha_i S_i^2}{1+\beta_i S_i^2}P^*(x,z,\omega).\qquad(2.34)$$

Considered as one cascaded calculation, Equation (2.34) can be written as the following expression

$$\frac{\omega^2}{v^2}\frac{\partial P^*}{\partial z} + \beta_i \frac{\partial^3 P^*}{\partial z \partial x^2} + \alpha_i \frac{i\omega}{v}\frac{\partial^2 P^*}{\partial x^2} = 0.\qquad(2.35)$$

Based on the implicit finite-difference approximation, Equation (2.35) is formulated into a tri-diagonal linear system

$$aP^*_{m+1,n+1} + bP^*_{m,n+1} + aPP^*_{m-1,n+1} = cP^*_{m+1,n} + dP^*_{m,n} + cP^*_{m-1,n},\qquad(2.36)$$

with the notation of

$$a = \frac{\beta_i}{\Delta z \Delta x^2} - \alpha_i \frac{i\omega}{2v\Delta x^2}, \quad b = \frac{\omega^2}{v^2 \Delta z} - \frac{2\beta_i}{\Delta z \Delta x^2} - 2\alpha_i \frac{i\omega}{2v\Delta x^2}, \qquad (2.37)$$

and

$$c = \frac{\beta_i}{\Delta z \Delta x^2} + \alpha_i \frac{i\omega}{2v\Delta x^2}, \quad d = \frac{\omega^2}{v^2 \Delta z} - \frac{2\beta_i}{\Delta z \Delta x^2} + 2\alpha_i \frac{i\omega}{v\Delta x^2}, \qquad (2.38)$$

which can be solved efficiently using the Crank-Nicholson method. The introduction of implicit finite-difference constrains the algorithm to be stable, while explicit wavefield extrapolation (Berkhout, 1981) has problems with computation stability.

2.3 Review of anisotropy

2.3.1 Introduction to anisotropy

In traditional seismic exploration, the area of interest in the Earth is assumed to be an isotropic medium, which means that seismic velocity doesn't change with the direction of wave travel. However, the subsurface layers generally do not adhere to the simple and ideal cases that we assume. Seismic anisotropy is the variation of velocity with direction, which is widely observed in seismic exploration activities and has been measured in shales, thin beds, and fractured rock formations (Jones and Wang, 1981; Thomsen, 1986; Johnston and Christensen, 1995; Leslie and Lawton, 1999).

There are many causes for seismic anisotropy (Thomsen, 1986), including the orientation of anisotropic mineral grains, the orientation of the shapes of isotropic minerals, the orientation of cracks, and thin bedding of isotropic or anisotropic layers. The most commonly considered type of anisotropy in seismic exploration is polar anisotropy. It has an axis of symmetry and typically the axis is perpendicular to bedding. The velocities on the plane normal to this axis are identical. When this axis of symmetry is vertical, the

media is termed vertically transversely isotropic (VTI) and isotropy is limited to the horizontal plane (Figure 2.2(a)). In the case of interbedded sandstones and shales in the field, the axis of symmetry is assumed to be bedding-plane normal, which means that the velocity is the same in all directions parallel to the bedding plane while the velocity decreases in the direction normal-to-bedding. When the axis of symmetry is not vertical, the media is referred to as tilted transversely isotropic (TTI) or dipping TI, which is the type of media my study focuses on (Figure 2.2(b)). In the Canadian Foothills (Lebel et al., 1996), thick sequences of dipping sandstones and shales often overlie reservoirs in fold and thrust belts. The dipping anisotropic strata in the overburden will cause positioning errors on the seismic below if velocity isotropy is assumed during data processing and imaging.
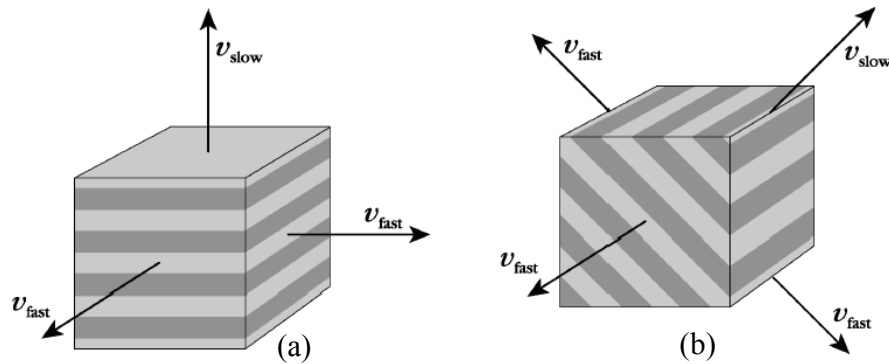
Figure 2.2 Polar anisotropic media (Vestrum, 2003): (a) transversely isotropic (TI) medium with a vertical axis of symmetry. (b) A TI medium with an arbitrarily tilted axis of symmetry.

2.3.2 Theory for polar anisotropy

In linear elastic media, the stress-strain relationship is linear and is described by the generalized Hooke's law

$$\sigma_{ij} = c_{ijkl}\varepsilon_{kl}, \quad i,j = 1,2,3, \tag{2.39}$$

where σ_{ij} is stress, ε_{ij} is strain and c_{ijkl} is the stiffness matrix. The symmetry of stress

($\sigma_{ij} = \sigma_{ji}$) and strain ($\varepsilon_{ij} = \varepsilon_{ji}$) reduces the number of independent σ_{ij} and ε_{ij} elements

to 6 and the number of independent c_{ijkl} elements to 36. The path independence of the

energy required to strain a material reduces the independent c_{ijkl} to 21 (Love, 1927).

According to the so-called "Voigt recipe", each pair of indices (*ij* and *kl*) can be replaced

by a single index: $11 \rightarrow 1$, $22 \rightarrow 2$, $33 \rightarrow 3$, $23 \rightarrow 4$, $13 \rightarrow 5$, $12 \rightarrow 6$. So the most general

stiffness matrix can be written as

$$C = \begin{bmatrix} C_{11} & C_{12} & C_{13} & C_{14} & C_{15} & C_{16} \\ & C_{22} & C_{23} & C_{24} & C_{25} & C_{26} \\ & & C_{33} & C_{34} & C_{35} & C_{36} \\ & \mathbf{SYM} & & C_{44} & C_{45} & C_{46} \\ & & & & C_{55} & C_{56} \\ & & & & & C_{66} \end{bmatrix}, \qquad (2.40)$$

where the lower left triangular portion of matrix C has been left to indicate the symmetry

of C_{mn} (e.g., $C_{mn} = C_{nm}$). The most general anisotropic model has 21 independent

stiffness elements as shown in the above matrix. For polar anisotropy (transverse

isotropy), the material only has 5 independent constants, C_{11}, C_{12}, C_{13}, C_{33} and C_{44}

(Love, 1927):

$$C = \begin{bmatrix} C_{11} & C_{12} & C_{13} & 0 & 0 & 0 \\ C_{12} & C_{11} & C_{13} & 0 & 0 & 0 \\ C_{13} & C_{13} & C_{33} & 0 & 0 & 0 \\ 0 & 0 & 0 & C_{44} & 0 & 0 \\ 0 & 0 & 0 & 0 & C_{44} & 0 \\ 0 & 0 & 0 & 0 & 0 & C_{66} \end{bmatrix}, \qquad (2.41)$$

where $C_{66} = \frac{1}{2}(C_{11} - C_{12})$. For isotropy, the matrix will reduce to

$$C = \begin{bmatrix} C_{33} & C_{33} - 2C_{44} & C_{33} - 2C_{44} & 0 & 0 & 0 \\ C_{33} - 2C_{44} & C_{33} & C_{33} - 2C_{44} & 0 & 0 & 0 \\ C_{33} - 2C_{44} & C_{33} - 2C_{44} & C_{33} & 0 & 0 & 0 \\ 0 & 0 & 0 & C_{44} & 0 & 0 \\ 0 & 0 & 0 & 0 & C_{44} & 0 \\ 0 & 0 & 0 & 0 & 0 & C_{44} \end{bmatrix}. \quad (2.42)$$

The number of independent stiffness elements becomes 3.

The wave equation for general anisotropic heterogeneous media satisfies (e.g., Aki and Richards, 1980)

$$\rho \frac{\partial^2 u_i}{\partial t^2} - \frac{\partial \sigma_{ij}}{\partial x_j} = f_i, \quad (2.43)$$

where ρ is the density, $\mathbf{u} = (u_1, u_2, u_3)$ is the displacement vector, $\mathbf{f} = (f_1, f_2, f_3)$ is the body force, t is the time and x_i is the Cartesian coordinate. Summation over $j = 1,2,3$ is implied. $i = 1,2,3$ is a free index. Substituting Equation (2.39) into Equation (2.43), we get

$$\rho \frac{\partial^2 u_i}{\partial t^2} - \frac{\partial c_{ijkl} e_{kl}}{\partial x_j} = f_i, \quad (2.44)$$

where stress (e_{kl}) is defined as

$$e_{kl} = \frac{1}{2}(\frac{\partial u_k}{\partial x_l} + \frac{\partial u_l}{\partial x_k}). \quad (2.45)$$

To give an analytic description of plane waves in anisotropic media, we make the equation homogenous by dropping the body force f:

$$\rho \frac{\partial^2 u_i}{\partial t^2} - c_{ijkl} \frac{\partial^2 u_k}{\partial x_j \partial x_l} = 0 .$$ (2.46)

The harmonic plane wave is used as a trial solution of Equation (2.46) and it is

$$u_k = U_k e^{i\omega(\frac{n_j x_j}{v} - t)} ,$$ (2.47)

where U_k are components of the polarization vector **U**, ω is the angular frequency, v is the velocity of wave propagation (usually called the phase velocity), and **n** is the unit vector orthogonal to the plane wavefront. Substituting the plane wave into Equation (2.46) leads to the so-called Christoffel equation for the phase velocity v and polarization vector **U**

$$\begin{bmatrix} G_{11} - \rho v^2 & G_{12} & G_{13} \\ G_{12} & G_{22} - \rho v^2 & G_{23} \\ G_{13} & G_{32} & G_{33} - \rho v^2 \end{bmatrix} \begin{bmatrix} U_1 \\ U_2 \\ U_3 \end{bmatrix} = 0 ;$$ (2.48)

here G_{ik} is the Christoffel matrix, which depends on the medium properties, i.e. stiffness, and the direction of wave propagation:

$$G_{ik} = c_{ijkl} n_j n_l .$$ (2.49)

Daley and Hron (1977) gave a clear solution of the Christoffel matrix to obtain three phase velocities of directional dependence:

$$\rho v_p^2(\theta) = \frac{1}{2}[C_{33} + C_{44} + (C_{11} - C_{33})\sin^2\theta + D(\theta)] ,$$ (2.50a)

$$\rho v_{SV}^2(\theta) = \frac{1}{2}[C_{33} + C_{44} + (C_{11} - C_{33})\sin^2\theta - D(\theta)] ,$$ (2.50b)

$$\rho v_{SH}^2(\theta) = C_{66} \sin^2\theta + C_{44} \cos^2\theta ,$$ (2.50c)

where θ is the phase angle between the wavefront normal and the unique (vertical) axis in Figure 2.3.

Phase (wavefront) angle θ and group (ray) ϕ
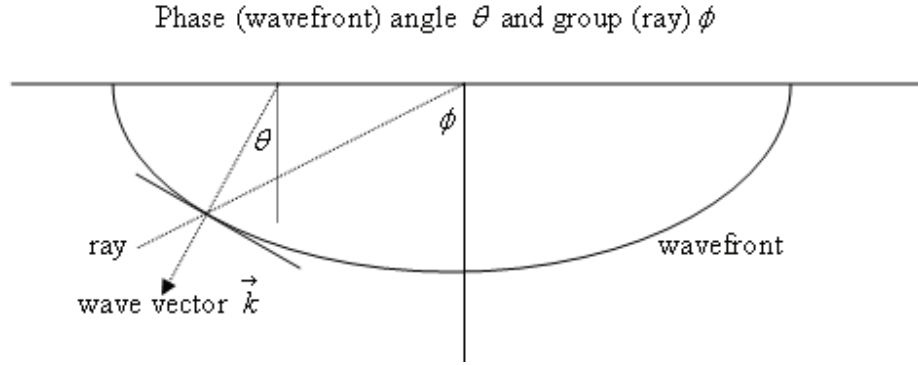
Figure 2.3 The definitions of phase (wavefront) angle and group (ray) angle (Thomsen, 1986).

$D(\theta)$ is compact notation for the quadratic combination

$$D(\theta) \equiv \{(C_{33} - C_{44})^2 + 2[2(C_{13} + C_{44})^2 - (C_{13} - C_{44})(C_{11} + C_{33} - 2C_{44})]\sin^2 \theta$$
$$+ [(C_{11} + C_{33} - 2C_{44})^2 - 4(C_{13} + C_{44})^2]\sin^4 \theta\}^{1/2} \qquad (2.51)$$

Equations 2.50(a), 2.50(b) and 2.50(c) denote the phase velocities of P-wave, SV-wave and SH-wave, respectively. When the wave travels in the horizontal ($\theta = 0°$) and vertical ($\theta = 90^0$) directions, the P-wave phase velocities become

$$v_p(0^0) = v_{p0} = \alpha_0 = \sqrt{\frac{C_{33}}{\rho}}, \text{ and } v_p(90^0) = \alpha_{90} = \sqrt{\frac{C_{11}}{\rho}}; \qquad (2.52)$$

where α_0 (v_{p0}) corresponds to the P-wave velocity measured parallel to the axis of TI symmetry and α_{90} is the P-wave velocity vertical to the axis of TI symmetry . The SV-wave phase velocities are:

$$v_{sv}(0^0) = v_{s0} = \beta_0 = \sqrt{\frac{C_{44}}{\rho}}, \quad \text{and } v_{sv}(90^0) = \beta_{90} = \sqrt{\frac{C_{44}}{\rho}}. \qquad (2.53)$$

The horizontal and vertical velocities (v_{s0} and β_{90}) are equal to each other for SV-waves. For SH-waves, we obtain

$$v_{sh}(0^0) = \gamma_0 = \sqrt{\frac{C_{44}}{\rho}} \text{ , and } v_{sh}(90^0) = \gamma_{90} = \sqrt{\frac{C_{66}}{\rho}} . \tag{2.54}$$

The SH-wave horizontal and vertical velocities (γ_0 and γ_{90}) will be the same in isotropic media due to the stiffness component $C_{44} = C_{66}$.

The phase velocities may seem trivial, but the equations discussed above have been simplified by Thomsen (1986) for practical application. Three key anisotropy parameters ε, δ and γ instead of 5 stiffness elements are defined as:

$$\varepsilon \equiv \frac{C_{11} - C_{33}}{2C_{33}}; \ \delta \equiv \frac{(C_{13} + C_{44})^2 - (C_{33} - C_{44})}{2C_{33}(C_{33} - C_{44})}; \text{ and } \gamma \equiv \frac{C_{66} - C_{44}}{2C_{44}} . \tag{2.55}$$

These three anisotropy parameters are non-dimensional and they reduce to zero for isotropic media. Definitions given for the anisotropy parameters show that their relationships are to measured velocities rather than to elastic stiffness components; ε is used to describe the P-wave velocity differences between parallel- and vertical-to TI axes of symmetry

$$\varepsilon = \frac{V_{//}^P - V_{\perp}^P}{V_{\perp}^P} = \frac{v_p(90^0) - v_p(0^0)}{v_p(0^0)} , \tag{2.56}$$

where $V_{//}^P$ and $V_{\perp}^P$ represent the horizontal and vertical P wave velocities, respectively; γ corresponds to the conventional meaning of "SH anisotropy", which is similar to ε and denoted by

$$\gamma = \frac{V_{//}^{SH} - V_{\perp}^{SH}}{V_{\perp}^{SH}} = \frac{v_{sh}(90°) - v_{sh}(0°)}{v_{sh}(0°)} , \tag{2.57}$$

where $V_{//}^{SH}$ and $V_{\perp}^{SH}$ are the horizontal and vertical SH-wave velocities, respectively; finally, Thomsen (1986) described δ in weak anisotropy as

$$\delta = 4[\frac{v_p(45°)}{\alpha_0} - 1] - \varepsilon. \tag{2.58}$$

Based on Equation (2.55), the five independent stiffness elements also can be described as the functions of v_p, v_s, ρ, ε, δ and γ:

$$C_{33} = \rho v_p^2, \tag{2.59a}$$

$$C_{44} = \rho v_s^2, \tag{2.59b}$$

$$C_{11} = (1 + 2\varepsilon)C_{33}, \tag{2.59c}$$

$$C_{66} = (1 + 2\gamma)C_{44}, \tag{2.59d}$$

$$C_{13} = \frac{1}{2}(-2C_{44} + \sqrt{(2C_{44})^2 - 4C_{33}(2C_{44}(1+\delta) - C_{33}(1+2\delta)))}. \tag{2.59e}$$

Using Thomsen's parameters to study the behaviour of the phase velocities of P- and SV-waves, we can obtain the exact P- and SV-wave phase-velocity function expressed through the Thomsen parameters (Tsvankin, 1996) as

$$\frac{v^2(\theta)}{v_{p0}^2} = 1 + \varepsilon \sin^2\theta - \frac{f}{2} \pm \frac{f}{2}\sqrt{1 + \frac{4\sin^2\theta}{f}(2\delta\cos^2\theta - \varepsilon\cos 2\theta) + \frac{4\varepsilon^2\sin^4\theta}{f^2}}, \tag{2.60}$$

where $f \equiv 1 - \frac{v_{s0}^2}{v_{p0}^2}$ is the only term containing the S-wave vertical velocity. For P-wave phase velocity, Equation (2.60) involves "+" sign calculation; the S-wave phase velocity, on the other hand, involves the "-" sign calculation in Equation (2.60). To gain analytical insight into the behaviour of phase velocity, Equation (2.60) can be simplified under the

assumption of weak anisotropy ($|\varepsilon| \leq 0.2$ and $|\delta| \leq 0.2$). Expanding the radical in

Equation (2.60) in a Taylor series and dropping quadratic terms in the anisotropy

parameters ε and δ, we have, for the P-wave,

$$\frac{v_p^2(\theta)}{v_{p0}^2} = 1 + 2\delta \sin^2 \theta \cos^2 \theta + 2\varepsilon \sin^4 \theta . \qquad (2.61)$$

Taking the square root and linearizing Equation (2.61) further in ε and δ results in

Thomsen's (1986) weak-anisotropy approximation:

$$v_p(\theta) = v_{p0}(1 + \delta \sin^2 \theta \cos^2 \theta + \varepsilon \sin^4 \theta) . \qquad (2.62)$$

For the SV-wave, linearizing Equation (2.60) gives the SV-wave phase velocity in

weak-anisotropy as

$$\frac{v_s^2(\theta)}{v_{p0}^2} = 1 - f + 2(\varepsilon - \delta)\sin^2 \theta \cos^2 \theta , \qquad (2.63a)$$

or

$$\frac{v_s^2(\theta)}{v_{s0}^2} = 1 + 2\sigma \sin^2 \theta \cos^2 \theta , \qquad (2.63b)$$

where σ is the following combination of Thomsen parameters (Tsvankin, 1996) and

$\sigma \equiv (\frac{v_{p0}^2}{v_{s0}^2})(\varepsilon - \delta)$. Equations (2.60), (2.61) and (2.62) will be frequently applied in the

anisotropic depth migration algorithms that comprise this thesis.

The above derivations and their corresponding equations all involve vertical transverse

isotropy. To obtain these equations for dipping TI media with the properties being

investigated, such as the stress-strain, stiffness matrix, and phase velocity, we turn to the

rotation of coordinates (Krebes, 2005). Figure 2.4 shows the dipping TI medium with two

sets of Cartesian coordinates rotated about the *y* axis. The coordinate system (*x, y, z*)

reflects the seismic observation. From the coordinate (*x', y', z'*), the dipping TI medium

becomes a VTI one. The matrix *R* describing the rotation about the *y* axis by angle θ is

$$R = \begin{bmatrix} \cos\theta & 0 & \sin\theta \\ 0 & 1 & 0 \\ -\sin\theta & 0 & \cos\theta \end{bmatrix}. \tag{2.64}$$
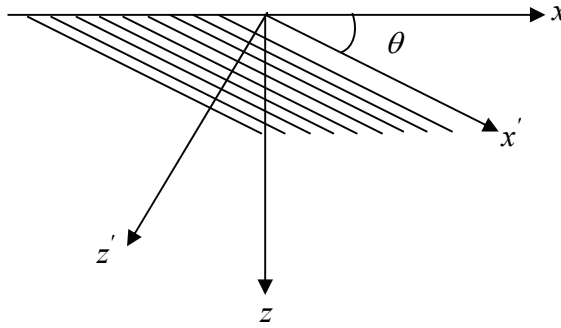
Figure 2.4 The rotation coordinates about the *y* axis.

In the observation coordinate system, with a Bond transform (Winterstein, 1990), the

stiffness matrix becomes

$$C' = MCM^T, \tag{2.65}$$

where *M* is constructed from Cartesian rotation operators:

$$M = \begin{bmatrix} R_{11}^2 & R_{12}^2 & R_{13}^2 & 2R_{12}R_{13} & 2R_{13}R_{11} & 2R_{11}R_{12} \\ R_{21}^2 & R_{22}^2 & R_{23}^2 & 2R_{22}R_{23} & 2R_{23}R_{21} & 2R_{21}R_{22} \\ R_{31}^2 & R_{32}^2 & R_{33}^2 & 2R_{32}R_{33} & 2R_{33}R_{31} & 2R_{31}R_{32} \\ R_{21}R_{31} & R_{22}R_{32} & R_{23}R_{33} & R_{22}R_{33}+R_{23}R_{32} & R_{21}R_{33}+R_{23}R_{31} & R_{22}R_{31}+R_{21}R_{32} \\ R_{31}R_{11} & R_{32}R_{12} & R_{33}R_{13} & R_{12}R_{33}+R_{13}R_{32} & R_{13}R_{31}+R_{11}R_{33} & R_{11}R_{32}+R_{12}R_{31} \\ R_{11}R_{21} & R_{12}R_{22} & R_{13}R_{23} & R_{12}R_{23}+R_{13}R_{22} & R_{13}R_{21}+R_{11}R_{23} & R_{11}R_{22}+R_{12}R_{21} \end{bmatrix}, \tag{2.66}$$

where R_{ij} is the component of Matrix **R**. Substituting Equation (2.64) to Equation (2.65),

M is

$$M = \begin{bmatrix} \cos^2\theta & 0 & \sin^2\theta & 0 & \sin 2\theta & 0 \\ 0 & 1 & 0 & 0 & 0 & 0 \\ \sin^2\theta & 0 & \cos^2\theta & 0 & -\sin 2\theta & 0 \\ 0 & 0 & 0 & \cos\theta & 0 & -\sin\theta \\ -\frac{1}{2}\sin 2\theta & 0 & \frac{1}{2}\sin 2\theta & 0 & \cos 2\theta & 0 \\ 0 & 0 & 0 & \sin\theta & 0 & \cos\theta \end{bmatrix}. \tag{2.67}$$

In the same way, when we substitute Equation (2.67) into Equation (2.65), we have a new stiffness matrix in the observation system

$$C' = \begin{bmatrix} C_{11}' & C_{12}' & C_{13}' & 0 & C_{15}' & 0 \\ C_{12}' & C_{22}' & C_{23}' & 0 & C_{25}' & 0 \\ C_{13}' & C_{23}' & C_{33}' & 0 & C_{35}' & 0 \\ 0 & 0 & 0 & C_{44}' & 0 & C_{46}' \\ C_{15}' & C_{25}' & C_{35}' & 0 & C_{55}' & 0 \\ 0 & 0 & 0 & C_{46}' & 0 & C_{66}' \end{bmatrix}. \tag{2.68}$$

After the rotation, the stiffness matrix C' is still symmetric and the number of independent elements in the matrix becomes 13, which can be applied to the elastic anisotropic wavefield simulation. With a similar derivation, substituting it into Equation (2.48), we also derive the P- and SV-wave phase velocities as:

$$\rho v_p^2(\theta) = \frac{1}{2}[(C_{11}' + C_{55}')\sin^2\theta + (C_{33}' + C_{55}')\cos^2\theta + 2(C_{15}' + C_{35}')\sin\theta\cos\theta + D'(\theta)], \tag{2.69}$$

and

$$\rho v_{SV}^2(\theta) = \frac{1}{2}[(C_{11}' + C_{55}')\sin^2\theta + (C_{33}' + C_{55}')\cos^2\theta + 2(C_{15}' + C_{35}')\sin\theta\cos\theta - D'(\theta)], \tag{2.70}$$

where

$$D'(\theta) \equiv \{[(C_{11}' - C_{55}')\sin^2\theta - (C_{33}' - C_{55}')\cos^2\theta + 2(C_{15}' - C_{35}')\sin\theta\cos\theta]^2 \\ + 4[(C_{13}' + C_{55}')\sin\theta\cos\theta + C_{15}'\sin^2\theta + C_{35}'\cos^2\theta]^2\}^{1/2} \tag{2.71}$$

Actually, we also can obtain phase velocities in dipping TI media by rotating phase angles from Equation (2.60)

$$\frac{v^2(\theta,\phi)}{v_{p0}^2} = 1 + \varepsilon \sin^2(\theta-\phi) - \frac{f}{2}$$
$$\pm \frac{f}{2}\sqrt{1 + \frac{4\sin^2(\theta-\phi)}{f}[2\delta\cos^2(\theta-\phi) - \varepsilon\cos 2(\theta-\phi)] + \frac{4\varepsilon^2\sin^4(\theta-\phi)}{f^2}}. \qquad (2.72)$$

From Equation (2.72), the P-SV phase velocities in dipping weak TI media are

$$\frac{v_p^2(\theta,\phi)}{v_{p0}^2} = 1 + 2\delta\sin^2(\theta-\phi)\cos^2(\theta-\phi) + 2\varepsilon\sin^4(\theta-\phi), \qquad (2.73)$$

and

$$\frac{v_s^2(\theta,\phi)}{v_{p0}^2} = 1 - f + 2(\varepsilon-\delta)\sin^2(\theta-\phi)\cos^2(\theta-\phi). \qquad (2.74)$$

The phase velocities of Equation (2.72) are equivalent to Equations (2.69) and (2.70), which will be verified by the following numerical tests. The anisotropy parameters chosen are $\rho = 1{,}000 kg/m^3$, $v_{p0} = 3{,}000$ m/s, $v_{s0} = 1{,}500$ m/s, $\varepsilon = 0.2$ and $\delta = 0.1$. In the first set of experiments, the dip angle is equal to 0°. In the second set, it is set at 45°. The phase velocities (P- and SV-waves) from the formula for rotating the stiffness matrix are compared with those from the formula for rotating the phase angle (including the true solution and weak approximation), which are shown in Figure 2.5. Figure 2.5(a) and Figure 2.5(b) correspond to the P- and SV-wave phase velocities with a dip angle of 0°, respectively, while Figure 2.5(c) and Figure 2.5(d) are the results of P- and SV-wave velocities with a 45° dip angle. In Figure 2.5(a) and Figure 2.5(c), there is no difference in P-wave phase velocities between rotating the stiffness matrix and rotating the phase

angle. We can reach the same conclusion for SV waves from Figure 2.5(b) and Figure 2.5(d). Due to the weak anisotropy approximation, only a small difference in P-wave velocities exists between the true formula and weak anisotropy approximation; however the difference is relatively obvious for S-wave velocities. Therefore, the weak approximation is more valid for P-waves than S-waves in weakly anisotropic media.
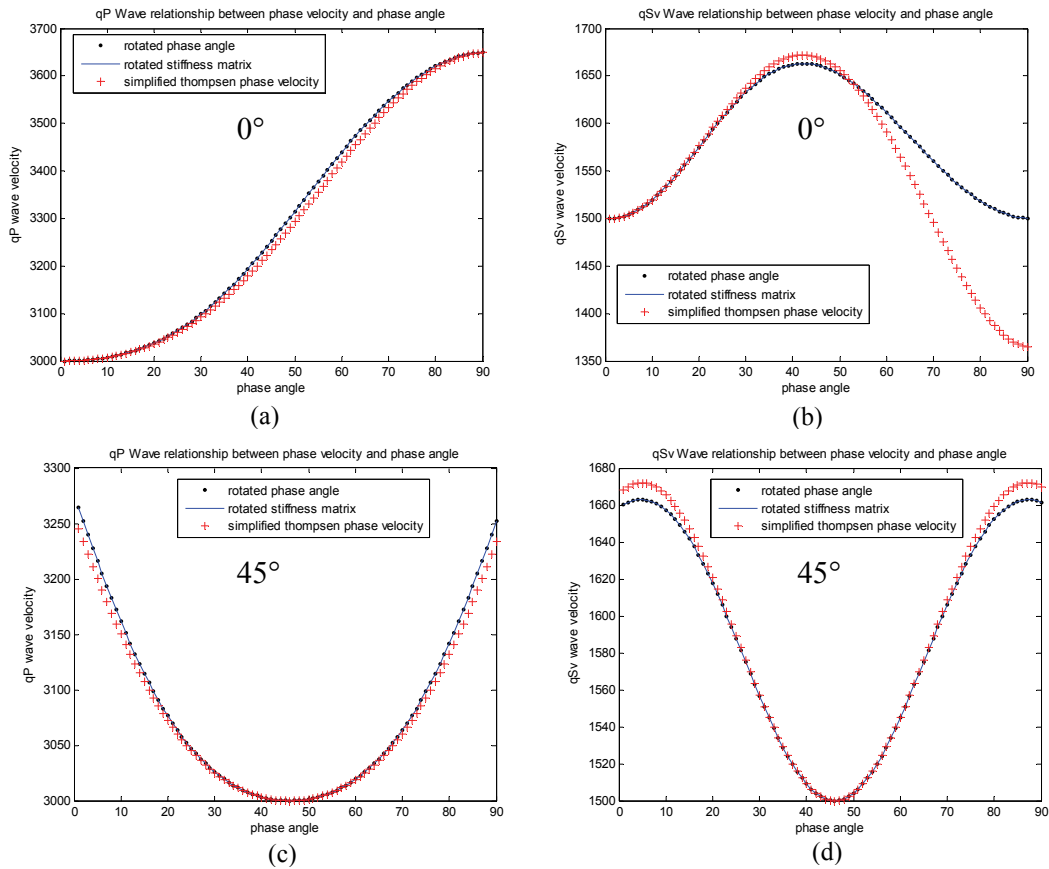
Figure 2.5 Phase velocity versus phase angle curves at different angles around the axis of symmetry. The blue solid lines in (a), (b), (c) and (d) represent the exact phase velocity from the formula for rotated symmetrical angles; the black dots denote the exact phase velocity from the formula for the rotated stiffness matrix; the red crosses show the phase velocity with linear approximation. (a) and (c) correspond to the P-wave phase velocity with 0° and 45° tilt angles around the axis of symmetry, respectively. (b) and (d) correspond to the SV-wave phase velocity with 0° and 45° tilt angles around the axis of symmetry, respectively.

Chapter Three: FE-FD operator for isotropic reverse-time migration

3.1 Introduction

In this chapter the FE-FD operator is introduced in detail. Its accuracy is analyzed and its stability limit is derived according to the order of the accuracy. The irregular grid discretization is applied for wavefield extrapolation, seismic modelling and reverse-time migration. To save hard disk space and computation cost, traveltime tables are computed using the upwind finite-difference method. These tables are used with the forward wavefields to correlate with the backward wavefield to implement prestack reverse-time with the zero-lag cross-correlation imaging condition. The post-stack and prestack Marmousi datasets are used to demonstrate the accuracy and stability of this operator. Kirchhoff and one-way wave equation downward-continuation methods are employed for comparison with the reverse-time method, and the characteristics of each method are described. The effect of traveltime accuracy on prestack reverse-time migration is also discussed.

3.2 FE-FD theory

The 2D acoustic wave equation is

$$\frac{\partial^2 u}{\partial x^2} + \frac{\partial^2 u}{\partial z^2} = \frac{1}{a^2(x,z)} \frac{\partial^2 u}{\partial t^2}, \text{ in } \Omega, \tag{3.1a}$$

where $u(x,z,t)$ denotes the wavefield at horizontal (lateral) coordinate x, vertical (depth) coordinate z, and time t, respectively; $a(x,z)$ is the medium velocity.

For seismic modelling, initial conditions are

$$u(x,z,t=0) = 0, \frac{\partial u(x,z,t=0)}{\partial t} = 0, \text{ in } \Omega, \tag{3.1b}$$

and the boundary condition is

$$u(x,z,t) = \varphi(x,z,t).$$ (3.1c)

There are five explicit boundary conditions that are required: source excitation, and the four edges of the finite-sized grid. Source excitation is solved using Alterman and Karal's (1968) approach. Absorbing boundary conditions (Clayton and Engquist, 1977) are chosen for the four edge boundary conditions.

For seismic migration, the initial conditions are

$$u(x,z,t=T) = 0, \quad \frac{\partial u(x,z,t=T)}{\partial t} = 0, \text{ in } \Omega,$$ (3.1d)

where T is the maximum traveltime. We have the top boundary condition as the form:

$$u(x,z=0,t) = \varphi(x,t).$$ (3.1e)

As for the other three boundary conditions, they are the same as the boundary conditions in the modelling. The purpose of reverse-time migration is to solve the above equation so that the recorded wavefield at t=T can propagate back to t=0.

3.2.1 FEM semi-discretization with the z-coordinate

P1 denotes the partial differential equation (Equation (3.1)). P2 denotes the corresponding Galerkin method of P1. P2 is obtained as follows:

Find $u \in S_\varphi^1$, such that for all $v \in S_0^1$

$$D(u,v) - F(v) = 0,$$ (3.2)

where

$$S_\varphi^1 = \left\{ u \mid \int \left[u^2 + \left(\frac{\partial u}{\partial z} \right)^2 \right] dz < \infty, \ u(x,z,t) = \begin{cases} \varphi(x,t) & z = 0 \\ 0 & z \neq 0 \end{cases}, \text{in } \partial\Omega \right\},$$

$$S_0^1 = \left\{ v \mid \int \left[v^2 + \left(\frac{\partial v}{\partial z} \right)^2 \right] dz < \infty, \ v(\partial\Omega) = 0 \right\},$$

$$D(u,v) = \int \left[\frac{\partial^2 u}{\partial x^2} + \frac{\partial^2 u}{\partial z^2} - \frac{1}{a^2(x,z)} \frac{\partial^2 u}{\partial t^2} \right] v dz, \ F(v) = 0.$$

$D(u,v)$ can be rewritten as

$$D(u,v) = \int_\Omega \left[\frac{\partial u}{\partial z} \frac{\partial v}{\partial z} - \frac{\partial^2 u}{\partial x^2} v + \frac{1}{a^2(x,z)} \frac{\partial^2 u}{\partial t^2} v \right] dz. \tag{3.3}$$

Semi-discretizing the vertical coordinate (z) in the region of [0, Z], we construct finite-element function space as

$$u_h(x,z,t) = \sum_{i=1}^{N_n} u_i(t,x) N_i(z), \tag{3.4a}$$

$$\frac{\partial}{\partial z} u_h(x,z,t) = \sum_{i=1}^{N_n} u_i(t,x) \frac{d}{dz} N_i(z) = \sum_{i=1}^{N_n} u_i(t,x) B_i(z), \tag{3.4b}$$

where N_n is the total number of nodes. By substituting Equations (3.3) and (3.4) into (3.2), we get the discrete style description of P2,

$$D(u_h, v_h) = \sum_{e=1}^{N_e} \int_\Omega \left[v_e^T B^T B u_e - v_e^T N^T N \frac{\partial^2 u_e}{\partial z^2} + \frac{1}{a^2(x,z)} v_e^T N^T N \frac{\partial^2 u_e}{\partial t^2} \right] dz = 0,$$

where u_e, v_e is the each cell vector, e meaning each cell. Since function v is arbitrary, this expression can be simplified as semi-discretized PDEs,

$$M \frac{\partial^2 u}{\partial t^2} + Ku = H \frac{\partial^2 u}{\partial x^2}, \tag{3.5a}$$

among them, where

$$M = \sum_{e=1}^{N_e} M_e \ , \ K = \sum_{e=1}^{N_e} K_e \ , \ H = \sum_{e=1}^{N_e} H_e \ , \tag{3.5b}$$

and

$$M_e = \int_e \frac{1}{a^2(x,z)} N^T N dz \ , K_e = \int_e B^T B dz \ , \ H_e = \int_e N^T N dz \ , \tag{3.5c}$$

where N_e is the total number of elements. It can be seen that the matrices M, K and H are all symmetric. M and H are positive-definite, and K is positive-semi-definite. It should be emphasized that only the matrix M varies with depth.

Consider a piecewise linear interpolation function. The linear element length is h and velocity is a. The interpolation function is $N(z) = \begin{cases} \xi, & z_{i-1} \leq z \leq z_i \\ 1-\xi, & z_i \leq z \leq z_{i+1} \end{cases}$, with

$\xi = \dfrac{z_{i+1} - z}{h}$, and $h = z_{i+1} - z_i$. The discretization along the z direction by the FEM can be seen in Figure 3.1. The interpolation functions at each node are shown in Figure 3.2. From them, we design the spacing interval according to the complexity of our research model.
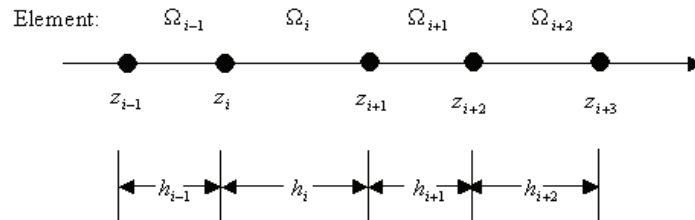
Figure 3.1 The discretization along the z direction by FEM.
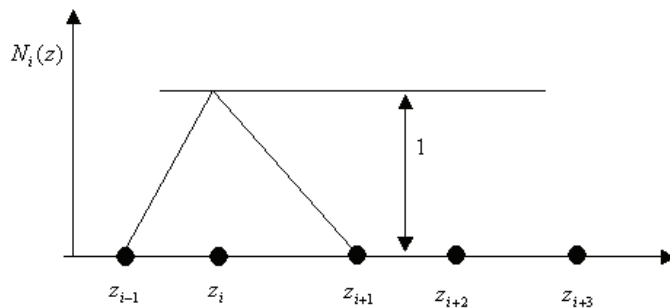
(a) The shape function at the node of z_i.
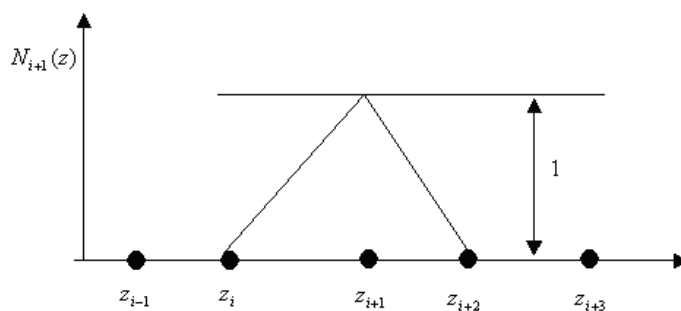
(b) The shape function at the node of z_{i+1}.
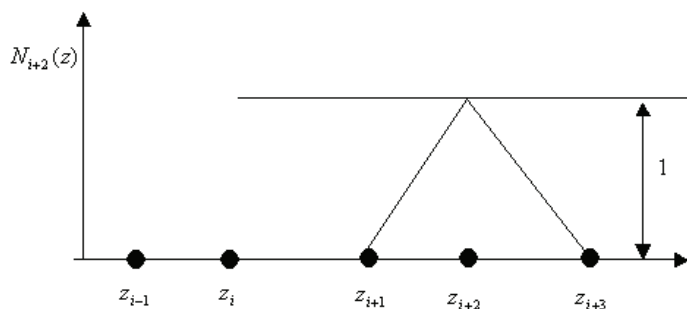
(c) The shape function at the node of z_{i+2}.

Figure 3.2 The shape function at different neighbouring nodes.

The unit matrix coefficient of Equation (3.5a) is

$$M_e = \frac{1}{6a^2}\begin{bmatrix} 2 & 1 \\ 1 & 2 \end{bmatrix}, \ K_e = \frac{1}{h^2}\begin{bmatrix} 1 & -1 \\ -1 & 1 \end{bmatrix}, \ H_e = \frac{1}{6}\begin{bmatrix} 2 & 1 \\ 1 & 2 \end{bmatrix}.$$

After all the elements are assembled, we get the global matrix. Considering the following assembled matrix A,

$$A = \begin{bmatrix} \gamma_1 & \beta_1 & & & & & & \\ \alpha_2 & \gamma_2 & \beta_2 & & & & & \\ & \alpha_3 & \gamma_3 & \beta_3 & & & & \\ & & \cdot & \cdot & \cdot & & & \\ & & & \cdot & \cdot & \cdot & & \\ & & & & \cdot & \cdot & \cdot & \\ & & & & & \alpha_{j-1} & \gamma_{j-1} & \beta_{j-1} \\ & & & & & & \alpha_j & \gamma_j & \beta_j \\ & & & & & & & \alpha_{j+1} & \gamma_{j+1} \end{bmatrix},$$

with $\alpha_{j+1} = \beta_j$ (which can denote the mass matrix and stiffness matrix), it is tridiagonal and symmetrical. When we assume the discretization has the same space interval, the assembled matrix is as follows:

and the assembled matrix M is similar to the assembled matrix H with each element divided by the velocity squared, which will be used in later numerical experiments.

3.2.2 FDM solution for matrix PDEs

A set of indices i, j and n is chosen to establish a discretization model with different grid spacing, Δx, Δy and Δt in x, y and t, respectively,

$$x = (i-1)\Delta x \qquad i = 1,2,...,I$$

$$z = (j-1)\Delta z \qquad j = 1,2,...,J$$

$$t = (n-1)\Delta t \qquad n = 1,2,...,N \,,$$

where I, J and N are the number of samples in x, z and t, respectively. One of the explicit schemes of FDM — the three-point central scheme (2nd order accuracy) or the five-point central scheme (4th order accuracy) in the x direction — is selected to solve Equation (3.5). The difference equation has the form

$$M \frac{1}{\tau^2}(u[i]_j^{n-1} - 2u[i]_j^n + u[i]_j^{n+1}) + Ku[i]_j^n = \frac{H}{l^2}(-u[i-1]_j^n + 2u[i]_j^n - u[i+1]_j^n), \quad (3.6a)$$

or

$$M \frac{1}{\tau^2}(u[i]_j^{n-1} - 2u[i]_j^n + u[i]_j^{n+1}) + Ku[i]_j^n =$$

$$\frac{H}{12l^2}(-u[i-2]_j^n + 16u[i-1]_j^n - 30u[i]_j^n + 16u[i+1]_j^n - u[i+2]_j^n) \qquad (3.6b)$$

where $u[i]_j^n$ represents the discrete value of the wavefield at the grid point (i, j) and at time n, and τ and l are the time and space steps, assumed constant. The local truncation error of this scheme has the form of $O(\tau^2 + l^2)$ (2nd order discretization in the lateral direction) or $O(\tau^2 + l^4)$ (4th order discretization in the lateral direction) (Durran, 1999). Figure 3.3 is a representation of the spatial grid computation with linear discretization

along the depth direction. In contrast to the central FDM, each grid computation at time $t - \tau$ or $t + \tau$ is related to nine points (2nd order accuracy in the x direction; Figure 3.3(a)) or fifteen points (4th order accuracy; Figure 3.3 (b)) at time t, which will affect the stability condition. As the order gets higher, the size of the operator increases, which also increases the area of assumed locally constant velocities.

(a)

(b)
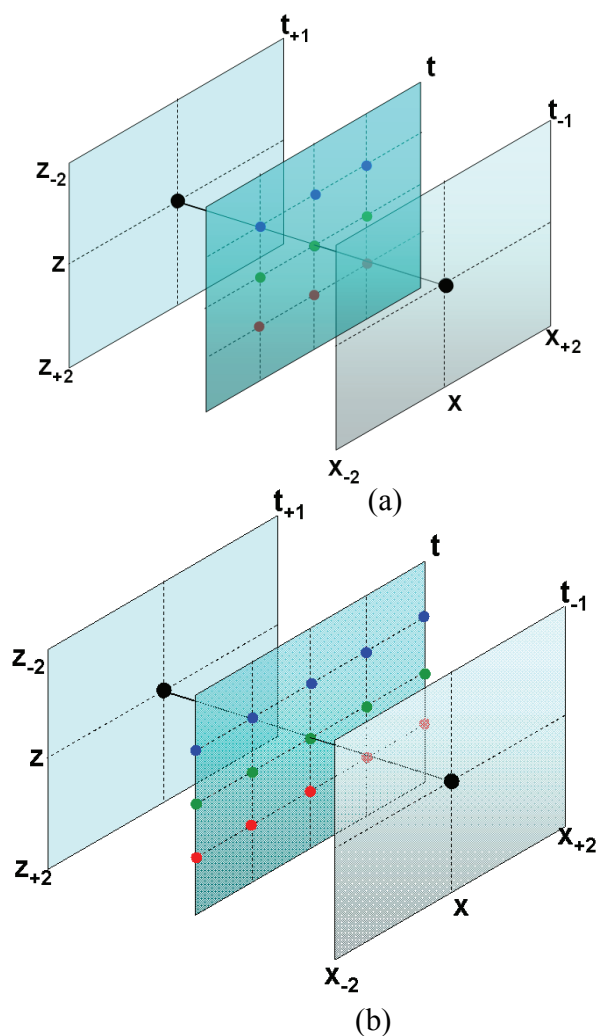
Figure 3.3 The grid computation in the space and time domains; (a) is the 2nd order accuracy finite-difference in the x direction with the linear element along the depth direction; (b) corresponds to the 4th order accuracy finite-difference in the x direction.

3.3 Accuracy and stability analysis of the FE-FD operator

3.3.1 Accuracy analysis of the 2nd order FE-FD operator

Case I: Comparison between the analytical solution and the numerical solution of the quarter-plane, and comparison between FE-FDM and FDM.

The quarter-plane problem is a particular case of the infinite-wedge problem. As underlined by Wait (1959), the solution can be found using image theory. A source S inside the medium induces three virtual image sources (Figure 3.4). Two imaging points S_x and S_z are symmetric with respect to the real source along the x-axis and z-axis edges. The third image S_c is symmetric to the real source with respect to the corner. For grid boundary conditions on the two edges, S_x and S_z are in opposite phase to S, while S_c is still in-phase with S. Waves emitted by S_c represent the constructive interference of waves emitted by S_x and S_z. This so-called corner wave is always in-phase with the incident wave. For a point source $S(x_s, z_s)$ with a time function $f(t_s)$, we can write the solution at point $M(x,z)$ as

$G(x,z,t,x_s,z_s,t_s) * f(t_s)$ incident wave,

$-G(x,z,t,x_s,-z_s,t_s) * f(t_s)$ edge reflection wave,

$-G(x,z,t,-x_s,z_s,t_s) * f(t_s)$ edge reflection wave,

$+G(x,z,t,-x_s,-z_s,t_s) * f(t_s)$ corner reflection wave,

where $G(x,z,t,x_s,z_s,t_s)$ is Green's function for the infinite medium given as

$H(t-r/c)/\sqrt{t^2 - r^2/c^2}$ with $r^2 = (x-x_s)^2 + (y-y_s)^2$.
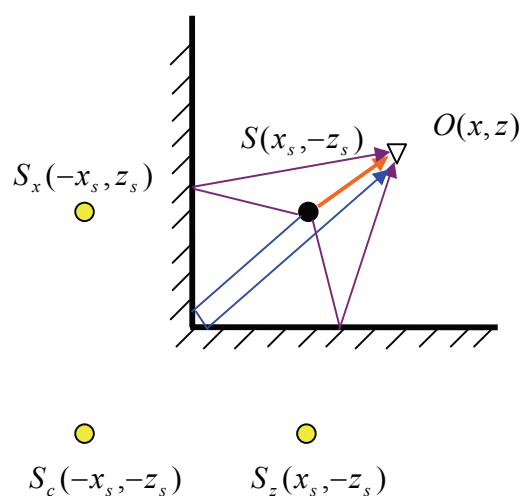
Figure 3.4 Quarter-plane geometry: Image theory interpretation.

Table 3.1 gives the physical parameters of the quarter-plane problem. Seismograms at the given points (Table 3.1) show more quantitatively the accuracy of the numerical solution in comparison to the analytical solution, given below. For the quarter-plane problem, the analytical solution and the numerical solution are shown in Figure 3.5. The solution for the two reflection pulses and one reflected impulse in-phase with the incident wave (the corner wave), is accurately matched between the numerical solution and the analytical solution.

Table 3.1 Quarter-plane parameters

Physical parameters	
Velocity	3000m/sec
Source and receiver information	$f_{main} = 50Hz$; source position: (250m, 250m); observer position: (150m, 150m).
Other parameters	dx = 5m, dz =5m, dt = 1.25E-3s, grid of 300*300 points
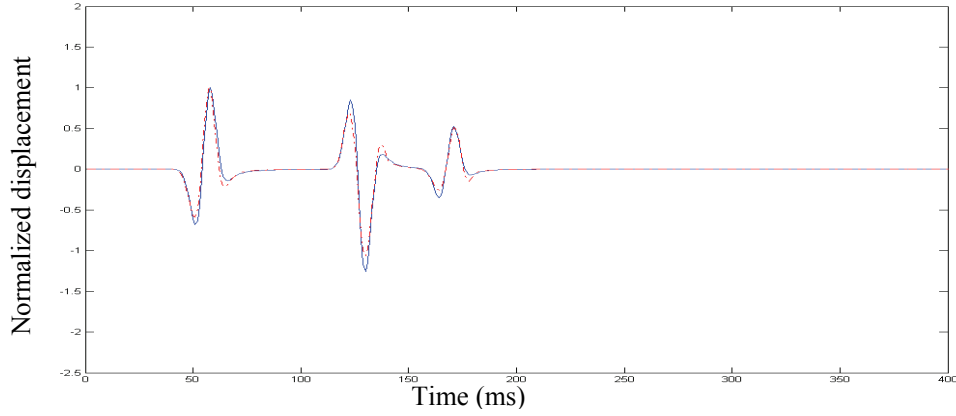
Figure 3.5 Seismogram at the given observer position (Table 3.1). The solid blue line represents the analytical solution, and the dashed red line represents the numerical solution by the FE-FDM.

3.3.2 Stability of the FE-FD operator with linear discretization along the z-direction

The computation error can be expanded in a Fourier series as

$$e_{i,j}^n = \sum_p \sum_q \Gamma_{p,q}^n \exp(\iota\, pi\Delta x)\exp(\iota\, qj\Delta z),$$

where $\iota = \sqrt{-1}$ and $\Gamma_{p,q}^n$ is a complex coefficient. It is sufficient to consider only one component

$$e_{i,j}^n = \Gamma^n \exp(\iota\, pi\Delta x)\exp(\iota\, qj\Delta z). \tag{3.7}$$

Considering the stability of Equation (3.6b), which has 2nd order FD accuracy in the time domain and 4th order FD in the x direction with linear discretization along the z direction, we substitute Equation (3.7) into Equation (3.6b) and obtain

$$\Gamma^{n+1} = -\Gamma^{n-1} + 2A\Gamma^n, \tag{3.8}$$

where

$$A = 1 + g_{i,j}^Z[\cos(q\Delta z) - 1] + \frac{1}{2}g_{i,j}^X[-\frac{1}{6}\cos(2p\Delta x) + \frac{16}{6}\cos(p\Delta x) - \frac{30}{6}][\frac{4}{6} + \frac{2}{6}\cos(q\Delta z)],$$

with $g_{i,j}^X = \dfrac{v_{i,j}^2 (\Delta t)^2}{(\Delta x)^2}$, and $g_{i,j}^Z = \dfrac{v_{i,j}^2 (\Delta t)^2}{(\Delta z)^2}$. Since A is real, the real part and the imaginary

part of Γ^n satisfy the same equation. So we can simply treat Γ^n as a real quantity.

Equation (3.8) is replaced by

$$\gamma^2 - 2Ar + 1 = 0. \tag{3.9}$$

Stability is assured if $-1 \le A \le 1$ as indicated by the computation result of Wu et al.

(1996). This requirement on A yields the result,

$$-1 \le 1 + g_{i,j}^Z \left\{ [\cos(p\Delta x) - 1] + \frac{1}{2} g_{i,j}^X [-\frac{1}{6}\cos(2p\Delta x) + \frac{16}{6}\cos(p\Delta x) - \frac{30}{6}][\frac{4}{6} + \frac{2}{6}\cos(q\Delta z)] \right\} \le 1. \tag{3.10}$$

We assume $\overline{g}_{i,j} = \dfrac{v_{i,j}^2 (\Delta t)^2}{\overline{h}}$, with $\overline{h} = \sqrt{\dfrac{2}{\dfrac{1}{(\Delta x)^2} + \dfrac{1}{(\Delta z)^2}}}$.

If $\Delta x = \Delta z = h$, the Equation (3.10) reduces to

$$-1 \le 1 +$$
$$\overline{g}_{i,j} \left\{ (\cos(q\Delta z) - 1) + \frac{1}{36}[2 + \cos(q\Delta z)(-\cos(2p\Delta x) + 16\cos(p\Delta x) - 30)] \right\} \le 1, \tag{3.11}$$

where $\overline{g}_{i,j}$ becomes $\overline{g}_{i,j} = \dfrac{v_{i,j}^2 (\Delta t)^2}{h^2}$. In order to analyze the Equation (3.11), we suppose

that

$$f(x,z) = (z-1) + \frac{1}{36}(2+z)[-(2x^2-1) + 16x - 30] \quad x,z \in [-1 \ \ 1], \tag{3.12}$$

where x denotes $\cos(p\Delta x)$, and z represents $\cos(q\Delta z)$. According to mathematical

analysis, we can know the first-order derivative of the function with respect to z has no

further dependence on z. The relationship of x, z and $f(x,z)$ is shown in Figure 3.6, and

the corresponding contour is described in Figure 3.7.
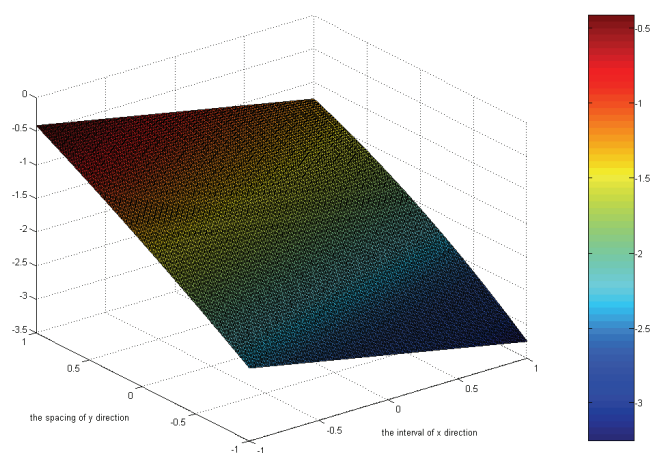
Figure 3.6 Three-dimensional graph of the objective function corresponding to the stability analysis.
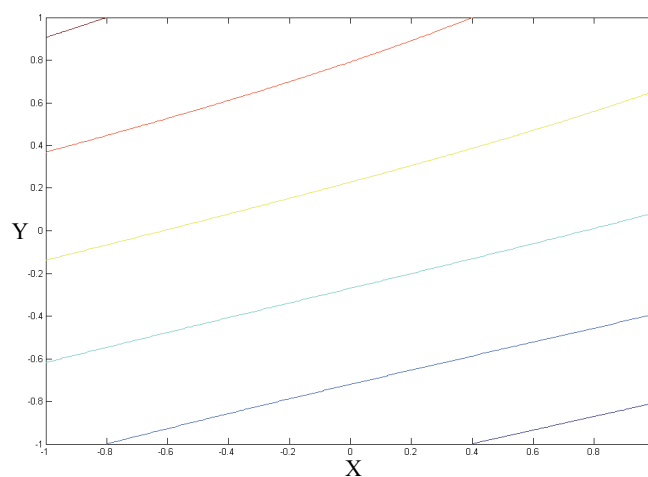
Figure 3.7 Contour graph of the objective function corresponding to the stability analysis.

By considering the variable range, we know that all of the values in it are less than zero.

So we only care about the minimum of the function. We find out that the minimum is

equal to $-\dfrac{13}{4}$ when x is equal to 1 and z is equal to -1. Hence, the Equation (3.11) can be

written as

$$\overline{g}_{i,j} = \frac{v_{i,j}^2 (\Delta t)^2}{h^2} \leq \frac{8}{13}. \tag{3.13}$$

Therefore the stability condition should satisfy

$$\frac{v_{i,j}\Delta t}{h} \leq \sqrt{\frac{8}{13}} , \qquad\qquad (3.14)$$

which is looser than the stability of second order central FDM and fourth order central

FDM (Lines et al., 1999), $\sqrt{\frac{1}{2}}$ and $\sqrt{\frac{3}{8}}$, respectively.

In the case of using the FEM in the z direction with the linear elements and using 2nd order FD in the x direction and in the time domain, we can derive the stability condition in the same way as the above derivation and find that it should satisfy

$$\frac{v_{i,j}\Delta t}{h} \leq \sqrt{\frac{3}{4}} . \qquad\qquad (3.15)$$

Hence, according to the above analysis of the stability condition, we find that the algorithm based on the FE-FDM has looser stability limits than those based on conventional FDM under the same accuracy condition.

To show the advantage of FE-FDM within the stability limit, we designed a homogenous model with the parameters shown in Table 3.2. According to the parameters and our previous analysis of the stability condition, we know the computation of the 2nd order accuracy FDM scheme will diverge, while that of FE-FDM will still remain convergent, which is also proven from the numerical simulation results shown in Figure 3.8(a) and Figure 3.8(b). Figure 3.8(a) is the result obtained from FE-FDM with 2nd order accuracy, and Figure 3.8(b) is that from 2nd order accuracy FDM. From Figure 3.8(a), we see that the wave propagates away from the source, while there is obvious numerical divergence in the traditional FD scheme from shown in Figure 3.8(b).

Table 3.2: Parameters for modelling wave propagation in a homogenous medium

Physical parameters	
Velocity	1500m/sec
Source and Observer Position	$f_{main} = 50Hz$; source position: 150*150m^2; observer time: 9ms.
Other parameters	$dx = 2m$, $dz = 2m$, $dt = 1.00E\text{-}3s$, grid of 300*300 points

(a)   (b)
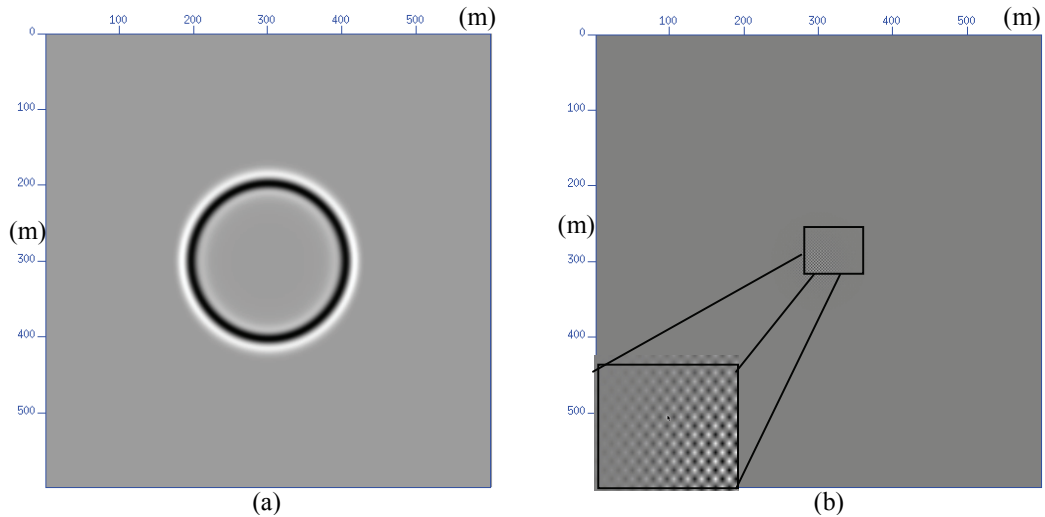
Figure 3.8 Modelling results from the FDM and FE-FDM methods. (a) Modelling by FE-FDM with 2nd order accuracy in the spaces. (b) Same modelling by 2nd order central FDM.

3.4 Wavefield extrapolation with the FE-FD operator for variable grids

In order to validate the algorithm for FE-FDM for irregular grids, three cases are chosen for modelling and migration. The numerical solution using irregular grids for the half-plane problem is compared with the corresponding analytical solution. For modelling, we present an example of efficiently modelling wave propagation in a thin-layer model. For

migration, an oblique interface model with variable velocities is chosen to show the computation efficiency of the irregular grids.

3.4.1 Comparison between the numerical solution with the irregular grids and analytical solution for the half-plane problem

For the half-plane with rigid boundary conditions, the image theory is still used. A source S inside the medium induces one virtual image source. The image $S^{'}$ is symmetric with respect to the real source. For a point source $S(x_s, z_s)$ with a time function $f(t_s)$, one can write the solution at the point $M(x, z)$ as

$$G(x, z, t, x_s, z_s, t_s) * f(t_s) \qquad \text{Incident wave,}$$

$$-G(x, z, t, x_s, -z_s, t_s) * f(t_s) \qquad \text{boundary reflection wave.}$$

Table 3.3 Half-plane parameters.

Physical parameters	
Velocity	3000 m/s
Source and Observer Position	$f_{main} = 50 Hz$; source position: (250, 250); observer position: (150, 150).
Other parameters	dx=5m, dz=4m(odd lines)/6m (even lines), dt=1.25E-3s, grids of 300×300 points

Table 3.3 gives the physical parameters of the half-plane problem. Considered the usual rule of using at least ten points for the shortest wavelength of the source in this FD scheme, the grid interval along the depth alternately changes between 4 meters and 6 meters. The seismogram at a given point (Table 3.3) shows more quantitatively the accuracy of the numerical solution in comparison to the analytical solution (Figure 3.9). They are accurately matched except small differences in the amplitude.
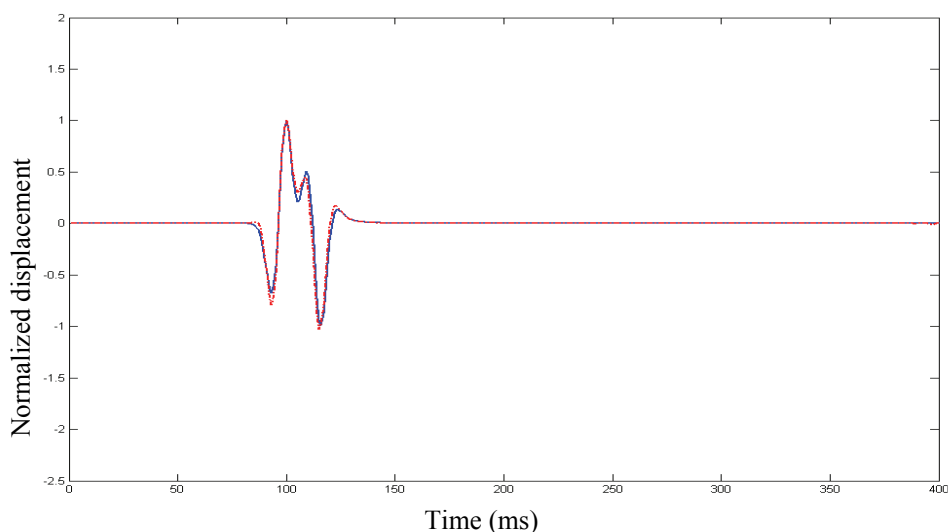
Figure 3.9 Seismogram at the given observer position (Table 3.2). The solid blue line is the analytical solution and the dashed red line is the numerical solution from FE-FDM with irregular grids.

3.4.2 Comparison between the numerical solution with regular grid and irregular grid for a thin-layer model

A thin-layer model is chosen to show the difference between FDM and FE-FDM for seismic modelling. Tests include both regular and irregular grid calculations. The size of the model is 1,500m×1,800m. A thin-layer, 12m thick, is embedded in the model. Our objective is to see if the effects of the thin-layer with lower velocity can be observed in snapshots of the wavefield. A Ricker wavelet of 50Hz is selected as the source centred in the horizontal direction and located 600m beneath the top. The velocity of the thin layer is 2,000m/s, while the background velocity is 4,000m/s, as shown in Figure 3.10. The horizontal grid spacing is 5m. For the regular grid calculation, a grid step of 6m vertical spacing is used. For the irregular mesh, the thin grid is used only in the region of lower velocity, as shown in Figure 3.10, and the grid interval is 3m. Grid spacing along the depth direction is 7m. Therefore, the regular grid requires a total of 300×300 points,

whereas the irregular one needs 300×260 points, which saves almost 24% of the points

of the regular case. The same time step ($\Delta t = 0.001$s) is used in both cases.
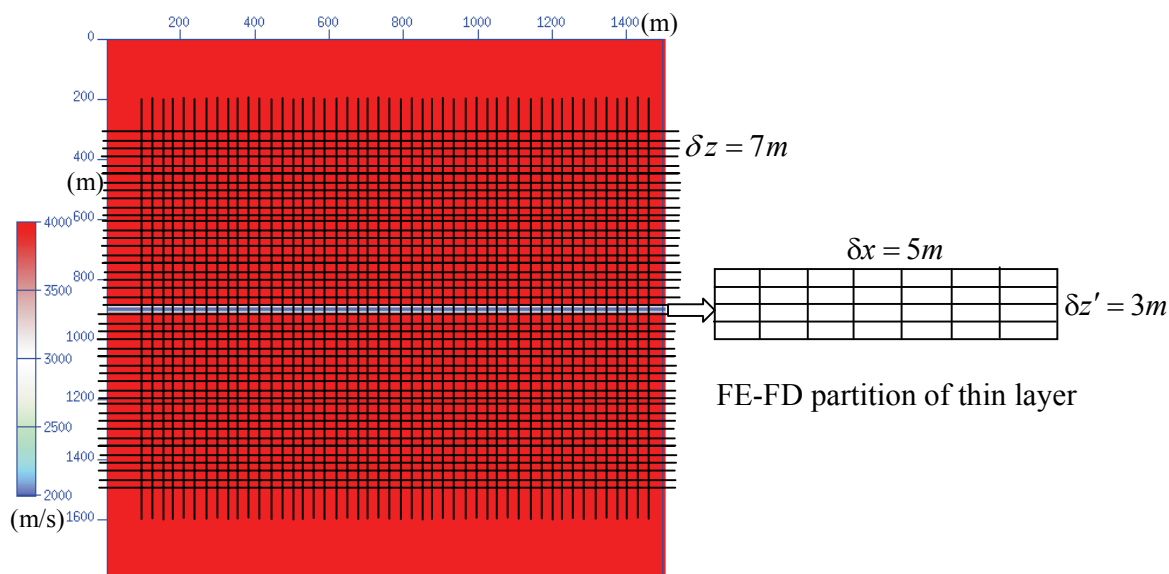
Figure 3.10 The velocity model and the grid partitions.

In order to show the result with the irregular grids, we apply a cubic spline interpolation

function to interpolate the part with the regular grids. We focus our attention on the

wavefield character when waves propagate into the thin-layer. Figure 3.11 shows a

wavefield snapshot at time 0.15s. Reflections and transmissions from the thin low-

velocity layer can be seen. In Figure 3.11 (a), there is frequency dispersion in the region

of the thin-layer because of the coarse grid used in the area, while the continuity of the

wavefield in the thin-layer is clear shown in Figure 3.11(b). Furthermore, the

computation cost with FE-DM is 85% that of FDM with the same fixed grid as identified

in Figure 3.12, which saves some computer time.

(a)   (b)
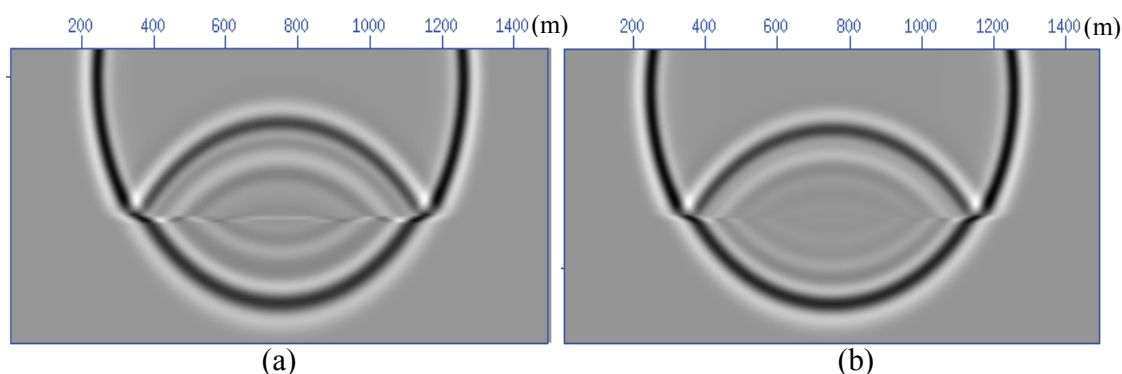
Figure 3.11 (a) Snapshot of the wavefield (*t*=0.15s) with the <u>regular</u> girds, and (b) snapshot of the wavefield (*t* = 0.15s) with the <u>irregular</u> grids.
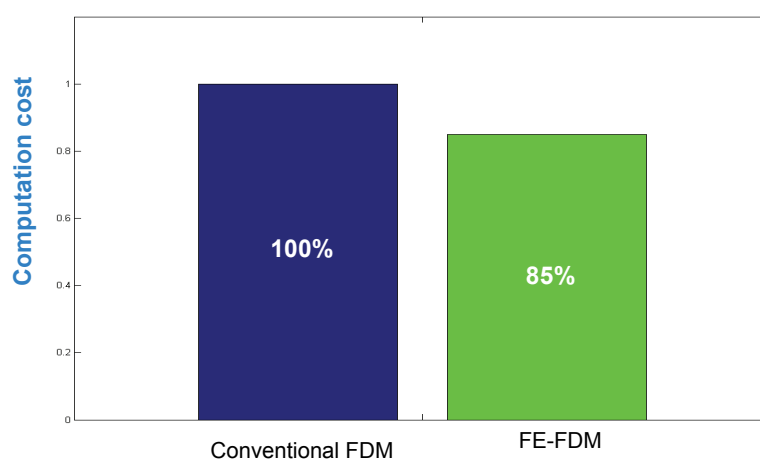
Figure 3.12 The computational efficiency comparison for modelling between FDM and FE-FDM.

3.4.3 Steeply oblique interface migration with variable velocities

The model for this section is shown in Figure 3.13. The velocity of the model increases both laterally and with depth. The velocity at the top left corner is 3,600m/s, and that at the bottom right is 4,600m/s. There are four reflection interfaces with dips of 0º, 23º, 45º, and 70º. The seismogram is computed using the ray-tracing module in the SU Software Kit, and is displayed in Figure 3.14. From it, one can see that there is a lot of diffraction energy from the edges of the reflectors.
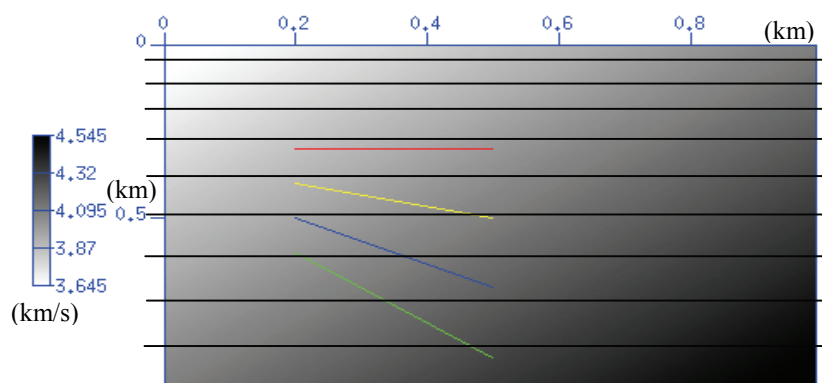
Figure 3.13 The steeply oblique model with variable velocities.
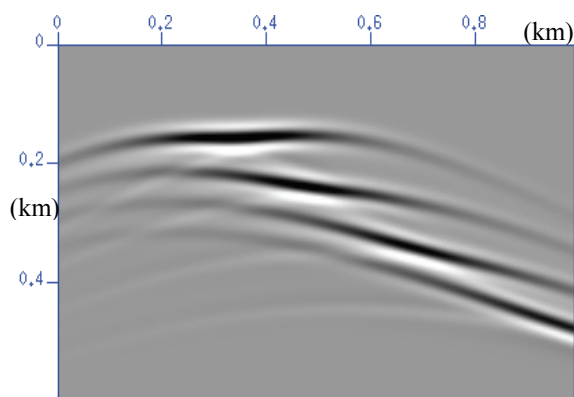
Figure 3.14 Seismogram generated by FDM.
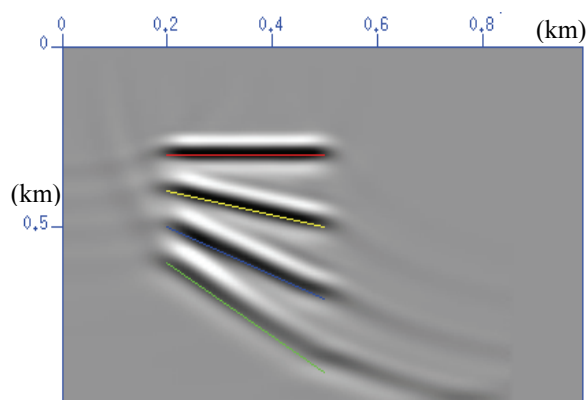
Figure 3.15 Reverse-time migration result ($\Delta z = 0.04$ m).
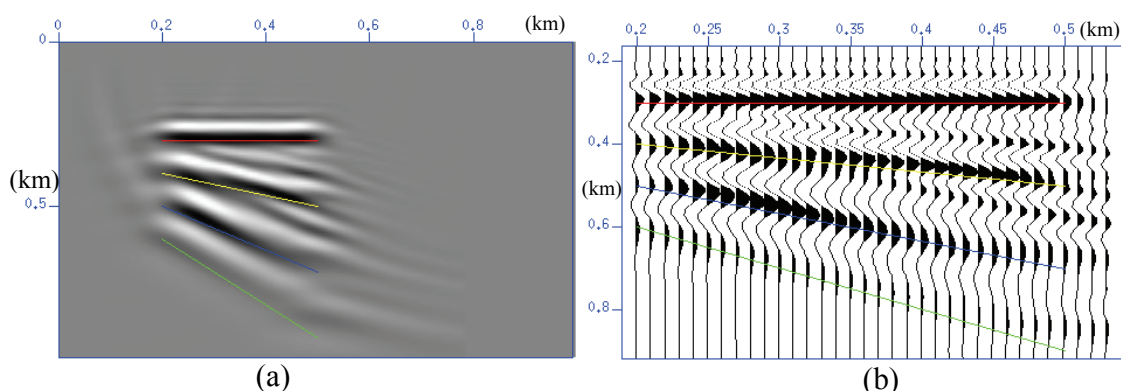
Figure 3.16 (a) A greyscale display of the reverse-time migration result ($\Delta z = 0.15m$), and (b) a wiggle trace display.

The parameters for the reverse-time migration start with a grid interval of 10m and increase by 0.04m on each grid to a final interval of 20m. The velocity increases in the spatial direction from 3,600 to 4,500m/s. The regular grid with 10m spacing requires a total of 100×100, while the irregular grid requires only 100×85, which saves some calculations. The grid partitions are also shown in Figure 3.13. Figure 3.15 is the reverse-time migration result, which correctly migrates the post-stack seismic section to the correct oblique interface. Since there is truncation of energy in the input seismogram, there is residual energy in the migration result. When the grid spacing increases to 0.15m, the irregular grid requires only 100×63, which saves a lot of memories and calculations. The migration results are shown in Figure 3.16. From Figure 3.16(a), we know there is an obvious frequency dispersion problem, but in Figure 3.16(b), there is still a good match between the events and the real interfaces. The computation cost of FE-FDM reduces to 63% that of FDM in Figure 3.17.
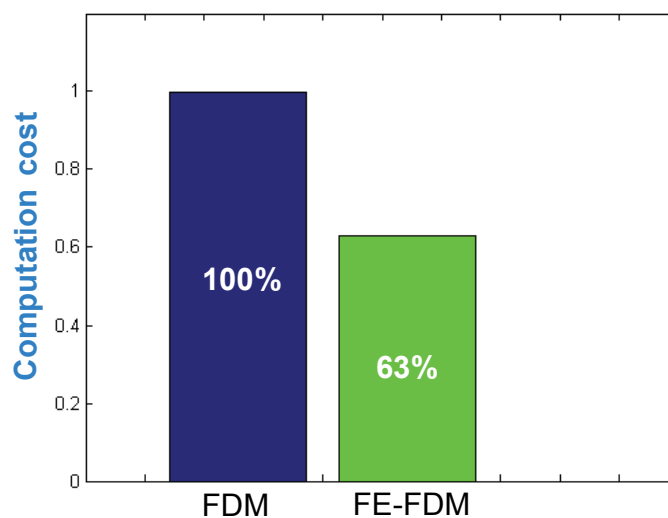
Figure 3.17 The computational efficiency comparison for reverse-time migration between FDM and FE-FDM.

3.5 Traveltime calculation with the upwind finite-difference method for prestack reverse-time migration and Kirchhoff depth migration in isotropic media

Traveltime calculations play an important role in many methods of seismic data processing such as Kirchhoff migration method, prestack reverse-time migration and seismic data modelling, which depend on traveltimes between survey points on the surface and depth points to create the velocity model. These traveltimes are often calculated by ray tracing (Cerveny and Hron, 1980); and because depth and surface points are usually distributed on a regular grid, the traveltimes along the rays are then interpolated onto the grid. For complicated velocity models, rays may cross each other or fail to penetrate shadow zones; interpolation is thus cumbersome and computationally expensive. Several methods have been introduced to calculate traveltimes directly on a regular grid. The key idea is to use a finite-difference approximation to the Eikonal equation, which is then integrated with a Runge-Kutta method. Vidale (1990)

approximated the Eikonal equation using a finite-difference scheme, and solved traveltimes directly using a planar or circular wavefront extrapolation. First-order upwind finite-difference was chosen to solve the Eikonal equation by Van Trier and Symes (1991), which is generally accurate enough. Note that this method only considers the first arrival traveltime not the maximum energy one. Based on its higher resolution, this traveltime method is applied in this thesis for Kirchhoff depth migration and prestack reverse-time migration. The basic principle will be described in the following paragraphs: The 2D Eikonal equation can be expressed as follows (Aki and Richard, 2002):

$$(\tau_x)^2 + (\tau_z)^2 = s^2(x,z),$$ (3.16)

where $s(x,z)$ is the 2D slowness of the model, $\tau(x,z)$ is the traveltime field, and subscripts x and z denote the traveltime partial derivative with respect to coordinates. Assuming the that gradient components of the Eikonal equation satisfies the hyperbolic conservation law, it can be written as

$$\tau_z = \sqrt{s^2 - u^2},$$ (3.17)

where $u = \tau_x$. Taking the derivative of Equation (3.17) with respect to x,

$$u_z = F_x(u),$$ (3.18)

where $F(u)$ is defined as (Van Trier and Symes, 1991)

$$F(u) = \sqrt{s^2 - u^2}.$$ (3.19)

$F(u)$ is conserved flux; if $F(u) = 0$, the rays cease flowing downward and travel horizontally. Thus by choosing a positive sign in front of the square root of the Eikonal

equation and by using $u = \tau_x$ instead of $w = \tau_z$ as the substitution variable, we limit our target to downward travelling rays.

As an alternate method, the Eikonal equation in polar coordinates (r, θ) can be written as

$$(\tau_r)^2 + (\frac{\tau_\theta}{r})^2 = s^2, \tag{3.20}$$

and solved along expanding circular fronts; the conserved flux function in polar coordinates becomes

$$F(u) = \sqrt{s^2 - (\frac{u}{r})^2}, \tag{3.21}$$

with $u = \tau_\theta$ satisfying

$$u_r = F_\theta(u). \tag{3.22}$$

The first-order backward and forward finite-differences in the spaces can be written respectively as

$$\Delta_- u = u_j - u_{j-1}, \tag{3.23}$$

and

$$\Delta_+ u = u_{j+1} - u_j, \tag{3.24}$$

where u_j is the discrete representation of $u(\theta)$ on the grid $\theta_j = j\Delta\theta$. The basic upwind scheme for Equation (3.22) is (Engquist and Osher, 1980)

$$\frac{u_j^{n+1} - u_j^n}{r} = \frac{1}{\Delta\theta} \begin{cases} \Delta_- F(u_j^n) & \text{if } F'(u_{j-1}^n), F'(u_j^n) \leq 0 \\ \Delta_+ F(u_j^n) & \text{if } F'(u_{j+1}^n), F'(u_j^n) > 0 \end{cases}, \tag{3.25}$$

with n, the discrete-radius index of the grid $r^n = n\Delta r$. The direction of the finite-difference operator depends on $F'(u)$, the derivative of the flux function with respect to

u. If the flux increases from left to right, it means the flow is to the left. When it decreases, flow is to the right. The various upwind schemes differ in the way in which the intermediate cases are handled. When the sign of $F'(u)$ changes among three points of the stencil, the formula will become

$$u_j^{n+1} = u_j^n + \frac{\Delta r}{\Delta \theta}(\Delta_+ F_-(u_j^n) + \Delta_- F_+(u_j^n)),\qquad(3.26)$$

where

$$F_-(u) = F(\max(u,\bar{u})), \ F_+(u) = F(\min(u,\bar{u})),\qquad(3.27)$$

and $\bar{u}$ is the stagnation point [$F'(u) = 0$]. To show the accuracy of the upwind finite-difference method in solving the Eikonal equation, a homogenous model is chosen to calculate traveltimes. The velocity of the model is 4,000m/s. The model is evenly sampled laterally and in depth, with a sample of 10m, and a size of 200×200. Figure 3.18 shows the traveltime function for a source on the surface and at the centre of the model with finite-difference in polar coordinates, and Figure 3.19 displays the difference between the function and the analytical solution, with symmetric errors on both sides of the source. Actually, the maximum error of the bottom horizontal line (Figure 3.20) is only about 0.005%, which is almost negligible.
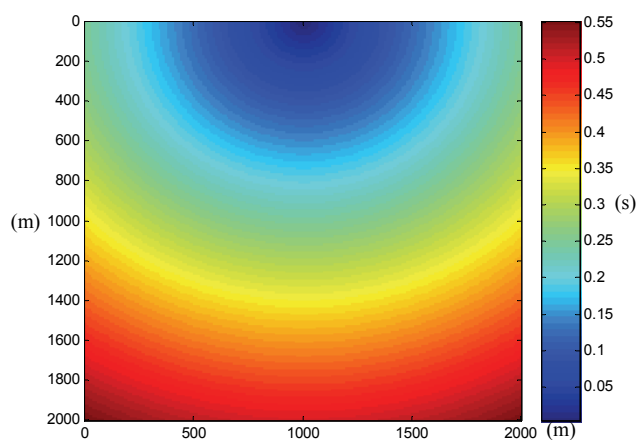
Figure 3.18 The traveltime contour in homogenous media with the upwind finite-difference solution.
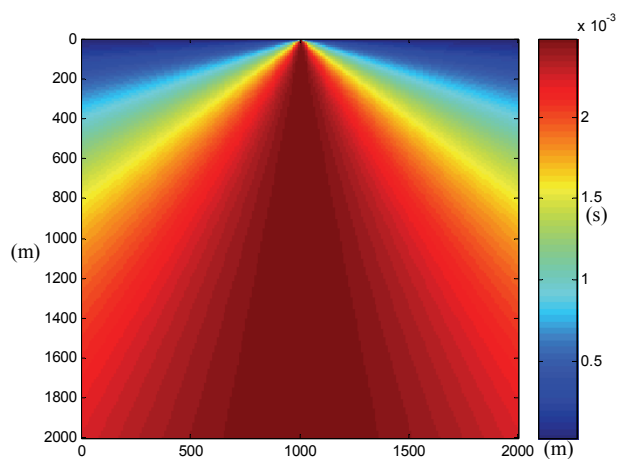
Figure 3.19 The traveltime absolute difference between the analytical and finite-difference solutions.
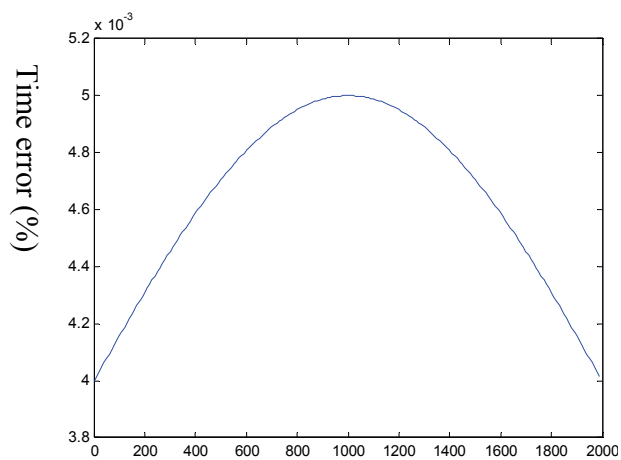
Figure 3.20 The relative maximum traveltime error of the bottom horizontal line in Figure 3.19.

3.6 Numerical and field data post-stack and prestack migration

The Marmousi model data presents a challenge to exploration geophysicists in imaging complex geological domains (Versteeg, 1993). The model (Figure 3.21) contains very complex geological features, especially shallow steep faults and the underlying high-velocity salt pillows. The target zone is shown with the black dashed rectangle. It has served as a standard test dataset for depth migration, inversion algorithms, and velocity analysis methods (Gray and May, 1994; Nichols, 1996; Zhu and Lines, 1998; Mi and Margrave, 2002a).

3.6.1 Post-stack migration comparison and analysis of the Marmousi dataset

Several different migration algorithms are applied to process the zero-offset synthetic data of the Marmousi model (Figure 3.22), including Kirchhoff depth migration, three one-way wave equation downward-continuation methods (the PSPI, split-step Fourier method and implicit finite-difference methods), and the reverse-time migration method with the FE-FD operator. The sampling interval of the synthetic data is 1ms and the lateral interval is 12.5m. Figure 3.23 is the migration result generated by Kirchhoff depth migration. Figure 3.24, Figure 3.25, and Figure 3.26 correspond to results from the PSPI, split-step Fourier, and implicit finite-difference methods, respectively. In the Kirchhoff depth migration, the shallow structures are clear whereas it is very difficult to describe the target zone since it suffers greatly from the difficulty of ray-tracing through the complex structures above. The three one-way wave equation downward-continuation methods show better imaging results than the ray-based method, with very clear structures and obvious target zone. Looking closely at the details of these three downward-continuation results, the PSPI migration result shows relatively clear

structures in the target zone compared with results from the implicit finite-difference and split-step methods, shown by the arrows annotating these figures. The implicit finite-difference result has some high-frequency noise due to the frequency dispersion problem. The anticlinal structure (dashed rectangle) appears to be difficult to image with the split-step Fourier method. Looking at the reverse-time migration with the FE-FD operator with 4th order accuracy in the spatial domain (Figure 3.27), the clear structures and reduced noise are obvious, with each structure correctly migrated to its true position. The wedge structures (white ellipse) are especially vivid, with a clarity that is absent in the other methods mentioned above. From this comparison and analysis, the reverse-time migration method reveals its greater capability for imaging complex structures, due to the fact that the two-way wave equation can better describe the characteristics of wave propagation. The different kinds of waves, such as overturned waves and multiple-reflections, are propagated back to their true position with the same reverse mechanism as wavefield modelling.
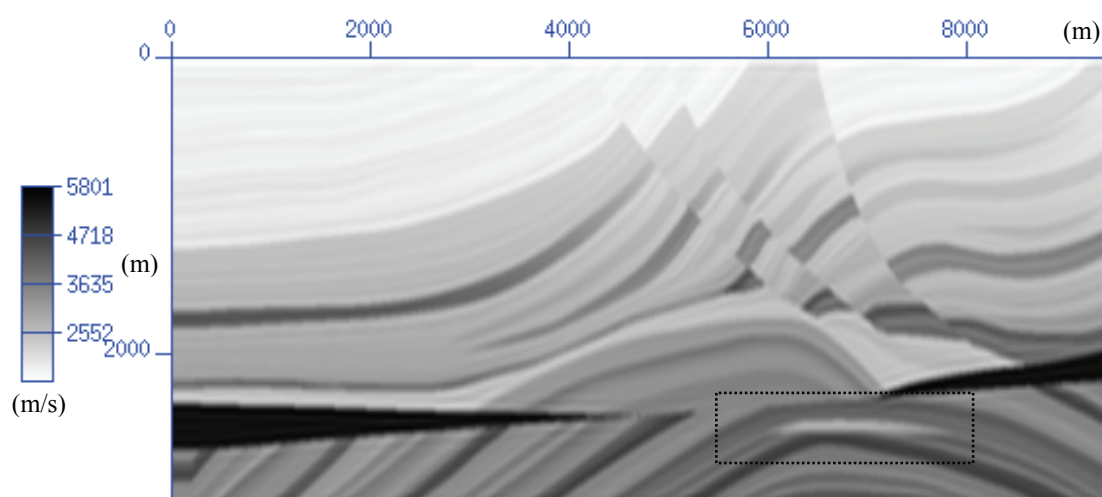
Figure 3.21 The Marmousi velocity model.
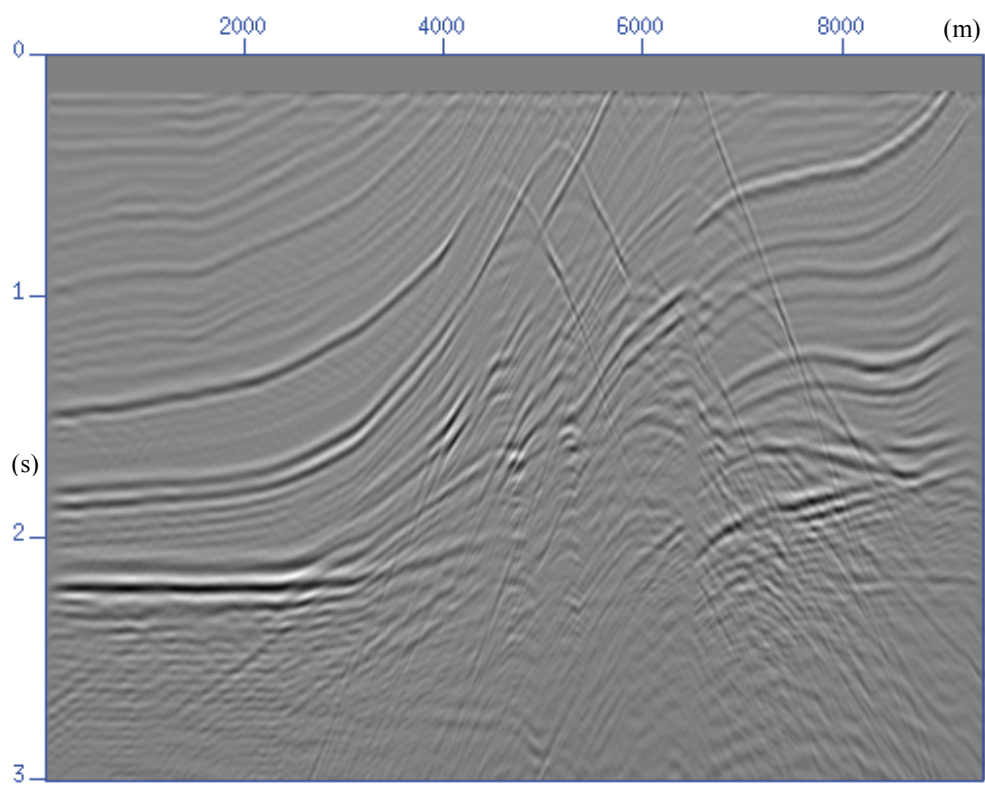
Figure 3.22 The zero-offset section of the Marmousi model.
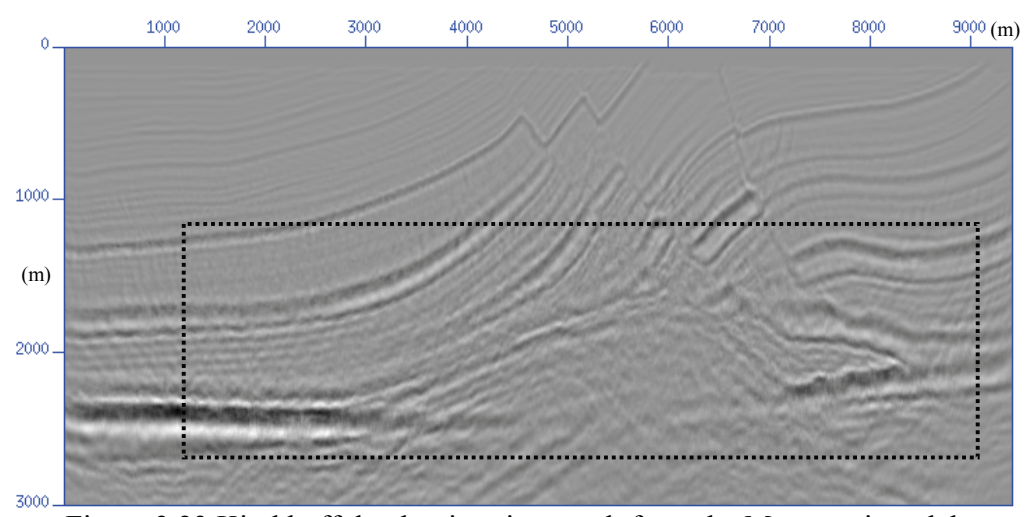
Figure 3.23 Kirchhoff depth migration result from the Marmousi model.
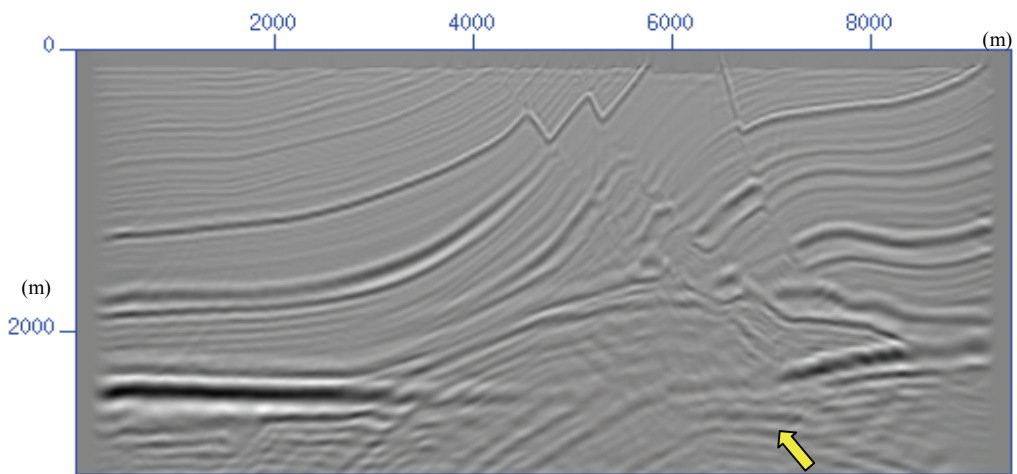
Figure 3.24 PSPI migration result from the Marmousi model.
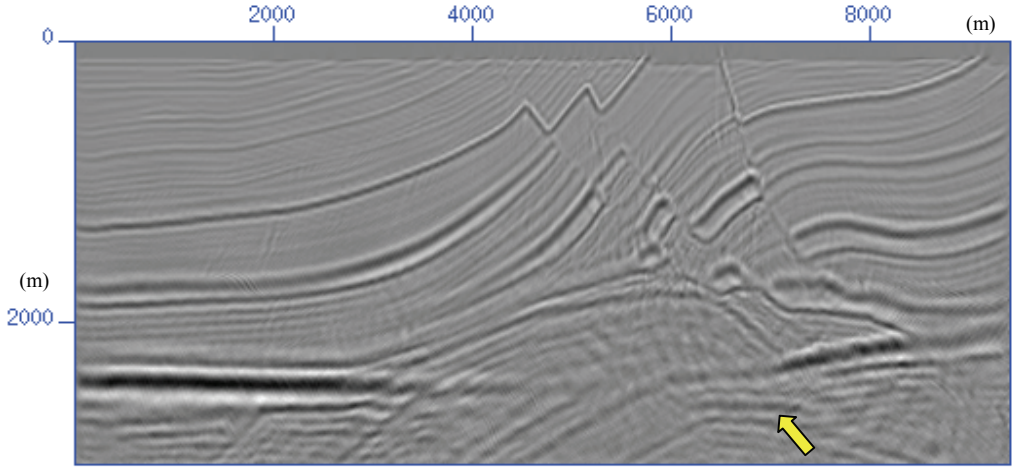
Figure 3.25 The implicit FD migration result from the Marmousi model.
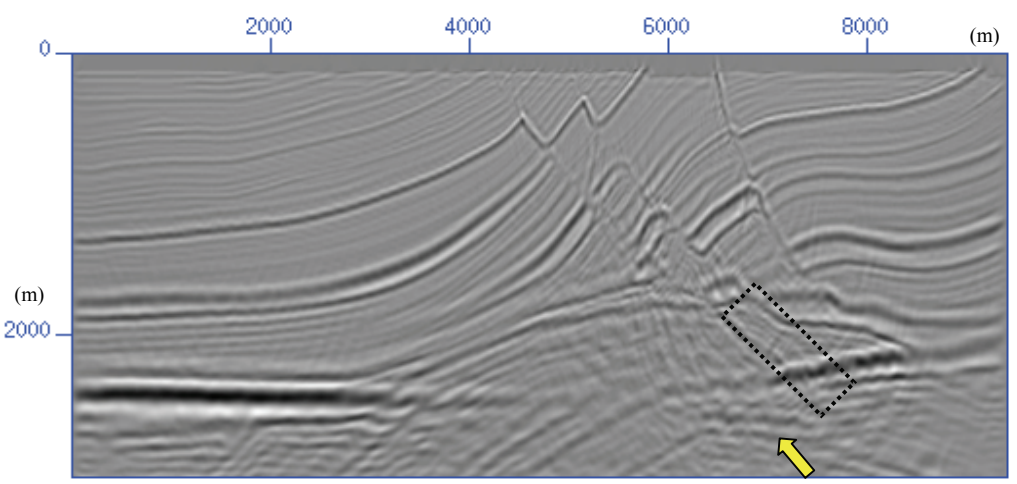
Figure 3.26 The split-step Fourier migration result from the Marmousi model.
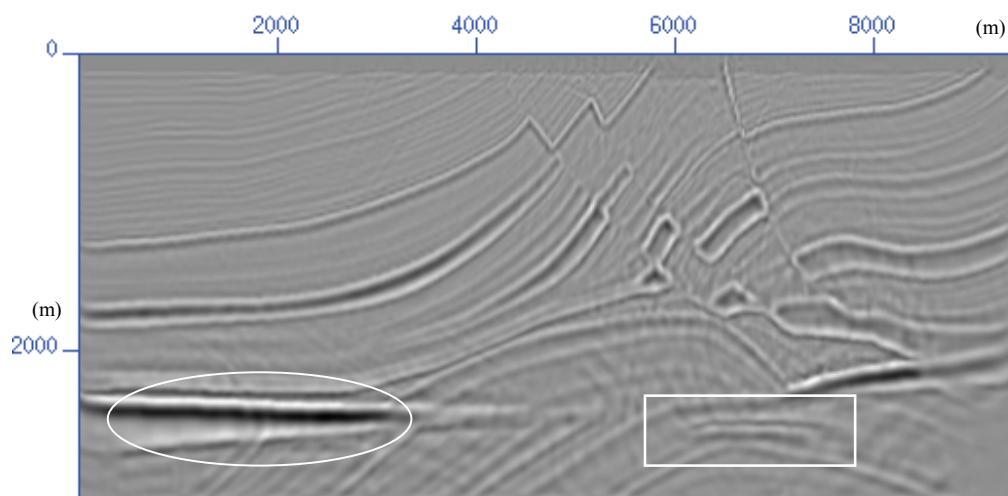
Figure 3.27 The reverse-time migration result from the Marmousi model.

3.6.2 Prestack migration of the Marmousi dataset — comparison and analysis.

Prestack synthetic data from the Marmousi model were also processed, including 240 shot gathers. Each shot has 120 traces with 12.5m trace intervals. Upwind finite-difference is employed to calculate the traveltime tables, which are used not only for the prestack Kirchhoff depth migration but also for the prestack reverse-time migration to save disk space and computational cost. Figure 3.28 corresponds to the prestack Kichhoff depth migration result. Although the resolution of prestack migration is higher than post-stack migration shown in Figure 3.17, the anticline structures and the target zones prove difficult to image using either method. The first arrival traveltime can't adequately provide enough information for Kirchhoff migration algorithm in complex structures. It also affects the prestack reverse-time migration algorithm, which is shown in Figure 3.29, although the resolution is quite a bit higher than the post-stack reverse-time result and the other post-stack downward-continuation migration results. However the structure of the target zone in the prestack migration result is not as clear as in post-stack result. The reason is that the traveltimes are used as the forward wavefield and applied to the

imaging condition. In fact, if we use source modelling as the forward wavefield, the result is as good as we want, but the large extra computational cost prevents this method from being used in the industry. Accurate traveltime calculations play a big role in the Kirchhoff depth and prestack reverse-time migrations.
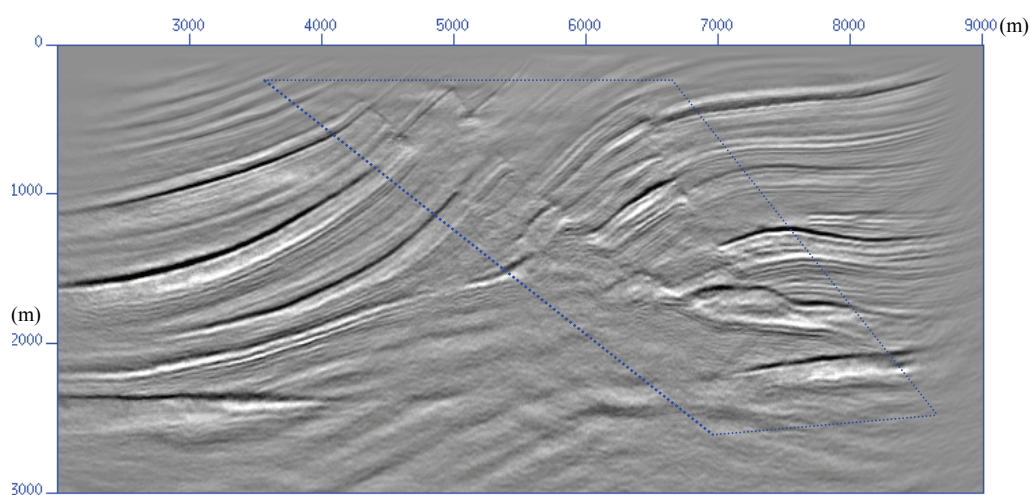
Figure 3.28 The prestack Kirchhoff depth migration result from the Marmousi dataset.
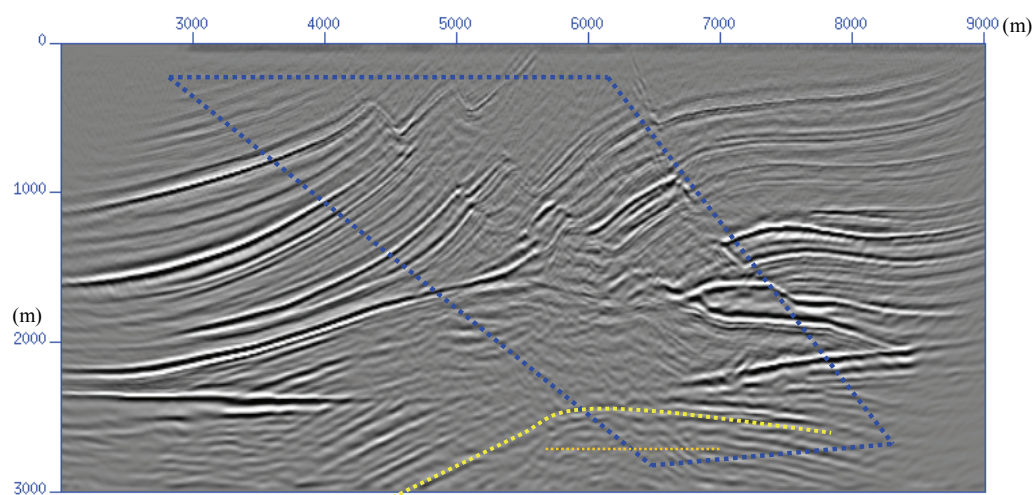
Figure 3.29 The prestack reverse-time depth migration result from the Marmousi dataset.

3.7 Chapter summary

A numerical method termed the finite element–finite difference method (FE-FDM) is presented in this chapter to solve the time-dependent differential equations such as parabolic and hyperbolic model equations. As numerical examples, 2D scalar wave equation modelling and reverse-time depth migration have been presented, and it is encouraging that the results are accurate and effective enough for the simulation of complex wavefields and steeply dipping interface migration.

This method combines FEM and FDM based upon the semi-discretization of the spatial domain. The main strengths of FEM (adaptation to arbitrary depth variation) and FDM (computational efficiency) are partially inherited. As for the FE-FDM with 2nd order FEM along the z direction and 2nd order or 4th order FDM along the x direction, it has looser stability conditions than FDM with the same accuracy. With irregular grid discretizations, although partitioning grids and assembling global matrices are tiresome, the efficiency and resolution are notably improved. The reverse-time migration with the FE-FD operator is applied to process the Marmousi post-stack synthetic data and demonstrates the superior imaging quality of the full wave equation when compared to the one-way wave equation methods, including PSPI, SSF and IFD.

The upwind finite-difference method is applied to obtain traveltime tables. With the traveltime tables, we implement the prestack Kirchhoff depth migration and prestack reverse-time migration. As with the Kirchhoff migration method, traveltime accuracy affects the prestack reverse-time migration method according to two migration results from the Marmousi model.

Chapter Four: Topography problem for one-way wave equation downward-continuation wavefield extrapolation methods

4.1 Introduction

Surface topography introduces a numerical problem for migration algorithms that are based on downward-continuation wavefield extrapolation. Since numerically efficient migration schemes start at a flat interface, wave-equation datuming (Berryhill, 1984; Shtivelman and Canning, 1988) is required prior to the migration. The computationally expensive datuming procedure is often replaced by a simple time-shift for the elevation to datum correction. For nonvertically travelling energy this correction is inaccurate. Subsequently, migration wrongly positions the reflectors in depth. Imaging from topography with wave equation methods is a natural extension of wave equation datuming techniques since they both are established on wavefield extrapolation theory.

This chapter will address the technique for downward-continuation wavefield extrapolation methods, including the prestack PSPI migration, prestack split-step Fourier (SSF) and prestack implicit finite-difference (IFD) methods. Comparisons among these three methods are made using the numerical and field data to evaluate the performance of each one with respect to efficiency and resolution.

4.2 Methodology for migration from topography using downward-continuation wavefield extrapolation methods

In the 2D Cartesian coordinate system, the downward-continuation wavefield extrapolation obeys the one-way wave equation,

$$k_z = \pm \sqrt{\frac{\omega^2}{v^2} - k_x^2} \, , \tag{4.1}$$

or

$$\frac{\partial P}{\partial z} = \pm ik_z P\,; \tag{4.2}$$

where the $\pm$ signs are downward and upward wavefields, respectively. For the PSPI and split-step Fourier methods reviewed in Chapter 2, downward-continuation wavefield extrapolation is involved in the wavenumber-frequency domain, applying a simple phase shift from one depth point to another:

$$P(z + dz, k_x, \omega) = P(z, k_x, \omega)e^{\pm ik_z dz}\,. \tag{4.3}$$

In contrast to the PSPI and split-step Fourier (dual-domain) methods, the extrapolation of the implicit finite-difference method is achieved only in the $x - \omega$ domain as in Equation (4.4),

$$\frac{\partial P(x, z, \omega)}{\partial z} = -\hat{i}\,\frac{\omega}{v}\,(1 + \sum_i \frac{\alpha_i \partial^2 / \partial x^2}{1 + \beta_i \partial^2 / \partial x^2})P(x, z, \omega)\,, \tag{4.4}$$

which has been discussed in Chapter 2. The technique presented in this thesis is not involved in detailed schemes of different downward-continuation migration methods since it only deals with the dataset after each wavefield extrapolation step. Given a flat datum above the topography with some constant velocity that approximates the average velocity of that depth step, the downward-continuation extrapolation can be described as

$$P(x, z + \Delta z, \omega) = \mathbf{OPER}[P(x, z, \omega)]W(x, z) + [1 - W(x, z)]P(x, z, \omega)\,, \tag{4.5}$$

where

$$\mathbf{OPER} = \begin{cases} SPLIT \\ PSPI \\ FD \end{cases}\,, \tag{4.6}$$

which represents different extrapolation schemes, and

$$W(x,z) = \begin{cases} 1 & z > h(x) \\ 0 & z \le h(x) \end{cases}, \qquad (4.7)$$

which is a spatial function to judge if the step of wavefield extrapolation has reached the

surface point, where $h(x)$ is the x-dependent topographic function shown in Figure 4.1.

With this equation, after the original dataset ($x-t$ domain) is transformed to the $x-\omega$

domain, we start wavefield extrapolation from the top of the grid that lies above the

highest surface point (seen in Figure 4.1). At each extrapolation step, for each trace, when

a surface point is reached, the new wavefield (in the $x-\omega$ domain) can be updated,

otherwise, it will keep the original input wavefield.
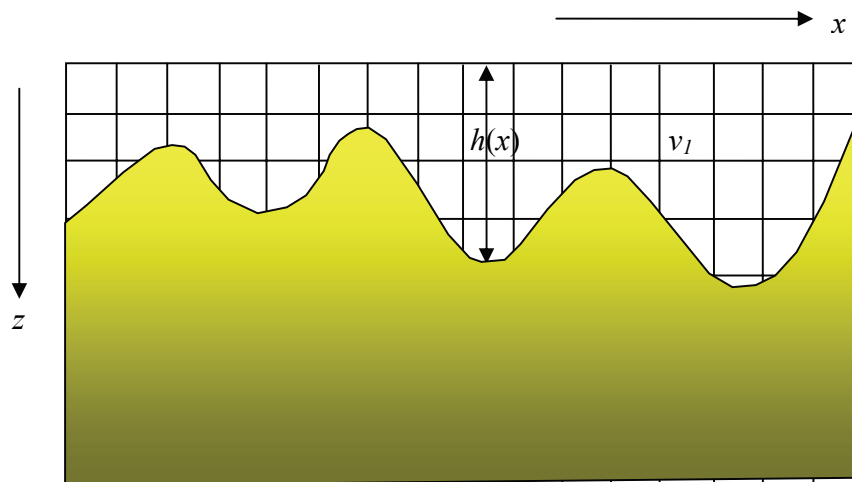
Figure 4.1 Representation of surface topography.

4.3 Comparisons among the phase-shift-plus-interpolation, split-step Fourier, and implicit finite-difference methods

A theoretical introduction to the phase-shift-plus-interpolation (PSPI), split-step Fourier

(SSF) and implicit finite-difference (IFD) methods has been given in Chapter 2. Here, we

further investigate their performance in terms of speed and accuracy, according to each

algorithm's mathematical principles. The adaptation of migration from the topographic technique for each algorithm will be subsequently discussed and analyzed.

The common basis of PSPI, SSF and IFD is that they are based on the same equation, the one-way acoustic wave equation, and their extrapolation occurs in the frequency domain. Figure 4.2, Figure 4.3 and Figure 4.4 show the computational scheme for PSPI, SSF and IFD for analyzing each algorithm. Compared with the scheme for IFD, which is only involved in the $x - \omega$ domain, PSPI and SSF are involved in dual domains, one part of the computation being done in the $x - \omega$ domain to implement time-shift using a linear phase shift, and the other part being carried out in the $k_x - \omega$ domain to complete the focussing phase-shift. The PSPI method accomplishes the time-shift ahead of the focussing phase-shift, while SSF does the opposite: using a minimum velocity chosen from lateral velocities at each depth step for the focussing phase-shift and then applying a corrected slowness (the difference between true slowness and minimum slowness) for the time-shift.

The minimum velocity and corrected slowness imply that SSF will fail in the case of strong variations in the field. However, it is very efficient due to the one-time phase-shift applied compared with PSPI, which is dependent on a reference number. The stronger the variation in the velocity field, the more reference velocities we require if we wish to obtain good imaging results. This also determines the method's efficiency. The PSPI method is more expensive than the SSF method but it delivers relatively greater accuracy. IFD usually carries out extrapolation directly in the $x - \omega$ domain, so the true velocity at each point will be applied, which means it is well adapted to strong variations in the velocity field. However, when the cascaded series approximate the one-way wave

equation, we reach the same conclusion as PSPI in that the more cascaded numbers, the more cascaded extrapolation. Han (1998) gave detailed statistics for several wavefield extrapolation methods. In general, IFD is the trade-off method of the three which is well adapted to arbitrary velocity variation; SSF is the most efficient method that involves the least computation possible; and PSPI is the slowest method even if we give relatively simple reference numbers for velocities. Since phase-shift calculation employs most of the computation cost, with the number of the reference velocities increasing, the computational expense increases proportionally.
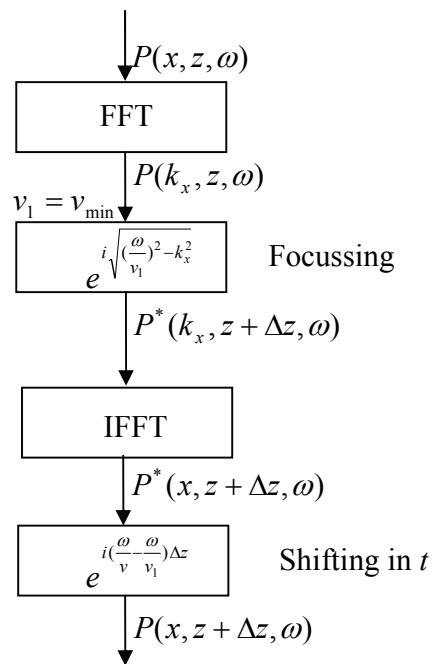
Figure 4.2 The extrapolation scheme for SSF.
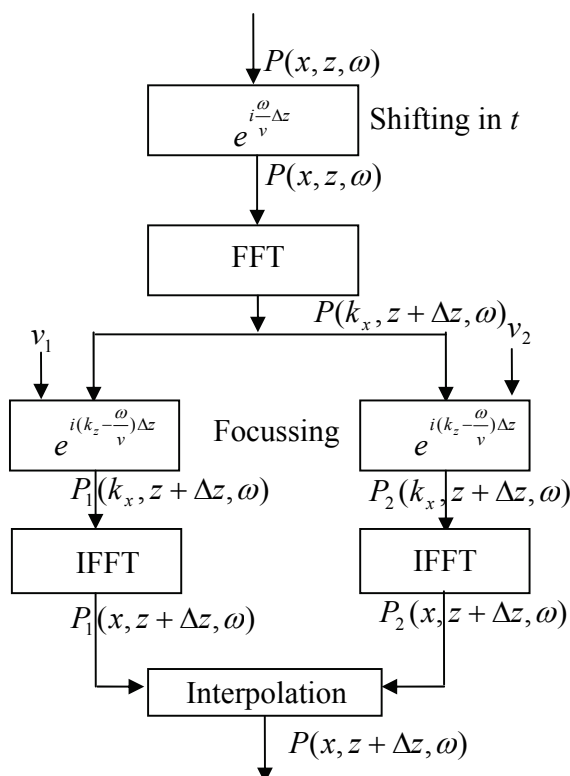
Figure 4.3 The extrapolation scheme for PSPI.
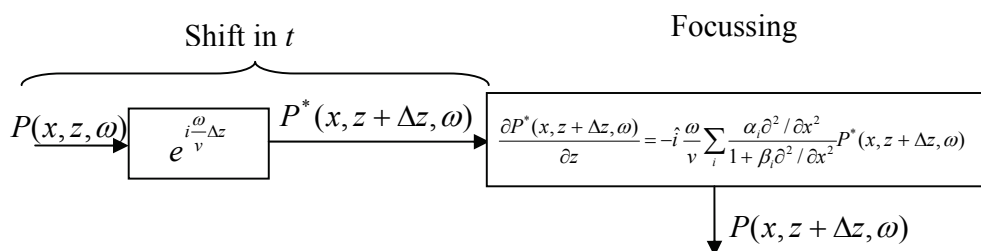
Figure 4.4 The extrapolation scheme for implicit finite-difference.

When the surface topography technique is applied to the downward-continuation methods discussed above, it won't affect the characteristics of each algorithm, which will be greatly strengthened by the following numerical and field data experiments. The shallow imaging quality will clearly reflect the resolution of each extrapolation algorithm.

4.4 Imaging conditions for prestack downward-continuation migration algorithms

To implement the prestack depth migration, we not only require extrapolating the recorded wavefield downwards, but also need to extrapolate the seismic source impulse downward into the Earth. The reason is that the shot gathers contain both the down-going wavefield information from the source and the up-going information to the receivers through the velocity field. The source extrapolation is the same as the receiver extrapolation except for the input wavefields. Estimation of reflectivity from wavefields at a certain depth level is called an imaging condition. We will use two methods to define the imaging conditions: one is a deconvolution imaging condition and the other is a cross-correlation imaging condition, which is typically done in the frequency domain.

The deconvolution imaging condition estimates reflectivity using the ratio between the receiver and source wavefields. The process uses the wavefields just after the reflection and just before reflection. Energy loss, due to geometrically spreading from both the source and the receiver, is automatically corrected. Each frequency slice produces a frequency-dependent estimation of the reflectivity and all are averaged to eliminate frequency-dependence. The deconvolution imaging condition can be written as (Claerbout, 1971)

$$\widetilde{r}_{decon}(x,z) = \frac{1}{\omega_{\max} - \omega_{\min}} \int_{\omega_{\min}}^{\omega_{\max}} \frac{\left|\psi_{refl}(x,z,\omega)\right|}{\left|\psi_{inc}(x,z,\omega)\right|} e^{i\left[\Phi_{refl}(x,z,\omega) - \Phi_{inc}(x,z,\omega)\right]} d\omega . \qquad (4.8)$$

This method involves both amplitude and phase correction and should be more accurately called an inversion process. The cross-correlation imaging condition sets the amplitude of the source wavefield to a constant value, normally 1.0, which means that the cross-correlation imaging condition involves only the phase and geometric-spreading

corrections to the receiver wavefield. Source-side geometric spreading loss is ignored. It can be written as (Claerbout, 1971)

$$\widetilde{r}_{xcorr}(x,z) = \frac{1}{\omega_{max} - \omega_{min}} \int_{\omega_{min}}^{\omega_{max}} |\psi_{refl}(x,z,\omega)||\psi_{inc}(x,z,\omega)| e^{i[\Phi_{refl}(x,z,\omega)-\Phi_{inc}(x,z,\omega)]} d\omega. \quad (4.9)$$

The deconvolution imaging condition is theoretically a true amplitude condition for migration; however, it is unstable for real seismic evaluations due to embedded noise. Furthermore, when compared with the cross-correlation imaging condition, it is obviously expensive. The cross-correlation imaging condition is more stable and image quality can be superior to the deconvolution imaging condition. The migration results from the prestack downward-continuation method have been computed using the cross-correlation imaging condition.

4.5 Numerical and field data migrations from topography

4.5.1 Numerical data migration from topography

A complex velocity model (Gray and Marfurt, 1995) has been designed to represent a geological cross-section (Figure 4.5), consisting of a number of faulted layers typical of mountainous thrust regions, such as the Canadian Foothills. High near-surface velocities present an additional challenge to depth migration algorithms. The model is 12,000m long, and the depth is 10,000m: the top of the model is 2,000m above sea level and the bottom of the model is 8,000m below the sea level. The top layer is air, and the surface of the Earth is indicated by the areas filled with a constant velocity (4,000m/s) (orange color) for wavefield extrapolation. The total relief of the Earth's surface along this cross-section is approximately 1,600m. The velocity of the model ranges from 3,500m/s (the reddest areas near the top) to 5,900m/s (the bluest areas near the bottom). A total of 278 2D

synthetic shot gathers were generated using an acoustic wave equation (implying cylindrical energy loss) with finite-difference modelling. The shot spacing is 90m, the sample interval is 4ms, and the sample intervals in the horizontal and vertical directions are 10m. Figure 4.6 is a shot gather located approximately in the middle of the model. Rapid topographic variation and a high velocity near-surface strongly affect the energy arrivals, such as the first arrivals (yellow arrow) and reflections (red arrows), which present significant challenges to depth migration algorithms.
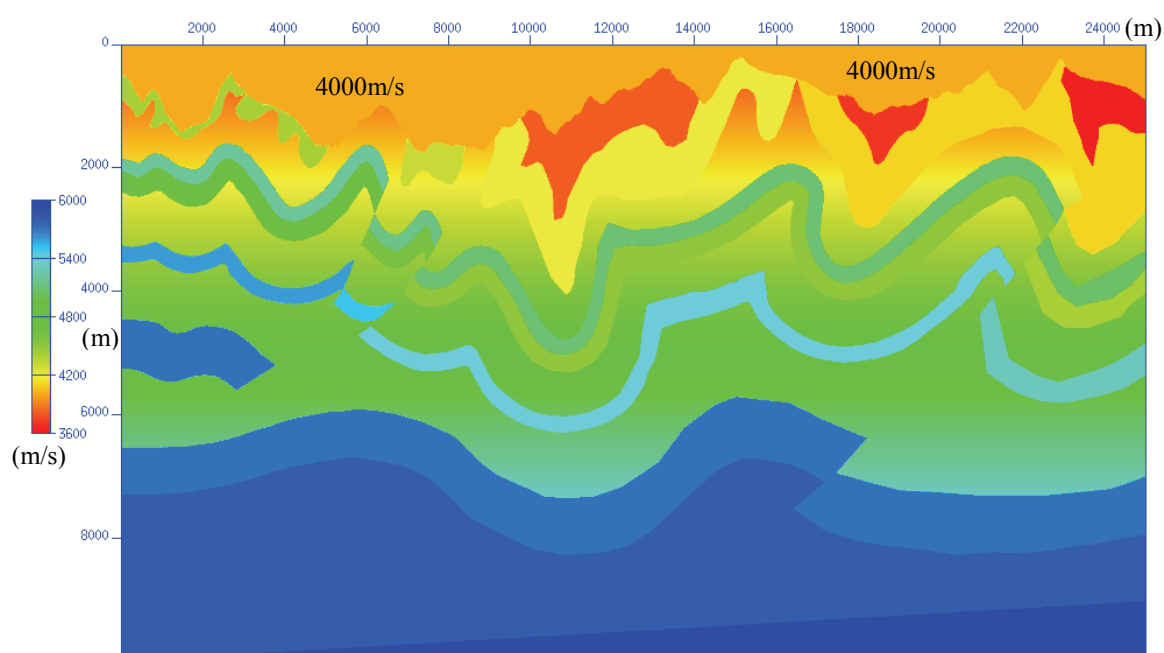
Figure 4.5 A velocity/depth model representative of northeastern British Columbia (after Gray and Marfurt, 1995). There is roughly 1600m of elevation relief along the seismic section.

No processing was done prior to prestack depth migration, such as the removal of direct waves and geometrical spreading correction. The dataset was not only used for the three prestack downward-continuation migration methods (a constant velocity of 4,000m/s is used to substitute the air), but also for the prestack Kirchhoff depth migration. The traveltime tables were calculated using the upwind finite-difference method with the

Eikonal equation, as illustrated in Chapter 3. With these tables, a Kirchhoff migration

algorithm provided by Don C. Lawton produced the depth migration.

The Kirchhoff depth migration result is shown in Figure 4.7. The folds, the thrusts, and

the inclined basement plain are clearly and correctly migrated except for some of the

shallower structures due to the algorithm placing lower priority on the resolution of

shallow parts. At the same time, the result strongly validates the accuracy of the

traveltime calculation obtained from the upwind finite-difference method with the

Eikonal equation mentioned in Chapter 3. The dashed rectangle in this figure shows

migration artifacts in a complex area, which is an obvious characteristic of Kirchhoff

depth migration.

For the three downward-continuation extrapolation methods, each shot was padded to 8

seconds in order to accommodate the energy wrapped around by the extrapolation and

Fourier transform, which becomes background noise if not properly handled. Each shot

was also padded in the horizontal direction with 15 traces on the both sides to increase

the imaging aperture when the source is located in the middle. These migrations were

done in a PC machine with a memory of 512M and CPU processor of 1.86G Hz. From

the migration results shown in Figure 4.8, Figure 4.9 and Figure 4.11, the three prestack

migration algorithms all successfully image the model structure, and delineate the faults,

thrust structures, and the inclined basement flat. Compared with the prestack Kirchhoff

migration result, these imaging results are clearer and more natural, with fewer artifacts.

The near-surface imaging is also clearer. There is no obvious difference between PSPI

and SSF, but minor differences are evident. Artifacts in the near-surface with PSPI are

fewer than that with SSF. The corresponding dashed blue rectangles in Figure 4.8 and

Figure 4.9 show slight imaging differences in this area, and it seems that PSPI looks better since more reference wavefields are computed.

Figure 4.10(a) shows the velocity information used for the shot gather of Figure 4.6, and its corresponding migration result (Figure 4.10(b)), which gives us a detailed comparison between model and migration results. The white dashed rectangle delineates the near-surface imaging, and yellow arrows show surface topography and fold structure. Figure 4.11 is the prestack migration result from the implicit finite-difference method with the 87° accuracy. Compared to results obtained by the two downward-continuation extrapolation methods involving the wavenumber domain, the result from the implicit finite-difference method shows better imaging for fold structure since the algorithm applied the true velocity at each point in the spaces. The white dashed rectangle shows the fold structure clearly imaged. The yellow arrows indicate more consistent fold structure imaging, which is not relatively obvious in Figure 4.8 and Figure 4.9. From the viewpoint of efficiency, measured by computation time in Figure 4.12, SSF is the most efficient method among three wave equation based methods that only employs one hour while PSPI is the slowest method (almost two hours run-time). In fact, IFD is the most preferred method as it is relatively fast (about one and half hours) while achieving the higher resolution. The Kirchhoff depth migration only costs about 40 minutes to obtain the reasonable result, which shows the dominant advantage in computer runtime over the wave equation based methods.
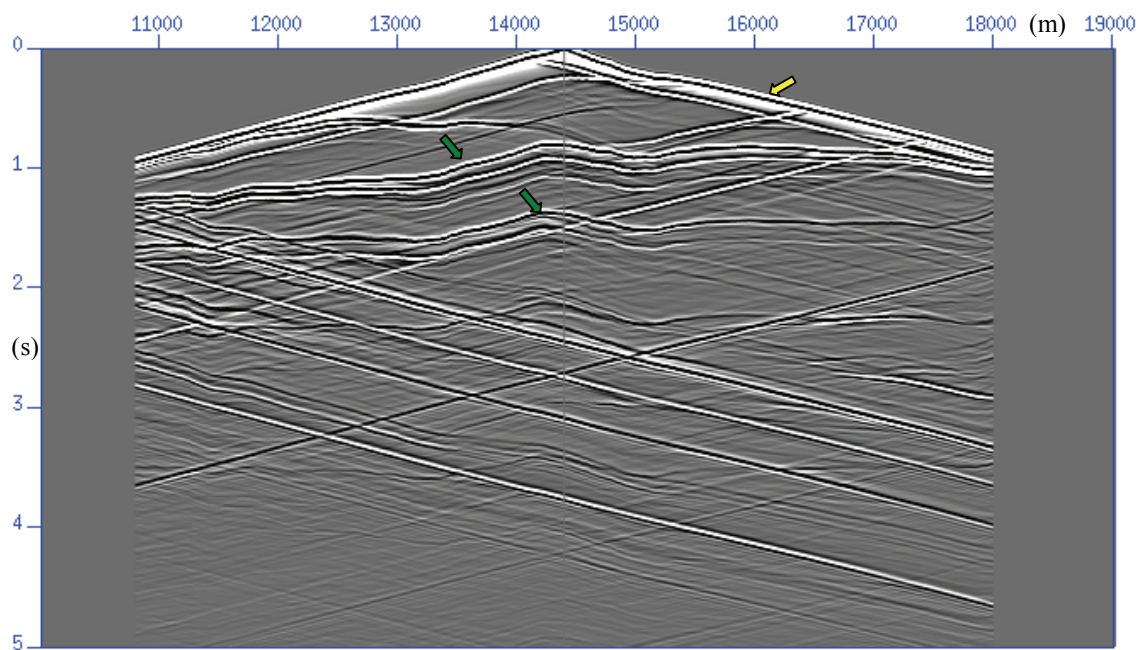
Figure 4.6 A shot gather located approximately at the mid-point of the model (14,500m position). The yellow arrow shows the uneven direct wave energy due to the effect of surface topography, and green arrows indicate reflections from the fault structures.
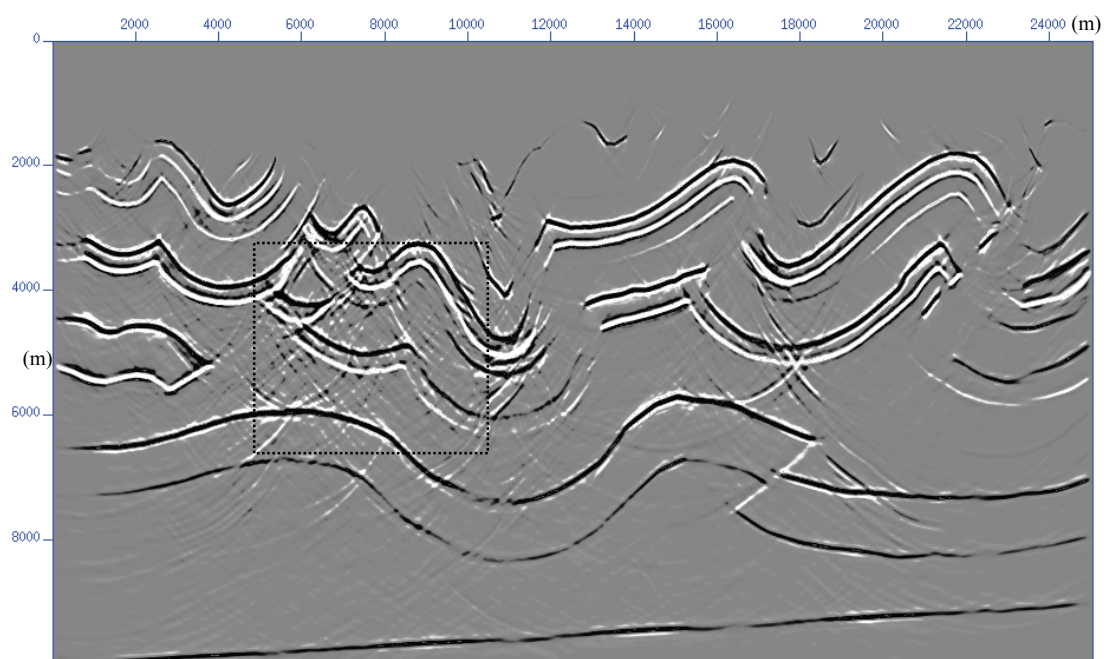
Figure 4.7 Result of the prestack Kirchhoff depth migration. The dashed rectangle shows the obvious smiles in complex areas.
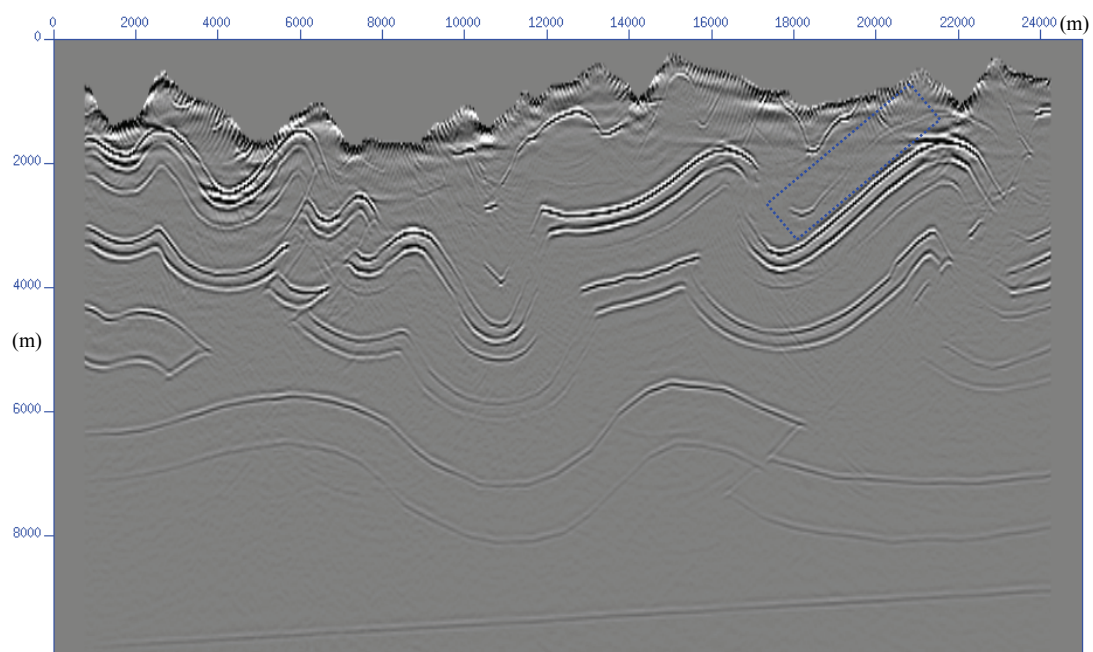
Figure 4.8 Result from the prestack PSPI migration. The blue rotated rectangle denotes the imaging of shallow structures for comparison with the SSF migration below.
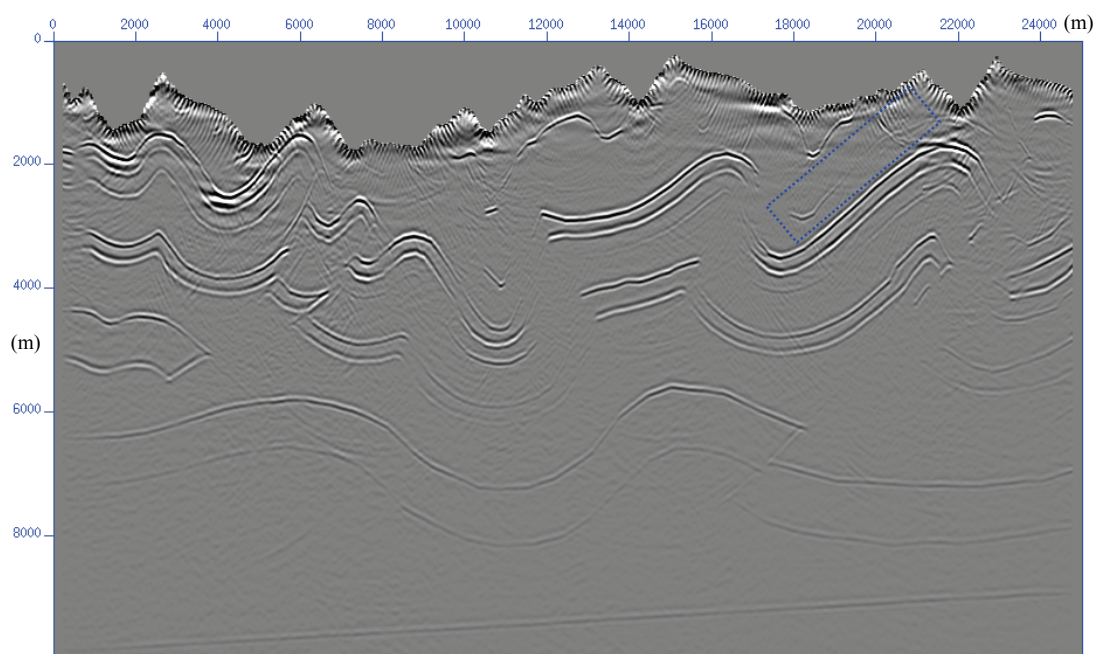
Figure 4.9 Result from the prestack SSF method. The dashed blue rotated rectangle denotes the imaging of shallow structures for comparison with the PSPI migration above
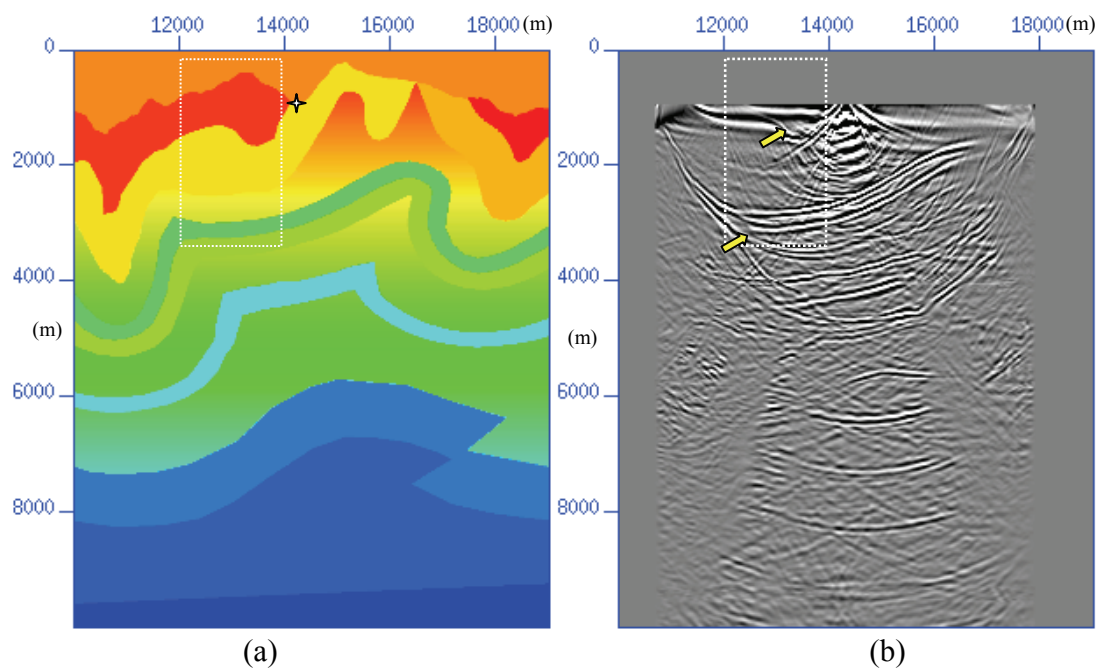
Figure 4.10 (a) Velocities used for migrating the shot shown in Figure 4.7; (b) the migration of the shot gather using the prestack SSF method. The yellow arrows shown in (b) indicate the imaging quality for shallow structures.
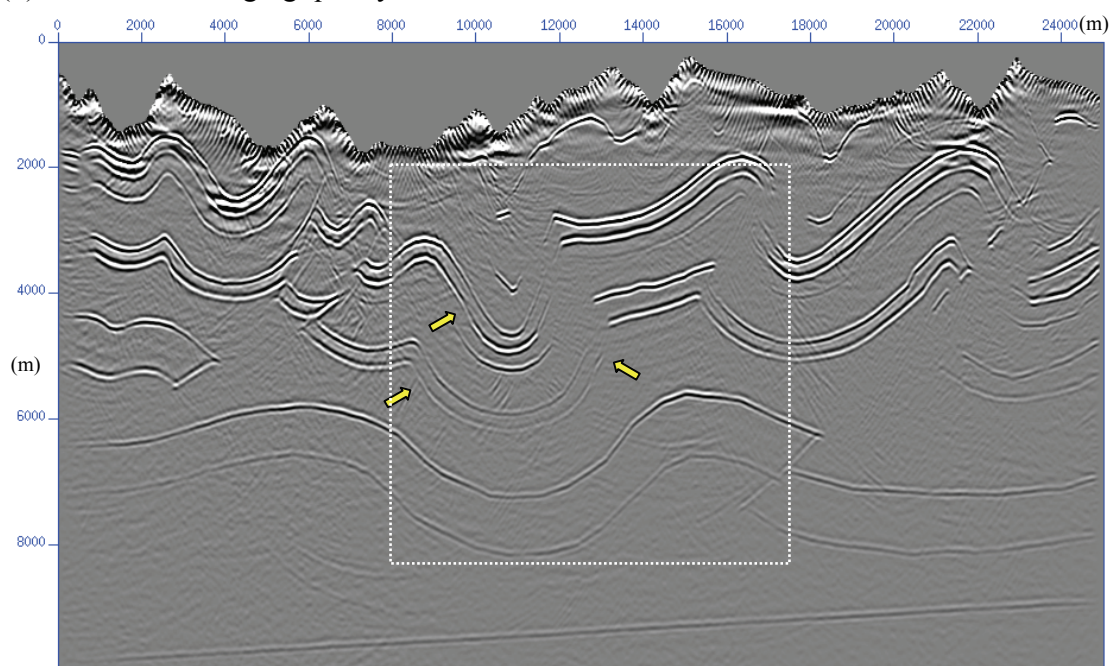
Figure 4.11 Result from the prestack implicit finite-difference migration. The white dashed rectangle delineates good fold structure imaging. The yellow arrows indicate more consistent fold structure imaging.
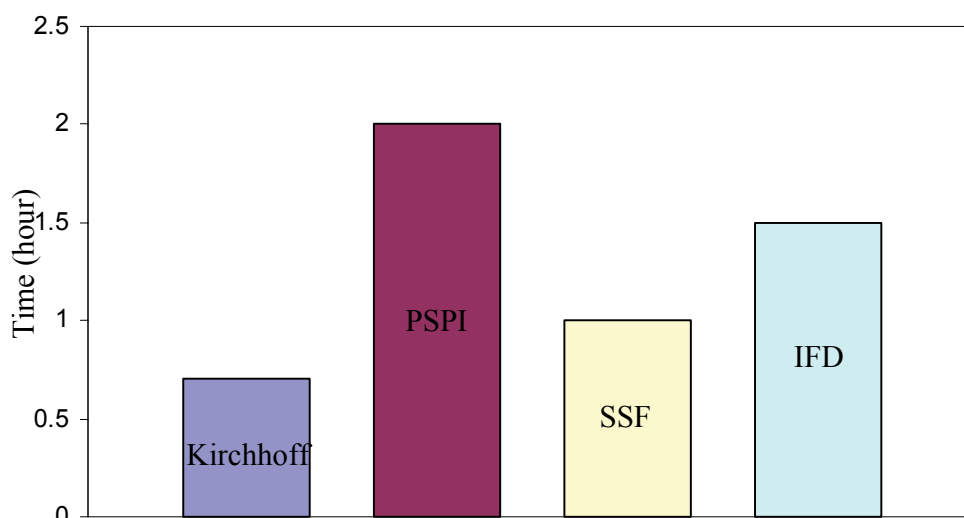
Figure 4.12 Computational time of prestack PSPI, SSF and IFD migration methods.

4.5.2 Field data migration from topography

The real data were sampled from an area of the Canadian Foothills. The surface topography model is shown in the Figure 4.13, where the top position to datum is almost 500m. The surface topography variation is not as severe as in the numerical model discussed as above. The investigated area is 12,000m long. There are 134 shot gathers. For each shot, the trace interval is 15m and temporal sample interval is 4ms. The shot spacing is 90m. There is no affordable velocity model for migration. However, in the experiment with constant velocity, the migration structures look reasonable. Two prestack migration methods are tried here — the prestack Kirchhoff depth migration and the prestack SSF methods. Due to the constant velocity model (4,200m/s), there are no differences between PSPI, SSF and IFD. Considering the computation cost, the efficient SSF method is chosen for the migration experiment. Figure 4.14 is the migration result from the prestack Kirchhoff migration method. The syncline structure is very clear in the near-surface area, as also shown in Figure 4.15, the migration result from the prestack

SSF method. In comparing the two results, the result from wave-equation-based method seems better than that of the ray-based method. The reflection energies indicated by white dashed rectangle in Figure 4.14 are more consistent than those of Figure 4.15. The yellow dashed ellipse shows a similar result. The reflector energy indicated by the yellow arrow is very strong in the SSF migration result while it is unnoticeable in the Kirchhoff migration result.

The prestack SSF method is also applied after elevation correction from the original data using convention "statics" processing. The result is shown in Figure 4.16, which is not as natural as the results in Figure 4.14 and Figure 4.15. It is common that a lot of traces appear "shaky". Many reflector events are not very consistent. Some structural shapes have obvious changes compared to the results migrated from surface topography, such as the structure denoted by the yellow arrow in Figure 4.16. So a simple time-shift for the elevation-to-datum correction can't guarantee the correctness of data for migration, which will result in wrongly positioned reflectors in depth.
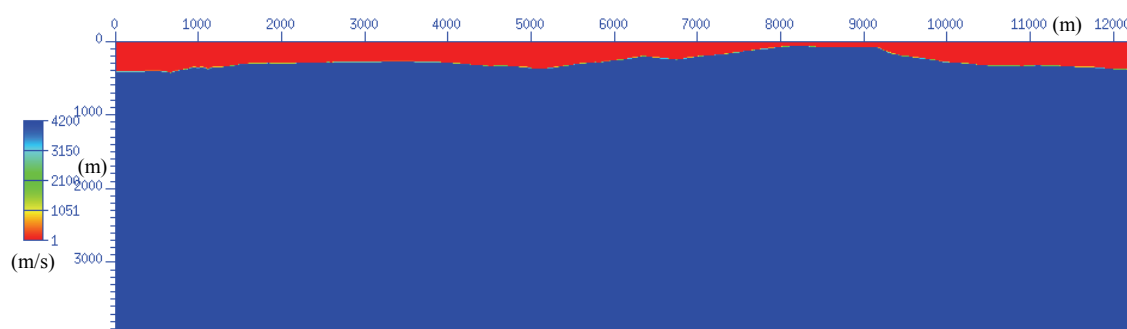
Figure 4.13 A constant velocity/depth model for real data depth migration. There is roughly 500m of elevation relief along the seismic section. The red colour denotes the air with velocity set as 1m/s.
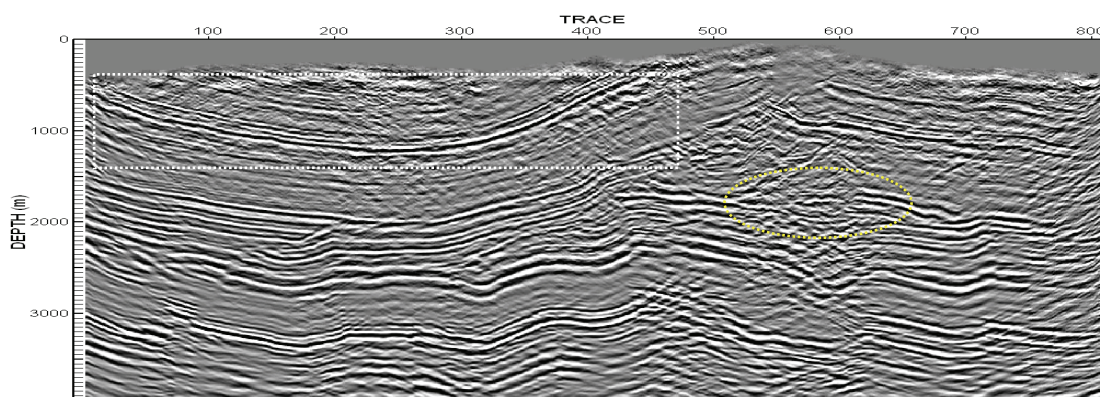
Figure 4.14 The result of prestack Kirchhoff depth migration with a constant velocity of 4,200m/s from surface topography. The dashed white rectangle and yellow ellipse shows the poor imaging quality when compared with the result from the prestack SSF method.
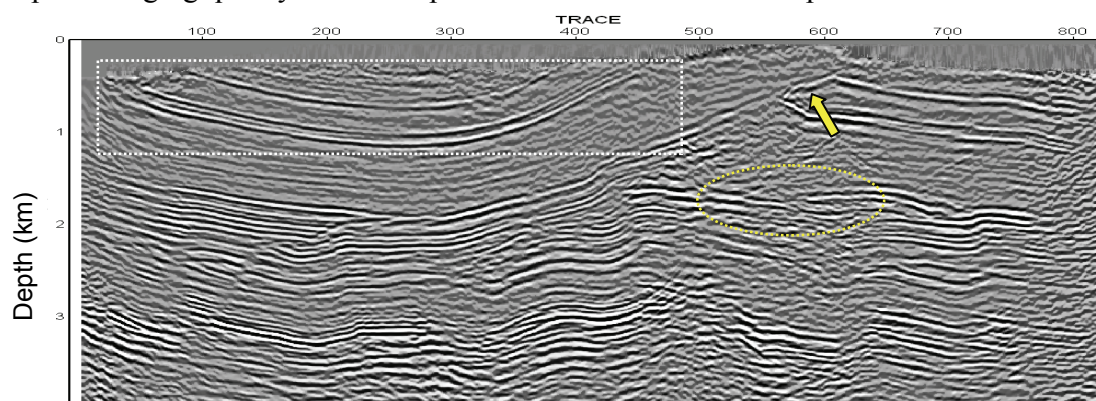
Figure 4.15 The result of prestack SSF depth migration with a constant velocity of 4,200m/s from surface topography. The dashed white rectangle and yellow ellipse shows the better imaging quality compared with the result from the prestack Kirchhoff depth method. The yellow arrow shows the structure unnoticeable in the Kirchhoff result.
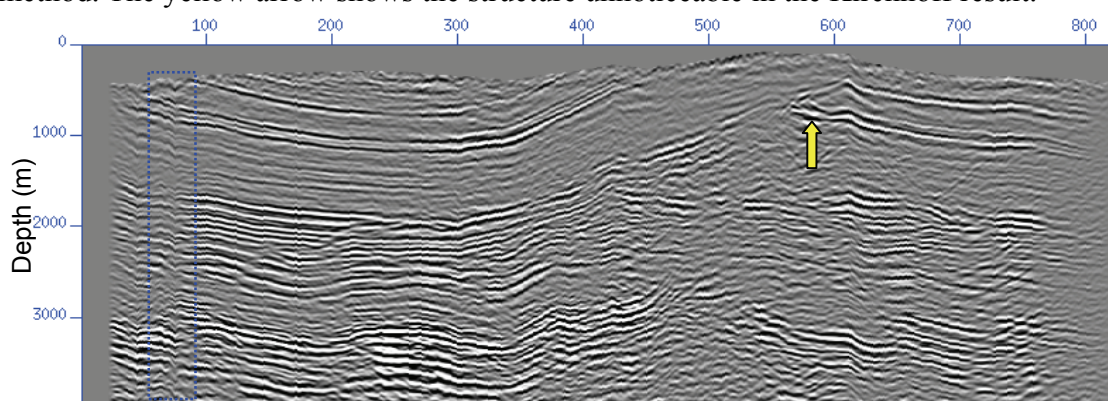
Figure 4.16 The result of prestack SSF depth migration with a constant velocity of 4,200m/s after elevation correction with filed statics. The dashed blue rectangle shows the phenomena of traces "shaking", and the arrow indicates the changed shape of the reflection event when compared with the results in Figures 4.13 and 4.14.

4.6 Chapter summary

A technique for downward-continuation wavefield extrapolation has been presented and applied to three prestack depth migration methods — PSPI, SSF and IFD. Details of three extrapolation methods from topography are given, and the characteristics of each algorithm are compared and analyzed for performance in terms of speed and accuracy. Three prestack depth migration algorithms are developed and applied to Foothills synthetic data and real data. The prestack Kirchhoff migration was also included in the comparison and analysis.

The three downward-continuation extrapolation methods from Foothills surface topography all demonstrate their excellent capability in handling extreme lateral-velocity and topographic variations. Comparisons among the downward-continuation methods show IFD is more capable of imaging the near surface while SSF exhibits higher efficiency with almost the same resolution as PSPI for this model. Comparisons between the images produced by the downward-continuation algorithms and that generated with the Kirchhoff algorithm indicate that the wave-equation-based algorithm is more capable of recovering the near-surface structures and high-angle fault planes. At the same time, the traveltimes generated by the upwind finite-difference method with the Eikonal equation are validated by the prestack Kirchhoff migration result. Comparisons between the SSF and Kirchhoff migrations on the field data highlight the imaging quality of wave-equation-based migration methods and the efficiency of ray-based migration methods.

Chapter Five: Prestack anisotropic reverse-time migration for tilted TI media

5.1 Introduction

To implement the prestack anisotropic reverse-time migration method for tilted transversely isotropic (TTI) media, we first need to derive the anisotropic P- and SV-wave equations. The pseudo-spectral numerical method is applied to solve these equations based on the characteristics of the derived equations. At the same time, the stability and accuracy of pseudo-spectral method for anisotropic P and SV wave equations are analyzed. Anisotropic ray-racing is used to obtain the traveltime of the forward wavefield. It will be correlated with the backward wavefield estimated by reverse-time extrapolation. The prestack depth migration will use the zero-lag cross-correlation imaging condition. Numerical and physical examples are processed with post-stack and prestack anisotropic reverse-time migration, which validate the algorithm and show its capacity to adapt to lateral variable velocities and anisotropy parameters.

5.2 Theory for P- and SV-wave equations for TTI media

5.2.1 Simplified P- and SV-wave equations for TTI media

To simulate acoustic wave propagation in a VTI medium, Alkhalifah (2000) proposed an acoustic wave equation by setting the shear wave velocity v_{s0} to 0. He showed that the new acoustic VTI wave equation yielded a kinematically acceptable approximation of P-wave propagation when compared to the full elastic solution in VTI media. Zhang et al. (2003) extended the acoustic wave equation for VTI media to one for TTI media. However, contrary to conventional wisdom, setting v_{s0} to 0 eliminates only the component in the principal axis and introduces diamond-shape artifacts, indicating that it does not eliminate the shear-wave phase velocity in the orthogonal directions. Grechka et

al. (2004) gave a detailed discussion about shear waves in acoustic anisotropic media. Alkhalifah (2000) proposed placing the source in a thin isotropic layer to reduce artifacts. This imposes limitations on his formulation not only for modelling anisotropic cases, but also for possible extensions to other seismic processing and imaging stages. Strong shear waves will contaminate P-wave data produced by any full-waveform modelling code (Grechka et al., 2004). Moreover, imaging techniques such as reverse-time migration will produce artifacts from these shear waves. Klie and Toro (2001) used a weak anisotropy approximation to successfully suppress these "artifacts". To implement the P- and SV-wave reverse-time migrations in TTI media, we require the individual P- and SV-wave equations. We start with the VTI phase-velocity equation (Tsvankin, 1996) written as

$$\frac{v^2(\theta)}{v_{p0}^2} = 1 + \varepsilon \sin^2 \theta - \frac{f}{2}$$
$$\pm \frac{f}{2}\sqrt{(1 + \frac{2\varepsilon \sin^2 \theta}{f})^2 - \frac{2(\varepsilon - \delta)\sin^2 2\theta}{f}}, \tag{5.1}$$

where the $\pm$ sign yields $v_p(\theta)$ and $v_s(\theta)$, respectively. When we rotate the symmetry axis from vertical to a tilt angle of ϕ, the phase velocity in the direction measured from the vertical direction is:

$$\frac{v^2(\theta,\phi)}{v_{p0}^2} = 1 + \varepsilon \sin^2 (\theta - \phi) - \frac{f}{2}$$
$$\pm \frac{f}{2}\sqrt{(1 + \frac{2\varepsilon \sin^2 (\theta - \phi)}{f})^2 - \frac{2(\varepsilon - \delta)\sin^2 2(\theta - \phi)}{f}}, \tag{5.2}$$

where θ is phase angle, $f = 1 - \frac{v_{s0}^2}{v_{p0}^2}$, and ε and δ are Thomsen parameters (Thomsen, 1986), which are defined as:

$$\varepsilon = \frac{c_{11} - c_{33}}{2c_{33}}, \text{ and } \delta = \frac{(c_{13} + c_{44})^2 - (c_{13} - c_{44})^2}{2c_{33}(c_{13} - c_{44})}, \tag{5.3}$$

where c_{ij} are the elastic moduli which have been reviewed in Chapter 2. Noting that anisotropic reverse-time migration is expensive and weak anisotropy is a reasonable assumption in many real cases (Thomsen, 1986), we will use the assumption of weak anisotropy, which also results in simpler equations that save computation effort while somewhat retaining accuracy. This allows us to simplify the phase-velocity expression of Equation (5.2). Expanding the radical in a Taylor series and dropping the quadratic and higher terms of the anisotropy parameters ε and δ, we obtain the P- and SV-wave phase velocity formula as:

$$\frac{v_p^2(\theta)}{v_{p0}^2} = 1 + 2\delta \sin^2 \theta \cos^2 \theta + 2\varepsilon \sin^4 \theta, \tag{5.4}$$

$$\frac{v_s^2(\theta)}{v_{p0}^2} = 1 - f + 2(\varepsilon - \delta) \sin^2 \theta \cos^2 \theta. \tag{5.5}$$

To obtain this acoustic wave equation for anisotropic VTI media, Alkhalifah (2000) set $v_{s0} = 0$, which makes $f = 1$. Then, from Equation (5.2), the acoustic wave equation can be written as

$$\frac{v_p^2(\theta)}{v_{p0}^2} = \frac{1}{2} + \varepsilon \sin^2 \theta + \frac{1}{2} \sqrt{(1 + 2\varepsilon \sin^2 \theta)^2 - 2(\varepsilon - \delta) \sin^2 2\theta}. \tag{5.6}$$

By rotating the symmetry axis from vertical to a tilt angle ϕ, we can get the phase velocity for P- and SV-waves in the direction measured from the vertical direction. The P- and SV-wave phase velocity formulas are shown as follows:

$$\frac{v_p^2(\theta,\phi)}{v_{p0}^2} = 1 + 2\delta\sin^2(\theta-\phi)\cos^2(\theta-\phi) + 2\varepsilon\sin^4(\theta-\phi), \quad (5.7)$$

$$\frac{v_s^2(\theta,\phi)}{v_{p0}^2} = 1 - f + 2(\varepsilon-\delta)\sin^2(\theta-\phi)\cos^2(\theta-\phi). \quad (5.8)$$

Using a similar approach, we can write Alkhalifah's acoustic wave equation for tilt angle ϕ as

$$\frac{v_p^2(\theta,\phi)}{v_{p0}^2} = \frac{1}{2} + \varepsilon\sin^2(\theta-\phi) + \frac{1}{2}\sqrt{(1+2\varepsilon\sin^2(\theta-\phi))^2 - 2(\varepsilon-\delta)\sin^2 2(\theta-\phi)}. \quad (5.9)$$

If we try to maintain higher accuracy for weak anisotropy, we can also expand the radical in Equation (5.2) in a Taylor series and retain the quadratic terms in ε and δ. We then obtain

$$\frac{v_p^2(\theta)}{v_{p0}^2} = 1 + 2\delta\sin^2\theta\cos^2\theta + 2\varepsilon\sin^4\theta + \frac{4}{f}(\varepsilon-\delta)(\varepsilon\sin^2\theta + \delta\cos^2\theta)\sin^4\theta\cos^2\theta, \quad (5.10)$$

$$\frac{v_s^2(\theta)}{v_{p0}^2} = 1 - f + 2(\varepsilon-\delta)\sin^2\theta\cos^2\theta - \frac{4}{f}(\varepsilon-\delta)(\varepsilon\sin^2\theta + \delta\cos^2\theta)\sin^4\theta\cos^2\theta. \quad (5.11)$$

For plane waves travelling in the vertical (x, z) plane, the phase angle is given by

$$\sin\theta = \frac{v(\theta,\phi)k_x}{\omega}, \quad \cos\theta = \frac{v(\theta,\phi)k_z}{\omega}, \quad (5.12)$$

where $v(\theta,\phi)$ is the phase velocity for tilted coordinates, k_x is the horizontal wavenumber and k_z is the vertical wavenumber. When we multiply Equations (5.7) and (5.8) with the wavefield in the Fourier domain $U(k_x, k_z, t)$, and apply an inverse Fourier

transform in frequency only with ($\omega \rightarrow i\dfrac{\partial}{\partial t}$), we can obtain P- and SV-wave equations in

the time-wavenumber domain for tilted TI media. The new P-wave equation for tilted

transversely isotropic media is

$$
\begin{aligned}
\frac{\partial^2 U_p(k_x,k_z,t)}{\partial t^2} = -v_{p0}^2 [k_x^2 + k_z^2 + (2\delta\sin^2\phi\cos^2\phi + 2\varepsilon\cos^4\phi)\frac{k_x^4}{k_x^2 + k_z^2} \\
+ (2\delta\sin^2\phi\cos^2\phi + 2\varepsilon\sin^4\phi)\frac{k_x^4}{k_x^2 + k_z^2} \\
+ (\text{-}\delta\sin^2 2\phi + 3\varepsilon\sin^2 2\phi + 2\delta\cos^2\phi)\frac{k_x^2 k_z^2}{k_x^2 + k_z^2} \\
+ (\delta\sin 4\phi - 4\varepsilon\sin 2\phi\cos^2\phi)\frac{k_x^3 k_z}{k_x^2 + k_z^2} \\
+ (-\delta\sin 4\phi - 4\varepsilon\sin 2\phi\sin^2\phi)\frac{k_z^3 k_x}{k_x^2 + k_z^2}] U_p(k_x,k_z,t)
\end{aligned}
\qquad (5.13)
$$

The new SV-wave equation for tilted transversely isotropic media is

$$
\begin{aligned}
\frac{\partial^2 U_s(k_x,k_z,t)}{\partial t^2} = -v_{s0}^2 [k_x^2 + k_z^2 + \frac{\sigma}{2}(\sin^2 2\phi\frac{k_x^4 + k_z^4 - 2k_x^2 k_z^2}{k_x^2 + k_z^2} + 4\cos^2 2\phi\frac{k_x^2 k_z^2}{k_x^2 + k_z^2} \\
+ 2\sin 4\phi\frac{k_x^3 k_z - k_x k_z^3}{k_x^2 + k_z^2})] U_s(k_x,k_z,t)
\end{aligned}
\qquad (5.14)
$$

The coefficient σ,

$$
\sigma = (\frac{v_{p0}}{v_{s0}})^2 (\varepsilon - \delta),
\qquad (5.15)
$$

which was introduced by Tsvankin and Thomsen (1994) as the influential parameter in

the SV-wave moveout and velocity equations. In anisotropic seismic modelling and

migration, we can use Equations (5.13) and (5.14) to obtain separate P and SV

wavefields.

5.2.2 Discussion of the simplified P- and SV-wave equations for TTI media

To evaluate the accuracy of the above wave equations, we demonstrate their impulse responses for axes of symmetry of 0°, 30°, 60° and 90°. We plot phase velocity versus phase angle using $\varepsilon = 0.25$ and $\delta = 0.1$. We compare the differences among Alkhalifah's acoustic wave formula, the weak anisotropy formula, the quadratic approximation anisotropy formula, and the exact P-wave phase velocity formula for TTI media in Figure 5.1. There is only a slight difference among the curves. Alkhalifah's formula and the quadratic approximation are closer to the exact solution. The accuracy of the weak anisotropic approximation is adequate for weak anisotropic media while saving considerable computer time. Figure 5.2 illustrates the SV-wave phase velocities for three cases: the weak anisotropy case with a linear approximation, the anisotropy case with a quadratic approximation, and the exact formula. The linear solution now differs from the exact one; however, if Equation (5.8) is modified by retaining the quadratic terms in ε and δ from the exact SV phase velocity formula, the accuracy is greatly improved. This, of course, results in an increase in computation cost.
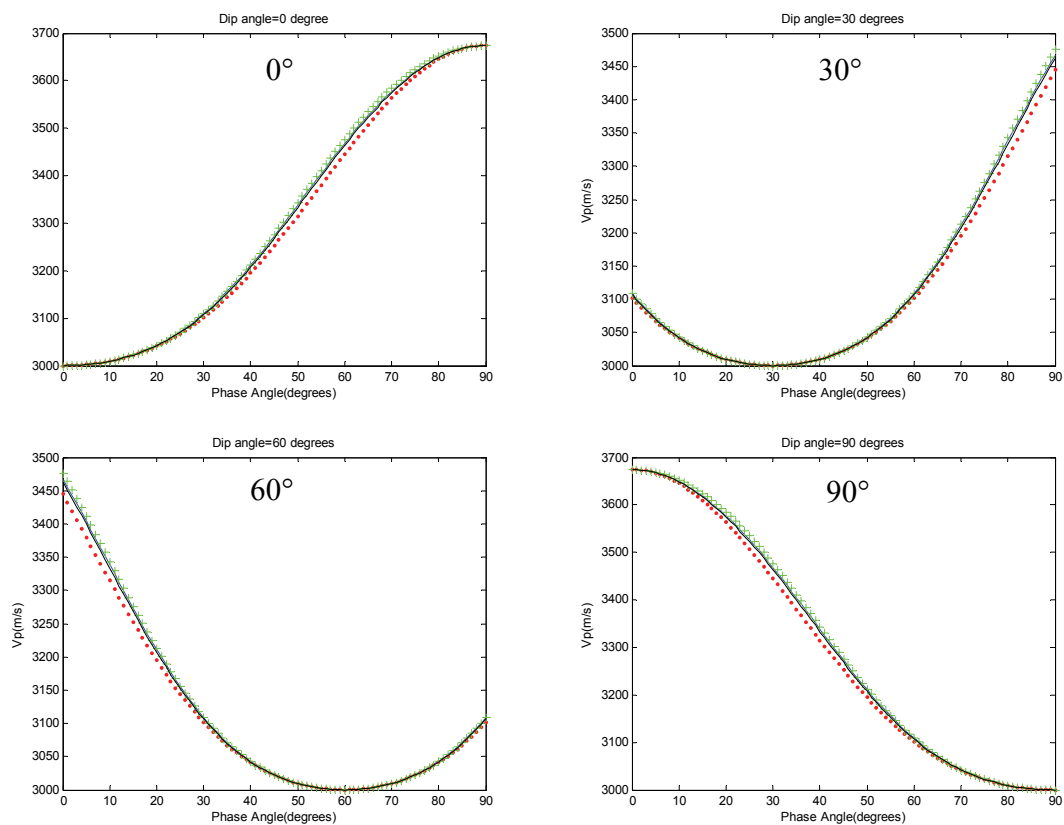
Figure 5.1 P-wave phase velocities for a TI medium with an axis of symmetry with angles of 0°, 30°, 60° and 90°. In each graph, the black line corresponds to P-wave phase velocities with the Alkhalifah formula, the red dotted line plots P-wave phase velocities with the weak anisotropy formula, the green x-line is the quadratic approximation formula, and the solid blue line plots the exact formula. The medium has a P-wave velocity of 3,000 m/s and a SV-wave velocity of 1,500 m/s in the direction parallel to the symmetry axis with Thomsen parameters $\varepsilon = 0.25$ and $\delta = 0.1$.
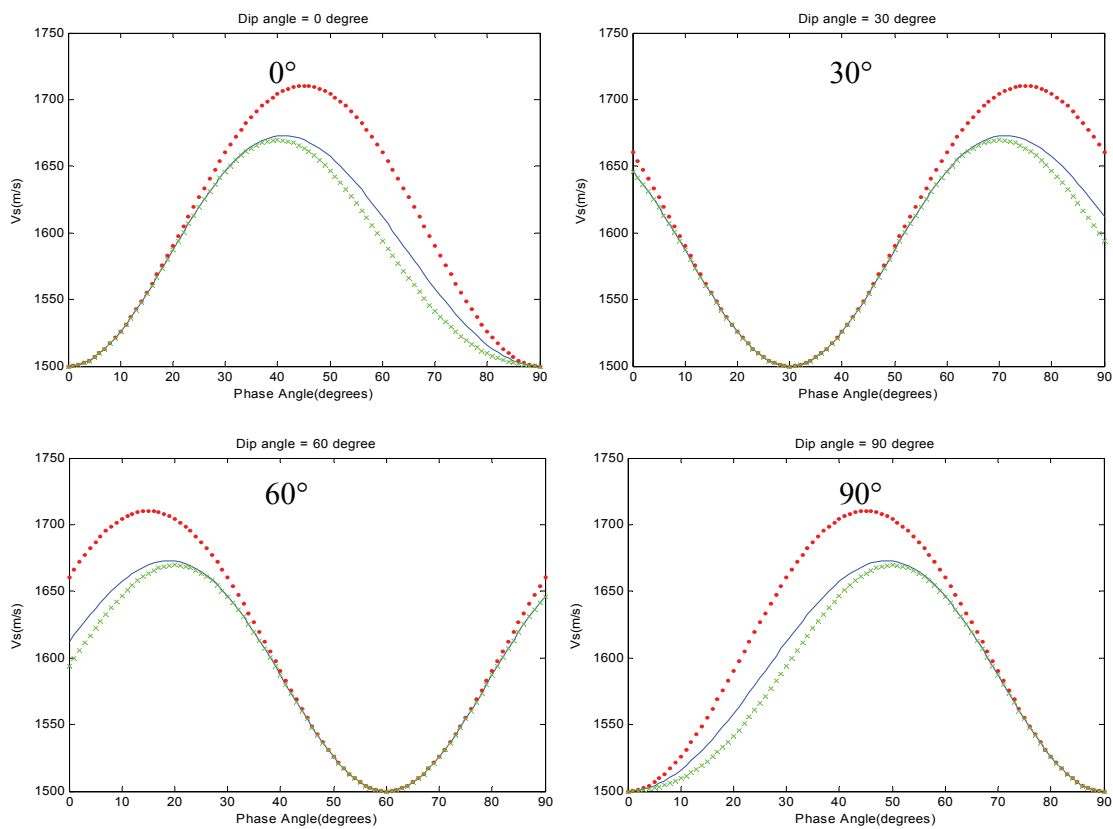
Figure 5.2 SV-wave phase velocities for a TI medium with a symmetry axis with angles of 0°, 30°, 60° and 90°. In each graph, the red dots correspond to SV-wave phase velocities from the weak anisotropy formula with linear approximation, the green x-line denotes SV-wave phase velocities from weak anisotropy with the quadratic approximation, and the blue line plots SV phase velocities with the exact formula. The velocities and Thomsen parameters are same as those in Figure 5.1.

Figure 5.3 shows the phase velocities of Figure 5.1 and Figure 5.2 in polar coordinates. The subfigures correspond to the wavefield snapshots in a homogeneous medium, where the blue solid lines are the exact phase velocities of the P- and SV-waves and the red-cross lines denote the velocity of the P- and SV-waves based on the simplified Thomsen formula. The upper subfigures show P-wave phase velocity curves with 0° and 30° axes of symmetry. The lower subfigures correspond to the SV-wave phase velocity curves with 60° and 90° axes of symmetry. In the case of P-waves, there is hardly any difference between the simplified and exact formulas. Some differences appear in the SV wave curves, but the shapes are fairly consistent.
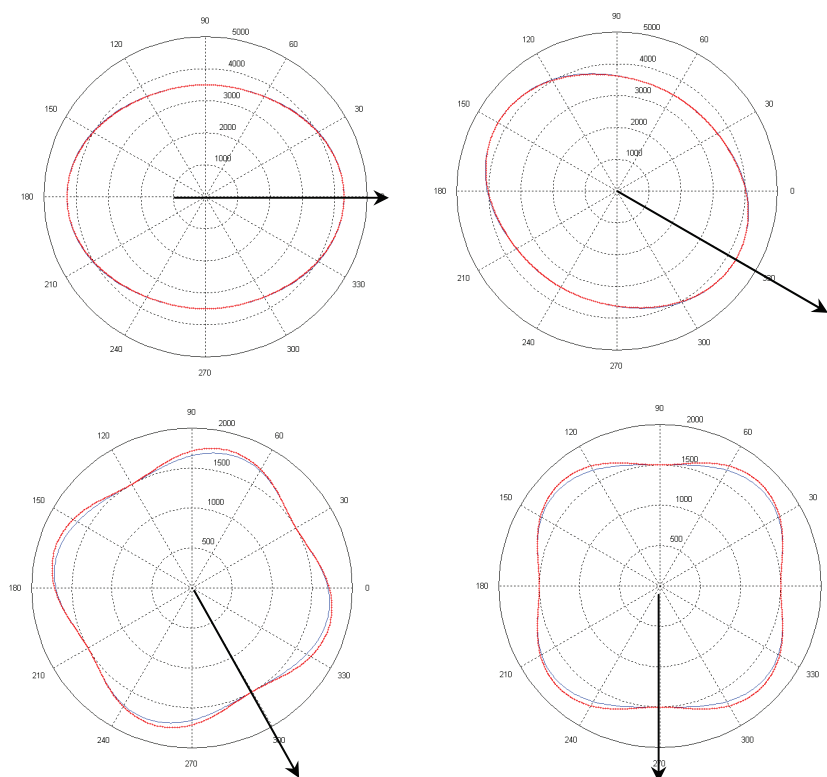
Figure 5.3 P and SV-wave phase velocities plotted in polar coordinates. The red line corresponds to the weak anisotropy formula and the solid blue line to the exact formula. The upper two graphs correspond to the P-wave with the symmetry axis having angles of 0° and 30°. The bottom two denote the SV-wave with the symmetry axis having angles of 60° and 90°. The velocities and Thomsen parameters are same as those in Figure 5.1.

In Figure 5.4, we now estimate a maximum difference between the true and the linear approximation phase velocities, which we refer to as the maximum velocity difference. The parameters ε and δ were varied from 0 to 0.25 in increments of 0.01 to estimate a distribution of absolute maximum relative velocity difference. The absolute maximum relative velocity difference for P-waves is plotted as a histogram in Figure 5.4(a). This figure shows that the absolute maximum relative velocity difference values are mainly distributed within a 2% range that indicates little deviation. Consequently, the simplified formula for P-wave can be accurately used in seismic modelling and processing in tilted

TI media. Figure 5.4(b) shows the absolute maximum relative differences between the simplified SV velocity formula values and the exact velocity values. The SV relative difference distribution area is larger than that of the P-wave distribution, which mainly ranges within a 5% margin of error. The simplified formula for SV waves can be effectively applied in cases of weak anisotropy.

(a)

(b)
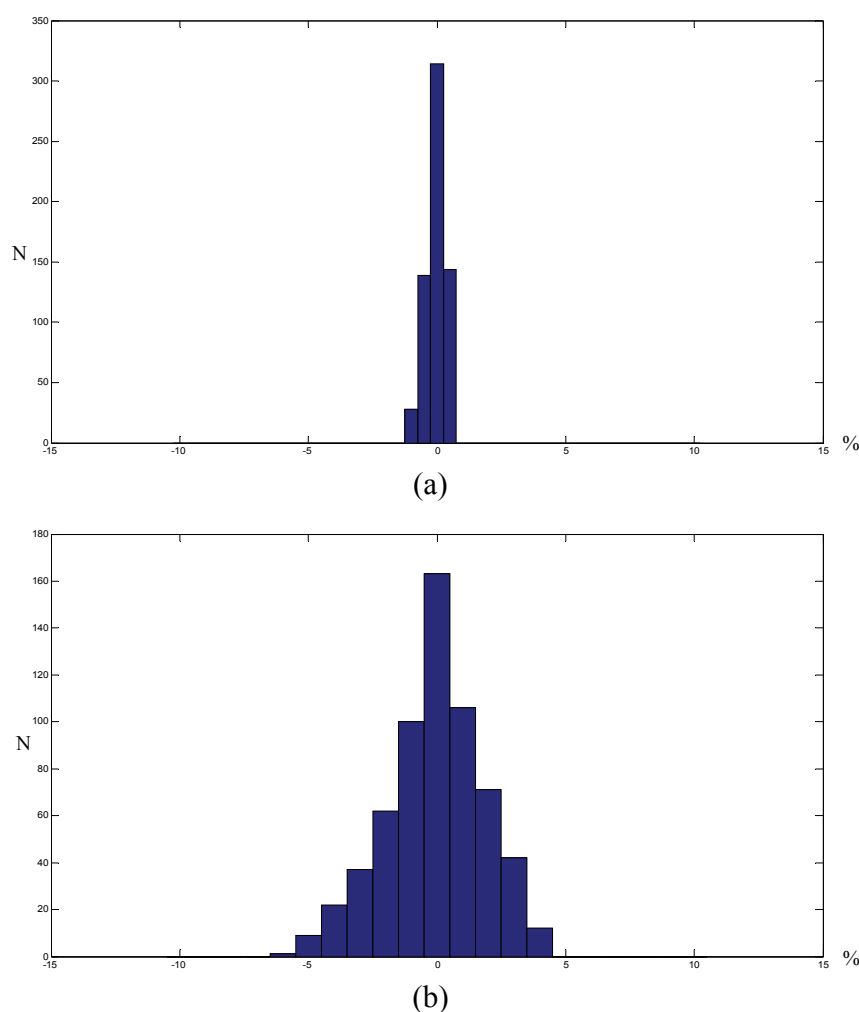
Figure 5.4 (a) The distribution of absolute maximum relative velocity differences between phase velocities from the simplified P-wave velocity formula and those from the exact formula. The medium has a qP-wave velocity of 3,000 m/s and a qSV-wave velocity of 1,500 m/s in the direction parallel to the axis of symmetry. The Thomsen parameters ε and δ both varied from 0 to 0.25 in increments of 0.01; (b) the corresponding analysis of simplified SV-wave.

5.3 Numerical solution method for P- and SV-wave equations for TTI media

The P- and SV-wave equations (Equations (5.13) and (5.14)) can also be written in the space-time domain. However, space and time are coupled in the terms $\partial^4 u / \partial x^2 \partial t^2$ and $\partial^4 u / \partial z^2 \partial t^2$, and these cause computation difficulties in finite-difference schemes which are avoided in the wavenumber-time domain. Therefore, we use the pseudo-spectral method (Fornberg, 1987) in reverse-time migration to solve these wave equations. The pseudo-spectral method has higher accuracy than lower order finite-difference methods, such as 2nd order and 4th order accuracy in the spatial domain, and thus it requires fewer grid points per wavelength to obtain the desired accuracy. It successfully eliminates the spatial frequency dispersion problem that results from a limited finite-difference operator in reverse-time migration. In the numerical computation, using Equations (5.13) and (5.14), we transform data from the spatial domain to the wavenumber domain,

$$\frac{\partial^2 U(k_x, k_z, t)}{\partial t^2} = U(k_x, k_z, t)[A_1(k_x, k_z)f_1(\varepsilon, \delta, \phi) + A_2(k_x, k_z)f_2(\varepsilon, \delta, \phi) + \ldots + A_5(k_x, k_z)f_5(\varepsilon, \delta, \phi)]; \quad (5.16)$$

perform the wavenumber calculation,

$$\frac{\partial^2 U(k_x, k_z, t)}{\partial t^2} = U_1(k_x, k_z, t)f_1(\varepsilon, \delta, \phi) + U_2(k_x, k_z, t)f_2(\varepsilon, \delta, \phi) + \ldots + U_5(k_x, k_z, t)f_5(\varepsilon, \delta, \phi)]; \quad (5.17)$$

return to spatial domain and apply the velocities and anisotropy parameters (ε, σ, ϕ) in the spatial domain,

$$\frac{\partial^2 U(k_x, k_z, t)}{\partial t^2} = U_1(x, z, t)f_1(\varepsilon, \delta, \phi) + U_2(x, z, t)f_2(\varepsilon, \delta, \phi) + \ldots + U_5(x, z, t)f_5(\varepsilon, \delta, \phi)] = U(k_x, k_z, t); \quad (5.18)$$

and then use the finite-difference method in the time domain to calculate the wavefields at the previous time. The process of each loop is continued for each reverse time step

until zero time, where we get our migration result. The calculation flow is illustrated in Figure 5.5.
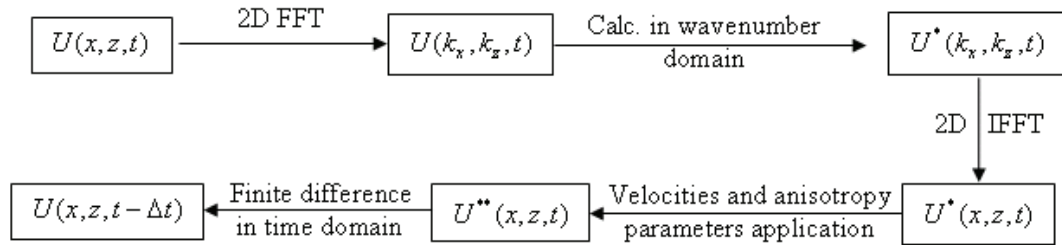
Figure 5.5 The computation flow for implementing anisotropic reverse-time migration

5.4 Analysis of accuracy and stability of pseudo-spectral methods for the anisotropic wave equation in tilted TI media

To analyze the accuracy and stability of pseudo-spectral method for the anisotropic wave equation in tilted TI media, we consider them by estimating the error in the solution methods discussed above. The error in a formula is commonly referred to as a "truncation error" because in the Taylor series type of derivation, the error comes from the truncation of the series (Hamming, 1962). The form of the error is written in terms of some high-order derivatives. We establish criteria for stability based on a model of uniform velocity through the entire domain. Using this model, we also estimate the truncation errors resulting from the time differencing schemes. When velocity and anisotropy parameters are constant, the solution to Equations (5.13) or (5.14) differs from the initial wavefield in that some phase shift is applied to the Fourier coefficients

$$u(x,z,t) = \iint U(k_x, k_z, t = 0)e^{i(k_x x + k_z z + \omega t)} dk_x dk_z . \qquad (5.19)$$

There is no interaction between Fourier modes, and thus each Fourier component maintains its identity; only its phase angle changes with increasing time. Consequently, such a model does not account for truncations in the spatial frequency domain. Aliasing,

the generation of spatial frequencies above the cut-off (Nyquist) frequency, is problem dependent. The magnitude of aliasing errors depends upon the relationship between the frequency spectrum of the true solution and the highest frequency which can be supported by the computation grid. The effect of truncation in the frequency domain is almost independent of the numerical method used. Therefore, aliasing effects are ignored when the accuracy of the method is considered.

Substituting trial solution $e^{i(k_x x + k_z z - \omega t)}$ in the discretized Equation (5.13) for the anisotropic P-wave with a 2nd order central finite-difference scheme gives the dispersion relation

$$
\begin{aligned}
\frac{2}{v_p \Delta t} \sin \frac{\omega t}{2} = sqrt[& k_x^2 + k_z^2 + (2\delta \sin^2 \phi \cos^2 \phi + 2\varepsilon \cos^4 \phi) \frac{k_x^4}{k_x^2 + k_z^2} \\
& + (2\delta \sin^2 \phi \cos^2 \phi + 2\varepsilon \sin^4 \phi) \frac{k_x^4}{k_x^2 + k_z^2} \\
& + (-\delta \sin^2 2\phi + 3\varepsilon \sin^2 2\phi + 2\delta \cos^2 \phi) \frac{k_x^2 k_z^2}{k_x^2 + k_z^2} \\
& + (\delta \sin 4\phi - 4\varepsilon \sin 2\phi \cos^2 \phi) \frac{k_x^3 k_z}{k_x^2 + k_z^2} \\
& + (-\delta \sin 4\phi - 4\varepsilon \sin 2\phi \sin^2 \phi) \frac{k_z^3 k_x}{k_x^2 + k_z^2})]
\end{aligned}
\qquad (5.20)
$$

The equation seems very complicated for stability analysis. Different anisotropy parameters determine the different stability limits, even when there are different tilt angles with the same Thomson parameters. In general, the stability constraints of vertical TI media are analyzed here. From Equation (5.20), setting ϕ equal to 0 for real ω,

$$
v_p \Delta t < 2 / sqrt[k_x^2 + k_z^2 + 2\varepsilon \frac{k_x^4}{k_x^2 + k_z^2} + 2\delta \frac{k_x^2 k_z^2}{k_x^2 + k_z^2}].
\qquad (5.21)
$$

Assuming $\alpha = \min\{abs(\varepsilon), abs(\delta)\}$, we obtain the following expression

$$\Delta t < \frac{2}{v_p[\sqrt{(1+2\alpha)k_x^2 + k_z^2}}.$$ (5.22)

With the Nyquist spatial frequencies in x and y and for a uniform Δd grid spacing in x and y, we obtain the 2D stability criterion

$$\frac{v_p \Delta t}{\Delta d} < \frac{2}{\pi\sqrt{(2+2\delta)}}.$$ (5.23)

A similar derivation for the stability criterion of SV-waves is applied and we get the inequality for SV-waves in vertical TI media

$$v_p \Delta t < 2/sqrt[k_x^2 + k_z^2 + 2\delta \frac{k_x^2 k_z^2}{k_x^2 + k_z^2}].$$ (5.24)

Finally, the stability for SV-waves in vertical TI media can be expressed as

$$\frac{v_s \Delta t}{\Delta d} < \frac{\sqrt{2}}{\pi}.$$ (5.25)

From Equations (5.23) and (5.25), the constraint of anisotropic P-wave equation is looser than that of anisotropic SV-wave.

To estimate the differencing error of these equations, we can express the theoretical values of p in the neighbourhood of t by Taylor series expansion

$$p_{th}(t \pm \Delta t) = \sum_{l=0}^{\infty} \frac{\partial^l p(t)}{\partial t^l} \frac{(\pm \Delta t)^l}{l!}$$ (5.26)

From the wavefield given at time t and $t - \Delta t$, we approximate its value at time $t + \Delta t$ by the expression

$$p(t + \Delta t) \cong 2p(t) - p(t - \Delta t) + \frac{\partial^2 p(t)}{\partial t^2}(\Delta t)^2 . \qquad (5.27)$$

Then we calculate the error as

$$\varepsilon(\Delta t) = p(t + \Delta t) - p_{th}(t + \Delta t) = 2p(t) - \frac{\partial^2 p(t)}{\partial t^2}(\Delta t)^2 - \sum_{l=0}^{\infty}\frac{\partial^l p(t)}{\partial t^l}\frac{(\Delta t)^l + (-\Delta t)^l}{l} . \qquad (5.28)$$

After taking into account the cancellation of terms with odd l values, we obtain

$$\varepsilon(\Delta t) = -2\sum_{l=4}^{\infty}\frac{\partial^l p(t)}{\partial t^l}\frac{(\Delta t)^l}{l!}; l = 4,6,8,... \qquad (5.29)$$

For most practical purposes, the lowest order error estimate,

$$\varepsilon(\Delta t) \cong -\frac{\partial^4 p(t)}{\partial t^4}\frac{(\Delta t)^4}{12} , \qquad (5.30)$$

is adequate.

5.5 Traveltime generation by ray-tracing for prestack reverse-time migration

5.5.1 Ray-tracing in anisotropic media

A 2D raytracer developed by Grech (2002) calculates the ray-path and traveltime. It still starts from the phase velocity equation with weak anisotropy approximation (Equation 5.4). The corresponding derivative $dv_p(\theta)/d\theta$ is also computed as given in the following equation:

$$\frac{dv_p(\theta)}{d\theta} = a_0\left\{2\delta[\cos^3\theta\sin\theta - \cos\theta\sin^3\theta] + 4\varepsilon\cos\theta\sin^3\theta\right\} . \qquad (5.31)$$

The relationship between the phase and group velocity is shown in Equations (5.32) and (5.33):

$$g = \sqrt{v_p^2 + \left(\frac{\partial v_p}{\partial \theta}\right)^2}, \tag{5.32}$$

and

$$\phi = \theta + \tan^{-1}\left(\frac{\partial v_p / \partial \theta}{v}\right), \tag{5.33}$$

where g is the group velocity of the P-waves, ϕ is the angle between the group velocity and symmetry axis, and θ is the angle between the phase velocity and symmetry axis. Equation (5.32) gives the relationship between the magnitude of phase and group vectors. Equation (5.33) shows the relationship between the angles of the two vectors relative to the symmetry axis. For anisotropic ray-tracing, we trace a ray across an interface with different anisotropy parameters according to Snell's law. Figure 5.6 illustrates the relationship between phase angle θ, ray angle ϕ, incident phase angle β, and incident ray angle α. At the same time, it can be found that

$$\alpha = \phi + \gamma, \qquad \beta = \theta + \gamma, \tag{5.34}$$

where γ is the angle of the TI symmetry axis. From the source position, a set of rays are emitted. When different rays arrive at the interface, the phase angles are obtained through scanning calculation and interpolation using Equation (5.34) for a range of phase angles from 0° to 90°. Since the ray parameter p is constant for a given ray across an interface, which is calculated from

$$p = \frac{\sin(\theta + \gamma)}{v(\theta)}, \tag{5.35}$$

we use the same method to get the refracted phase angle. In each layer, Equation (5.32) is used to obtain the group velocity. Consequently the traveltime is generated with ray path length over the group velocity. Through the traveltime interpolation, we get the traveltime table for each grid in the spaces.
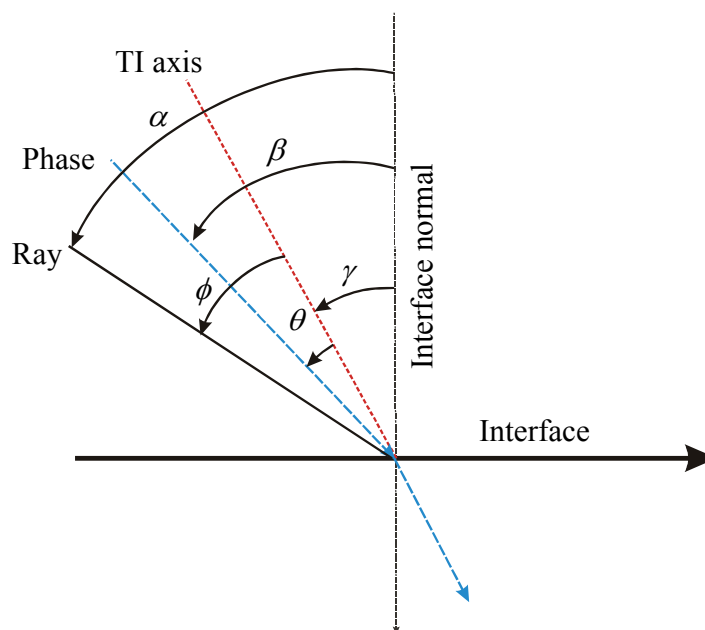
Figure 5.6 The relationship between the ray and phase angles with the TI axis (Grech, 2002).

5.6 The implementation of prestack anisotropic reverse-time migration

The procedure (seen in Figure 5.7) has four parts:

1. Determine the excitation-time imaging condition by ray-tracing to obtain traveltimes from source position.

2. Extrapolate the receiver wavefields backward in time using P- or SV-wave equations in anisotropic media.

3. Apply the zero-lag cross-correlation imaging condition.

4. Sum the individual migrated shot to produce the final migration result.
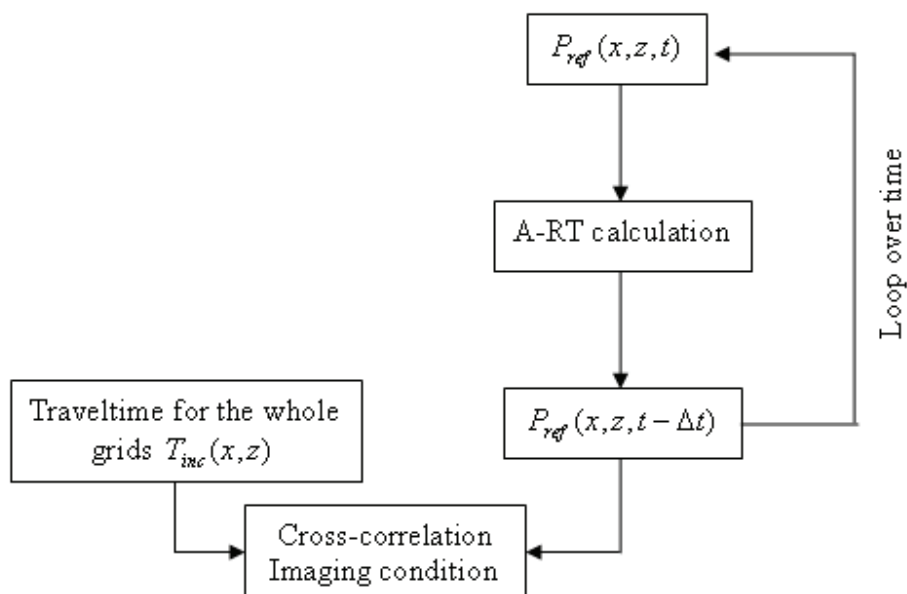
Figure 5.7 The wavefield extrapolation scheme for prestack anisotropic reverse-time migration

5.7 Numerical examples

To verify the anisotropic reverse-time migration's effectiveness and accuracy, two numerical models were used. The first model was used to show the impulse responses of P and SV waves in a homogeneous, anisotropic medium. The second model was used for an anisotropic depth migration with a variable velocity model with constant anisotropy parameters. The P- and SV-wave impulse responses show excellent dipping angle imaging ability and are comparable with the phase-shift wave extrapolation shown in Zhang, et al. (2001). The variable velocity model with constant anisotropy parameters is designed to exhibit the accurate imaging ability of anisotropic reverse-time migration in TTI media.

5.7.1 P- and SV-wave impulse response

Figure 5.8 shows the P-wave impulse response in a tilted TI medium with tilt angles of

0°, 30°, 60°, and 90°. Figure 5.9 shows the corresponding SV-wave impulse response.

The vertical tilt velocity of the P-wave is 3,500m/s and that of the SV-wave is 1,500m/s.

The homogeneous medium has Thomsen anisotropy parameters of $\varepsilon = 0.25$ and $\delta = 0.1$.

When tilt angles are changed, the symmetry axis changes accordingly. The advantage of

reverse-time migration is illustrated with energy reaching dips of 90°. Although the

amplitude of the SV-impulse response is weaker at higher angles (due to obliquity

effects), it is non-zero that is similar to the amplitude of a semicircular response in an

isotropic medium. The effect of anisotropy causes the wavefronts of P- and SV-waves to

differ from the circular ones of an isotropic medium and is consistent with the results

shown in Figure 5.3.
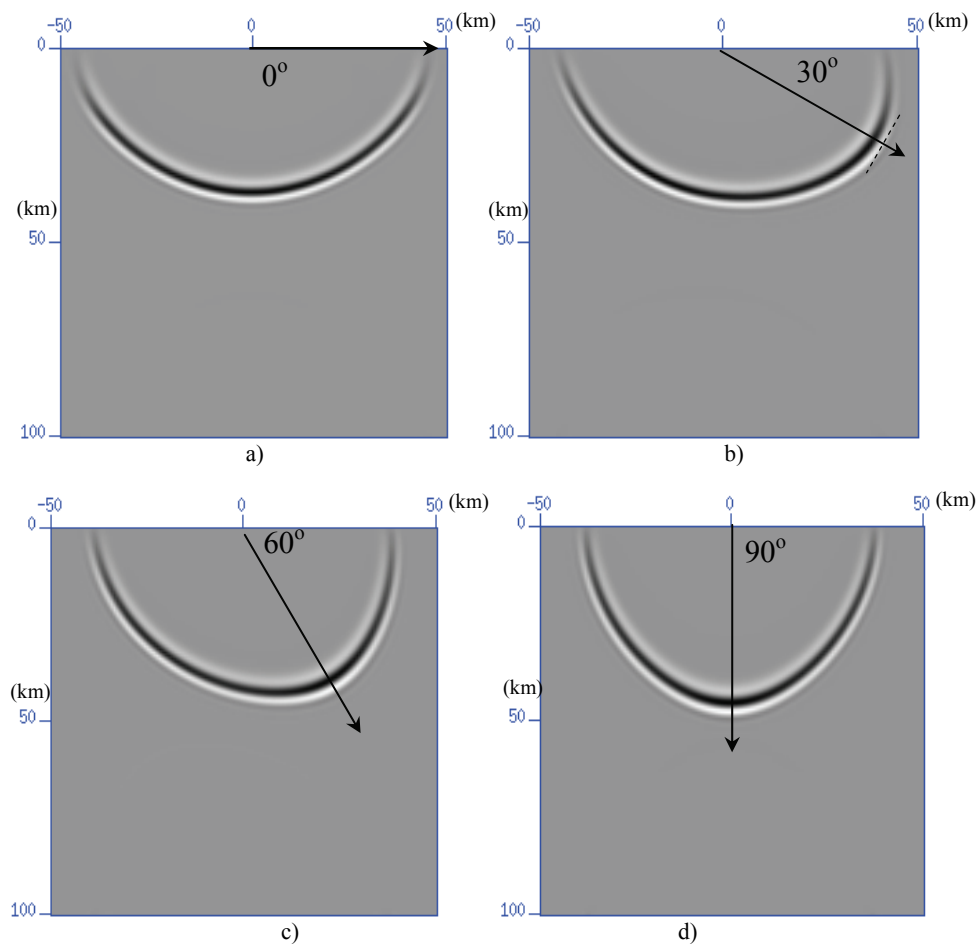
Figure 5.8 P-wave impulse response. (a), (b), (c) and (d) correspond to the results from symmetry axis tilt angles of 0°, 30°, 60°, and 90° as indicated by the arrows. The vertical velocity of the P-wave is 3,500m/s and that of the SV-wave is 1,500m/s. The homogenous medium has Thomsen parameters of $\varepsilon = 0.25$ and $\delta = 0.1$.
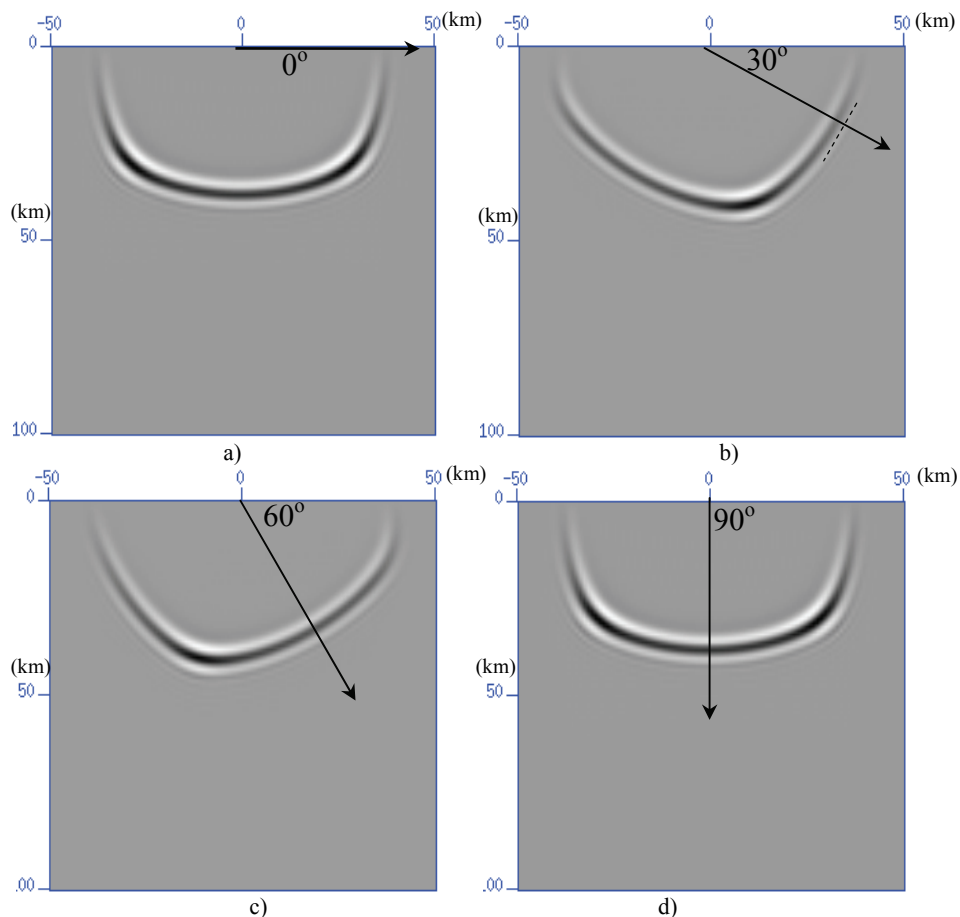
Figure 5.9 SV-wave impulse responses. (a), (b), (c) and (d) correspond to the results from symmetry axis tilt angles of 0°, 30°, 60°, and 90°. The velocities and Thomsen parameters are the same as those in Figure 5.8.

5.7.2 Anisotropic depth migration for a variable velocity model

A variable velocity model is shown in Figure 5.10 consisting of one reflector with three horizontal and three dipping segments. The media has anisotropy parameters of $\varepsilon = 0.2$ and $\delta = 0.1$, and the tilt angle is 60°. The P-wave velocity in the direction parallel to the symmetry axis of the model is $v(x, z) = 1,500 + 0.3z + 0.1x$(m/s). Figure 5.11 shows a synthetic zero-offset section for this model. Figure 5.12 is the isotropic migration result

obtained from isotropic reverse-time migration using the finite-difference method of 4th order accuracy in space and 2nd order accuracy in time. Figure 5.13 shows an anisotropic reverse-time migration result. The correct medium anisotropy parameters and velocity values are used in the anisotropic reverse-time migration method. We find that the migration result is an excellent match with the exact model interface. Clearly the image in Figure 5.13 is superior to that in Figure 5.12. The image from the isotropic migration (Figure 5.12) is not only undermigrated but it also has reflectors at shallow depths. Thus the anisotropic RT method gives a substantially better image than the corresponding isotropic RT method. However, the overall runtime of the anisotropic RT method is approximately five times longer than the isotropic case.
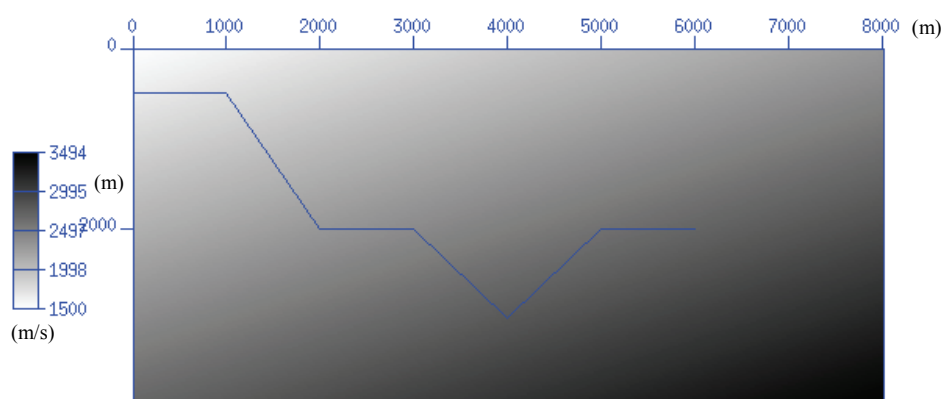
Figure 5.10 Variable velocity model with homogenous Thomsen parameters of $\varepsilon = 0.2$ and $\delta = 0.1$, and a tilt angle $\phi = 60°$. P-wave velocities parallel to the symmetry axis vary along the distance and depth as $v(x, z) = 1,500 + 0.3z + 0.1x$ (m/s).
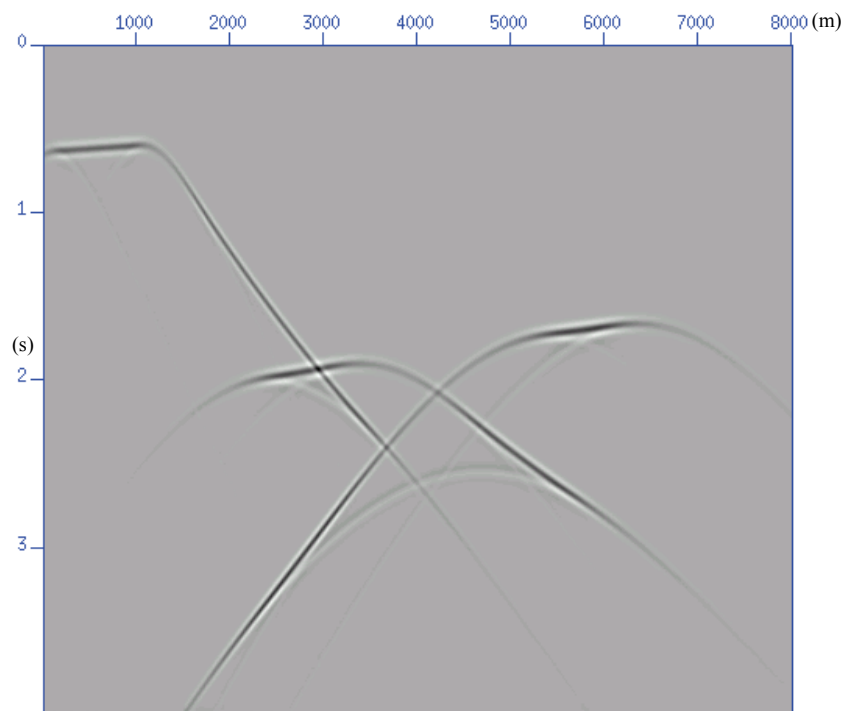
Figure 5.11 Synthetic zero-offset seismogram obtained using SU code from the Center for Wave Phenomena (CWP) for the structural model shown in Figure 5.10 of a tilted TI medium.
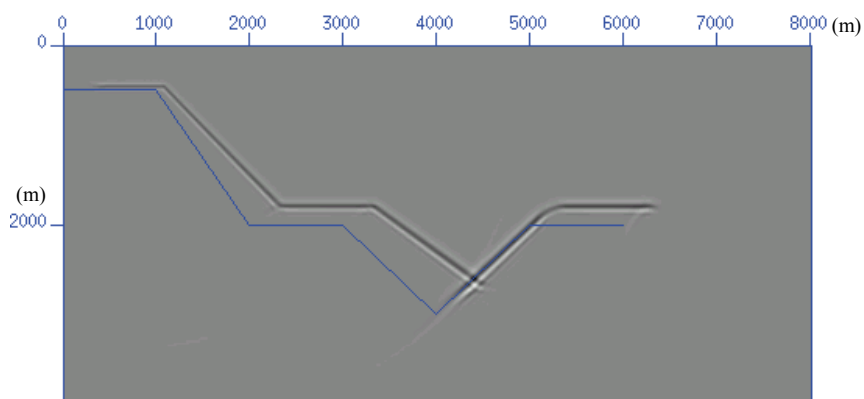
Figure 5.12 Migration result from the isotropic reverse-time migration method. The P-wave velocity model in Figure 5.10 is used without taking into consideration the effect of anisotropy. The blue lines represent the true position of interfaces.
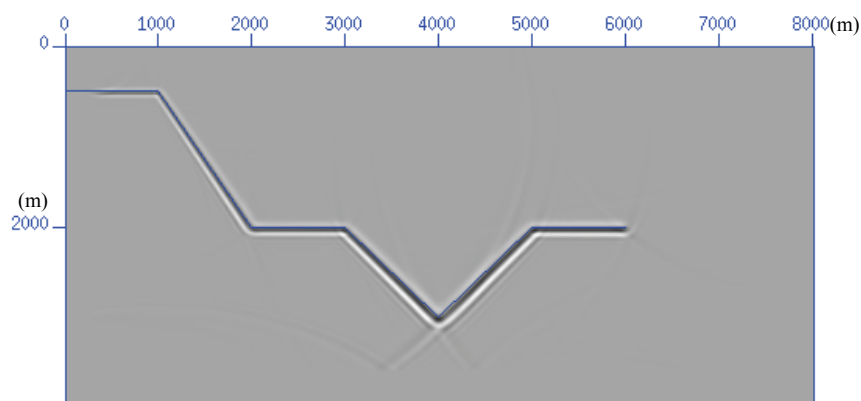
Figure 5.13 Migration result from the <u>anisotropic</u> reverse-time migration method. The exact velocity model and Thomson parameters have been applied. The migration result exactly matches the true interfaces.

5.8 A physical model example

A scaled physical model, including an isotropic reef with a TTI overburden, was constructed by the Foothills Research Project (FRP) at the University of Calgary. It was used to compare the magnitude of imaging errors incurred in using isotropic processing routines when there is seismic velocity anisotropy present in the dipping overburden. Post-stack and prestack migrations of the collected seismic data show that anisotropic reverse-time migration yields accurate image positioning while isotropic migration gives considerable errors in physical position and energy focus.

Seismic data were recorded on the anisotropic physical model described by Isaac and Lawton (1999) and used to test the post-stack and prestack migration algorithm. The model represents an isotropic reef below a TTI overburden. The modelling system used a scale factor of 1:10,000 to relate the model dimensions to field dimensions. Field dimensions are used here for easier reference to practical application. This physical model is very relevant for the exploration situation where we are trying to image targets

beneath anisotropic dipping layers such as dipping shale layers in the Canadian Foothills (the Banff shale).

The cross-section of this model is shown in Figure 5.14; it includes a TTI overburden layer with the axis of symmetry dipping at 45°. The layer has parameters v_{p0} = 2,950m/s, $\varepsilon = 0.241$, and $\delta = 0.100$. An isotropic layer that contains a simulated reef edge with v_{p0} =2,740 m/s underlies this anisotropic overburden. Figure 5.15 shows a zero-offset seismic section with the surface wave muted. Since the dipping angle is 45° in the anisotropic overburden, we adopt the measured velocity along vertical direction ($v_{45} = 3{,}145$ m/s) for the upper layer in isotropic depth migration.

Migrating the zero-offset section using isotropic reverse-time migration yields an image of the reef edge which is displaced by about 350m to the left of its true position (Figure 5.16). Migration by anisotropic reverse-time migration correctly positions the edge of reef, as shown in Figure 5.17. In this case, the input to the migration consisted of a grid containing values of v_{p0}, ε, δ, and the tilt of the symmetry axis at each node. Although there are some artifacts caused by interface reflections, which are shown by the blue dashed rectangles in Figure 5.16 and Figure 5.17, these do not affect the basement. For all practical purposes, the reef is imaged to its true position. The prestack data has 43 shot gathers and the receiver interval is 20m. The prestack isotropic migration result is shown in Figure 5.18, in which the same lateral shift of about 350m can be measured. The interface aliasing reflections are hardly noticeable compared with the post-stack isotropic migration. Although the lateral shift exists in the prestack isotropic migration result, it has higher resolution than the post-stack reverse-time migration result. As for the

prestack anisotropic reverse-time migration result in Figure 5.19, a clear and correct image is obtained. Given the cost statistics of the isotropic and anisotropic migration of the data, the increased cost for prestack anisotropic reverse-time migration is still almost five times that of the prestack isotropic case.
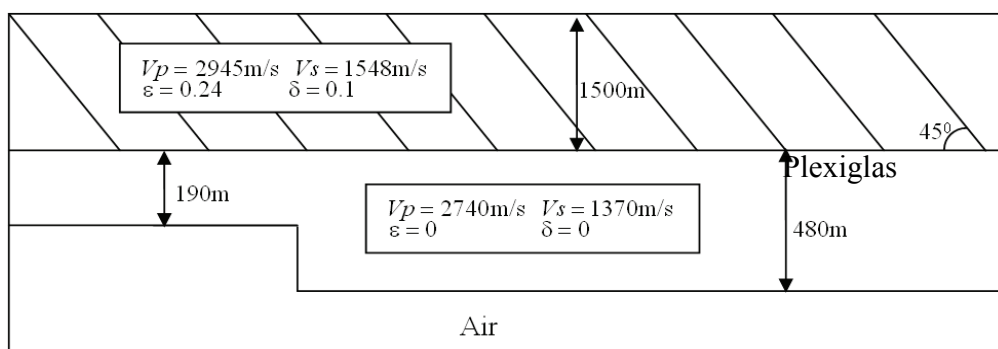
Figure 5.14 Model of an isotropic reef with an anisotropic overburden from the Foothills Research Project showing the 45° dipping anisotropic overburden above horizontal reflectors. The Plexiglas layer is isotropic.
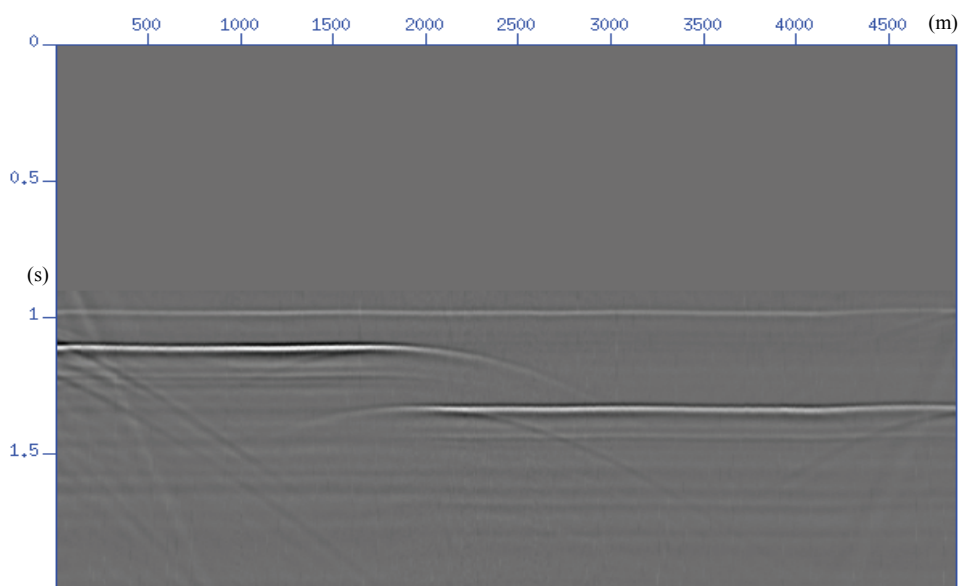
Figure 5.15 Seismic data acquired with coincident source and receiver (the true offset scales to about 200m).
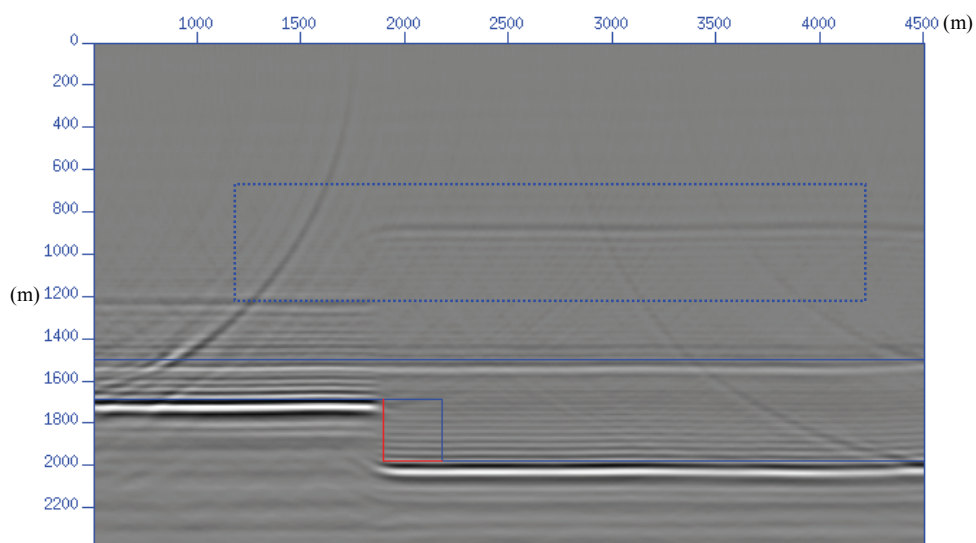
Figure 5.16 <u>Isotropic</u> reverse-time migration result for the reef model. The measured velocity along the vertical direction for the anisotropic overburden and the exact velocity of the isotropic layer are used. The isotropic migration images the reef edge ~ 350 m left of its true position. The blue lines represent the true reef interface while the red lines denote the misplaced migration position.
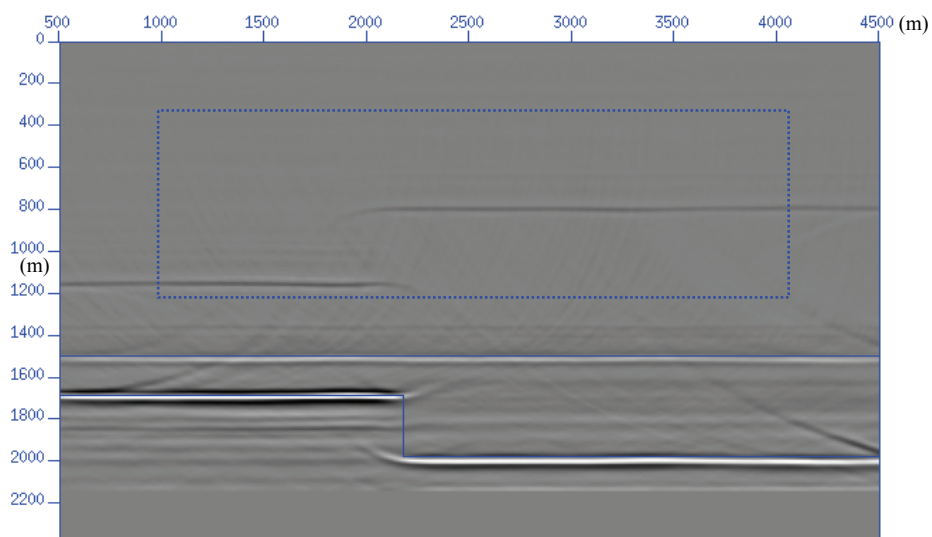
Figure 5.17 <u>Anisotropic</u> migration result from the reef model with an exact velocity model and Thomsen parameters. Anisotropic migration provides a correct image, and the events exactly fit the interfaces.
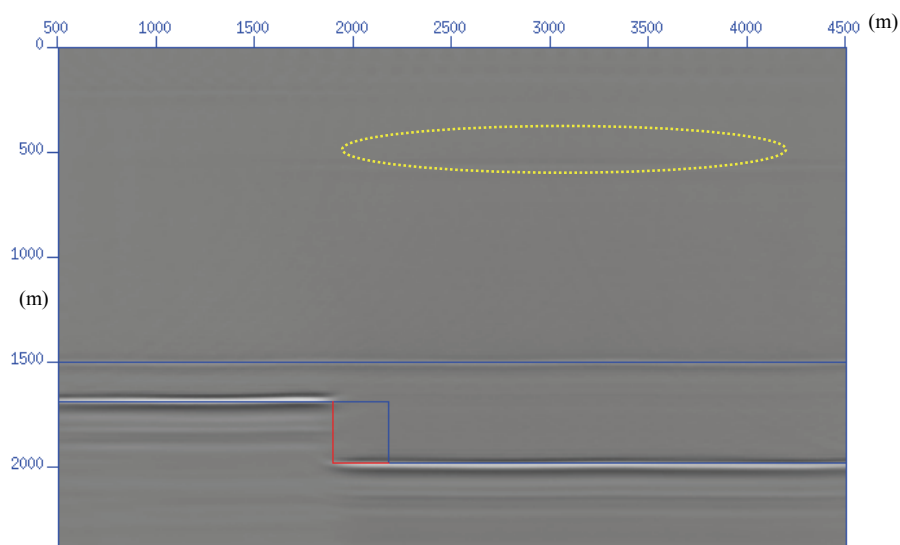
Figure 5.18 Prestack <u>isotropic</u> reverse-time migration result from the reef model. The measured velocity along the vertical direction for the anisotropic overburden and the exact velocity of the isotropic layer are used. The isotropic migration images the reef edge ~ 350 m left of its true position. The blue lines represent the true reef interface while the red lines denote the misplaced migration position.
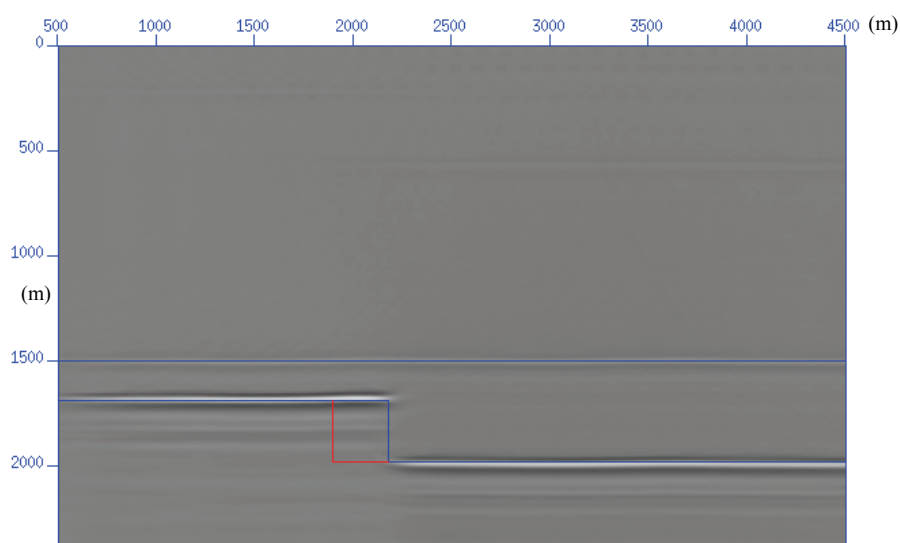
Figure 5.19 Prestack <u>anisotropic</u> reverse-time migration result from the reef model with an exact velocity model and Thomsen parameters. Anisotropic migration provides a correct image, and the events exactly fit the interfaces.

5.9 Chapter summary

 The above analysis demonstrates that anisotropy has a large influence in obtaining accurate migrated images. Using a migration algorithm that takes anisotropy into account can substantially improve images when anisotropy is present.

To implement the reverse-time migration in tilted TI media, we first obtained an appropriate P-wave equation to use in place of the isotropic acoustic wave equation employed in isotropic reverse-time migration. With Thomson's weak anisotropy assumption, the wave equations for weakly anisotropic P-waves and SV-waves in tilted transversely isotropic media were derived. Furthermore, the accuracy of the P- and SV-wave equations was analyzed and compared with other acoustic wave equations for TTI media. The pseudo-spectral method was used to solve these equations in implementing a reverse-time migration. The anisotropic ray-tracing method was used to obtain traveltimes as the forward wavefield, which was used in conjunction with a backward wavefield by reverse-time extrapolation for prestack depth imaging using zero-lag cross-correlation imaging. According to the results obtained from numerical and physical model seismic data, anisotropic reverse-time migration yields high accuracy for TTI media. The post-stack anisotropic algorithm, the anisotropic traveltime table computation and the prestack anisotropic depth migration algorithm were all successfully tested for their correctness. Although there is a large increase in computer run-time from isotropic reverse-time migration to anisotropic reverse-time migration, it is still promising and increasingly feasible with the rapid development of computer hardware.

Chapter Six: Prestack anisotropic phase-shift-plus-interpolation for tilted TI media

6.1 Introduction

This chapter covers post-stack and prestack anisotropic PSPI for tilted TI media, based on the one-way wave equation using downward-continuation migration methods that are extended from the corresponding isotropic algorithms. In contrast to the phase velocity being independent of phase angles in the isotropic algorithm, here phase velocity is determined by phase angle, which results in two challenging problems. One is the difficulty of calculating the vertical wavenumber k_z. The other is the number of reference wavefields. Rather than use an approximated solution of k_z, such as table-driven interpolation (Rousseau, 1997) and polynomial interpolation (Ferguson and Margrave, 1998), we solve k_z analytically from the quartic dispersion equation. The assumption for the reference anisotropy parameters is that the variation in anisotropy parameters is the same as that of lateral velocities at each step when the anisotropy parameters vary laterally as well. The extra run-time is roughly counted when considering anisotropy parameters. Numerical and physical examples are applied to validate the anisotropic PSPI algorithm (A-PSPI) and demonstrate its characteristics as well.

6.2 Prestack anisotropic phase-shift-plus interpolation migration

Since the anisotropic phase-shift-plus-interpolation migration is derived from PSPI to which we gave a detailed introduction in Chapter 2, here we quickly review the basic PSPI approach and describe the relationship between them.

Given a homogeneous velocity field in the frequency-wavenumber domain, the 2D acoustic wave equation is given by

$$k_x^2 P - \frac{\partial^2 P}{\partial z^2} = \frac{\omega^2}{v^2} P, \qquad (6.1)$$

where P is the pressure field, z is the depth, ω is the circular frequency, v is phase velocity and k_x is the wavenumber in the lateral direction. Its corresponding one-way wave equation is

$$\frac{\partial P}{\partial z} = \pm i k_z P. \qquad (6.2)$$

Assuming that $v(z)$ is constant over the depth interval dz, we can get the analytic solutions for the one-way wave equation

$$P(z + \Delta z, k_x, \omega) = e^{\pm i k_z z} P(z, k_x, \omega). \qquad (6.3)$$

Thus the wavefield in depth involves a simple phase-shift in the frequency-wavenumber domain. The above theory is provided by the Gazdag phase shift migration (Gazdag, 1978). The advantage of this method is its stability with no special requirement for grid spacing and its accuracy up to 90° dip. When the velocity field varies laterally, the phase-shift method fails, for it assumes that the velocity is constant along depth increment Δz. Thus, Gazdag and Sguazzero (1984) introduced the phase-shift-plus-interpolation method that used several reference velocities to account for the lateral velocity variation at each step. The true wavefield is obtained by linearly interpolating the reference wavefield using the relationship between the local velocity and reference velocities.

When the velocity field varies not only with lateral direction but also with the phase angle in anisotropic media, k_z is a function of vertical velocities and the anisotropy parameters. Similar to the isotropic case, we have the anisotropic dispersion relationship,

$$k_z = \pm \sqrt{\frac{\omega^2}{v^2(\theta,\phi)} - k_x^2} \, , \tag{6.4}$$

where ω is the frequency, $v(\theta,\phi)$ is the angle-dependent velocity, θ is the phase angle with the symmetry axis and ϕ is the tilt angle of the symmetry axis. For all the phase-shift-based migration algorithms, the key is to relate k_z to k_x with known k_x. In the isotropic case, ω and v are constant, so k_z can be readily computed from k_x, ω and v using the isotropic frequency dispersion equation. In anisotropic media, the angle-dependence of velocity makes the computation more complicated.

Similar to the basic derivation in Chapter 5 for anisotropic P- and SV-wave equations, we still start from the phase velocity for tilted TI media:

$$\frac{v^2(\theta,\phi)}{v_{p0}^2} = 1 + \varepsilon \sin^2(\theta-\phi) - \frac{f}{2} \\ + \frac{f}{2}\sqrt{(1 + \frac{2\varepsilon\sin^2(\theta-\phi)}{f})^2 - \frac{2(\varepsilon-\delta)\sin^2 2(\theta-\phi)}{f}} \, . \tag{6.5}$$

Considering weak anisotropy is common in nature and using the weak-anisotropic assumption, the expression for the anisotropic phase velocity can be simplified by expanding it to first order in the small parameters ε and δ:

$$\frac{v_p^2(\theta,\phi)}{v_{p0}^2} = 1 + 2\delta \sin^2(\theta-\phi)\cos^2(\theta-\phi) + 2\varepsilon \sin^4(\theta-\phi). \tag{6.6}$$

Using Equation (6.5) as the starting point, Rousseau (1997) developed an anisotropic PSPI algorithm for migration wherein he precomputed a table of $k_z(\theta)$ and $k_x(\theta)$ while considering the angle dependence of velocity for the anisotropy parameters, located or interpolated a given input k_x in a table, and found the corresponding k_z. The accuracy of this table-driven algorithm is directly related to the size of the table — the finer the increment in phase angle θ, the better the result. With a larger table, it is obvious that searching is time-consuming. Ferguson and Margrave (1998) suggested using an interpolating polynomial to get approximated solutions of k_z. They first estimated an empirical polynomial relationship between phase angle θ and horizontal slowness p by a series of numerical experiments, and then used the θ expression to calculate vertical slowness to get k_z. A difficulty presents itself when the axis of symmetry ϕ of a TI medium is non-zero. The horizontal slowness versus phase angle for a dipping TI medium shows that some values of p correspond to two values of θ, so we have to turn to other methods for a remedy. Du et al. (2005) analytically solved the vertical wavenumber directly through Equation (6.4).

6.2.1 The solution of the vertical wavenumber for tilted TI media

For plane waves travelling in the vertical (x, z)-plane, the phase angle is given by

$$\sin\theta = \frac{v(\theta,\phi)k_x}{\omega}, \quad \cos\theta = \frac{v(\theta,\phi)k_z}{\omega}. \tag{6.7}$$

Substituting Equation (6.7) into the phase velocity Equation (6.6), we can obtain a quartic equation, from which k_z can be analytically solved (see Appendix A:). The quartic equation is

$$k_z^4 + a_3 k_z^3 + a_2 k_z^2 + a_1 k_z^1 + a_0 = 0, \tag{6.8}$$

where a_i ($i = 0, 1, 2, 3$) is related to k_x, ε, δ, v_{p0} and ϕ. Two roots of the four in the quartic dispersion equation are chosen for down- and upgoing-qP waves, respectively. Figure 6.1 shows a solution of the quartic dispersion equation for a TI medium with a tilt angle of 0°, 30°, 60°, 90°. The solutions from the table-driven method (Rousseau, 1997) are shown in this figure in cyan color. As for the analytical solutions, the black solid lines denote the real part of k_z, the blue dashed lines are the imaginary part of k_z. The analytical solutions exactly match those obtained by the table-driven method.

6.2.2 The reference wavefield assumption for tilted TI media

The accuracy of isotropic PSPI is directly related to the number of reference velocities used at each depth step and that number is dependent on the amount of lateral velocity variation at that step. Ideally, reference wavefields would be generated for each velocity, which would be very expensive. In an effort to do automatic reference velocity picking, Bagaini et al. (1995) proposed an adaptive choice for the reference velocities at any step determined by a statistical distribution of the velocity with that depth step. As in the isotropic PSPI algorithm, several sets of reference parameters must be used for the anisotropic PSPI migration. Considering five reference values are used for the four Thomsen parameters v_{p0}, ε, δ and ϕ, we would require 625 different sets of reference parameters. To make the computation affordable, it is assumed that parameters v_{p0}, ε and δ have related lateral variation. Since tilt angle ϕ has a big effect on the wavefront dip direction, we take full account of the tilt angle. For anisotropic PSPI, balancing the computation cost and the number of reference parameters remains an unresolved issue.

The same issue of treating independent lateral variations in all four Thomsen parameters exists for a lot of anisotropic algorithms such as the explicit downward-continuation method (Uzcategui, 1994).
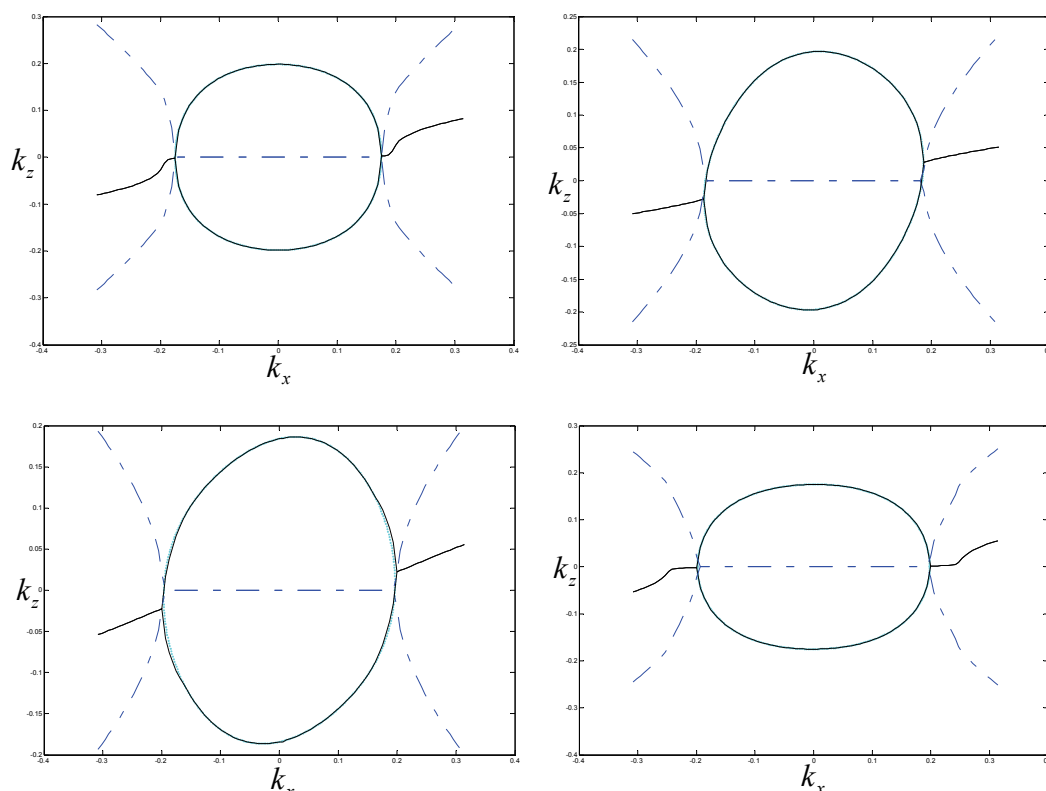
Figure 6.1 Dispersion relationship of P-waves in a TI medium. (a), (b), (c) and (d) correspond to the result of a tilt angle of 0°, 30°, 60°, and 90°. The black solid lines denote the real part of k_z, the blue dashed lines are imaginary parts of k_z and the cyan solid lines represent the solutions obtained by the Rousseau method.

6.2.3 Implementation of the prestack anisotropic PSPI algorithm

The wavefield extrapolation for the anisotropic PSPI algorithm is shown in Figure 6.2. There is no obvious distinction between the A-PSPI and PSPI algorithms, just differences in the phase-shift calculation. Only the reference velocity is considered in the isotropic algorithm whereas anisotropy parameters are used for anisotropic media. With the assumption of the relationship between velocity and anisotropy parameters, the number

of reference wavefields for TI media is the same as that where anisotropy isn't considered

if there is no variation in the tilt angle in polar anisotropic media. The cross-correlation

imaging condition is applied in the prestack A-PSPI, and the whole algorithm procedure

is shown in Figure 6.3.

$$P(x,z,\omega)$$

$$e^{i\frac{\omega}{v}\Delta z}$$

$$P(x,z,\omega)$$

FFT

$$P(k_x,z+\Delta z,\omega)$$

$$v_1,\varepsilon_1,\delta_1 \qquad\qquad v_2,\varepsilon_2,\delta_2$$

$$e^{i(k_z-\frac{\omega}{v})\Delta z} \qquad\qquad e^{i(k_z-\frac{\omega}{v})\Delta z}$$

$$P_1(k_x,z+\Delta z,\omega) \qquad P_2(k_x,z+\Delta z,\omega)$$

IFFT IFFT

$$P_1(x,z+\Delta z,\omega) \qquad P_2(x,z+\Delta z,\omega)$$

Interpolation

$$P(x,z+\Delta z,\omega)$$
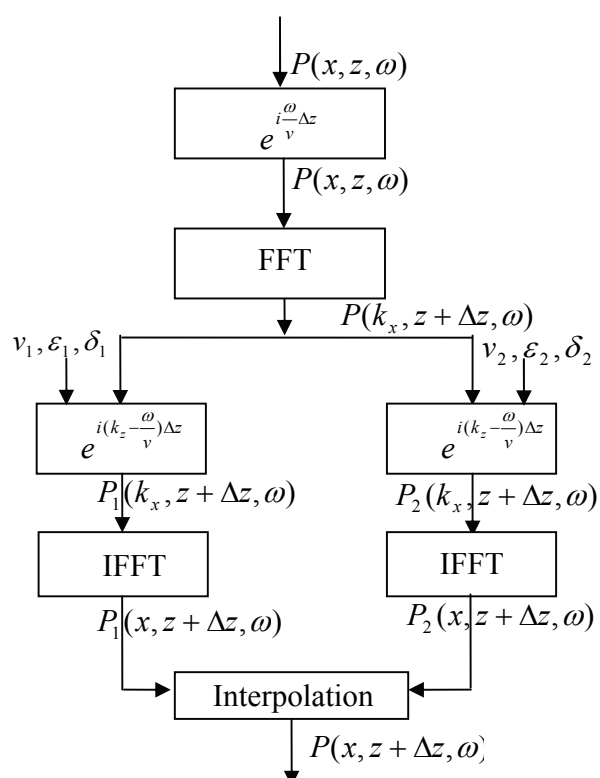
Figure 6.2 The wavefield extrapolation scheme for anisotropic PSPI.

$$P_{inc}(x,z,\omega)$$

$$P_{refl}(x,z,\omega)$$

Loop over depth

| A-PSPI phase-shift |

| A-PSPI phase-shift |

$$P_{inc}(x,z+\Delta z,\omega)$$

$$P_{refl}(x,z+\Delta z,\omega)$$

| Cross-correlation imaging condition |

$$R(x,z+\Delta z,\omega)$$
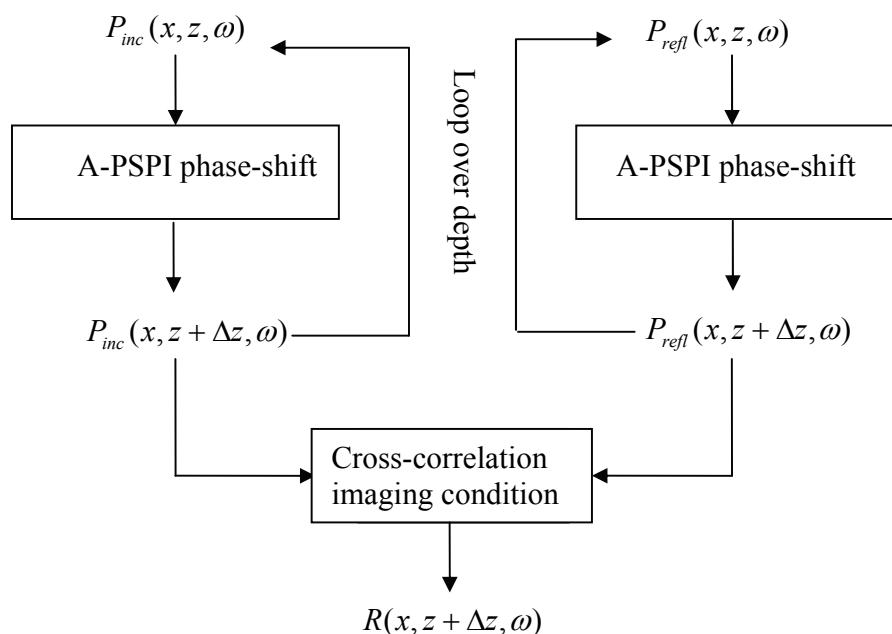
Figure 6.3 The procedure for prestack anisotropic PSPI.

After downward-continuation extrapolation at each step, the incident extrapolation wavefields are cross-correlated with reflection extrapolation wavefields to achieve reflectivity in space-frequency domain. At the same time, with the new extrapolation wavefields, the next-step wavefield is extrapolated in the same way until the final step. The performance of the phase-shift operator can be exemplified through a study of migration impulse response. As with the anisotropic reverse-time impulse response, we employ the anisotropy parameters $\varepsilon = 0.24$ and $\delta = 0.1$. Figure 6.4 illustrates the impulse response of the P-wave propagation modes with tilt angles of 0°, 30°, 60°, and 90°. The arrows represent the symmetry axis which shows a good correspondence with each tilt angle. Furthermore, the phase-shift method exhibits excellent performance in dipping angles up to 90° that are better than the optimum explicit operators by Zhang et al. (2001).

(a)

(b)

(c)

(d)
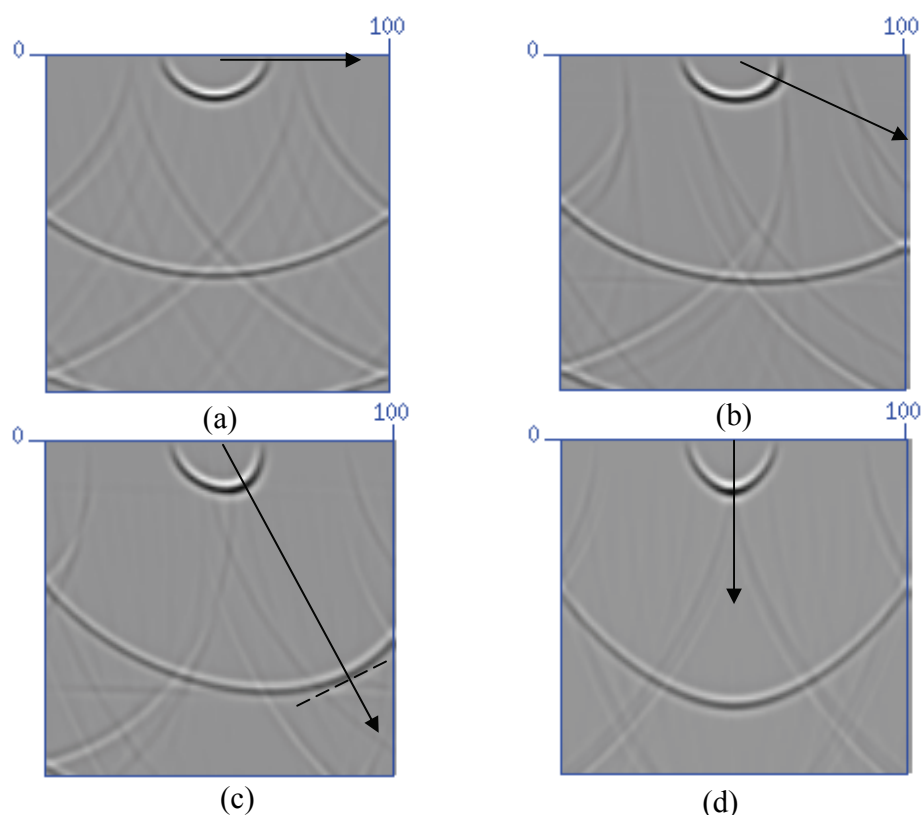
Figure 6.4 P-wave impulse responses. (a), (b), (c) and (d) correspond to the results of tilt angles of 0°, 30°, 60°, and 90° as indicated by the arrows.

6.3 Numerical and physical examples

To validate the A-PSPI algorithm, we will use one similar numerical example and physical example for anisotropic reverse-time migration.

6.3.1 Anisotropic imaging reflectors with different angles using a variable velocity model

Although the same variable velocity model and anisotropic parameters as the numerical model in Chapter 5 (Figure 6.5) was adopted, the tilt angle is different and the value is 0° (i.e., VTI media is simulated), which results in a different zero-offset section (Figure 6.6) and different isotropic migration results (Figure 6.7). The isotropic migration result is obtained using the isotropic PSPI migration method with true vertical velocity. There are

obvious differences between the isotropic PSPI migration result and that generated by isotropic reverse-time migration (Figure 5.12). Although both results are undermigrated and energy is unfocused, migration positions are different due to tilt angle. The correct imaging result, using anisotropic PSPI with exact vertical velocity and anisotropy parameters, is shown in Figure 6.8. The migration reflectors exactly match with those of the model. When we compare computer run-time between the isotropic and anisotropic cases for this algorithm, the computational cost does not change much. This is because the homogenous anisotropic media is designed with just one reference anisotropic parameter and a relatively simple vertical wavenumber calculation for the vertical TI media issued. In such homogenous anisotropic media, we only need to care about the reference velocity. The vertical wavenumber is calculated with the reference velocity and anisotropy parameters. The vertical wavenumber calculation in vertical TI media also shows that the solution of quartic equation (Equation (6.8)) is effective in special cases when the tilt angle is zero.
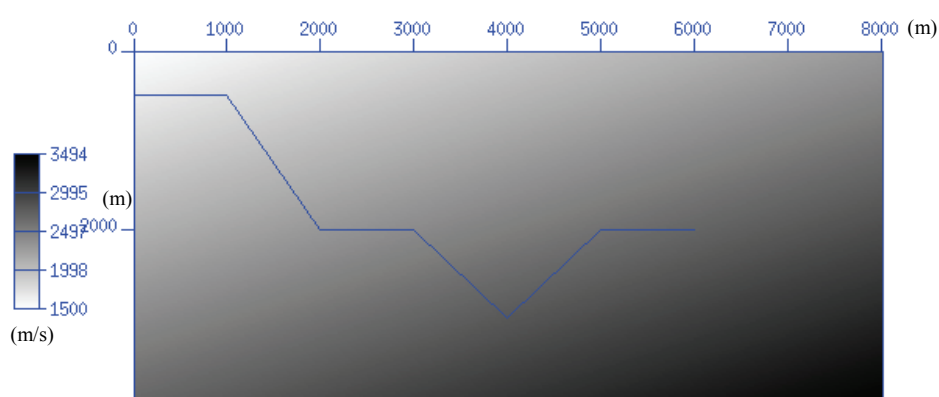
Figure 6.5 Variable velocity model with homogenous Thomsen parameters $\varepsilon = 0.2$ and $\delta = 0.1$, and a tilt angle $\phi = 60°$. P-wave velocities parallel to the axis of symmetry vary along the distance and depth as $v(x, z) = 1,500 + 0.3z + 0.1x$ (m/s).
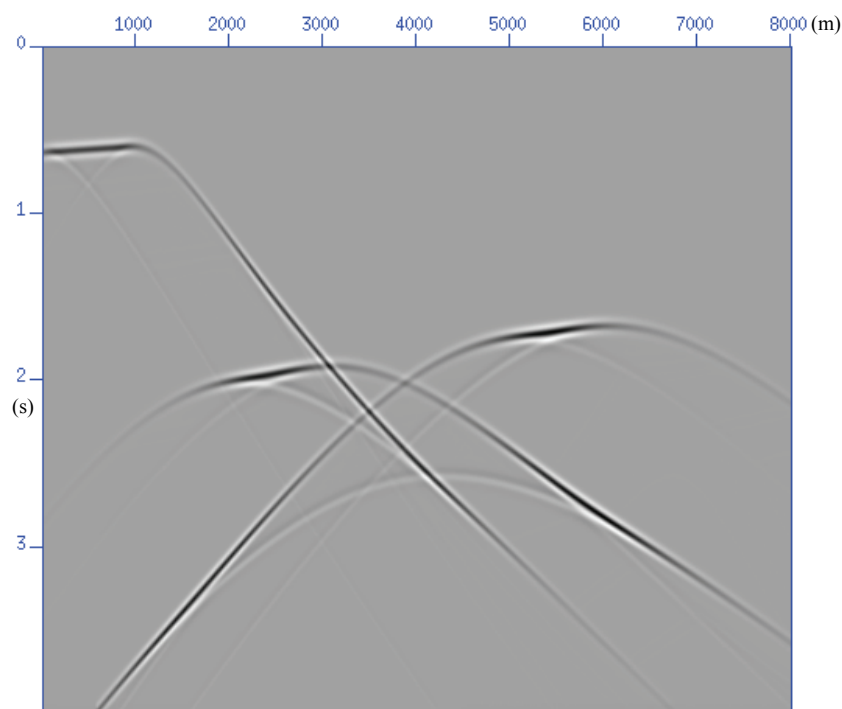
Figure 6.6 Synthetic zero-offset seismogram obtained using an SU routine from the Center for Wave Phenomena (CWP) for the structural model shown in Figure 6.5 in tilted TI media.
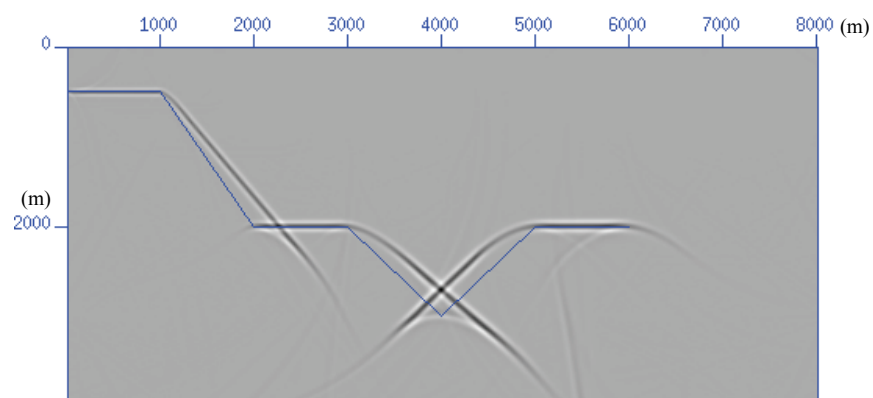
Figure 6.7 Migration result from the isotropic PSPI migration method. The P-wave velocity model in Figure 6.5 is used without considering the effect of anisotropy. The blue lines represent the true position of interfaces.
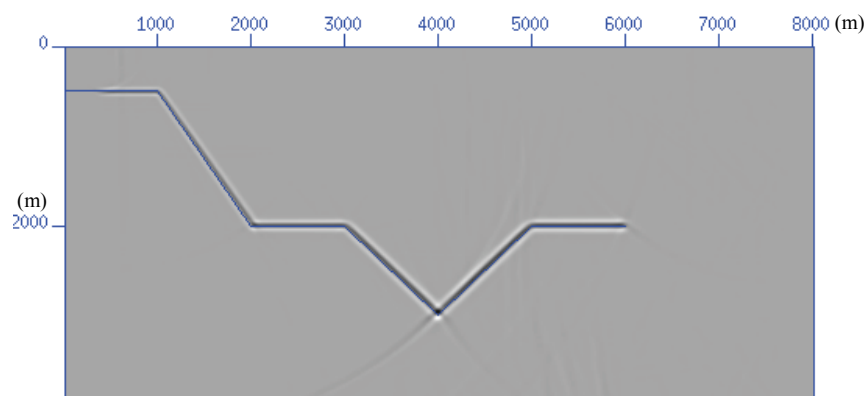
Figure 6.8 Migration result from the <u>anisotropic</u> PSPI migration method. The P-wave velocity model in Figure 6.5 is used taking into account the effect of anisotropy. The blue lines represent the true position of interfaces, and the true position exactly matches with the migration result of A-PSPI.

6.3.2 Depth migration for an isotropic reef with a TTI overburden

The same isotropic reef with a tilted TI overburden model as discussed in Chapter 5 is also used for the anisotropic PSPI method, as repeated in Figure 6.9. Figure 6.10 shows a zero-offset seismic section, again with the surface wave muted. The same isotropic velocity model is also used for isotropic migration algorithm to produce a similarly incorrect result to the one generated by isotropic reverse-time migration, where measure vertical velocity v_{45^0} is applied for the upper layer.

The post-stack migration result (Figure 6.11) of the zero-offset section by isotropic PSPI yields an image of the reef edge which is displaced by about 350m to the left of its true position, the same as the isotropic reverse-time migration result except for the multiple artifact reflection. The post-stack anisotropic PSPI result with true velocity and anisotropic parameters shows the correctly positioned reef edge, as shown in Figure 6.12, which appears superior to the anisotropic reverse-time migration since there are some reflection artifacts evident in the Anisotropic reverse-time migration result in Figure 5.17

due to velocity interfaces. Since the anisotropic model is relatively simple, the computational cost of A-PSPI increases by less than that for the isotropic PSPI method. The 43 shot gathers are also applied to the implementation of the prestack migration and summed together. Isotropic and anisotropic algorithms are both used. Figure 6.13 and Figure 6.14 correspond to the isotropic migration result and the anisotropic result with true anisotropy parameters. The lateral shift of about 350m to the left of its true position is verified again in the prestack migration result that doesn't consider anisotropy (Figure 6.13). In comparison to the post-stack migration results, the two prestack migration results yields higher resolution and fewer artifacts, which are shown in the blue dashed rectangle and ellipse (Figure 6.11 and Figure 6.12).
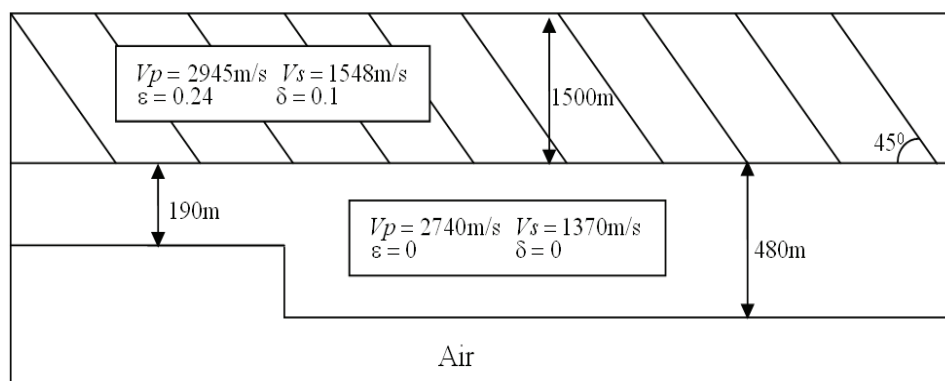
Figure 6.9 Isotropic reef with a TTI overburden.
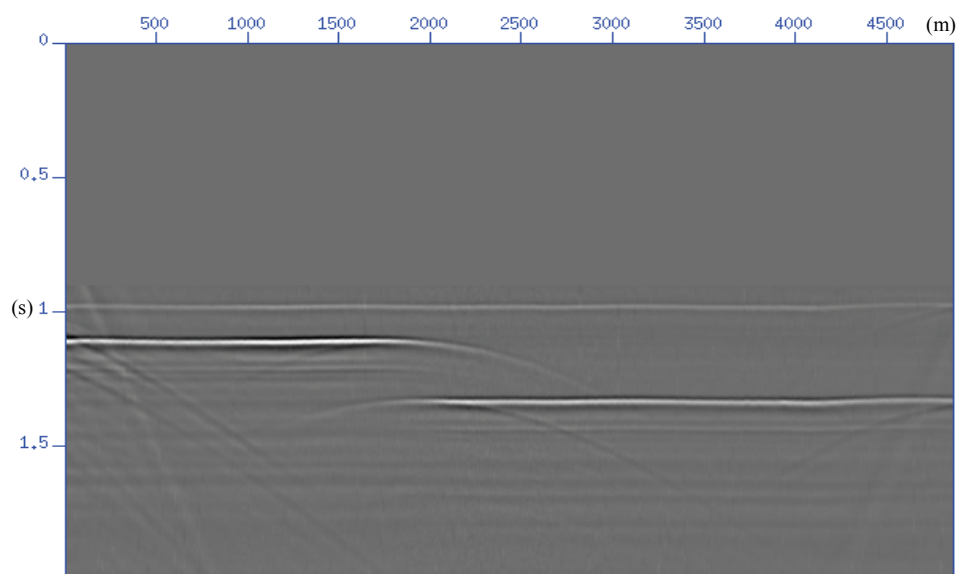
Figure 6.10 Zero-offset seismic section of the reef model.
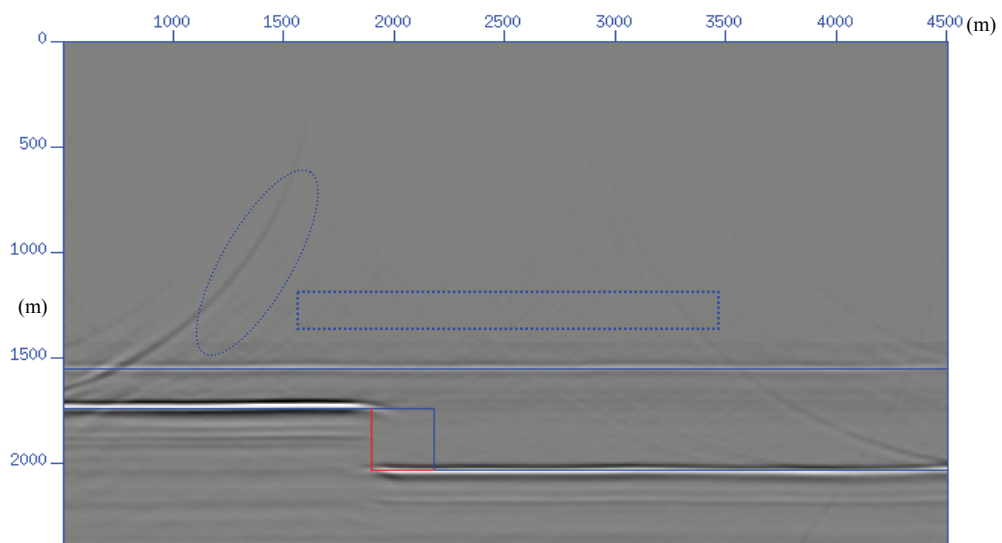
Figure 6.11 Post-stack <u>isotropic</u> PSPI migration result from the reef model.
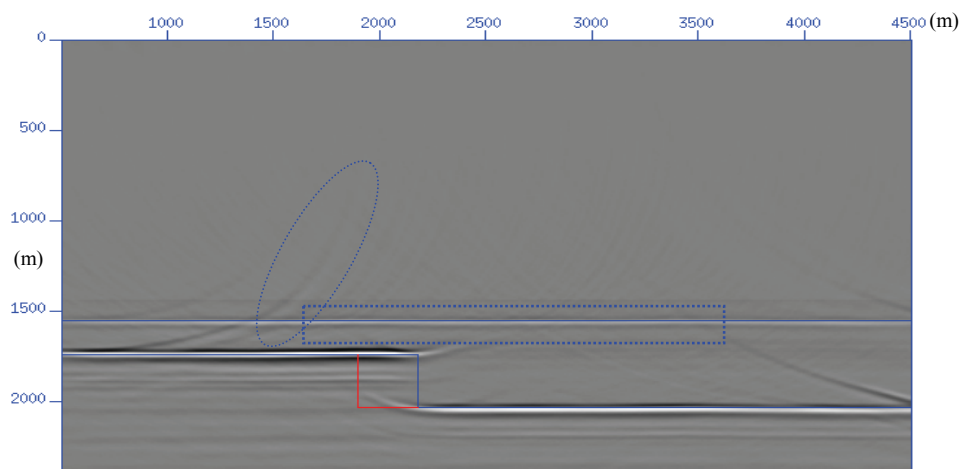
Figure 6.12 Post-stack <u>anisotropic</u> PSPI migration result from the reef model.
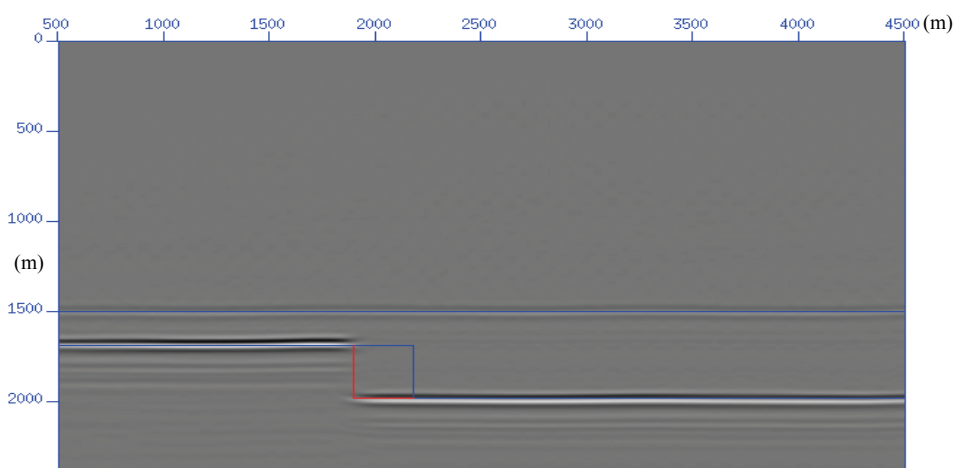
Figure 6.13 Prestack <u>isotropic</u> PSPI migration result from the reef model.
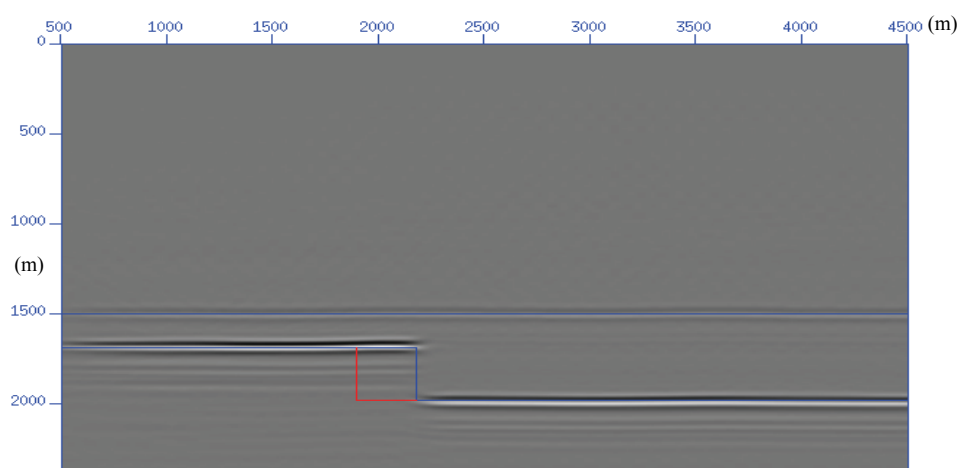
Figure 6.14 Prestack <u>anisotropic</u> PSPI migration result from the reef model.

6.4 Chapter summary

In this chapter, the PSPI algorithm has been extended to deal with tilted TI media. A new technique to obtain an analytical solution for the vertical wavenumber of tilted TI media is presented. Compared to other methods of solving the vertical wavenumber, this method is more efficient and accurate. The assumption that variable anisotropic parameters keep pace with variable lateral velocity is made to reduce the calculation of reference wavefields and improve efficiency. With these techniques and assumptions, post-stack and prestack anisotropic PSPI migration algorithms have been developed. Through numerical and physical examples, anisotropic PSPI has been successfully verified as accurate method using true vertical velocity and anisotropic parameters. In addition, the computational cost of A-PSPI is only slightly more than that of isotropic PSPI for relatively simple anisotropic models and will be discussed in Chapter 7.

Chapter Seven: Evaluations of prestack anisotropic Kirchhoff, phase-shift-plus-interpolation and reverse-time depth migration methods for tilted TI media

7.1 Introduction

The previous two chapters introduced the prestack anisotropic PSPI migration and prestack anisotropic reverse-time migration methods. To illustrate the characteristics of the two different migration methods, in conjunction with prestack anisotropic Kirchhoff depth migration method, some evaluations of these three anisotropic migration algorithms are given from the point of accuracy and efficiency. Each algorithm is analyzed with regard to the theory behind the three anisotropic migration methods, and taking into account the increase in computation cost between each anisotropic migration algorithm and its corresponding isotropic case. A numerical example with different dipping reflectors is designed to show the dipping angle imaging capability of three methods, and physical model data applied to prestack depth migration demonstrates the algorithms' efficiency in performance. Note that anisotropic IFD and SSF are not considered in this section as IFD has not been extended to the tilted TI case and SSF only handle simple anisotropic media.

7.2 Theory

Anisotropic depth migration methods, as with isotropic methods, can be based on various approaches such as ray-tracing, one-way wave equation, and two-way wave equation. The prestack anisotropic Kirchhoff migration method presented in this chapter is based on ray-tracing theory. The prestack anisotropic PSPI starts from the one-way wave equation and carries out downward-continuation wavefield extrapolation. The prestack anisotropic reverse-time migration employs recursive extrapolation backward in time

using the full wave equation. The three representative methods are chosen to demonstrate their characteristics for dipping TI media in terms of performance, accuracy and efficiency.

The Kirchhoff migration method is still the most popular migration in the industry for its effective imaging and low cost. There is little variation between isotropic and anisotropic Kirchhoff depth migration algorithms except for changing the traveltime tables in the presence of TI media. Vestrum et al. (1999) similarly adopted a ray-tracing algorithm to get the traveltime to image structures below dipping TI media. Kumar et al. (2004) developed a direct method of traveltime computation in dipping TI media for use in Kirchhoff anisotropic depth migration. As with the case in isotropic media, traveltime calculation in TI media pushes the Kirchhoff method further in terms of accuracy as well as practical application to seismic imaging.

In contrast to the Kirchhoff migration algorithm, which remains unchanged in anisotropic media, the prestack anisotropic PSPI migration algorithm involves complicated phase-shift calculations compared to its counterpart isotropic algorithm, introduced in Chapter 6. The PSPI depth migration method adapts to lateral velocity variation through wavefield interpolation; however, with anisotropy parameters also varying in the lateral direction, it is very important to identify the relationship between the anisotropic parameters and velocity to reduce the calculations of the reference wavefields.

Compared with the above two migration methods, reverse-time migration is the most expensive method, propagating the measured wavefield backward in time using a hyperbolic wave equation, as discussed in Chapter 5. However, with the two-way hyperbolic wave equation, it does not suffer from the dip limitation of one-way

downward continuation algorithms and handles multi-arrivals, steep dips, and overturned reflections. Furthermore, the algorithm is well adapted to arbitrary variable velocities and parameters in spaces.

7.2.1 The anisotropic Kirchhoff depth migration

The anisotropic Kirchhoff migration approach can be described mathematically as the integral solution to the scalar wave equation (Schneider, 1978; Berryhill, 1984). The solution is expressed as a surface integral over the known seismic observations. Based on the WKBJ approximation of Green's function to the Kirchhoff integral solution of the acoustic wave equation, the migration integral of a single shot can be expressed by the surface integral

$$R(\mathbf{x},\mathbf{x}_s)=\int_{\Sigma}\mathbf{n}\cdot\nabla\tau_r(\mathbf{x}_r,\mathbf{x},\mathbf{x}_s)A(\mathbf{x}_r,\mathbf{x},\mathbf{x}_s)u^{1/2}(\mathbf{x}_r,\tau_s(\mathbf{x},\mathbf{x}_s)+\tau_r(\mathbf{x},\mathbf{x}_s),\mathbf{x}_s)d\mathbf{x}_r, \quad (7.1)$$

where Σ is the recording surface; τ_s and τ_r are the traveltimes from the source position $\mathbf{x}_s$ to the subsurface position $\mathbf{x}_r$, and $\mathbf{n}$ is the outward normal of the surface Σ. Here, $u^{1/2}$ denotes the time derivative of the recorded traces for the 2D case. The term $A(x_r,x,x_s)$ is the geometrical spreading term that functions here as an amplitude modulator to the recording traces. Using the far-field approximation, a migration using the Equation (7.1) is basically a weighted summation of the derivative travelling along the presumed diffraction trajectory $t=\tau_s+\tau_r$. The weights are often approximated based on a constant velocity model. In such cases, the weights can be analytically expressed as a function of velocity, travelled distance, and obliquity of the emergence ray at the recoding surface. Thus, the determination of traveltimes plays the key role in the calculation of the integral. These determinations are traditionally accomplished by ray-

tracing. Ray-tracing will essentially yield all the information about τ_s and τ_r, and will simultaneously give us the directions of the rays. For post-stack constant velocity migration, an input sample on the unmigrated time section (x, t) is mapped onto a semicircle in the output space (x, z). The migrated image is formed by superimposing all the semicircles corresponding to each sample on the unmigrated time section. In the prestack constant velocity case, where the source and receiver are physically separated, the semicircles are replaced by ellipses, as illustrated in Figure 7.1. In this figure, the sum of the source traveltime τ_s and the receiver traveltime τ_r remain constant along the ellipse.

Kirchhoff migration is one of the most versatile migration schemes. It can be easily modified to account for irregular recording geometry, topography, converted-wave imaging, and anisotropic depth migration. As there is no change in the depth migration algorithm itself in the presence of TI media, the computation cost remains the same as in the isotropic case. Although the change is the traveltime table, that only accounts for a very small part of depth migration process.
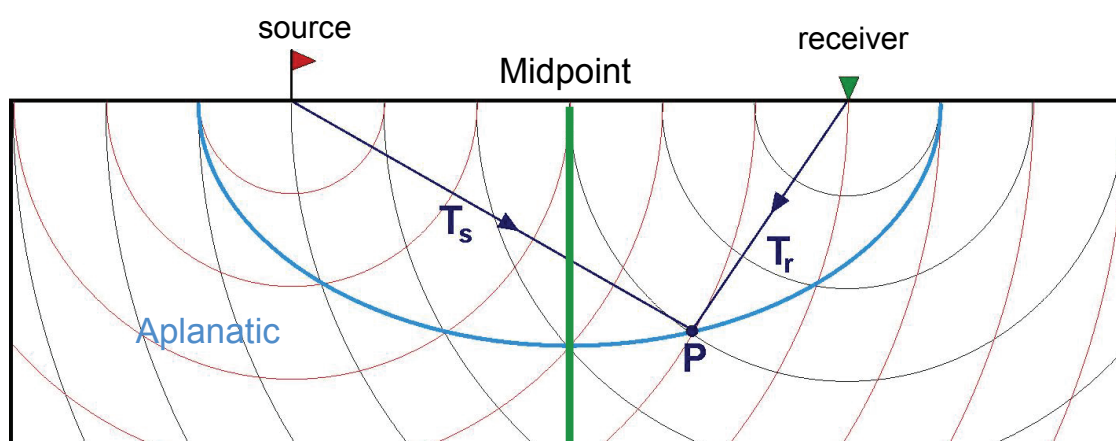
Figure 7.1 Prestack Kirchhoff migrations (Bancroft, 2006).

7.2.2 The anisotropic PSPI and reverse-time depth migrations

As for anisotropic PSPI and reverse-time depth migration algorithms, since we gave detailed introductions in Chapters 5 and 6, here we give only a quick review of the two methods. Making the isotropic PSPI algorithm an anisotropic PSPI algorithm depends on two key techniques. The first is the vertical wavenumber calculation in tilted TI media. The other is an assumption of the number of reference anisotropy parameters. The vertical wavenumber is successfully solved by the analytical solution, which will increase computational costs since the quartic equation is solved as many times as the number of frequency, reference velocity, and anisotropy parameters. The more complicated the anisotropy model involved, the greater the computer time required. The second technique is still an unresolved issue, although some assumptions are made, such as the variation of the anisotropy parameters keeping pace with that of lateral velocity at each step where the anisotropy parameters vary strongly. With this assumption, the anisotropic PSPI method works well for relatively simple anisotropic models, which has been proven through the numerical and physical examples shown in Chapter 6. Resolution greatly decreases when facing complex anisotropic models with strong laterally varying anisotropic parameters.

It is straightforward to implement the isotropic reverse-time migration with the acoustic equation. However, for anisotropic reverse-time migration, we should first get an appropriate P-wave equation for dipping TI media. Du et al., (2005) discussed the individual P- and SV-wave equations for dipping TI media. A pseudo-spectral method is applied to solve them due to the complexity of the two equations. Anisotropic ray-tracing is used to obtain the traveltime tables, which are used for the forward wavefield to correlate with the reverse-time backward. This method reduces computer time by half

when compared to the modelling methods used to obtain the forward wavefield, making traveltime computation quite efficient. The post-stack and prestack anisotropic reverse-time migration algorithms have been verified in Chapter 5. Unlike the Kirchhoff depth migration in Kumar et al. (2004), or the optimized depth extrapolator operator in Zhang et al. (2001), which incurs minor cost increases when transferred from isotropic to anisotropic cases, anisotropic reverse-time migration is a much more expensive calculation in comparison to its isotropic counterpart because so many more elements need to be calculated. However, its advantage — excellent adaptability to arbitrary complex variable anisotropy parameters and velocity in the spatial domain — is also quite significant.

7.2.3 Performance evaluations

Anisotropic Kirchhoff depth migration differs from the isotropic case only in the adjustment of the traveltime calculation, so the increase in computational expense is a very small part of the whole imaging process. Based on ray theory, it does not possess the high degree of accuracy of wave equation migration methods. For anisotropic PSPI algorithm, there is no obvious improvement in computer run-time if we obtain the vertical wavenumber before the wavefield extrapolation calculation. We make the assumption that strong variable anisotropy parameters are related to the lateral velocity. However, if the algorithm encounters a complicated geometry model with strong variable anisotropy parameters and dipping angles, the method will fail.

Although anisotropic reverse-time migration can be well adapted to arbitrary variable velocity and anisotropy parameters in dipping TI media, it faces a big challenge in computation cost. Compared to the isotropic algorithm, it takes almost five times as long

to run (based on our understanding of the anisotropic wave equation shown in Chapter 6). A general comparison of the three anisotropic migration algorithms is shown in Table 7.1, which is based on a model of $N_x \times N_z$ grid points and the shot gathers of N traces, with N_t spatial sampling numbers and N_f frequency sampling numbers.

Table 7.1 Differences between anisotropic Kirchhoff, PSPI, and reverse-time migrations for shot gathers

	Kirchhoff	PSPI	Reverse-time
Recursive	No	Yes	Yes
Selective window	Yes	No	No
Accuracy	good	Very good	Excellent
Favor frequency	High f	High f	Low f
Inclusion of topography	Easy	With some effort	Reasonably easy
Computation cost	$O(N_x^{'} N_z N)$	$O(N_x^{'} N_z N_f)$	$O(N_x^{'} N_z N_t)$
Cost and frequency	$\propto f \sim f^2$	$\propto f \sim f^2$	$\propto f^3$
Vectorization	Good	Good	Excellent
Parrallelization	Excellent	Excellent	Excellent
Data preparation	Easy	Easy	With some effort

7.3 Examples

7.3.1 Imaging reflectors with different angles for a variable velocity model

A variable velocity model is shown in Figure 7.2 that consists of seven dipping reflectors (0°, 15°, 30°, 45°, 60°, 75°, and 90°). The media has homogenous anisotropy parameters of $\varepsilon = 0.2$, $\delta = 0.1$ and a tilt angle of 0. The velocity of the model is $v(x, z)$ =1,500+0.3z +0.3x (m/s). The zero-offset synthetic data is shown in Figure 7.3. Figure 7.4 is the isotropic migration result obtained using the isotropic PSPI migration method, which shows unfocused energy and incorrect migration positions. Correct imaging results, using anisotropic Kirchhoff, anisotropic PSPI and anisotropic RT migration algorithms with exact anisotropy parameters, are shown in Figure 7.5, Figure 7.6 and Figure 7.7. The

energy from the 90° reflector is weak for the anisotropic Kirchhoff and A-PSPI migration results while in the A-RT migration it seems stronger. The energy from the 75° and 60° reflectors in A-RT is stronger than that from the anisotropic Kirchhoff and A-PSPI methods as well. It is obvious that A-RT demonstrates a greater ability in dipping angle imaging compared with other two methods. With regard to computation cost, anisotropic Kirchhoff only requires 1 minute, A-PSPI 5 minutes, and A-RT 8 minutes run-time. Anisotropic Kirchhoff exhibits excellent computational efficiency and A-PSPI strikes a balance between accuracy and efficiency. By comparison, run-times are 1 minute, 4 minutes and 5 minutes for isotropic Kirchhoff, PSPI and RT, respectively. An overall comparison of computational cost is shown in Figure 7.8. There isn't any cost increase between isotropic and anisotropic Kirchhoff migration methods. When we compare computer run-times among the isotropic and anisotropic cases for PSPI and reverse-time migration algorithms, although there is some increasing computation cost for anisotropic cases over isotropic cases, the change is not very significant due to the relatively simple anisotropic model.
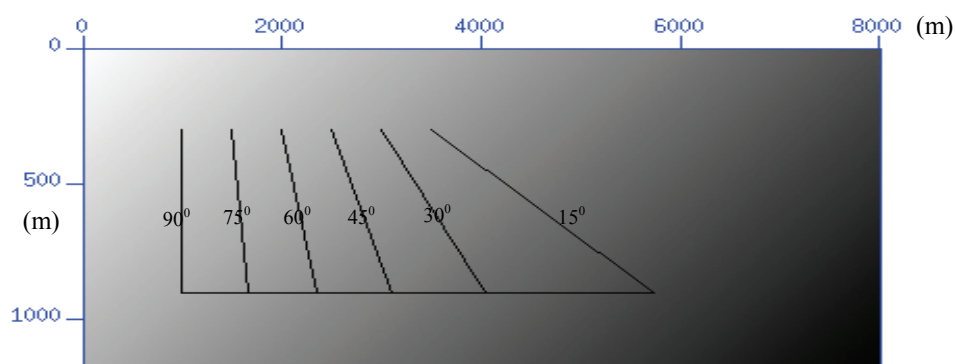
Figure 7.2 A variable velocity model with homogenous anisotropy parameters that consist of six dipping reflectors.
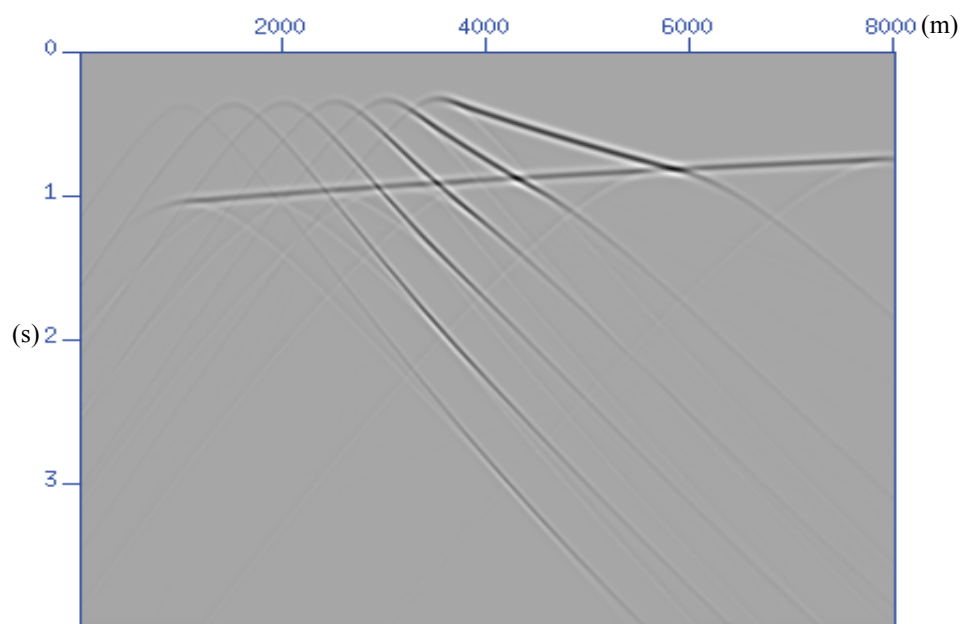
Figure 7.3 The synthetic data for six dipping reflectors in the model shown in Figure 7.2.
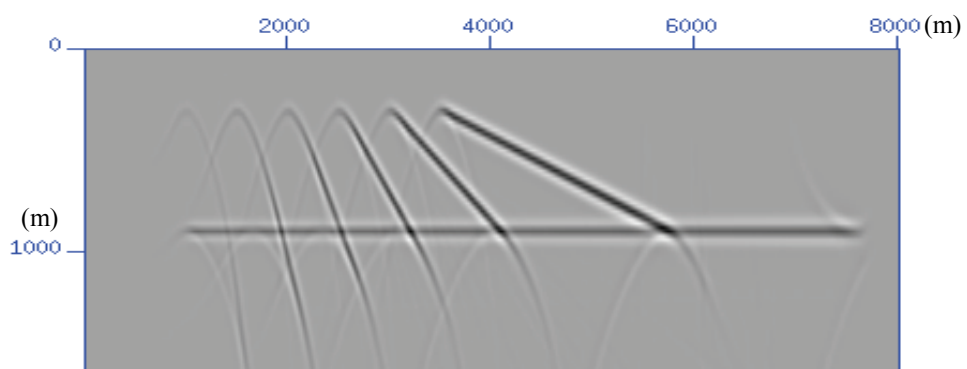
Figure 7.4 Migration result from the <u>isotropic</u> PSPI method.
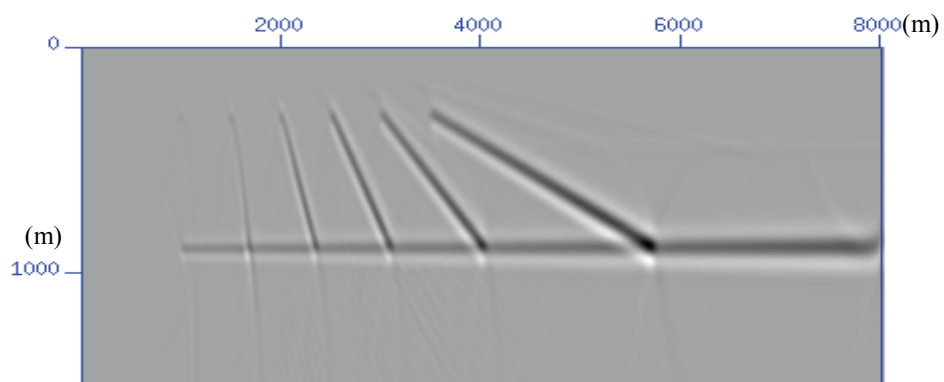
Figure 7.5 Migration result from the <u>anisotropic</u> Kirchhoff method.
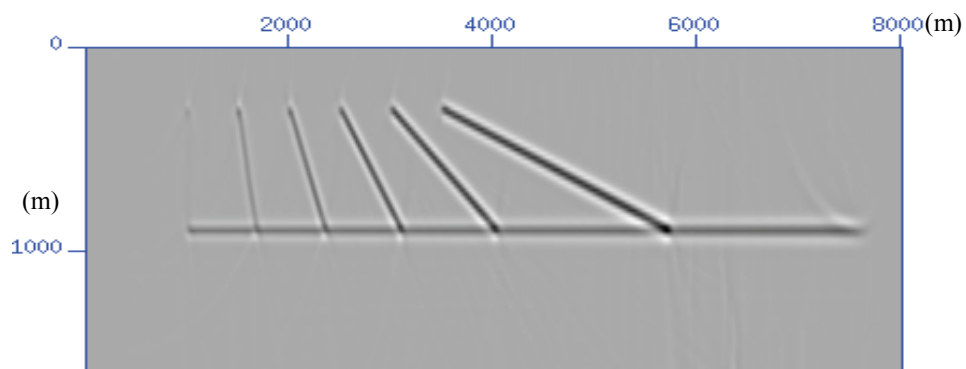
Figure 7.6 Migration result from the anisotropic PSPI method.
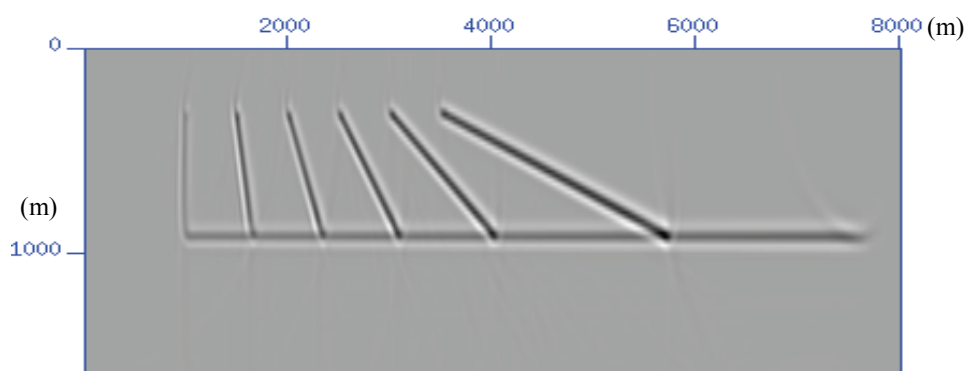
Figure 7.7 Migration result from the anisotropic reverse-time method.
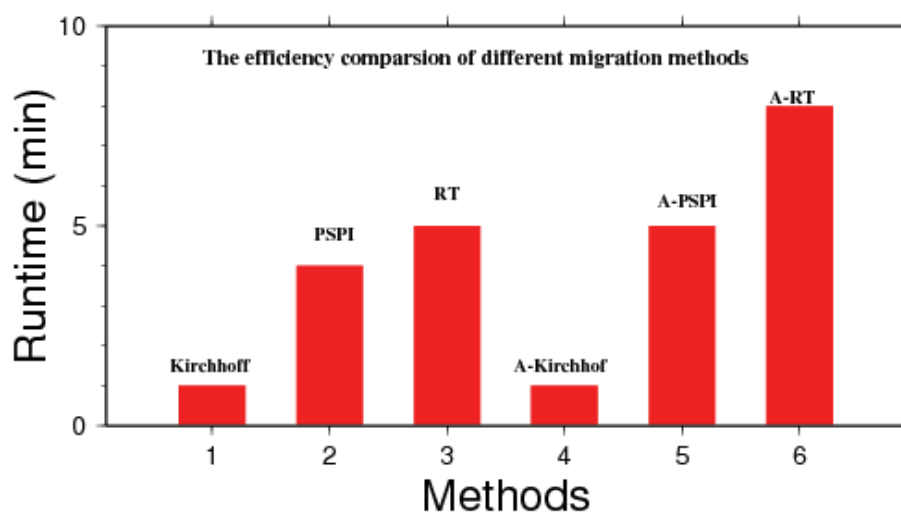
Figure 7.8 Efficiency comparison of the different methods (Post-stack depth migration).

7.3.2 Migration for a TTI thrust sheet in an isotropic background

7.3.2.1 Migration of seismic data sampled in the physical model

The physical model (Figure 7.9) is a deep flat reflector overlain by a TI thrust sheet embedded in an isotropic background. The thrust sheet is composed of four blocks; each with a unique axis of symmetry. They have parameters of $v_{p0} = 2,925$m/s, $\varepsilon = 0.224$ and $\delta = 0.100$. The isotropic background has a flat basement with $v_{p0} = 2,740$m/s. The prestack seismic dataset has 86 shot gathers acquired at 60m intervals along the line. Each source gather consists of 256 traces and 512 samples per trace with a 4ms sample rate. Figure 7.10 corresponds to the zero-offset seismic section, where the high velocity of the thrust structure results in the "pull-up" phenomena (identified by the dashed blue rectangle) of the flat basement.

A shot gather is shown in Figure 7.11 with a source location at 2,040m, spanning the first 4,000m of the model. The major reflection at the bottom of the gather corresponds to the flat basement. The apparent moveout of the reflection to the left side of the source is continuous because most of the energy is propagated through the isotropic material part of the model and the TI block with the vertical axis of symmetry. The reflection energy to the right of the source has propagated through the three blocks with tilted axes of TI symmetry and so appears discontinuous (Ferguson, 1999). The surface wave and head wave are very strong, but we didn't do any processing to investigate the sensitivity of migration algorithms to noise. High-frequency noise is dominant due to the physical sample in the labs.

Isotropic prestack Kirchhoff, PSPI, and reverse-time migrations produce very similar results in Figure 7.12, Figure 7.14 and Figure 7.19, respectively. Although the basement

is partially flat, the basement beneath the thrust sheets exhibits substantial "pull up" and the energy cannot be focused through them. Looking closely at the blue rotated arrow in each of these three figures, we easily see the bottom dipping events becoming progressively clearer from the prestack isotropic Kirchhoff depth migration algorithm, through the prestack isotropic PSPI migration algorithm, to the prestack isotropic reverse-time algorithm, whereas the computation cost becomes more and more expensive. The run-times are 8 minutes, 11 minutes and 15 minutes, respectively, which implies that the cost difference is not so much due to the model being less complicated.

Migration results from the prestack anisotropic Kirchhoff, PSPI, and RT migration methods (Figure 7.13, Figure 7.15 and Figure 7.20) show more accurate positioning of the reflectors and an almost flattened basement reflection. Prestack anisotropic reverse-time migration shows stronger reflection energy in the dipping interfaces of the thrust structure, which is emphasized by displaced yellow arrows in the corresponding figure. At the same time, the traveltime table calculation obtained by anisotropic ray-tracing is also verified. Figure 7.16 and Figure 7.17 show the traveltime contour results generated by isotropic ray-tracing and anisotropic ray-tracing, respectively, at the same source position. It is obvious that the P-waves propagate faster through the four TI blocks, because they propagate almost parallel to their bedding. This can also be observed in the traveltime difference contour in Figure 7.18. The prestack anisotropic Kirchhoff method (Figure 7.13) also produces reasonable results, due to fewer multiple arrivals observed with this model. However, the imaging of the thrust structure in the anisotropic PSPI migration result (Figure 7.15) is not as clear because limited reference wavefields are applied for the wavefield interpolation. Regarding computation cost, there is no increase

(7 minutes) for the prestack anisotropic Kirchhoff depth migration over that for the isotropic case because anisotropy only affects the traveltime calculation. As mentioned previously, the traveltime calculation only accounts for a small part of the imaging process. However, due to the relatively complex physical model, when compared to the isotropic reef with TTI overburden in Chapters 5 and 6, the anisotropic wave equation migration algorithms greatly increase computation time. Isotropic PSPI takes 11 minutes whereas anisotropic PSPI takes almost 24 minutes. Isotropic reverse-time migration takes 15 minutes, which is similar to the PSPI methods, but anisotropic reverse-time migration takes almost 60 minutes. The overall efficiency comparison is shown in Figure 7.21. A big computational cost jump occurs for prestack anisotropic reverse-time migration over the isotropic case. However the prestack anisotropic Kirchhoff exhibits an enormous advantage in the efficiency. Although the prestack anisotropic PSPI algorithm is expected to be a trade-off method, the interpolation issue is not yet resolved, indicating further investigation is required.
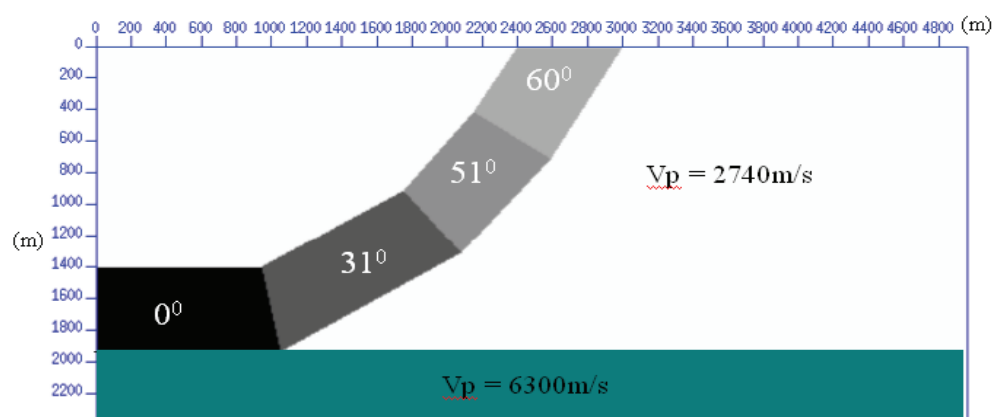
Figure 7.9 Model of an anisotropic thrust sheet embedded in an isotropic background with the same anisotropy parameters and different dipping angles.
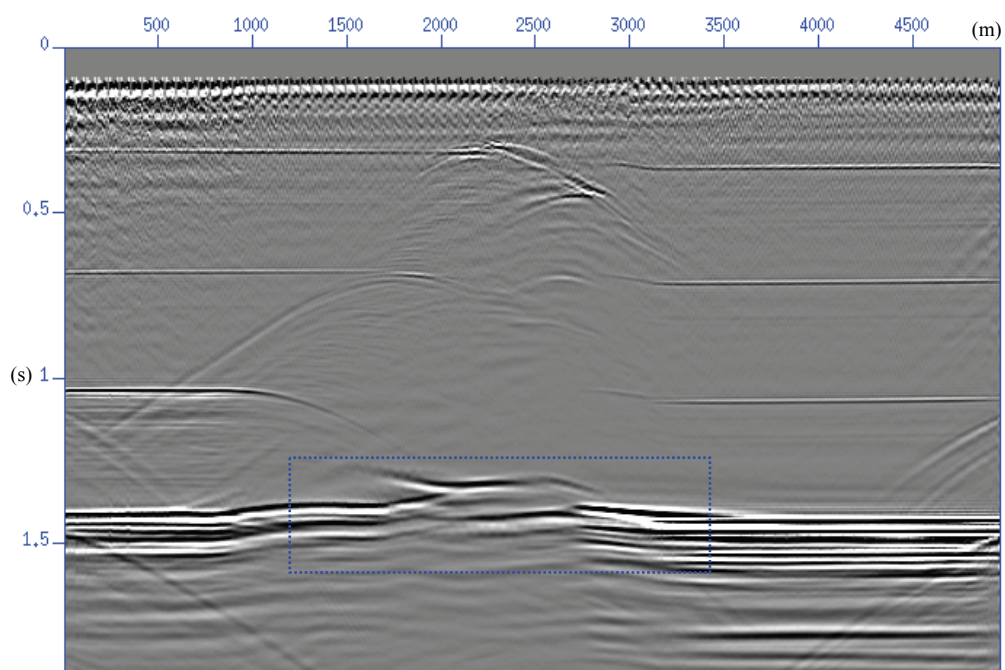
Figure 7.10 Zero-offset seismic section of the TTI thrust model.
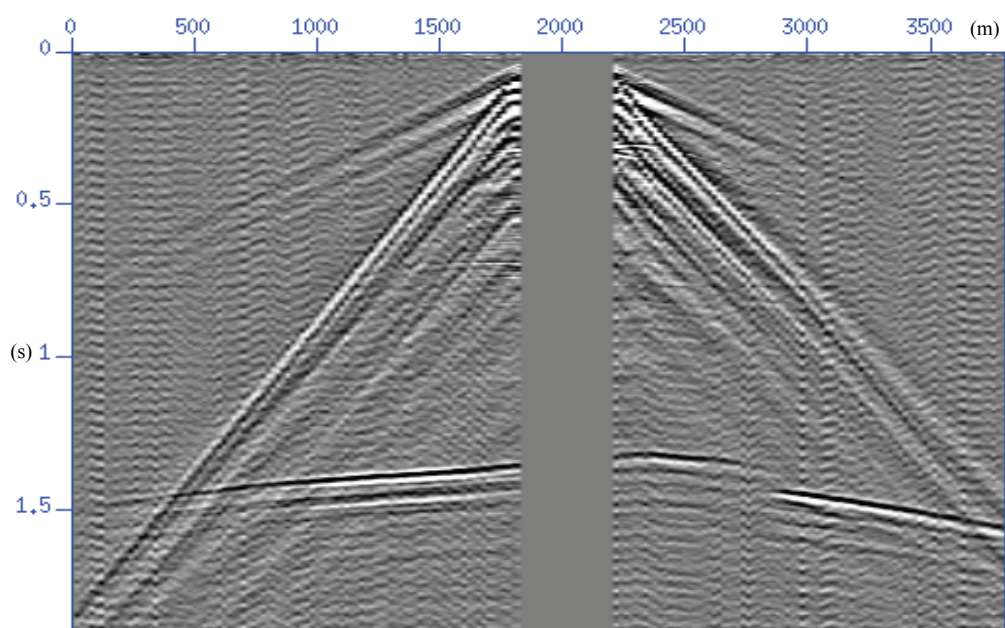
Figure 7.11 Physical model and shot gather corresponding to source location 2,040m.
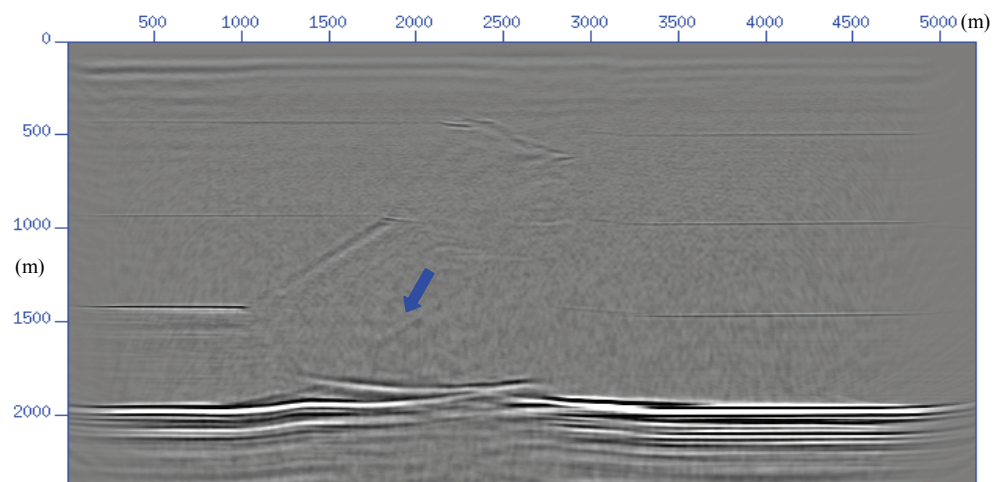
Figure 7.12 Prestack <u>isotropic</u> Kichhoff depth migration result from the TTI thrust model.
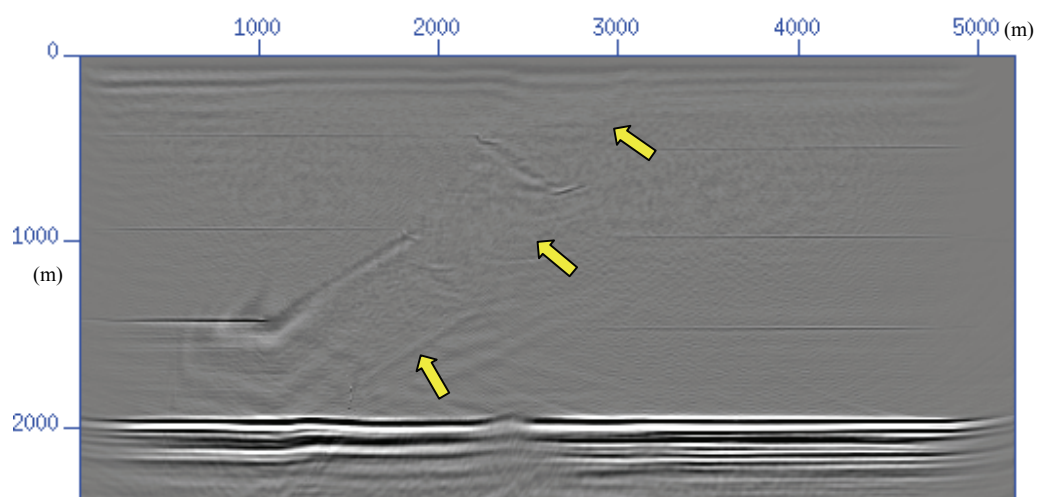
Figure 7.13 Prestack <u>anisotropic</u> Kirchhoff depth migration result from the TTI thrust model.
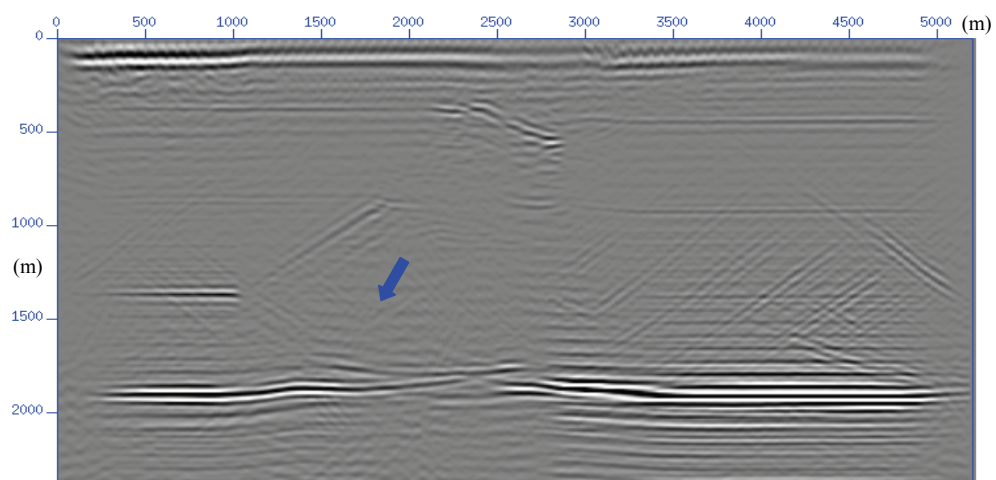
Figure 7.14 Prestack isotropic PSPI migration result from the TTI thrust model.
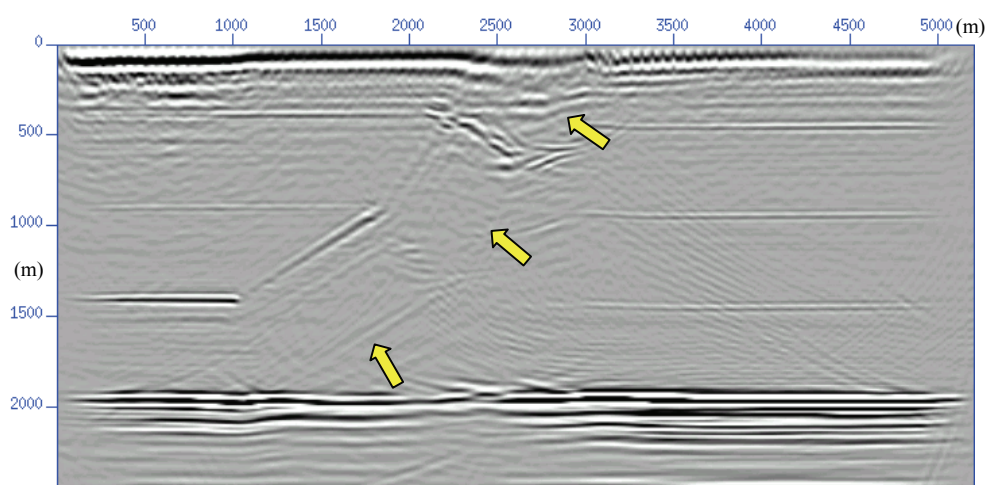
Figure 7.15 Prestack anisotropic PSPI depth migration result from the TTI thrust model.
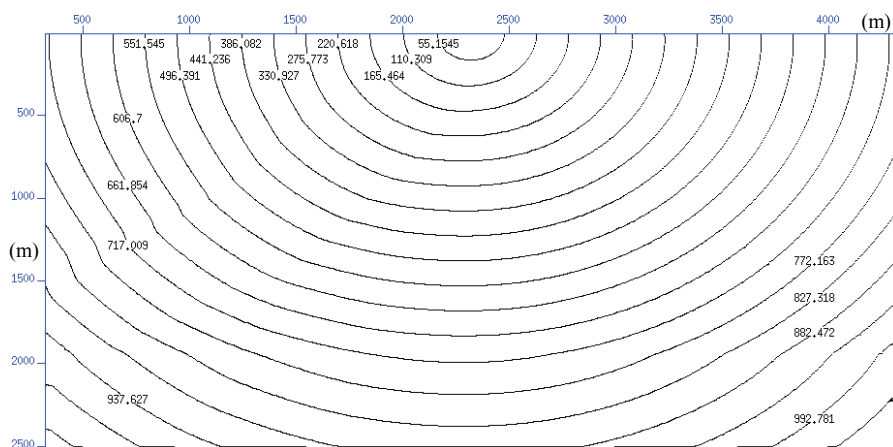
Figure 7.16 The traveltime contours ignoring the anisotropic effect when the source position is located at the centre of the model.
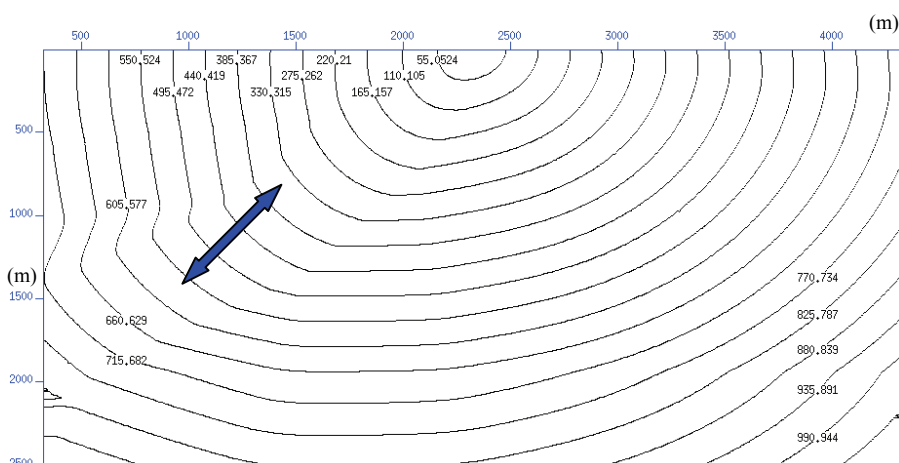
Figure 7.17 The traveltime contours showing the effect of anisotropy when the source position is located at the centre of the model.
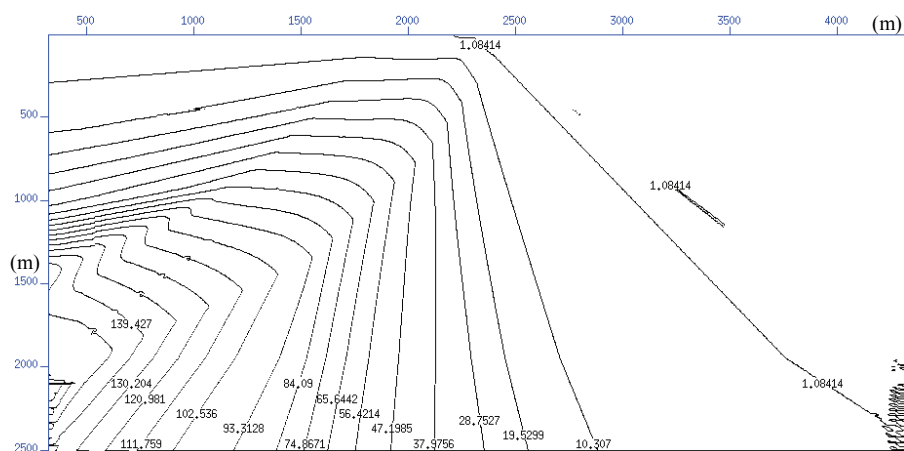
Figure 7.18 The traveltime difference contours between Figure 7.17 and Figure 7.16.
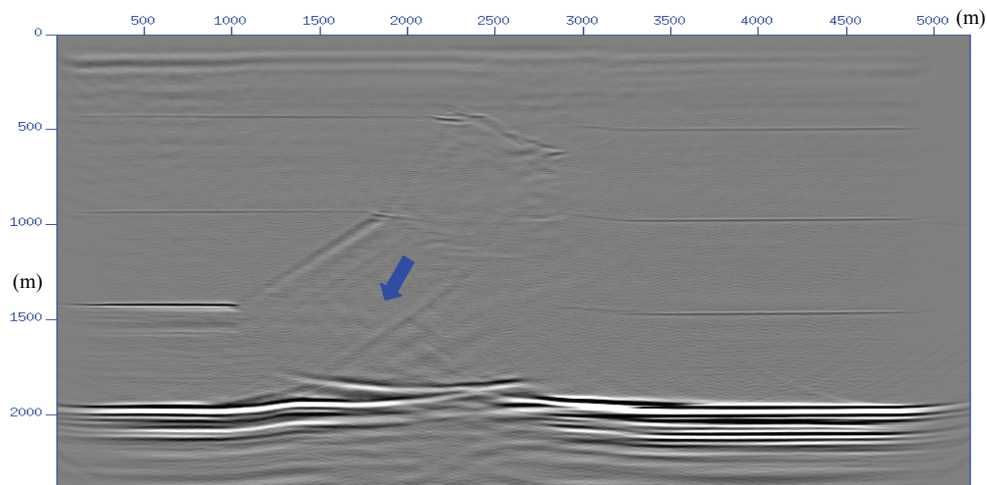
Figure 7.19 Prestack <u>isotropic</u> reverse-time migration result from the TTI thrust model.
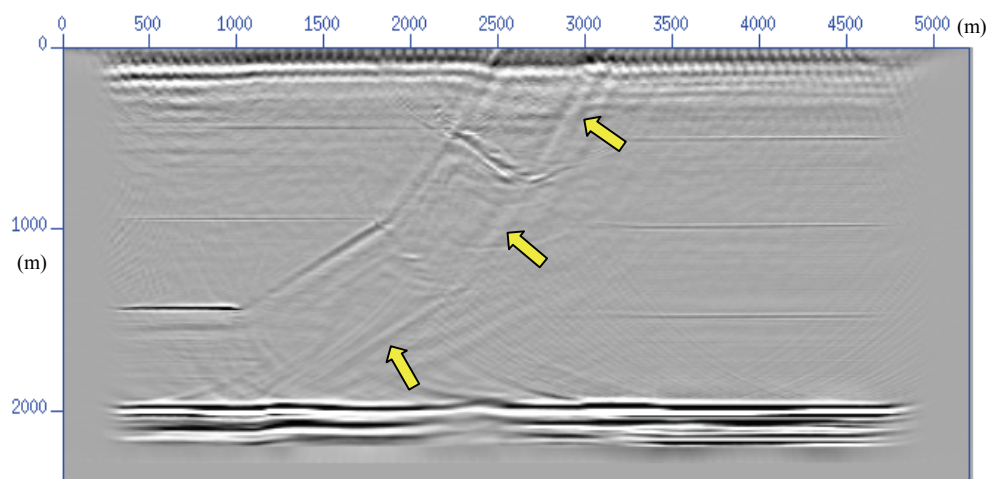
Figure 7.20 Prestack <u>anisotropic</u> reverse-time migration result from the TTI thrust model.
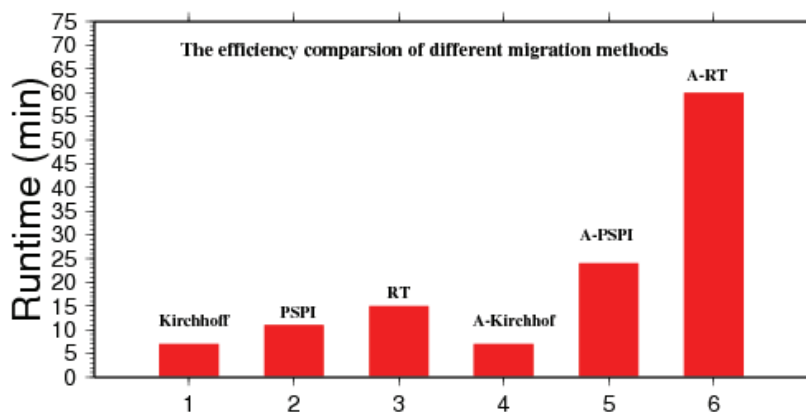
Figure 7.21 Efficiency comparison of the different methods used with the TTI thrust model (Prestack depth migration).

7.3.2.2 Migration of numerical simulation data from the same model

Although the physically modelled seismic data amply demonstrate the performance of the three anisotropic algorithms, the imaging quality is not perfect in that the physical model lacks certain natural characteristics, such as energy absorption and attenuation.

Numerical simulation data are generated according to anisotropy theory, so ideal migration results are ensured with the correct parameters and migration algorithms. We used the same processing as with the physical sampled data — isotropic and anisotropic Kirchhoff depth migrations, isotropic and anisotropic PSPI migrations, and isotropic and anisotropic RT migrations.

The three isotropic migration results, Figure 7.22, Figure 7.25 and Figure 7.28, give almost the same results, with unfocused energy and partially flat horizontal basement reflections. The three anisotropic migration results (Figure 7.23, Figure 7.26 and Figure 7.29) are ideal, with clear thrust segments and flat basement reflections. Regardless of isotropic or anisotropic algorithms, the migrations from numerical data yield higher resolution results than those from physical data. Figure 7.24 shows partial migrated sections of shot gathers using the anisotropic PSPI migration method. They correspond to source locations at 1,140m, 1,740m and 2,340m, respectively. Top subfigures are the isotropic PSPI migration results at these source positions; bottom subfigures correspond to the anisotropic PSPI results of these same shot gathers. The anisotropic results each correspond with the isotropic results directly above them. The yellow arrows indicate the differences between them. The anisotropic algorithm successfully focuses the reflection energy from the basement and flattens the interface. Figure 7.27 generated by anisotropic reverse-time migration, shows similar results to Figure 7.24, except for some low-

frequency noise. Consequently, the anisotropic algorithms successfully migrate the energy to its true position with correct parameters.
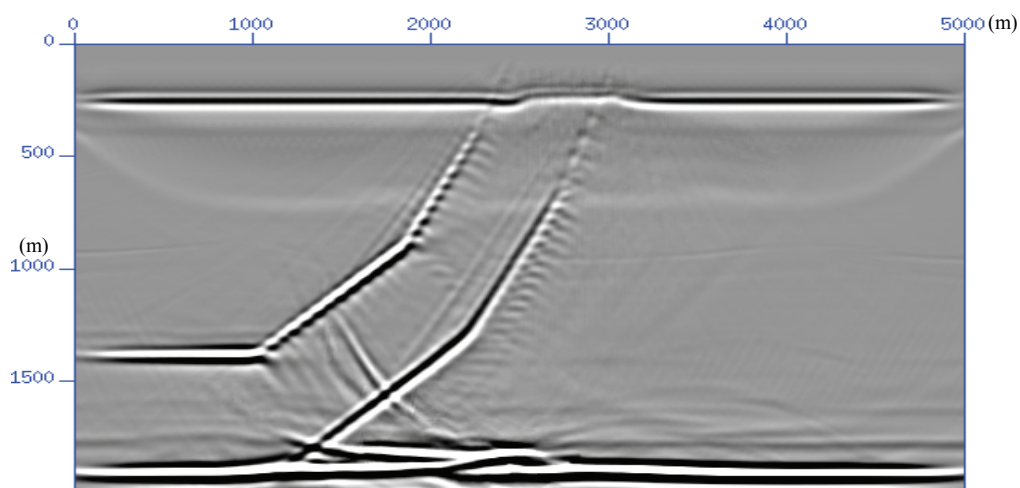
Figure 7.22 The prestack isotropic Kirchhoff depth migration from the numerical dataset.
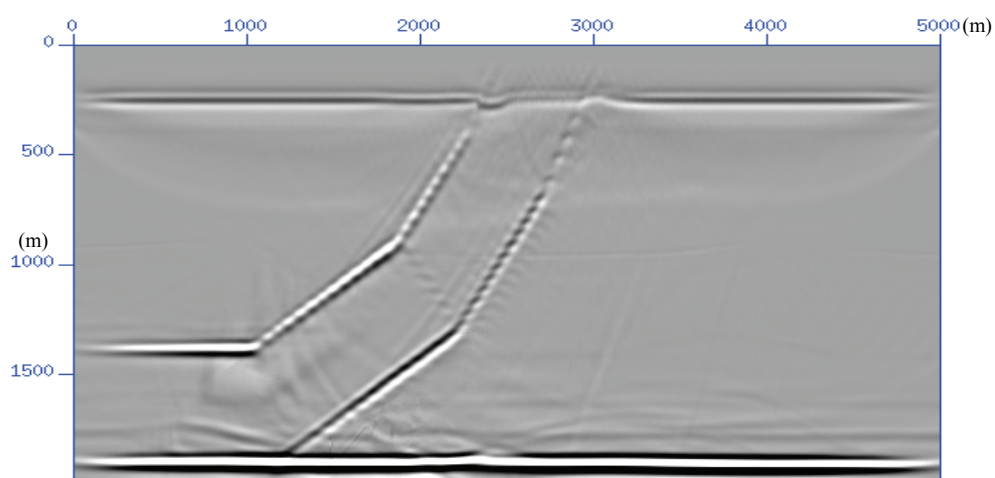
Figure 7.23 The prestack anisotropic Kirchhoff depth migration from the numerical dataset.
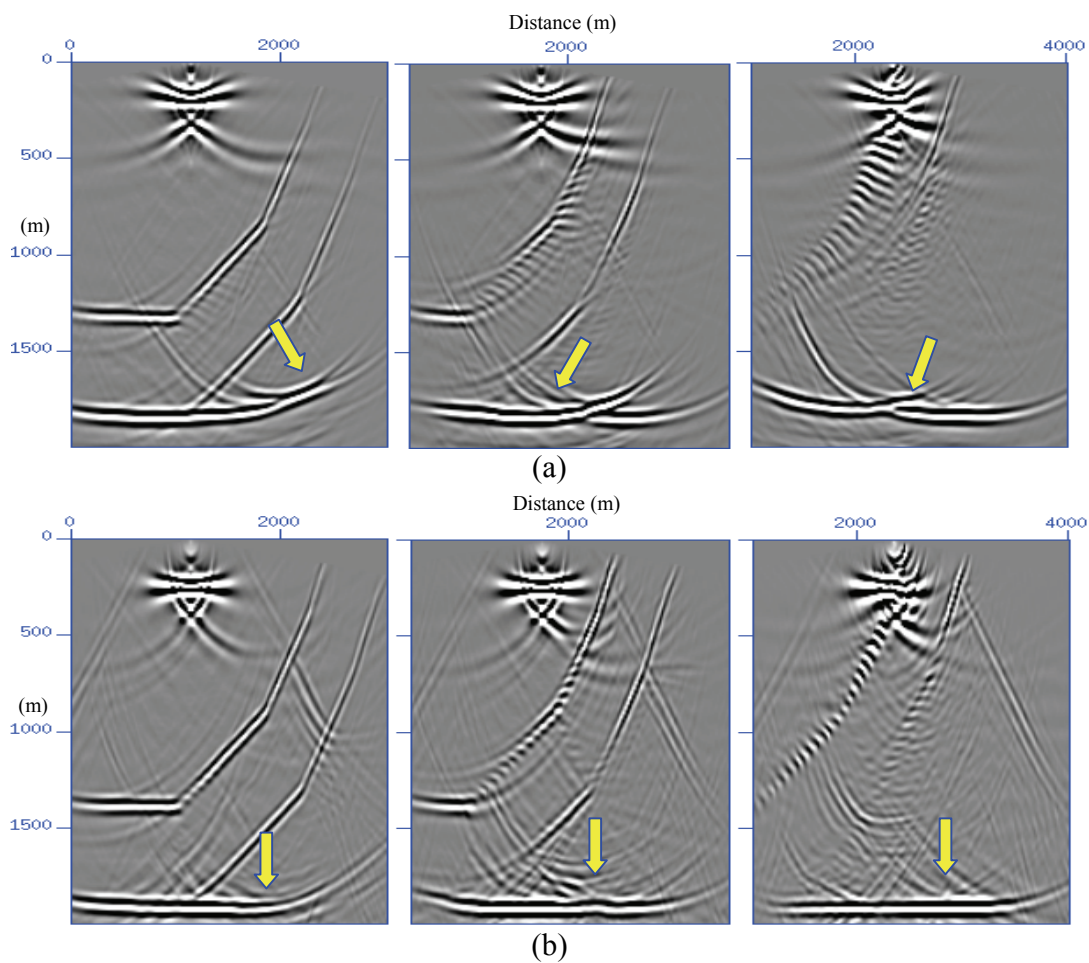
Figure 7.24 Migration sections of shot gathers corresponding to source location at 1,140m, 1,740m and 2,340m, respectively. Top subfigures (a) are the isotropic PSPI migration results at these source positions; bottom subfigures (b) are the anisotropic PSPI results of these same shot gathers. The results on top correspond to those directly beneath them. The yellow arrows emphasize the differences between them. The anisotropic migration algorithm successfully focuses the reflection energy from the basement and flattens the interface.
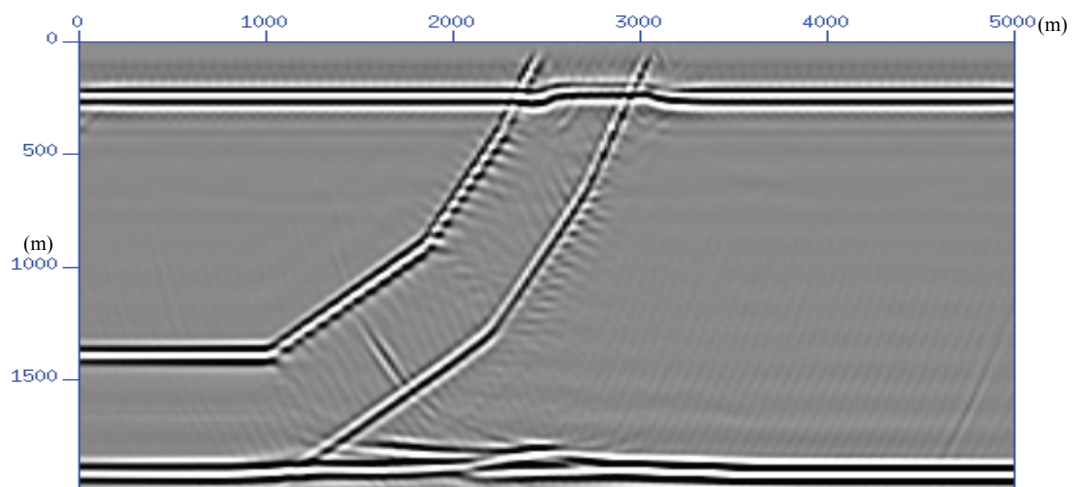
Figure 7.25 The prestack <u>isotropic</u> PSPI migration result from the numerical dataset.
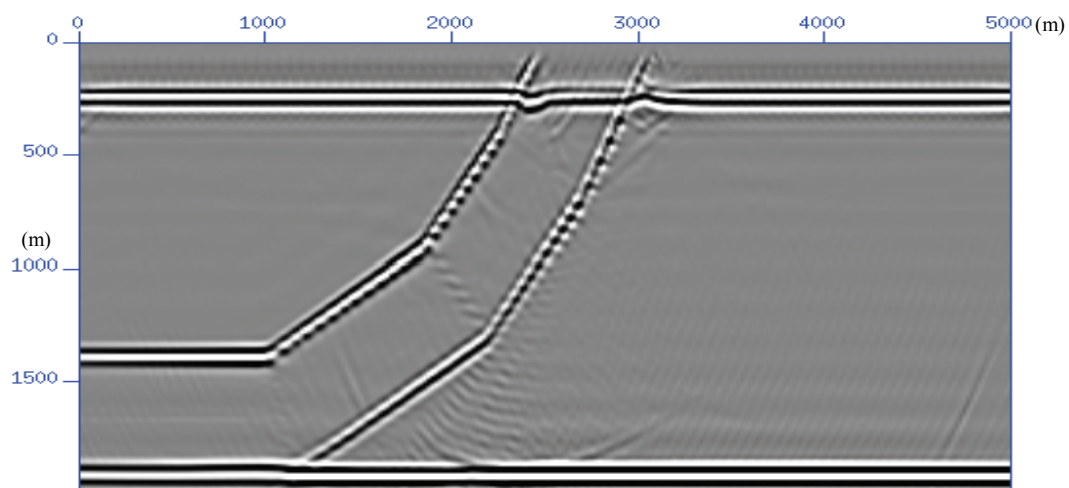
Figure 7.26 The prestack <u>anisotropic</u> PSPI migration result with correct velocity and anisotropy parameters.

(a)

(b)
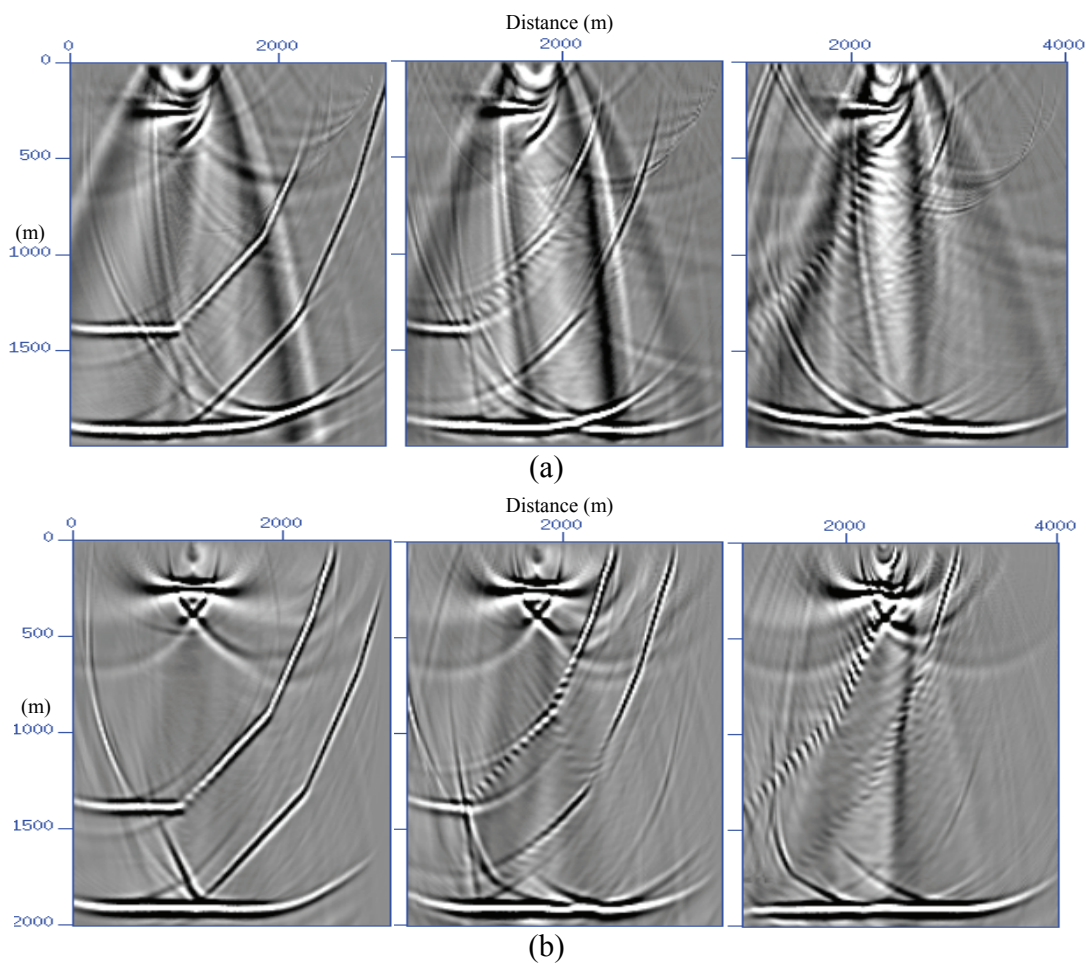
Figure 7.27 Migration sections of shot gathers corresponding to source locations at 1,140m, 1,740m and 2,340m, respectively, which are similar to the migration analyses of Figure 7.24. Top subfigures are the isotropic RT migration results at these source positions; bottom subfigures correspond to the anisotropic RT results of these same shot gathers. When compared to the migration results in Figure 7.24, the RT methods exhibit obvious low-frequency noise, which is easily removed by a low-frequency filter. The isotropic and anisotropic RT migration algorithms show the same characteristics as the corresponding examples of the PSPI methods.
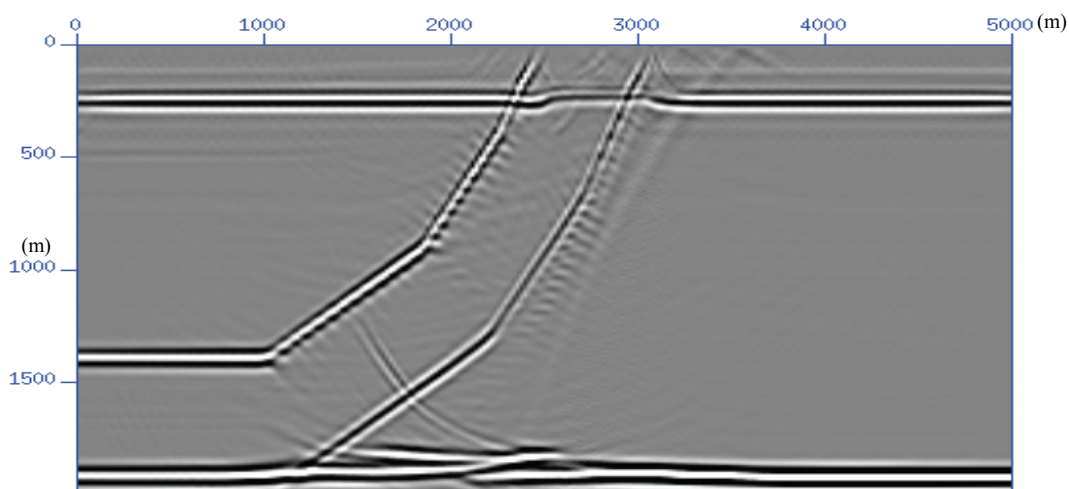
Figure 7.28 The prestack <u>isotropic</u> RT migration result from the numerical dataset
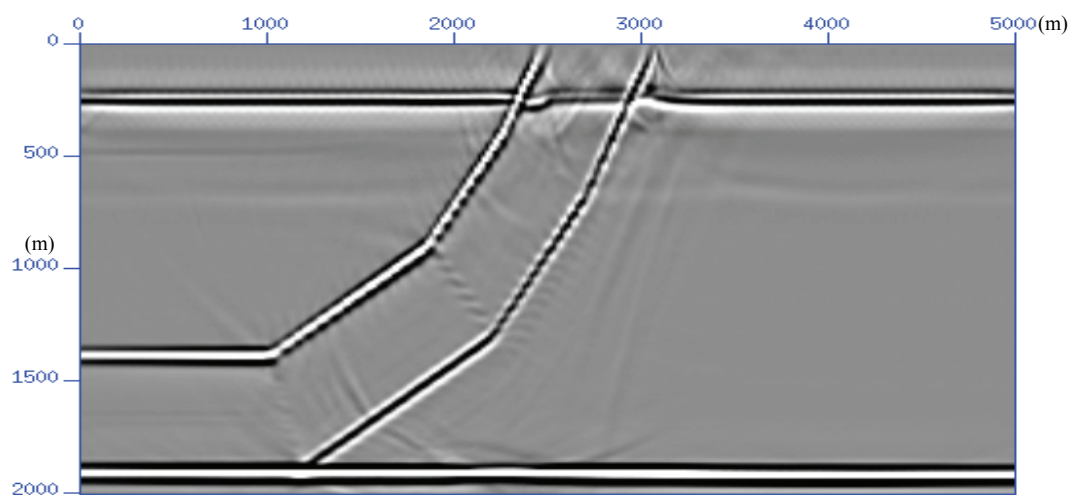
Figure 7.29 The prestack <u>anisotropic</u> RT migration result with correct velocity and anisotropy parameters.

7.4 Chapter summary

The chapter briefly reviews the theory governing the prestack anisotropic Kirchhoff, prestack anisotropic PSPI and prestack anisotropic reverse-time migration methods for TTI media. An overall analysis for the three algorithms is given, both for isotropic and anisotropic cases with respect to both accuracy and efficiency. Numerical and physical

examples are presented. We find the prestack anisotropic Kirchhoff, PSPI, and RT results are promising and encourage further investigation. The anisotropic Kirchhoff migration maintains the greatest advantage in the computation cost. The anisotropic RT migration shows excellent capability for dip angle imaging, whereas the anisotropic PSPI strikes a good balance between accuracy and efficiency. The anisotropic Kirchhoff depth migration doesn't involve any extra cost when handling any complex anisotropic media due to its unchanged migration algorithm. The anisotropic PSPI uses almost twice the computation time of isotropic PSPI, while the computational cost of the anisotropic RT is nearly five times larger than that for the isotropic RT. However, with the rapid development of computer hardware, the two wave-equation-based anisotropic depth migration algorithms are likely to become widely used for more accurate seismic imaging.

Chapter Eight: Challenging problems for the anisotropic implicit finite-difference and anisotropic split-step Fourier methods from isotropic cases

8.1 Introduction

In Chapters 5 and 6, two prestack depth migration algorithms, reverse-time and PSPI, were successfully extended from handling isotropic media to dealing with tilted TI media. In this chapter, implicit finite-difference (IFD) and split-step Fourier (SSF) methods are studied in their handling of TI media. The anisotropic implicit finite-difference method (A-IFD) can well accommodate VTI media, whereas at this point in time, the anisotropic split-step method (A-SSF) can only deal with TI media with simple anisotropy parameters. Both algorithms face challenging problems to process tilted TI media.

8.2 Anisotropic implicit finite-difference method

Ristow and Ruhl (1997) first extended the implicit finite-difference method to handle VTI media using implicit operators. Two schemes are available to obtain implicit operators, of which one is the Taylor series expansion method and the other is via the optimization method. Shan (2006) emphasized the optimization method and demonstrated the technique's ability to cope with a complex VTI model with laterally varying anisotropy parameters. Two schemes are also presented here and together demonstrate calculation accuracy in complex VTI media. With these operators, the anisotropic implicit finite-difference extrapolation is almost same as that in the isotropic case.

8.2.1 Taylor series expansion method for VTI media with weak anisotropy approximation

The Taylor series expansion method is actually an analytical method, which approximately obtains the vertical wavenumber as the function of the Thomsen parameters and the horizontal wavenumber. As in the case of anisotropic PSPI, we start from the frequency-dispersion equation for TI media with a vertical axis of symmetry,

$$k_z = \sqrt{\frac{\omega^2}{v_p^2(\theta)} - k_x^2} \,,$$

(8.1)

where $v_p(\theta)$ is the phase velocity we mentioned in the A-RT and A-PSPI algorithms. Considering that the exact phase velocity is quite complicated, we turn to the weak anisotropic formula shown below to obtain the approximate solution:

$$v_p^2(\theta) = v_{p0}^2 (1 + 2\delta \sin^2 \theta \cos^2 \theta + 2\varepsilon \sin^4 \theta) \,.$$

(8.2)

Introducing φ, which refers to the phase angle in isotropic media with same vertical velocity as the TI media, we have the following relationship of isotropic and anisotropic phase angles:

$$\sin \theta = \frac{v_p(\theta) k_x}{\omega} \,, \quad \sin \varphi = \frac{v_{p0} k_x}{\omega} = u \,.$$

(8.3)

With the help of Equations (8.2) and (8.3), the dispersion equation can be written after solving a quadratic equation and Taylor series expansion:

$$k_z = \frac{\omega}{v_{p0}} \sqrt{1 - (1 + 2\delta) \sin^2 \varphi - 4(\varepsilon - \delta)\delta \sin^6 \varphi - ...} \,.$$

(8.4)

The vertical wavenumber in TI media becomes a function of frequency, vertical velocity, isotropic phase angle and anisotropy parameters. Based on the principle of IFD, the one-way equation (Lee and Suh, 1985) can be written as

$$\frac{v_{p0}k_z}{\omega} = \frac{v_{p0}}{v_p(\theta)}\sqrt{1-\sin^2\theta} = 1 - \sum_{i=1}^{N}\frac{a_i\left(\frac{v_{p0}}{v_p(\theta)}\sin\theta\right)^2}{1-b_i\left(\frac{v_{p0}}{v_p(\theta)}\sin\theta\right)^2} = 1 - \sum_{i=1}^{N}\frac{a_i(\sin\varphi)^2}{1-b_i(\sin\varphi)^2}. \quad (8.5)$$

Making full use of Equations (8.4) and (8.5), and expanding both in a Taylor series, we can obtain a different approximation for the one-way wave equation in TI media,

$$R_1 = 1 - a_1 u^2, \quad (8.6)$$

where $a_1 = \frac{1+2\delta}{2}$, and $b_1 = 0$. Assuming that $\delta = 0$, the coefficients become a 15^0 isotropic operator.

An improved approximation is given by:

$$R_2 = 1 - \frac{a_1 u^2}{1-b_1 u^2}, \quad (8.7)$$

where $a_1 = \frac{1+2\delta}{2}$, and $b_1 = \frac{2(\varepsilon-\delta)}{1+2\delta} + \frac{1+2\delta}{4}$. The coefficients become the well-known 45° isotropic operator when ε and δ are assumed 0.

A further improvement for the maximum dip migration is

$$R_3 = 1 - \frac{a_1 u^2}{1-b_1 u^2} - \frac{a_2 u^2}{1-b_2 u^2}, \quad (8.8)$$

where

$$a_2 = \frac{(\varepsilon - \delta) + (1 + 2\delta)^2 / 8}{b_2}, \ b_2 = \frac{2(\varepsilon - \delta)\delta + 0.5(\varepsilon - \delta)(1 + 2\delta) + (1 + 2\delta)^3 / 16}{(\varepsilon - \delta) + 0.125(1 + 2\delta)^2},$$

$a_1 = 0.5(1 + 2\delta) - a_2$, and $b_1 = 0$.

We should mention that the coefficients should satisfy the constraint condition

$$a_i > 0, \text{ and } b_i > 0, \tag{8.9}$$

so we can achieve a recursive wavefield extrapolation. In addition, the coefficient can only be used in weakly anisotropic media since so many approximations are applied to the coefficient derivation.

8.2.2 Optimization method for VTI media

Lee and Suh (1985) forwarded the linear least-squares optimization method to approximate the one-way wave equation for implicit wavefields. The technique can be similarly applied for TI media. The difference lies in the fact that phase velocity is dependent on phase angle. The objective function can be denoted as

$$E_{2n}(\theta) = \frac{\displaystyle\sum_{i=1}^{n} a_i \left(\frac{v_{p0}}{v_p(\theta)} \sin\theta \right)^2}{1 + \displaystyle\sum_{i=1}^{n} b_i \left(\frac{v_{p0}}{v_p(\theta)} \sin\theta \right)^2} + 1 - \frac{v_{p0}}{v_p(\theta)} \cos\theta, \tag{8.10}$$

which is the error due to the truncation of the rational approximation of the square-root equation. The optimization procedure is to estimate the coefficients by minimizing the integral:

$$J = \int_0^\phi E_{2n}^2(\theta) d\theta. \tag{8.11}$$

With the linear least-square principle, we have

$$\frac{\partial J}{\partial a_i} = 0 \text{, and } \frac{\partial J}{\partial b_i} = 0 . \tag{8.12}$$

After solving the normal equations, we can get the optimization coefficients. The more variables involved, the higher the accuracy obtained.

When we compare the two schemes, the characteristics of each method become apparent. The Taylor series expansion method is very straightforward and highly efficient, but is only used in simple calculations, and only applied to weakly anisotropic media. The optimization method can be widely used on any anisotropic media, but requires pre-computation of the coefficient tables according to each group of anisotropy parameters, which seems very troublesome due to solving many linear equations according to different anisotropy parameters. With two schemes to obtain the coefficients for TI media, we can give a clear analysis of them in the following paragraphs.

8.2.3 Comparisons of implicit operators obtained from the Taylor series expansion method and the optimization method

8.2.3.1 Experiment I.

Coefficients from Equation (8.8) are calculated to represent the Taylor series expansion method. Fourth-order accuracy coefficients are obtained using the optimization method. Table 8.1 shows the coefficients obtained from the two schemes when the anisotropy parameters are $\varepsilon = 0.2$, and $\delta = 0.1$. With these coefficients, Figure 8.1 shows the dispersion curves. The blue solid line is the true dispersion relationship; the blue dashed point is the approximation dispersion of the Taylor series expansion method; and the line of red crosses is the approximation dispersion of the optimization method with 4th order accuracy. Two approximation curves approach the true curve at different levels. The dispersion curve from the optimization method almost matches with the true solution,

whereas the curve from the Taylor series expansion method strays far from the true curve with increasing dipping angles, which is also clearly seen in relation to the curves of the vertical wavenumber versus phase angle (Figure 8.2). The maximum migration angle from the Taylor series expansion method is approximately 65° while the one from the optimization method is almost 90°.

Table 8.1 Coefficients for wavefield extrapolation in TI media with $\varepsilon = 0.2$, $\delta = 0.1$

	Coefficients for anisotropy parameters $\varepsilon = 0.2$, $\delta = 0.1$	
Power series expansion method	$a_1 = 0.1830$,	$b_1 = 0$
	$a_2 = 0.4170$,	$b_2 = 0.6714$
Optimized method	$a_1 = 0.0065204$,	$b_1 = 1.3118$
	$a_2 = 0.56315$,	$b_2 = 0.49113$
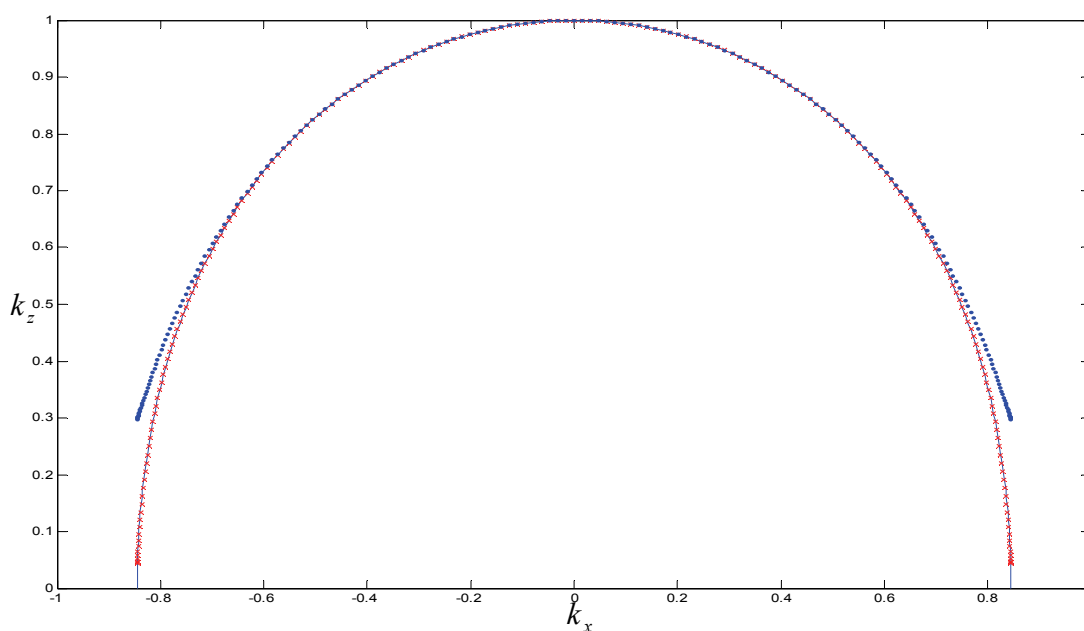
Figure 8.1 Dispersion relationship for anisotropy parameters $\varepsilon = 0.2$, $\delta = 0.1$: blue solid line is the true dispersion relation; blue dashed point is the approximation dispersion by Taylor-series analysis; red cross is the approximation dispersion by the 4th order optimization.
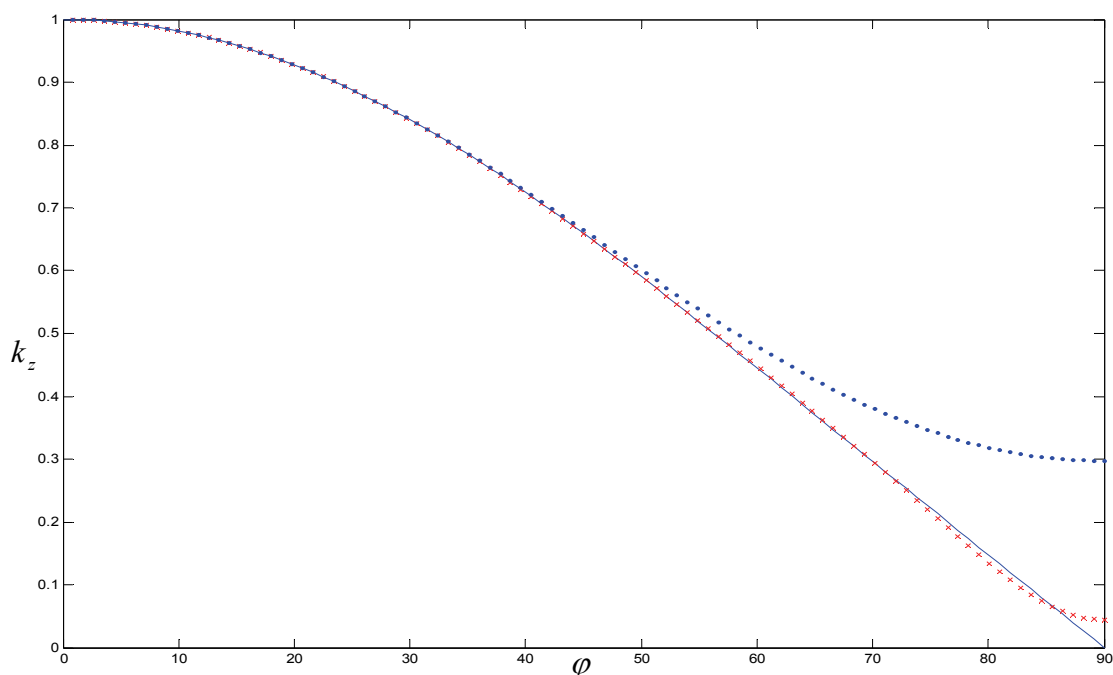
Figure 8.2 The relationship curve of the vertical wavenumber versus phase angle for anisotropy parameters $\varepsilon = 0.2$, $\delta = 0.1$ in Figure 8.1: blue solid line is the true dispersion relation; blue dashed point is the approximation dispersion by Taylor-series analysis; line indicated by red crosses is the approximation dispersion by the 4th order optimization.

The model with different dipping events, described in Chapter Seven is chosen again for the migration with these coefficients. The model has homogenous anisotropy parameters $\varepsilon = 0.2$ and $\delta = 0.1$ and the tilt angle is 0°. The vertical velocity of the model is $v(x, z)$ =1,500+0.3z +0.3x(m/s). Figure 8.3, Figure 8.4, and Figure 8.5, respectively, show the isotropic migration result with vertical velocity, anisotropic migration result with coefficients from the Taylor series expansion method, and anisotropic migration result with coefficients from the optimization method. Figure 8.3 shows an under-migrated result. The dip-imaging capability just attains 65° in Figure 8.4 while with the optimization method it is 90° in Figure 8.5, which verifies the accuracy of this method as illustrated in Figure 8.2.
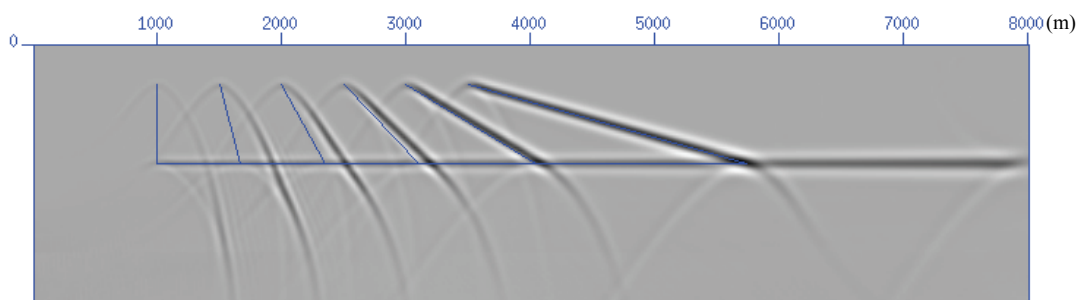
Figure 8.3 Migration result from the <u>isotropic</u> implicit FD method.
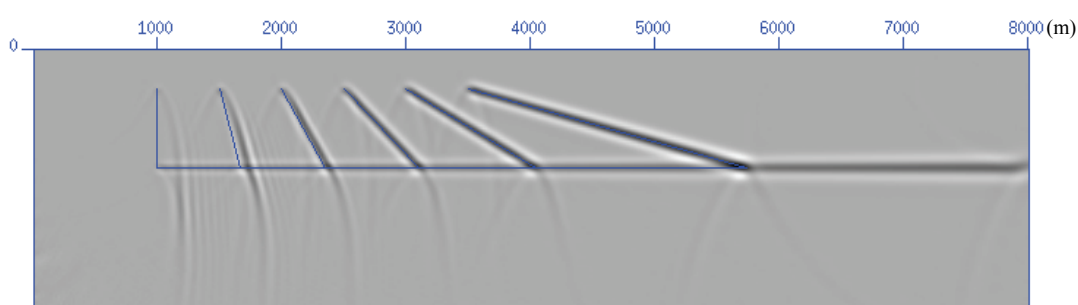
Figure 8.4 Migration result from the <u>anisotropic</u> implicit FD method with coefficients obtained using the Taylor-series expansion method.
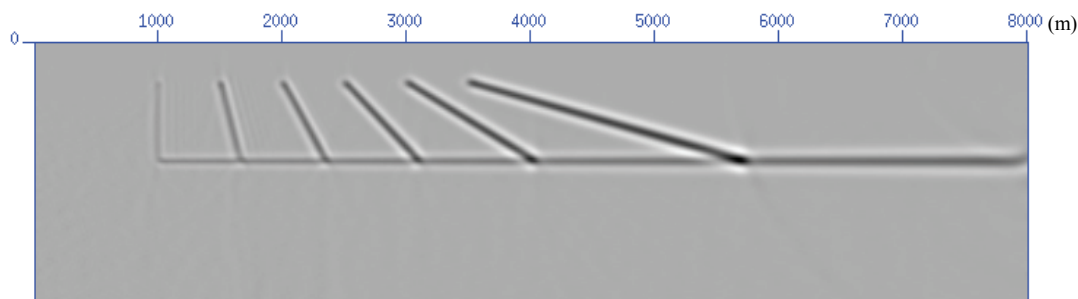
Figure 8.5 Migration result from the <u>anisotropic</u> implicit FD method with 4th order accuracy coefficients obtained using the optimized method.

8.2.3.2 Experiment II

We only need to change the anisotropy parameters to do the similar experiment. The new anisotropy parameters are $\varepsilon = 0$ and $\delta = 0.2$. The coefficients with 6th order accuracy are additionally computed through the optimization method. Table 8.2 shows the coefficients obtained from the two schemes. Note that the coefficients from the Taylor

series expansion method can't be applied since they can't satisfy the constraint condition of Equation (8.9). The same curves as Figure 8.1 and Figure 8.2 are correspondingly shown in Figure 8.3 and Figure 8.4 except for the addition of the curve with coefficients of 6th order accuracy. It's hard to tell the difference between 4th order and 6th order coefficients from Figure 8.3 and Figure 8.4. They both approximate the true solution.

The same model with different dipping events that was employed in Experiment I is chosen again, with the anisotropy parameters changed to $\varepsilon = 0$ and $\delta = 0.2$. Figure 8.8 and Figure 8.9 give almost the same correct migration results, which correspond to the 4th order and 6th order coefficients, respectively. It is obviously that 4th order accuracy has achieved adequate dipping angle imaging capability in this model.

Table 8.2 Coefficients for wavefield extrapolation in TI media with $\varepsilon = 0$, $\delta = -0.2$

	Coefficients for anisotropy parameters $\varepsilon = 0$, $\delta = -0.2$	
Taylor series expansion method	$a_1 = 9.5346$,	$b_1 = 0$
	$a_2 = $ -9.2346,	$b_2 = $ -0.026531
Optimized method (4th order accuracy)	$a_1 = 0.0065204$,	$b_1 = 0.97664$
	$a_2 = 0.30382$,	$b_2 = 0.56739$
Optimized method (6th order accuracy)	$a_1 = 0.167$,	$b_1 = 0.018$
	$a_2 = 0.0822$,	$b_2 = 0.803$
	$a_3 = 0.050$,	$b_3 = 0.83$
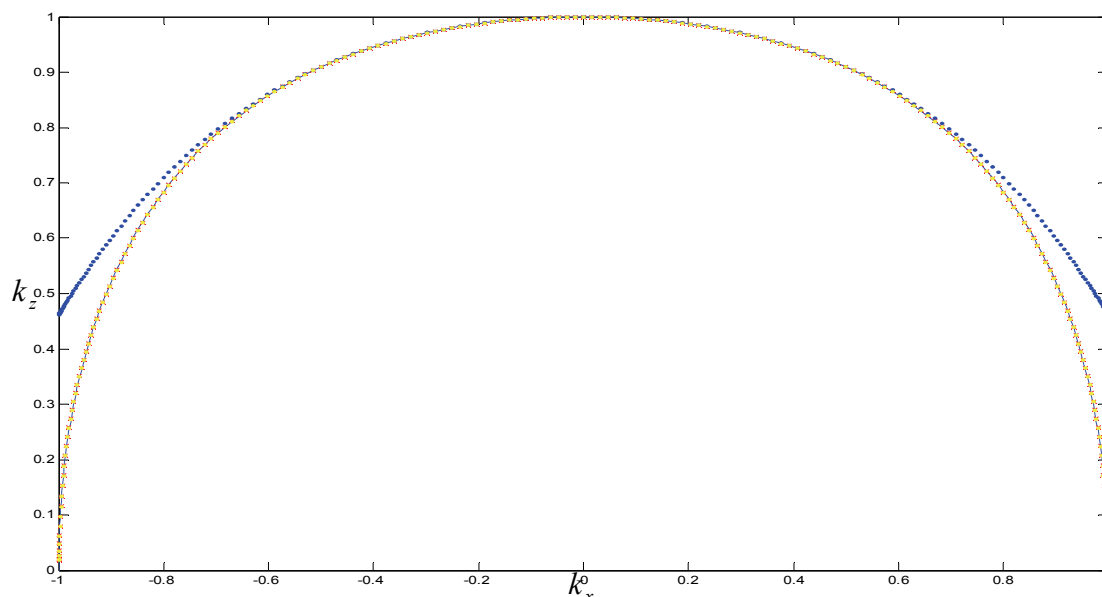
Figure 8.6 Dispersion relationship for anisotropy parameters $\varepsilon = 0$, $\delta = -0.2$: blue solid line is the true dispersion relationship; blue dashed point is the approximation dispersion by Taylor-series analysis; line of red crosses is the approximation dispersion by the 4th order accuracy optimization; yellow dot that closely matches with red crosses is the approximation dispersion by the 6th order accuracy optimization.
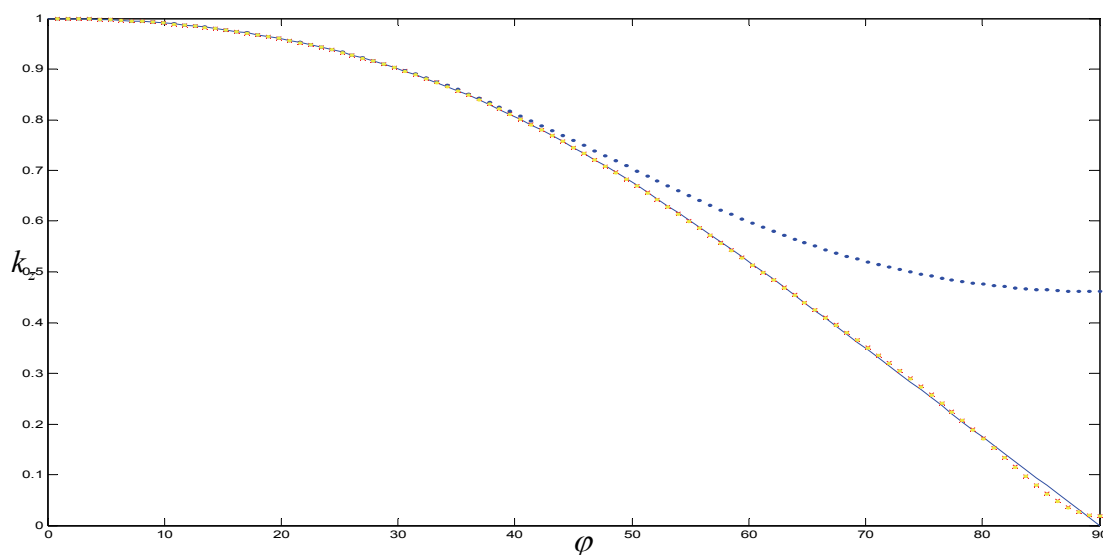
Figure 8.7 The relationship curve for the vertical wavenumber versus phase angle for anisotropy parameters $\varepsilon = 0$, $\delta = -0.2$ shown in Figure 8.6: blue solid line is the true dispersion relationship; broken blue line is the approximation dispersion by Taylor-series analysis; red crosses indicate the approximation dispersion by the 4th order accuracy optimization; yellow dot that closely matches with red crosses is the approximation dispersion by the 6th order optimization.
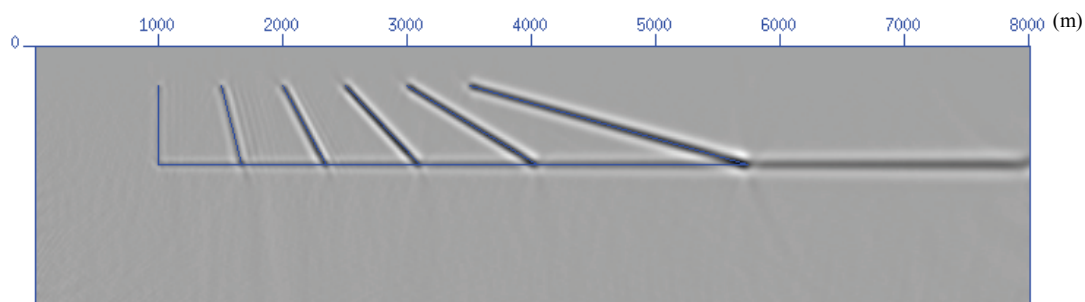
Figure 8.8 Migration result from the <u>anisotropic</u> implicit FD method with 4th order accuracy coefficients obtained through the optimized method.
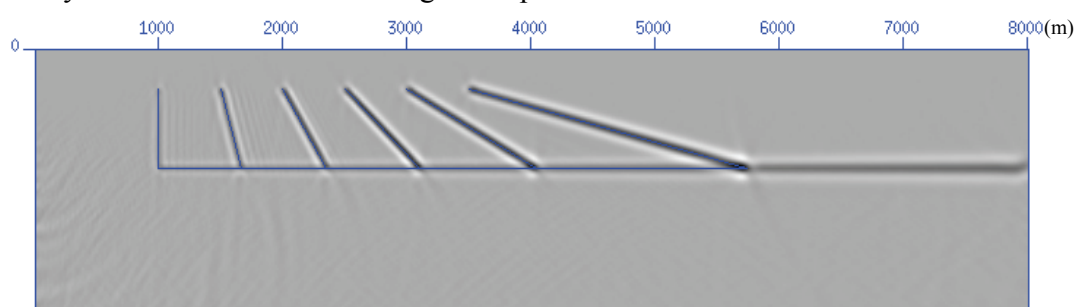
Figure 8.9 Migration result from the <u>anisotropic</u> implicit FD method with 6th order accuracy coefficients obtained through the optimized method.

8.2.4 The anisotropic Marmousi model and migrations

To demonstrate the anisotropic A-IFD algorithm, the complex Marmousi model is chosen again. The anisotropy parameters are put in the shallow overburden, which are shown in Figure 8.10. The pseudo-spectral method is applied to generate zero-offset synthetic data with the exploding reflector principle. The synthetic seismic section processed without consideration for anisotropy (Figure 8.11(a)) is based on the acoustic wave equation. Figure 8.11(b) corresponds to the zero-offset seismogram based on the anisotropic P-wave equation (Du, et al., 2005). The reflectors in Figure 8.11(b) all move up, in comparison to the isotropic case, due to the effect of anisotropy, as indicated by the yellow arrows. Isotropic and anisotropic IFDs are adopted to process the anisotropic synthetic data, in order to investigate the imaging differences.
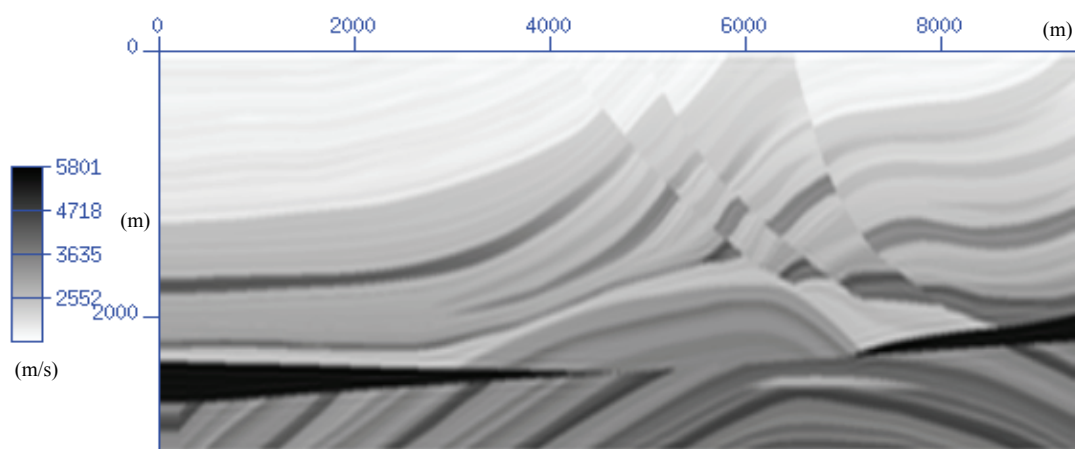
(a)
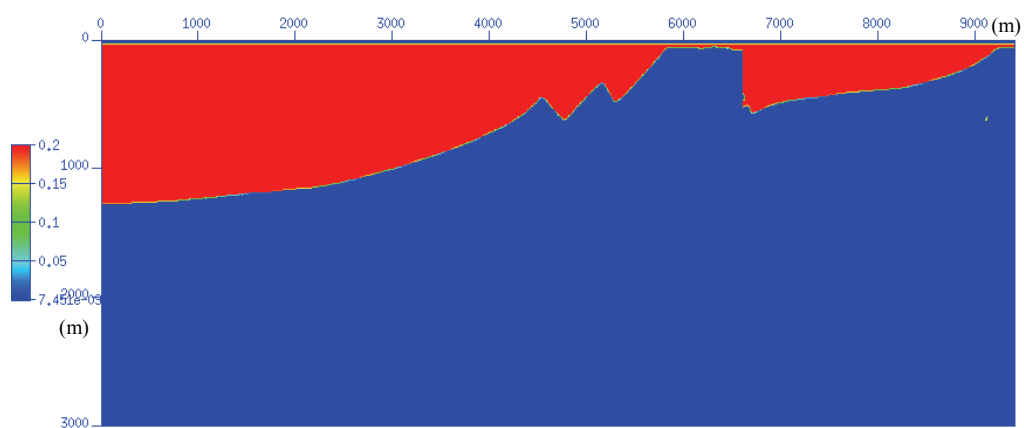
(b)
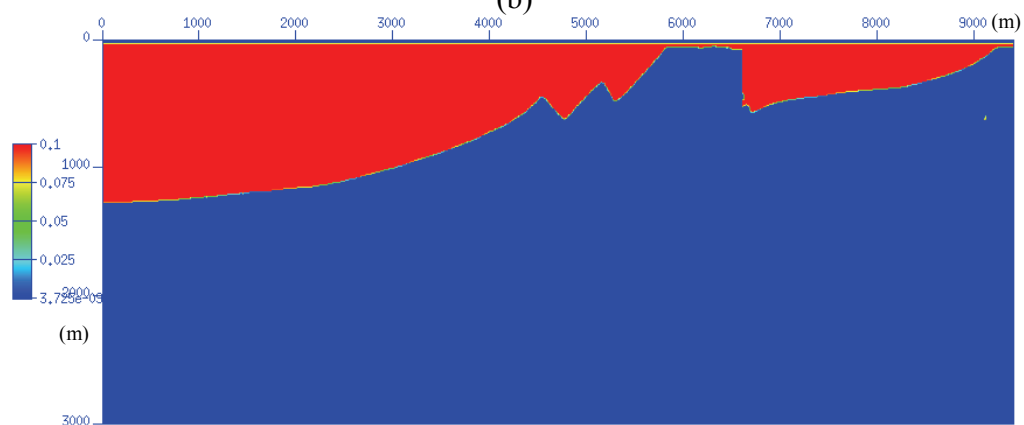
(c)

Figure 8.10 Vertical velocity and anisotropy parameters of the Marmousi model: (a) vertical velocity; (b) anisotropy parameter ε; (c) anisotropy parameter δ.
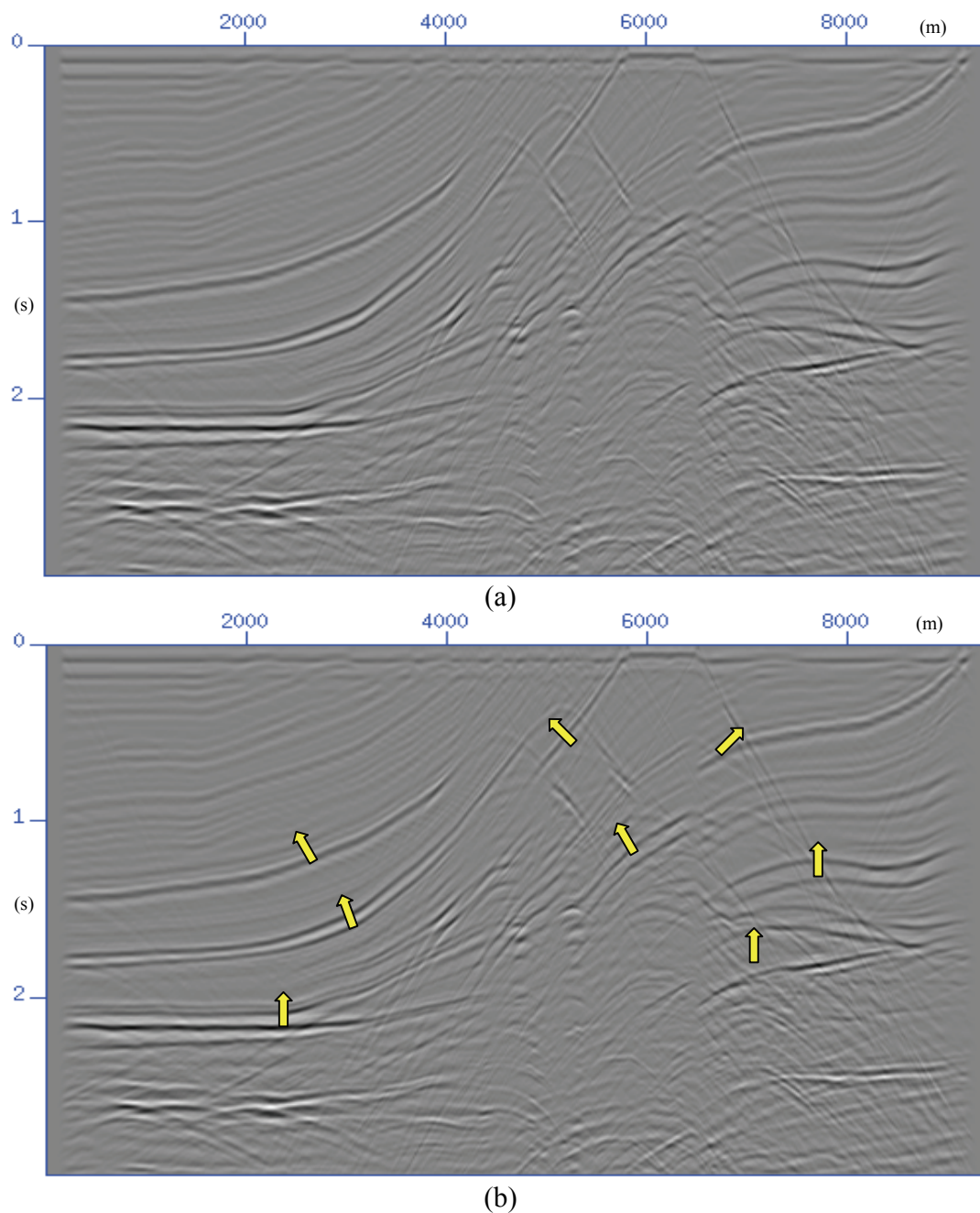
Figure 8.11 Zero-offset seismic sections from the pseudo-spectral method: (a) isotropic synthetic data based on the acoustic wave equation; (b) anisotropic synthetic data based on the anisotropic P-wave equation (Du et al., 2005). All the events from the anisotropic modelling in subfigure (a) move up due to the effect of anisotropy when compared with those from the isotropic modelling in subfigure (b), as indicated by the yellow arrows.
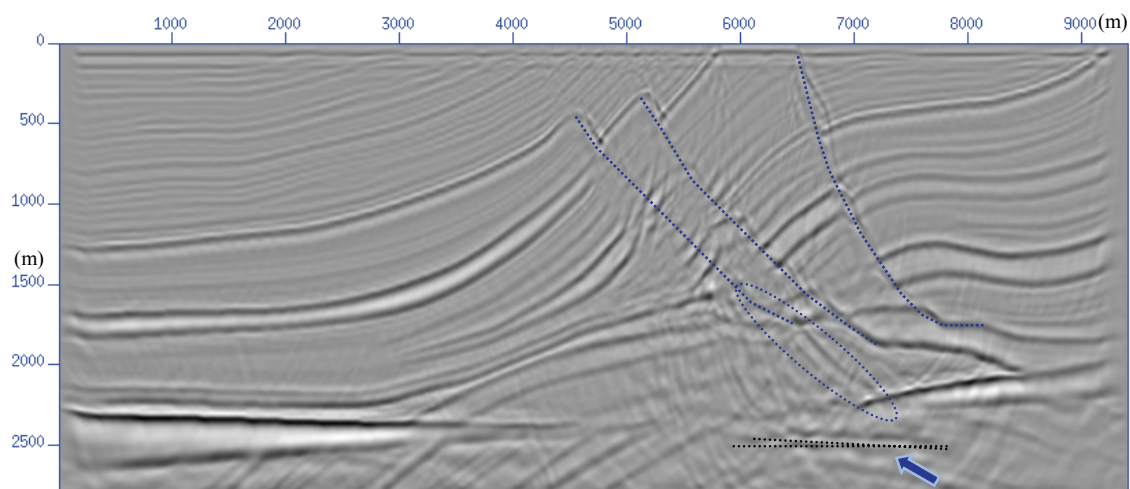
Figure 8.12 <u>Isotropic</u> implicit FD migration result with the vertical velocity shown in Figure 8.10. The fault planes are not in their correct positions, delineated by blue curves; the diffraction energy can't be focused; the anticline is distorted (dashed ellipse); and the objective target zone (dashed black lines) obliquely moves up.
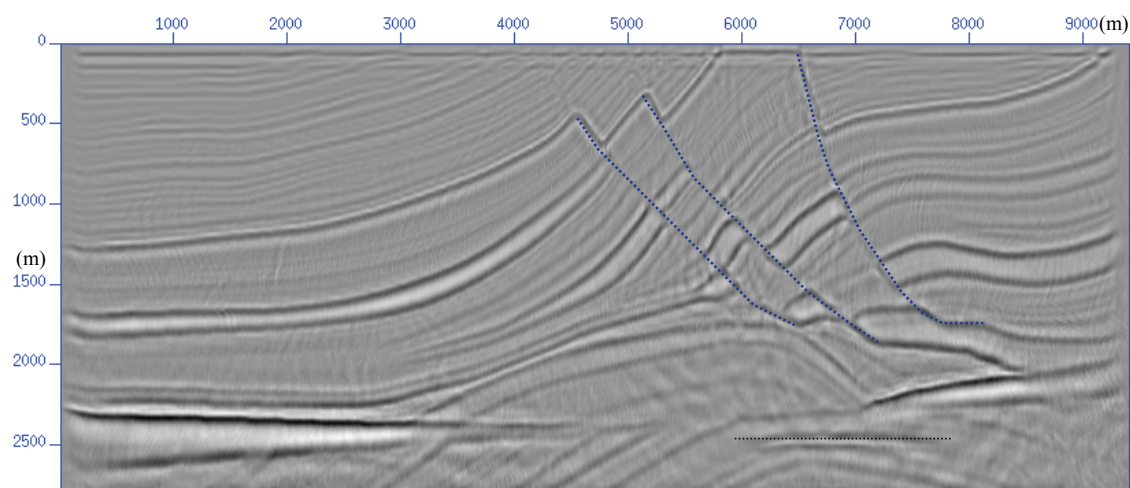
Figure 8.13 <u>Anisotropic</u> implicit FD migration result with the vertical velocity and anisotropy parameters in Figure 8.10. The fault planes are in accord with the true model as the anisotropic effect of the overburden is accounted for. The reflections are correctly migrated to their true positions, as is the target zone.

Considering the complexity of the model, the optimization coefficients of 4th order accuracy are chosen for implicit wavefield extrapolation. Figure 8.12 is the isotropic migration result. It is obvious that the fault planes are not in their correct positions delineated by blue curves. In addition, the diffraction energy can't be focused, the anticline is distorted (dashed ellipse), and the objective of target zone (dashed black lines) obliquely moves up. The anisotropic IFD migration result gives us a correct image with focused energy and clear structures, which achieves good correspondence with the true model. From the viewpoint of computation cost, there is a slight increase from the IFD to the A-IFD algorithm since calculating the coefficients tables only accounts for a very small proportion of the total calculation. It seems that the A-IFD migration algorithm has a distinct advantage in computation time compared with the A-PSPI and A-RT algorithms.

8.2.5 The challenging problem for the anisotropic implicit finite-difference method

Compared with the A-PSPI algorithm, A-IFD can well adapt to variations in lateral velocity and anisotropy parameters. When compared with the A-RT algorithm, it has the dominant advantage in computational efficiency. Currently, however, A-IFD can only deal with VTI media. Furthermore, it is very difficult to adapt the algorithm to handle tilted TI media. When the axis of symmetry isn't vertical to the observation system for TI media, the phase velocity becomes asymmetric while the implicit wavefield assumes that the operator is symmetric.

Things become more promising if the observation coordinates are rotated to match the axes of symmetry of the TI media, so that the problem of TTI can be handled by the

solution to VTI media discussed in the above. However, the "diffraction item" of the implicit finite-difference method,

$$\frac{\omega^2}{v^2}\frac{\partial P^*}{\partial z}+\beta_i\frac{\partial^3 P^*}{\partial z\partial x^2}+\alpha_i\frac{i\omega}{v}\frac{\partial^2 P^*}{\partial x^2}=0\,,\qquad (8.13)$$

becomes quite complicated after the coordinates are rotated, becoming a 4th order partial differential equation over depth. The challenging problem of solving this equation awaits further investigation.

8.3 The anisotropic split-step Fourier method

The split-step Fourier method is based on velocity perturbation theory and was discussed in Chapters 2 and 3. When phase velocity is dependent on phase angle, the usefulness of this method becomes comparatively restricted. The phase shift based on the anisotropic vertical wavenumber computed by the reference slowness can't compensate for the effect caused by the variable anisotropy parameters at each step. Neither can the second phase-shift correction, due to perturbation in slowness in the space and frequency domains, take into account anisotropy parameters. Therefore the extended split-step Fourier method can only deal with simple anisotropic models, such as cases with no laterally varying anisotropy parameters or velocities. When Shan and Biondi (2005) imaged steeply dipping reflections in TI media using wavefield extrapolation, the split-step method was only used to handle the isotropic operator.

The synthetic data, velocity model, and anisotropy parameters from the different dipping reflectors model, which were applied to test the anisotropic IFD algorithm in Experiment I, were also chosen to identify the limitations of the anisotropic SSF method. The migration result is shown in Figure 8.14. We can see that the reflectors under 45° are

undermigrated whereas the reflectors above 45° are over-migrated. When we chose homogenous anisotropy parameters and reduce velocity so that it only varies with depth, such as $v(x,z) = 1,500 + 0.3z$ (m), as viewed in Figure 8.15, we obtained the correct and clear migration result in Figure 8.16. There is a significant amount of theoretical work waiting to be done to adapt the split-step Fourier method for use on any complex anisotropic media.
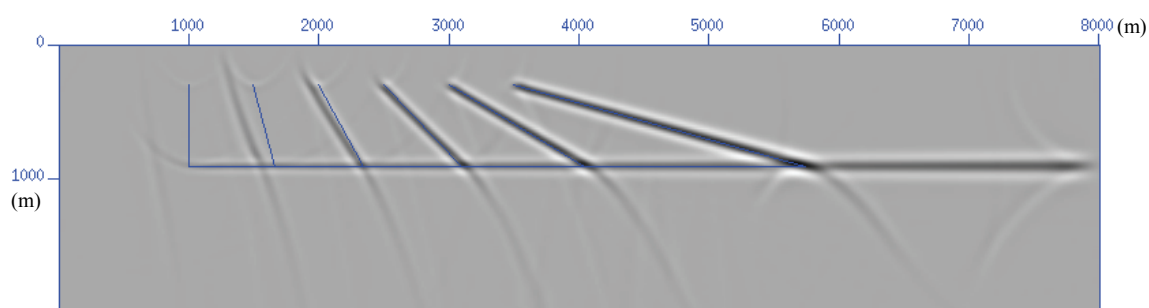
Figure 8.14 Anisotropic split-step Fourier migration result from the same vertical model and with the same anisotropy parameters as the anisotropic implicit FD shown in Figure 8.5. The vertical velocity function of this model is $v(x,z) = 1,500 + 0.1x + 0.3z$ (m/s), and the homogenous anisotropy parameters of the model are $\varepsilon = 0.2$ and $\delta = 0.1$. The synthetic data for migration was generated with the above parameters. The migration result is partially over- and undermigrated since the anisotropic algorithm can't deal with cases possessing lateral velocity variation.
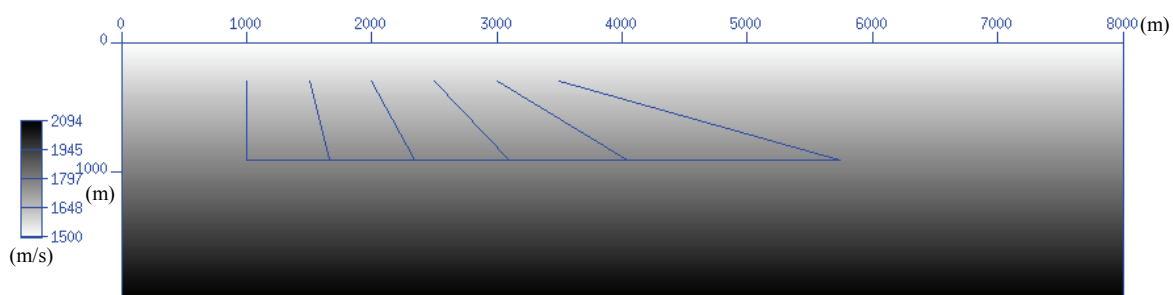
Figure 8.15 Vertical variable velocity $v(x,z) = 1,500 + 0.3z$ (m/s).
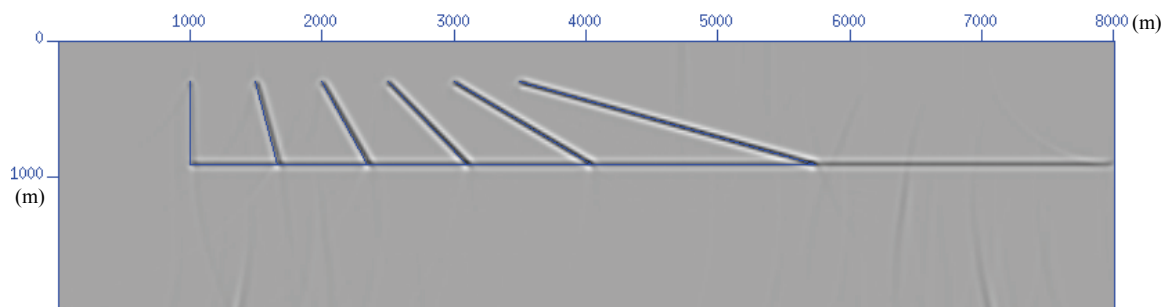
Figure 8.16 <u>Anisotropic</u> split-step Fourier migration result where velocity has no lateral variation. The vertical velocity function of this model is $v(x,z) = 1{,}500 + 0.3z$ (m/s), and the homogenous anisotropy parameters of the model are $\varepsilon = 0.2$ and $\delta = 0.1$. The synthetic data for migration was generated using the above parameters. The migration result shows the six dipping reflectors correctly migrated since the anisotropy parameters are homogenous and there is no lateral vertical velocity variation.

8.4 Summary

The implicit finite-difference algorithm has been extended to handle VTI media. Two methods to obtain the implicit operators are presented and analyzed. The dipping reflectors model is employed to show the dip-angle imaging capability of the two operators. The anisotropic Marmousi model is used to show the excellent adaptability of A-IFD to variable velocity and anisotropy parameters. At the same time, the challenging problem of A-IFD for tilted TI media is presented and a possible technique to solve the problem is proposed for future investigation.

The split-step Fourier method for TI media is also discussed. Because of the principles underlying this method, it is very difficult to extend SSF to handle complex anisotropic models. Currently, it only handles models with no laterally varying velocities or anisotropy parameters. The dipping reflectors model is used to verify this conclusion. To adapt this method for lateral variations, challenging theoretical work needs to be done in the future.

Chapter Nine: Conclusions

This thesis has focused on prestack depth migration methods, not only for isotropic media but also polar anisotropic media. Three types of migration algorithms are discussed, based on ray-tracing, one-way wave equation, and two-way wave equation, respectively.

In conjunction with the migration algorithms discussed in this thesis, theoretical reviews are presented of the two-way wave equation (reverse-time) and one-way downward-continuation methods, including the PSPI, SSF, and IFD methods. Theories of anisotropy are discussed in detail. Two categories of phase velocities for dipping TI media — rotating phase angle and rotating stiffness matrix — are each derived and proved.

The FE-FD operator is presented and analyzed for accuracy and stability in wavefield modelling and reverse-time migration. Compared to the finite-difference operator at the same order of accuracy, it exhibits looser stability constraints. The operator allows for irregular discretization along the depth direction with a looser stability condition than FD, which can adaptively adjust the grid spacing to improve efficiency and avoid frequency dispersion according to velocity variations. As an example, the reverse-time migration is used to process the Marmousi post-stack synthetic data and demonstrates the superior imaging quality of the full wave equation when compared to the one-way wave equation downward-continuation methods, including PSPI, SSF and IFD. In conjunction with calculating traveltimes using the upwind finite-difference method based on the Eikonal equation, a prestack reverse-time depth migration has been developed and used on Marmousi prestack synthetic data. As with the Kirchhoff migration method, traveltime

accuracy affects the reverse-time migration method according to two migration results presented here.

To implement migration from near-surface topography, a technique was formulated for downward-continuation Fourier migration methods (including prestack PSPI prestack SFF, and prestack IFD). Three algorithms to handle surface topography for prestack depth imaging were developed. The technique was successfully applied with three extrapolation schemes to a Foothills synthetic dataset specifically developed for investigating migration from surface topography. They are all proven to be highly capable of handling high near-surface velocities and extensive topographic variation. Compared with other methods, the prestack split-step method demonstrates its greater efficiency in computational performance. The prestack implicit finite-difference method exhibits a trade-off between resolution and speed. The prestack Kirchhoff method is applied as well, and structures (folds and thrusts) are well imaged when using the Marmousi model, which demonstrates that first-arrival traveltimes are suitable for this kind of area. The Foothills real data is processed using the prestack Kirchhoff and split-step methods with constant velocity. The split-step algorithm, as a wave-equation migration method, yields higher resolution than the ray-based Kirchhoff algorithm.

The individual P- and SV-wave equations for tilted TI media are also derived and analyzed. The linear simplified equations can be effectively used in weakly anisotropic media. The pseudo-spectral method is applied to implement the anisotropic post-stack reverse-time migration. The Fourier method's stability and accuracy with the anisotropic wave equation has been demonstrated. In a similar manner to the prestack isotropic

reverse-time migration, a prestack anisotropic reverse-time migration was developed with traveltimes calculated using the anisotropic ray-tracing method for tilted TI media. Numerical synthetic data from the anisotropic variable velocity model, and physical data from the anisotropic reef model were processed to validate the post-stack and prestack anisotropic reverse-time migration algorithms.

A quartic equation for wavenumbers and anisotropy parameters was obtained from the dispersion equation for tilted TI media, and analytically solved to obtain the vertical wavenumber. Two solutions are chosen from four possible solutions and applied to the phase-shift calculation in the anisotropic PSPI migration algorithm. An assumption regarding the relationship between reference anisotropy parameters and reference lateral velocities was made to limit the number of reference wavefields. A cross-correlation imaging condition was used for the prestack PSPI migration algorithm. Using numerical synthetic data from the anisotropic variable velocity model and physical data from the anisotropic reef model, the post-stack and prestack migration results validate the anisotropic PSPI migration algorithm.

Performance comparisons in terms of speed and accuracy were made between the anisotropic Kirchhoff depth migration method and the two newly developed anisotropic migration methods, which are based on ray-theory, one-way, and two-way wave equations, respectively. To demonstrate dipping angle imaging ability, a numerical model with six dipping reflectors in an anisotropic variable velocity media was designed and a physical model with anisotropic thrust structures was chosen. Post-stack and prestack migrations were both processed. The anisotropic reverse-time maintains its high imaging

quality but the computation cost shows a big jump, becoming very expensive. The anisotropic Kirchhoff migration method will maintain its popularity in the oil industry since there is eventually no change for the migration algorithm itself, only with the traveltime calculations. On the other hand, the cost of the anisotropic PSPI method seems relatively cheap; but as an interpolation method, the reference wavefields are not only dependent on lateral velocity variations but also on Thomsen's three anisotropy parameters, which cause interpolation to become more complicated in complex anisotropic media.

The implicit finite-difference and split-step Fourier methods have not been successfully extended to handle tilted TI media. The implicit finite-difference algorithm can currently handle VTI media well. Two methods to obtain the implicit operators were presented and analyzed. An anisotropic Marmousi model was designed and used to demonstrate the excellent adaptability of A-IFD to variable velocities and anisotropy parameters. The challenging problem for A-IFD in tilted TI media is to solve the 4th order partial differential equation. The split-step Fourier method for TI media was also discussed. Due to the principles underlying this method, it is very difficult to extend it to handle complex anisotropic models. With the vertical wavenumber in TI media, it only deals with cases in which there are no variations in lateral velocities and anisotropic parameters. In order to adapt this method to handle lateral variations, challenging theoretical work needs be done in the future.

References

Abramowitz, M., and Stegun, I. A., 1970, Handbook of mathematical functions. Dover Publications, Inc.

Aki, K., and Richards, P.G., 2002, Quantitative Seismology: Second Edition, University Science Books, Sausalito, California.

Alkhalifah, T., 1995, Gaussian beam depth migration for anisotropic media: Geophysics, 60, 1474–1484.

Alkhalifah, T., 2000, An acoustic wave equation for anisotropic media: Geophysics, 65, 1239-1250.

Alkhalifah, T., and Larner, K., 1994, Migration error in transversely isotropic media: Geophysics, 59, 1405–1418.

Alterman, Z., and Kornfeld, P., 1968, Finite difference solution for pulse propagation in a sphere: Israel J. of Technology, 6, 138-149.

Bancroft J. C., 2005, A practical understanding of pre- and post-stack migrations: Course Notes, University of Calgary.

Baumstein, A., and Anderson, J., 2003, Wavefield extrapolation in laterally varying VTI media: 73rd Ann. Internat. Mtg.: Soc. of Expl. Geophys., 945-948.

Baysal, E., Kosloff, D. D., and Sherwood, J. W. C., 1983, Reverse-time migration: Geophysics, 48, 1514-1524.

Bagaini, C., Bonomi, E., and Pieroni E., 1995, Data parallel implementation of 3D PSPI: 65th Ann. Internat. Mtg.: Soc. of Expl. Geophys., 188-191.

Banik, N. C., 1984, Velocity anisotropy of shales and depth estimation in the North Sea basin: Geophysics, 49, 1411-1419.

Beasley C. and Lynn W., 1992, The zero-velocity layer: Migration from irregular surfaces: Geophysics, 57, 1435-1443.

Berryhill J. R., 1984, Wave equation datuming before stack: Geophysics, 49, 2064-2066.

Bevc, D., 1997, Imaging complex structures with semirecursive Kirchhoff migration: Geophysics, 48, 1514-1525.

Bevc, D., and Biondi, B., 2002, Which depth imaging method should we use? A road map in the maze of 3-D depth imaging: 72nd Ann. Internat. Mtg., Soc. of Expl. Geophys., Expanded Abstracts, 1236-1239.

Berkhout, A. J., 1981, Wave field extrapolation techniques in seismic migration, a tutorial: Geophysics, 46, 1638-1656.

Berryhill, J. R., 1984, Wave equation datuming before stack (short note): Geophysics, 49, 2064-2067.

Cerveny, V., and Hron, F., 1980, The ray series method and dynamic ray-tracing system for three-dimensional inhomogeneous media: Bull. Seis. Soc. Am., 70, 47-77.

Chang W. F., and McMechan G. A., 1987a, Reverse-time migration of offset vertical seismic profiling data using the excitation-time imaging condition: Geophysics, 51, 67-84.

Chang W. F., and McMechan G. A., 1987b, Elastic reverse-time migration: Geophysics, 52, 1365-1375.

Chang, W. F., and McMechan, G. A., 1994, 3-D elastic prestack reverse-time depth migration: Geophysics, 59, 597-609.

Claerbout, J. F., 1971, Toward a unified theory of reflector mapping: Geophysics, 36, 467-481.

Claerbout, J.F., 1985, Imaging the Earth's interior: Blackwell Scientific Publications, Inc.

Clayton, R., and Engquist, B., 1977, Absorbing boundary conditions for acoustic and elastic wave equations: Bull. Seis. Soc. Am., 67, 1529-1540.

Crampin, S., 1985, Evaluation of anisotropy by shear-wave splitting: Geophysics, 50, 142-152.

Dablain, M. A., 1986, The application of higher differencing to the scalar wave equation: Geophysics, 51, 54-66.

Daley, P. F., and Hron, F., 1977, Reflection and transmission coefficients for transversely isotropic media: Bull., Seis. Soc. Am., 67, 661-675.

Dong Y., Multi-wave NMO velocity fracture detection and finite element–finite difference reverse-time migration, Ph.D. thesis: Tsinghua University, 2000.

Du, X., Bancroft J. C., 2004, 2-D wave equation modeling and migration by a new finite difference scheme based on the Galerkin method: 74th Mtg. Soc. Expl. Geophys., Expanded Abstracts, 1107-1110.

Du, X., Bancroft, J., C., 2005, 2-D scalar wave extrapolator using FE-FD operator for irregular grids: 2005 CSEG National Convention, 101-104.

Du, X., Bancroft J. C. and Lines L. R., 2005, Reverse-time migration for tilted TI media: 75th Mtg. Soc. Expl. Geophys., Expanded Abstracts, 1930-1933.

Du, X., Bancroft J. C., Lawton D. C. and Lines L. R., 2006, Evaluations of prestack anisotropic Kirchhoff, phase-shift-plus-interpolation and reverse-time depth migration methods for dipping TI media: 76th Mtg. Soc. Expl. Geophys., Expanded Abstracts, 179-183.

Engquist, B., and Osher, S., 1980, Stable and entropy satisfying approximations for transonic flow calculations: Math. Comp., 34. no 149 45-75.

Ferguson R. J., 1999, Seismic imaging in heterogeneous anisotropic media by nonstationary phase shift: Ph.D. thesis, University of Calgary.

Ferguson, R., and Margrave G. F., 1998, Depth migration in TI media by non-stationary phase shift. 68th SEG meeting, New Orleans, U.S.A., Expanded Abstracts, 1831-1834.

Fletcher, R. f., Flowler, P., and Kitchenside, P., 2005, Suppressing artificats in prestack reverse time migration: 75th Ann. Internat. Mtg., Soc. Of Expl. Geophys., 2048-2051.

Fornberg, B. 1987, The pseudospectral method - Comparisons with finite differences for the elastic wave equation: Geophysics, 52, 483-501.

Gazdag, J., 1978, Wave-equation migration by phase shift: Geophysics, 43, 1342-1351.

Gazdag, J. and Sguazzero, P., 1984, Migration of seismic data by phase shift plus interpolation: Geophysics, 49, 124-131.

Gray, S. H., Etgen, J., Dellinger, J. and Whitmore, D., 2001, Seismic migration problems and solutions: Geophysics, 66, 1622-1640.

Gray, S. H. and Marfurt, K. J., 1995, Migration from topography: Improving the near surface image: Can. J. Expl. Geophys., 31, 18-24.

Gray, S. H., and May, W. P., 1994, Kirchhoff migration using eikonal equation traveltimes: Geophysics, 59, 810–817.

Grechka, V., Zhang, L. and Rector, J., 2004, Shear waves in acoustic anisotropic media: Geophysics, 69, 576-582.

Grech, K. M. G., 2002, Depth imagining of fault-fold structures: Ph.D. thesis, University of Calgary.

Hamming. A. R., 1962, Numerical methods for scientists and engineers: New York. McGraw-Hill Book Company. Inc.

Han, B., 1998, A comparison of four depth-migration methods: 68th Ann. Internat. Mtg., Soc. Of Expl. Geophys., 1104-1107.

Han, B., 2000, Two prestack converted-wave migration algorithms for vertical transverse isotropy: 70th Ann. Internat. Mtg., Soc. Of Expl. Geophys., 461-464.

Hill, N. R., 2001, Prestack Gaussian-beam depth migration: Geophysics, 66, 1240-1250.

Hughes, Thomas J. R., 1987, The finite element method: linear static and dynamic finite element analysis, Prentice-Hall, Inc.

Isaac, J. H., and Lawton, D. C., 1999, Image mispositioning due to dipping TI media: A physical seismic modeling study: Geophysics, 64, 1230–1238.

Johnston, J. E., and Christensen, N. I., 1995, Seismic anisotropy of shales: Journal of Geophysical Prospecting, 7, 158-182.

Jones, L. E. A, and Wang, H. F., 1981, Ultrasonic velocities in Cretaceous shales from the Williston Basin: Geophysics, 46, 288-297.

Kay I. and Krebes E. S., 1999, Applying finite element analysis to the memory variable formulation of wave propagation in anelastic media: Geophysics, 64, 299-307.

Klie, H., and Toro, W., 2001, A new acoustic wave equation for modeling in anisotropic media: 72nd Annual International meeting, SEG, Expanded Abstracts, 1171–1174.

Krebes, E. S., 2003, Seismic theory and methods: Course Notes, University of Calgary.

Kumar, D., Sen M. K., and Ferguson, R. J., 2004, Traveltime calculation and prestack depth migration in tilted transversely isotropic media: Geophysics, 69, 37-44.

Larner, K., and Cohen, J. K., 1993, Migration error in transversely isotropic media with linear velocity variation with depth: Geophysics, 58, 1454-1467.

Lebel, D., Langenberg, W., and Mountjoy, E. W., 1996, Structure of the central Canadian Cordilleran thrust-and-fold belt, Athabasca-Brazeau area, Alberta: A large complex intercutaneous wedge: Bull. Can. Petr. Geol., 44, 282–298.

Lee, M. W., and S. Y. Suh, 1985, Optimization of one-way wave equations: Geophysics,

50, 1634–1637.

Leslie, J. M., and Lawton, D. C., 1999, A refraction-seismic field study to determine the anisotropic parameters of shales: Geophysics, 64, 1247-1252.

Lines, L. R., Slawinski, R. and Bording P., 1999, A recipe for stability of finite-difference wave-equation computations: Geophysics, 64, 967-969.

Lines, L., Wu, W., Lu, H., Burton, A. and Zhu, J., 1996, Migration from topography: experience with an Alberta Foothills data set: Can. J. Expl. Geophys., 32, no. 01, 24-30.

Love, A. E. H., 1927, A treatise on the mathematical theory of elasticity: Cambridge University Press, Cambridge.

Lysmer, J., and Drake, L.A., 1972, A finite element method for seismology; Ch.6 in B. Alder, S. Fernbach and B.A. Bolt, Ed., Methods in Computational Physics 11, Seismology, Aca. Press.

Margrave, G. F., and Ferguson, R. J., 1999, Wavefield extrapolation by nonstationary phase shift: Geophysics, 64, 1067-1078.

McMechan, G. A., 1983, Migration by extrapolation of time-dependent boundary values: Geophysical Prospecting, 31, 413-420.

Mi, Y., and Margrave, G. F., 2001a, Dual extrapolation algorithms for Fourier shot record migration, 71st Ann. Internat. Mtg, Soc. Expl. Geophys., Expanded Abstract, 1021-1024.

Mi, Y., and Margrave, G. F., 2001b, Prestack depth imaging from topography with a Fourier method, 71st Ann. Internat. Mtg, Soc. Expl. Geophys., Expanded Abstract, 1045-1048.

Mulder W. A., and Plessix R. E., 2004, One-way and two-way wave equation migration: Geophysics, 69, 1491-1504.

Mulder,W. A., and Plessix R.-E., 2002, Time-versus frequency-domain modelling of seismic wave propagation: 64th Annual Conference & Exhibition, European Association of Geoscientists and Engineers, Extended Abstracts, E015.

Mufti I. R., Pita J. A., and Huntley R. W., 1996, Finite-difference depth migration of exploration-scale 3-D seismic data: Geophysics, 61, 776-794.

Nichols, D. E., 1996, Maximum energy traveltimes calculated in the seismic frequency band, Geophysics, 61, 253-263.

Popovici M., and Sethian J., 1998, Three dimensional traveltimes using the fast marching method, 60th annual Conference & Exhibition, European Association of Geoscientists and Engineers, Extended Abstracts, E666.

Reshelf M., 1991, Depth migration from irregular surfaces with depth extrapolation methods: Geophysics, 56, 119-122.

Ristow, D., and Ruhl, T., 1994, Fourier finite-difference migration: Geophysics, 59, 1882–1893.

Ristow, D., and Ruhl, T., 1997, Migration in transversely isotropic media using implicit operators: Soc. of Expl. Geophys., 67th Ann. Internat. Mtg, 1699-1702.

Rousseau, J. H. L., 1997, Depth migration in heterogeneous, transversely isotropic media with the phase-shift-plus-interpolation method: 67th Annual International Meeting, SEG, Expanded Abstracts, 1703–1706.

Schneider, W., 1978, Integral formulation of migration in two and three dimension: Geophysics, 43, 49-76.

Shan, G., 2006, Optimized implicit finite-difference migration for VTI media: 76th Annual International Meeting, SEG, Expanded Abstracts, 2367–2370.

Shan, G., and B. Biondi, 2005, Imaging steeply dipping reflectors in TI media by wavefield extrapolation: 75th Annual International Meeting, SEG, Expanded Abstracts, 1906–1909.

Shtivelman, V., and Canning, A., 1988, Datum correction by wave equation extrapolation: Geophysics, 53, 1311-1322.

Soubaras, R., 2002, Comparison of Kirchhoff and wave-equation prestack migration on OBC data: 72nd Ann. Internat. Mtg., Soc. of Expl. Geopohys., Expanded Abstracts, 1244-1247.

Stoffa, P. L., Fokkema, J. T., de Luna Freire, R. M. and Kessinger, W. P., 1990, Split step Fourier migration: Geophysics, 55, 410-421.

Teng, Y. C., and Dai, T. F, 1989, Finite-element prestack reverse-time migration for elastic wave: Geophysics 54, 1204-1208.

Tsvankin, I., 1996, P-wave signatures and notation for transversely isotropic media: An overview: Geophysics, 61, 467-483.

Tsvankin I., and Thomsen L., 1994, Nonhyperbolic reflection moveout in anisotropic media: Geophysics, 59, 1290-1304.

Tong F., Joe A. D., Gary E. M., Jeffrey L. H., and Samuel H. G., 1998, Anisotropic true-amplitude migration: SEG Expanded Abstracts 17, 1677－1679.

Thomsen, L., 1986, Weak elastic anisotropy: Geophysics, 51, 1954–1966.

Uzcategui, O., 1995, Depth migration in transversely isotropic media with explicit operators.: Geophysics, 60, 1819-1829.

Valenciano, A. A., and Biondi, B., 2002, Deconvolution imaging condition for reverse-time migration: SEP Report, 112, 83-96.

Van Trier, J., and Symes, W. W., 1991, Upwind finite-difference calculation of traveltimes: Geophysics, 56, 812-821.

Vernik, L., and Liu, X., 1997, Velocity anisotropy in shales: A petrophysical study: Geophysics, 62, 521-532.

Versteeg, R., 1993, Sensitivity of prestack depth migration to the velocity model: Geophysics, 58, 873–882.

Vestrum, R. W., 2003, Imaging below dipping anisotropic strata: Ph.D. thesis, University of Calgary.

Vestrum, R. W., Lawton, D. C. and Schmid, R., 1999, Imaging structures below dipping TI media: Geophysics, 64, 1239-1246.

Vidale, J. E., 1990, Finite-difference calculation of traveltimes in three dimensions: Geophysics, 55, 521-526.

Virieux J., 1986, P-SV wave propagation in heterogeneous media: Velocity-stress finite-difference method, Geophysics, 51, 889-900.

Wait, J. R., 1959, Electro-magnetic radiation from cylindrical structures: Pergamon Press Inc.

Whitmore, N. D., 1983, Iterative depth migration by backward time propagation: 53rd Ann. Internat. Mtg., Sot. Expl. Geophys., Expanded Abstracts, 382-385.

Wu W.-J., Lines, L. R., Burton A., Lu H.-X., Zhu J., Jamison W. and Bording R. P., 1998, Prestack depth migration of an Alberta Foothills data set – Husky experience: Geophysics, 63, 392-398.

Wu, W., Lines, L. R., and Lu, H., 1996, Analysis of higher-order finite difference schemes in 3-D reverse-time migration: Geophysics, 61, 845–856.

Xu, S., chauris, H., Lambare, G., and Nobel, M., 1998, Common angle image gather: a strategy for imaging complex media. 68th Ann. Internat. Mtg., Soc. Expl. Geophys., Expanded Abstracts, 1538-1541.

Yilmaz, O., 1987, Seismic Data Processing: Society of Exploration Geophysicists.

Yoon, K., Shin, C, Suh, S., Lines, L. R., and Hong S., 2003, 3D reverse-time migration using acoustic wave equation: An experience with the SEG/EAGE data set: The Leading Edge, 22, 38-41.

Yoon, K., Marfurt, K. J., and Starr, W., 2004, Challengers in reverse-time migration: 74th Ann. Internat. Mtg., Soc. Of Expl. Geophys., MIG4.8, 1057-1060

Zhang, L., Rector, J. W., and Hoversten, G. M., 2002, An eikonal solver in tilted TI media: 72nd Annual International Meeting, SEG, Expanded Abstracts, 1955–1958.

Zhang, L., Rector, J. W., and Hoversten, G. M., 2003, An acoustic wave equation for modeling in tilted TI media: 73rd Annual International Meeting, SEG, Expanded Abstracts, 153–156.

Zhang, J., Verschuur, D. J., and Wapenaar, C. P. A., 2001, Depth migration of shot records in heterogeneous, transversely isotropic media using optimum explicit operators: Geophys. Prosp., 49, 287-299.

Zhu J., and Lines L.R., 1998, Comparison of Kirchhoff and reverse-time migration methods with applications to prestack depth imaging of complex structures: Geophysics, 63, 1166-1176.

Zhu T. -F., Gram S. H., and Wang D.-L., 2006, Prestack Gaussian-beam depth migration in anisotropic media: 76th Ann. Internat. Mtg., Soc. of Expl. Geophys., 2362-2365.

Appendix A: A quartic dispersion equation for P-waves in weakly anisotropic media and its analytical solution

The frequency dispersion relationship can be described with the following equation

$$(k_x^2 + k_z^2)\frac{\omega^2}{v_{p0}^2} = (k_x^2 + k_z^2)^2 + (2\delta\sin^2\phi\cos^2\phi + 2\varepsilon\cos^4\phi)k_x^4 + (2\delta\sin^2\phi\cos^2\phi + 2\varepsilon\sin^4\phi)k_z^4$$

$$+ (-\delta\sin^2 2\phi + 3\varepsilon\sin^2 2\phi + 2\delta\cos^2 2\phi)k_x^2 k_z^2 + (\delta\sin4\phi - 4\varepsilon\sin2\phi\cos^2\phi)k_x^3 k_z \quad . \text{(A-1)}$$

$$+ (-\delta\sin4\phi - 4\varepsilon\sin2\phi\sin^2\phi)k_x k_z^3$$

To simplify the expression, it can be written as the following quartic equation

$$k_z^4 + a_3 k_z^3 + a_2 k_z^2 + a_1 k_z + a_0 = 0, \tag{A-2}$$

where

$$a_4 : 2\delta\sin^2\phi\cos^2\phi + 2\varepsilon\sin^4\phi + 1,$$

$$a_3 : (-\delta\sin4\phi - 4\varepsilon\sin2\phi\sin^2\phi)k_x / a_4,$$

$$a_2 : [(-\delta\sin^2 2\phi + 3\varepsilon\sin^2 2\phi + 2\delta\cos^2\phi + 2)k_x^2 - \frac{\omega^2}{v_{p0}^2}]/a_4,$$

$$a_1 : (\delta\sin4\phi - 4\varepsilon\sin2\phi\cos^2\phi)k_x^3 / a_4,$$

$$a_0 : [(2\delta\sin^2\phi\cos^2\phi + 2\varepsilon\cos^4\phi + 1)k_x^4 - \frac{\omega^2}{v_{p0}^2}k_x^2]/a_4.$$

To get the analytical solution, we try to find the real root of the cubic equation

$$u^3 - a_2 u^2 + (a_1 a_3 - 4a_0)u - (a_1^2 + a_0 a_3^2 - 4a_0 a_2) = 0, \tag{A-3}$$

and determine the four roots of the quartic as solutions of the two quadratic equations (Abramowitz and Stegun, 1970)

$$v^2 + [\frac{a_3}{2} \mp (\frac{a_3^2}{4} + u_1 - a_2)^{\frac{1}{2}}] + \frac{u_1}{2} \mp [(\frac{u_1}{2})^2 - a_0]^{\frac{1}{2}} = 0. \tag{A-4}$$

Considering the cubic equation $z^3 + a_2 z^2 + a_1 z + a_0 = 0$, let

$$m = \frac{1}{3} a_1 - \frac{1}{9} a_2^2, \quad n = \frac{1}{6}(a_1 a_2 - 3a_0) - \frac{1}{27} a_2^3.$$

If $m^3 + n^2 > 0$, one real root and a pair of complex conjugate roots,

If $m^3 + n^2 = 0$, all roots real and at least two are equal,

If $m^3 + n^2 < 0$, all roots real.

As for the cubic equation (A-2), the three roots are given as follows (Abramowitz and Stegun, 1970):

Let $s_1 = [r + (q^3 + r^2)^{\frac{1}{2}}]^{\frac{1}{3}}$, $s_2 = [r - (q^3 + r^2)^{\frac{1}{2}}]^{\frac{1}{3}}$,

where

$$q = \frac{1}{3} a_1 a_3 - \frac{1}{9} a_2^2 - \frac{4}{3} a_0, \quad r = \frac{1}{27} a_2^3 + \frac{1}{2} a_1^2 + \frac{1}{2} a_0 a_3^2 - \frac{4}{3} a_0 a_2 - \frac{1}{6} a_1 a_2 a_3,$$

then

$$R_1 = (s_1 + s_2) + \frac{a_2}{3},$$

$$R_2 = \frac{1}{2}(s_1 + s_2) + \frac{a_2}{3} + \frac{i\sqrt{3}}{2}(s_1 - s_2),$$

$$R_3 = \frac{1}{2}(s_1 + s_2) + \frac{a_2}{3} - \frac{i\sqrt{3}}{2}(s_1 - s_2).$$